Short-Period Building Collapse Performance and Recommendations for Improving Seismic Design

Volume 3 – Study of One-to-Four Story Special Reinforced Masonry Shear Wall Buildings

FEMA P-2139-3 / October 2020

FEMA

nehrp

Short-Period Building Collapse Performance and Recommendations for Improving Seismic Design

Volume 3 – Study of One-to-Four Story Special Reinforced Masonry Shear Wall Buildings

Prepared by

APPLIED TECHNOLOGY COUNCIL
201 Redwood Shores Parkway, Suite 240
Redwood City, California 94065
www.ATCouncil.org

Prepared for

FEDERAL EMERGENCY MANAGEMENT AGENCY
Mai (Mike) Tong, Project Officer
Robert D. Hanson, Technical Advisor
Washington, D.C.

APPLIED TECHNOLOGY COUNCIL
Jon A. Heintz, Project Executive
Justin Moresco, Project Manager
Scott D. Schiff, Associate Project Manager

PROJECT TECHNICAL COMMITTEE
Charles A. Kircher (Project Tech. Director)
Jeffrey W. Berman
Kelly Cobeen
J. Daniel Dolan
Andre Filiatrault
James R. Harris
Gregory Kingsley
Dawn Lehman
Weichiang Pang
P. Benson Shing

SOIL-STRUCTURE INTERACTION WORKING GROUP
Lisa Star
Jonathan P. Stewart

PROJECT REVIEW PANEL
Anthony Court*
William T. Holmes
Onder Kustu
James O. Malley
Steve Pryor
Jason Thompson

MASONRY WORKING GROUP
Jianyu Cheng
Jeff Corson
Andreas A. Koutras
Linda Peters

*ATC Board Representative

FEMA

nehrp

Notice

Any opinions, findings, conclusions, or recommendations expressed in this publication do not necessarily reflect the views of the Applied Technology Council (ATC), the Department of Homeland Security (DHS), or the Federal Emergency Management Agency (FEMA). Additionally, neither ATC, DHS, FEMA, nor any of their employees, makes any warranty, expressed or implied, nor assumes any legal liability or responsibility for the accuracy, completeness, or usefulness of any information, product, or process included in this publication. Users of information from this publication assume all liability arising from such use.

Cover photograph – Two-story special reinforced masonry shear wall building (credit: T. Escobar, Masonry Institute of America).

Foreword

Most buildings in the United States are less than five stories tall. These low-rise buildings typically possess fundamental periods less than one-half second and thus are referred to as short-period buildings. Many commonly used analytical models have predicted that short-period buildings designed to current building codes are likely to suffer severe damage or collapse during design-level earthquakes. However, post-earthquake field investigations have not confirmed these predictions. Since this uncertainty is found across all types of building structures and construction materials permitted by current building codes and standards, it decreases confidence in the earthquake resilience of such code-compliant buildings. This technical resource series provides the findings and conclusions related to this issue and recommendations for improving seismic design of short-period buildings.

The National Earthquake Hazards Reduction Program (NEHRP) at the Federal Emergency Management Agency (FEMA) has a responsibility to help translate and implement new knowledge and research results to increase earthquake resilience nationwide. This FEMA-supported multi-year project series has successfully applied new analytical modeling techniques to investigate the long-standing problem of short-period building seismic collapse performance. This report is the third volume of the series, and it summarizes a study on one-to-four story special reinforced masonry shear wall buildings designed in accordance with the ASCE/SEI 7-10 standard for high-seismic regions. The study has examined various contributing factors to the uncertainty. Through advanced modeling and parametric evaluation, the study has shown that the uncertainty can be resolved and further improvements to seismic design of special reinforced masonry shear wall buildings can be achieved.

FEMA is grateful to the Applied Technology Council (ATC) for managing this sophisticated multi-year project series to a successful completion, to the Project Technical Committee and the Project Review Panel for their dedicated effort leading to invaluable technical findings and recommendations. FEMA is also thankful to the project workshop participants for their scrutiny and valuable comments. Resolving the uncertainty in short-period building seismic collapse performance will strengthen confidence in seismic building codes. This project series will also contribute to improving seismic design and predicting collapse potential of short-period buildings in high-seismic communities in the nation.

Federal Emergency Management Agency

Preface

Recent analytical studies investigating a wide range of modern seismic-force-resisting systems have predicted collapse rates for short-period buildings that are significantly larger than those observed in earthquakes during the past 50 years. This gap between analytically predicted and historically observed collapse rates is known as the *short-period building seismic performance paradox*. Analytically predicted collapse rates for short-period buildings are also generally larger than maximum collapse rates used in national model codes and standards to establish seismic design requirements. If these analytical predictions are accurate, it means that the goal of acceptable collapse performance for all seismic-force-resisting systems at all building periods is not being achieved.

In 2013, the Applied Technology Council (ATC) was awarded the first in a series of task orders under contracts HSFE60-12-D-0242 and HSFE60-17-D-0002 with the Federal Emergency Management Agency (FEMA) to investigate "Solutions to the Issue of Short Period Building Performance," designated the ATC-116 Project series. The purpose of this series of projects was to investigate the response behavior and collapse performance of different structural systems and to identify causes and develop solutions for the short-period building seismic performance paradox. Studies investigated three structural systems: wood light-frame, special reinforced masonry shear wall, and steel special concentrically braced frame (SCBF) systems.

This report, which focuses on the investigation of special reinforced masonry shear wall systems, is one of four principal products of the ATC-116 series of projects:

- FEMA P-2139-1, *Short-Period Building Collapse Performance and Recommendations for Improving Seismic Design, Volume 1 – Overarching Findings, Conclusions, and Recommendations*
- FEMA P-2139-2, *Short-Period Building Collapse Performance and Recommendations for Improving Seismic Design, Volume 2 – Study of One-to-Four Story Wood Light-Frame Buildings*
- FEMA P-2139-3, *Short-Period Building Collapse Performance and Recommendations for Improving Seismic Design, Volume 3 – Study of One-to-Four Story Special Reinforced Masonry Shear Wall Buildings*

- FEMA P-2139-4, *Short-Period Building Collapse Performance and Recommendations for Improving Seismic Design, Volume 4 – Study of One-to-Four Story Steel Special Concentrically Braced Frame Buildings*

These reports are the result of a collaborative effort of more than 30 individuals tasked with the design of archetypes, development of numerical models, and interpretation of results across all three structural systems, in addition to the many others who participated in review workshops where draft versions of the reports were presented and discussed. ATC is indebted to the leadership of Charlie Kircher, Project Technical Director, and to the other members of the ATC-116 project team for their efforts in developing these reports. The Project Technical Committee, consisting of Jeff Berman, Kelly Cobeen, Dan Dolan, Andre Filiatrault, Jim Harris, Greg Kingsley, Dawn Lehman, Weichiang Pang, and Benson Shing, managed and performed the technical development effort.

Jeff Corson and Linda Peters assisted in the development of the design of the reinforced masonry archetypes, and Jianyu Cheng and Andreas Koutras assisted in the reinforced masonry numerical modeling. Lisa Star provided technical guidance on the development of the reinforced masonry soil-structure interaction and foundation flexibility parametric study. The Project Review Panel, consisting of Tony Court, Bill Holmes, Onder Kustu, Jim Malley, Steve Pryor, and Jason Thompson, provided technical review and advice at key stages of the work.

ATC also gratefully acknowledges Mike Tong (FEMA Project Officer) and Bob Hanson (FEMA Technical Advisor) for their input and guidance in the preparation of this report, Scott Schiff who assisted in ATC project management, and Carrie J. Perna who provided ATC report production services. The names and affiliations of all who contributed to this report, including those who participated in the review workshop focused on reinforced masonry systems, are provided in the list of Project Participants at the end of this report.

Justin Moresco
ATC Director of Projects

Jon A. Heintz
ATC Executive Director

Table of Contents

List of Figures

List of Tables

Chapter 1
Introduction

This report describes the approach, analyses, findings, conclusions, and recommendations for one in a series of studies on the gap between analytically predicted and historically observed earthquake-induced collapse rates of short-period buildings. It presents work focused on special reinforced masonry shear wall buildings (herein referred to as "reinforced masonry" systems). The Applied Technology Council (ATC) was commissioned by the Federal Emergency Management Agency (FEMA) to conduct these studies as part of the ATC-116 Project series, "Solutions to the Issue of Short Period Building Performance."

Short-period buildings, such as low-rise residential and commercial buildings, comprise a major portion of the building stock in U.S. communities with high-seismic hazard. The gap between analytically predicted and historically observed collapse rates for short-period buildings exists across many seismic-force-resisting systems and construction materials. As a result, it is believed that the seismic collapse performance for short-period buildings is not accurately predicted by current analytical models. Based on a review of previous studies and available research and data, three seismic-force-resisting systems were selected for investigation: wood light-frame, reinforced masonry, and steel special concentrically braced frame (SCBF) systems.

The subject of this report is buildings constructed using reinforced masonry systems. Studies on buildings constructed using wood light-frame or steel SCBF systems are described in separate reports. An additional report compares results from all three studies to identify commonalities for the possible extension of the findings, conclusions, and recommendations to other seismic-force-resisting systems and construction materials. The FEMA P-2139 series of reports include the following:

- FEMA P-2139-1, *Short-Period Building Collapse Performance and Recommendations for Improving Seismic Design, Volume 1 – Overarching Findings, Conclusions, and Recommendations*
- FEMA P-2139-2, *Short-Period Building Collapse Performance and Recommendations for Improving Seismic Design, Volume 2 – Study of One-to-Four Story Wood Light-Frame Buildings*

- FEMA P-2139-3, *Short-Period Building Collapse Performance and Recommendations for Improving Seismic Design, Volume 3 – Study of One-to-Four Story Special Reinforced Masonry Shear Wall Buildings*
- FEMA P-2139-4, *Short-Period Building Collapse Performance and Recommendations for Improving Seismic Design, Volume 4 – Study of One-to-Four Story Steel Special Concentrically Braced Frame Buildings*

1.1 Background and Purpose

At the time this study began, commercial buildings were designed in accordance with ASCE/SEI 7-10, *Minimum Design Loads for Buildings and Other Structures* (ASCE, 2010), which was adopted by reference in the 2015 edition of the *International Building Code* (IBC) (ICC, 2015). Design seismic loads in ASCE/SEI 7-10 are based on the risk-targeted maximum considered earthquake (MCE_R) ground motions, which were introduced in FEMA P-750, *NEHRP Recommended Seismic Provisions for New Buildings and Other Structures* (FEMA, 2009a). Buildings designed and constructed in accordance with national model codes and seismic design standards (e.g., ASCE/SEI 7-10) are expected to meet general seismic performance targets, which are described in terms of not exceeding a specified percent probability of collapse given MCE_R ground motions. For reference, a collapse probability of no more than 10 percent, given MCE_R ground motions, is the anticipated "reliability" in ASCE/SEI 7-10 (Table C1.3.1b) for Risk Category II buildings, which constitute the vast majority of all buildings. Further, the use of MCE_R ground motions in building design is intended to provide a reasonable assurance of seismic performance for all buildings—regardless of building period, seismic-force-resisting system, or other characteristic—designed in accordance with the governing building code.

Studies conducted before the start of the ATC-116 Project series have used the methodology described in FEMA P-695, *Quantification of Building Seismic Performance Factors* (FEMA, 2009b), to evaluate the collapse performance of common code-permitted seismic-force-resisting systems. For example, one widely cited previous collapse performance study is described in NIST GCR 12-917-20, *Tentative Framework for Development of Advanced Seismic Design Criteria for New Buildings* (NIST, 2012a). This and other similar studies have shown that many seismic-force-resisting systems achieve the collapse performance target (i.e., less than a 10 percent probability of collapse given MCE_R ground motions). However, these studies have also found that shorter-period buildings have calculated probabilities of collapse that exceed those of longer-period buildings, and generally exceed the 10 percent target for acceptable collapse performance.

This can be observed in Figure 1-1, taken from NIST GCR 12-917-20. The figure plots the calculated collapse probabilities for groups of structural systems, as identified in Table 12.2-1 of ASCE/SEI 7-10, over a range of periods. Bearing wall systems (diamonds) include special reinforced masonry shear walls (A.7), which are the focus of this report, ordinary reinforced masonry shear walls (A.9), and light-frame (wood) walls with wood structural panel sheathing (A.15). Building frame systems (squares) include steel special concentrically braced frames (B.2), special reinforced concrete shear walls (B.4), ordinary reinforced concrete shear walls (B.5), and steel buckling-restrained braced frames (B.25). Moment frame systems (triangles) include steel special moment frames (C.1), special reinforced concrete moment frames (C.5), and ordinary reinforced concrete moment frames (C.7)

In the figure, FEMA P-695 collapse performance studies on a variety of structural systems over a range of periods suggest that, for systems with design periods less than about 0.5 seconds, the probability of collapse given MCE_R ground motions increases significantly as the design period decreases. If these analytical predictions are accurate, then the goal of acceptable collapse performance for all seismic-force-resisting systems at all building periods is not being achieved, and short-period buildings are exceeding the 10 percent collapse performance target of ASCE/SEI 7.

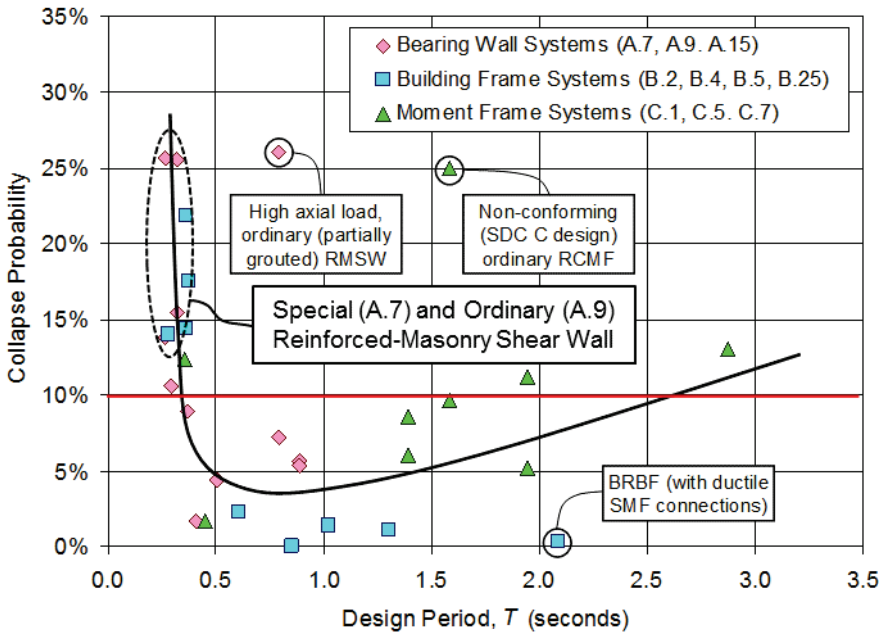

Figure 1-1 Trends in the probability of collapse of selected systems as a function of design period (adapted from NIST, 2012a).

The importance of building period on the calculation of peak response of inelastic systems dates back to studies of response and design spectra in the 1960s and 1970s by Veletsos, Newmark, and others (e.g., Veletsos and Newmark, 1960). These studies found that the ratio of inelastic displacement to elastic displacement of simple single-degree-of-freedom numerical models was period dependent and increased as the periods of the numerical models decreased, implying worse collapse performance for shorter-period buildings.

Findings from other numerical studies of earthquake response and collapse performance are consistent and suggest that seismic design coefficients (e.g., R) could be period dependent or more stringent for shorter-period buildings (e.g., Miranda and Bertero, 1994). Although ASCE/SEI 7 does not include period-dependent seismic modification factors, the underlying concepts can be found in other seismic codes. For example, Section 5.2.3 of Eurocode 8 (CEN, 2004) increases inelastic seismic demands as a function of period for detailing of reinforced-concrete elements in areas of plastic hinging when the building period is relatively short (i.e., T less than T_s, where T_s is the code-defined transition period between spectral response domains of constant acceleration and constant velocity). Explicit incorporation of period-dependent properties can also be found in the "coefficient method" of ASCE/SEI 41-17, *Seismic Evaluation and Retrofit of Existing Buildings* (ASCE, 2017).

Trends in observed earthquake damage of short-period buildings, however, do not support the high collapse probabilities shown in Figure 1-1. Analysis of available historical data on short-period building performance is described in Chapter 2. For example, reconnaissance following the 1994 Northridge earthquake found that modern reinforced masonry buildings experienced little damage, and studies of reinforced masonry buildings within the Central Business District after the 2011 Christchurch, New Zealand earthquake documented only 5 percent having severe damage. These observations are contrary to the results of analytical studies used to predict collapse probabilities. Because observed damage in short-period buildings is less than what is implied by the body of analytical results available in the literature, the opinion of many structural engineers suggests that numerical models overestimate the actual collapse risk of short-period buildings.

The apparent discrepancy between analytical prediction of collapse performance and the opinions and observations of structural engineers has been designated the *short-period building seismic performance paradox*. With the standardized collapse evaluation methodology of FEMA P-695, additional testing of structural elements and assemblies, and the evolution of high-speed computer processing, we now have the capability to effectively investigate and resolve this paradox.

Given this context, the purpose of the ATC-116 Project series was to investigate the response behavior and collapse performance of different structural systems. The results of this work are intended to:

- Identify the causes of the short-period building seismic performance paradox, quantify factors contributing to short-period building performance, and develop solution concepts.
- Improve and validate numerical modeling methods for short-period buildings to more accurately capture response behavior and collapse performance characteristics.
- Improve code seismic design methods and engineering practices for short-period buildings so that seismic performance targets are achieved across all seismic-force-resisting systems and all design periods.
- Inform future research so that better data and improved numerical modeling can be used in the development of more efficient and effective structural systems, seismic assessment methodologies, and engineering design procedures.

1.2 Approach and Scope

A phased approach for investigation was developed and presented in the ATC-116 report, *Roadmap for Solutions to the Issue of Short Period Building Performance* (ATC, 2015). Many factors are thought to contribute to the apparent discrepancy between analyzed and observed seismic performance of short-period buildings. Reasons for the paradox could include an underestimation of the peak strength and post-peak capacity of short-period buildings, an overestimation of the demands on short-period buildings, or a combination of both. Possible causes include building configuration issues (e.g., incorporation of all structural and nonstructural components, including interior and exterior wall finishes, that contribute to building strength and stiffness), hysteretic response backbone curve issues (e.g., realistic characterization of peak strength and collapse displacement capacity), and other factors (e.g., soil-structure interaction and foundation flexibility) that affect building response behavior and collapse performance.

Overall, the approach was to: (1) establish benchmarks for the historically observed performance of short-period buildings; (2) conduct parametric analytical studies on archetypical short-period buildings using advanced numerical models and the latest available research and test data; and (3) identify modeling parameters or building characteristics that provide the best match between the simulated and benchmark performance.

Although there are a number of parameters by which seismic performance can be measured, these studies were primarily interested in collapse performance as measured by the conditional probability of collapse given a ground motion intensity (e.g., MCE_R ground motions), based on observations from historical earthquake data, as described in Chapter 2, or collapse statistics obtained from Incremental Dynamic Analysis (IDA), as described in Chapter 5.

For the purpose of these studies, short-period buildings were defined as buildings with first-mode periods less than about 0.5 seconds. Studies investigated different systems, configurations, and materials commonly used in the United States for design and construction of new short-period buildings in regions of moderate, high, and very high seismicity.

To study reinforced masonry shear wall systems, a suite of archetypes, with variations in occupancy, height, and seismic-design level, were selected. Archetypes were intended to represent code-compliant modern construction for common occupancies classified under Risk Category II that routinely adopt a reinforced masonry structural system.

Three occupancies were selected for study: commercial buildings (COM); multi-family residential and hotel buildings (RES); and retail, industrial and warehouse buildings (BOX). Archetypes included one-story, two-story, and four-story buildings, all with fundamental periods below (or slightly greater than) 0.5 seconds. The key configuration and seismic-design criteria for the reinforced masonry archetypes are provided in Table 1-1, where the design period ($T = C_u T_a$) and the seismic response coefficient (C_s) were calculated in accordance with Section 12.8.2 and Section 12.8.1.1 of ASCE/SEI 7-10, respectively. The development of the reinforced masonry archetypes is described in detail in Chapter 3.

The archetype design methods and details represented typical modern practice exercised in areas of significant seismicity using the normal standard of care. In contrast with prior FEMA P-695 collapse studies, archetype configurations for each occupancy were selected to be realistic and representative of actual buildings in terms of size and proportion. They were designed to meet code-minimum base shear strength requirements, but were not biased with overstrength through deliberate conservatism in the design or understrength caused by the use of member sizes that would be considered unrealistic based on gravity load or architectural considerations.

Table 1-1 Key Configuration and Seismic Design Criteria for Reinforced Masonry Archetypes

Archetype ID	No. of Stories	Seismic Design Criteria				
		Design Period* $T = C_u T_a$ (sec)	Seismic Design Category (SDC)	MCE_R Design Parameter, S_{MS} (g)	Response Modification Coefficient (R)	Seismic Response Coefficient, C_s (g)
Commercial Buildings: High Seismic						
COM1	1	0.25	D	1.5	5	0.20
COM2	2	0.30	D	1.5	5	0.20
COM3	4	0.51	D	1.5	5	0.20
Commercial Buildings: Very High Seismic						
COM4	1	0.25	E	2.25	5	0.30
COM5	2	0.30	E	2.25	5	0.30
COM6	4	0.51	E	2.25	5	0.30
Commercial Buildings: Moderate Seismic						
COM7	1	0.25	C	0.75	5	0.10
COM8	2	0.33	C	0.75	5	0.10
COM9	4	0.55	C	0.75	5	0.10
Multi-Family Residential/Hotel Buildings: High Seismic						
RES1	4	0.51	D	1.5	5	0.20
Multi-Family Residential/Hotel Buildings: Very High Seismic						
RES2	4	0.51	E	2.25	5	0.30
Multi-Family Residential/Hotel Buildings: Moderate Seismic						
RES3	4	0.55	C	0.75	5	0.10
Retail/Industrial/Warehouse Buildings: High Seismic						
BOX1	1	0.30	D	1.5	5	0.20
Retail/Industrial/Warehouse Buildings: Very High Seismic						
BOX2	1	0.30	E	2.25	5	0.30
Retail/Industrial/Warehouse Buildings: Moderate Seismic						
BOX3	1	0.33	C	0.75	5	0.10

* $T = C_u T_a \geq 0.25$ seconds, in accordance with the analysis requirements of FEMA P-695, where the values of the parameters C_u and T_a are specified by ASCE/SEI 7-10. However, as is described in Section A.2.5, the archetypes were designed using T_a.

Archetypes were designed to capture a range of seismic ground-motion levels. "Moderate-seismic" archetypes were designed for a value of short-period MCE_R spectral response acceleration adjusted for site class effects (S_{MS}) of 0.75g. "High-seismic" archetypes were designed for an S_{MS} of 1.5g, and "very high-seismic" archetypes were designed for an S_{MS} of 2.25g. This highest value of S_{MS} is not required by FEMA P-695 (e.g., for evaluation of a

new seismic-force-resisting system proposed for ASCE/SEI 7) but was used in this study to investigate the collapse performance of short-period buildings for MCE_R ground motions that are unlikely but could occur in areas of very high seismicity (e.g., at sites located relatively close to fault rupture).

Archetype designs provided the basis for advanced numerical models. First, for each building archetype, a refined finite-element model was developed and subjected to pushover and time-history analyses. Second, the results obtained were then used to calibrate computationally efficient frame models for incremental dynamic analysis (IDA). Following FEMA P-695 procedures, the IDA results provided collapse performance metrics in terms of the conditional probability of collapse given the MCE_R ground-motion level.

To investigate the apparent discrepancy between analyzed and observed seismic performance of reinforced masonry systems, five parametric studies were performed. These included: (1) baseline configuration; (2) displacement capacity; (3) soil-structure interaction and foundation flexibility; (4) slab-induced wall coupling; and (5) coupling of flanged walls. Parametric studies are described in detail in Chapter 4 and summarized below:

Baseline Configuration Parametric Study: investigated variation in the response behavior and collapse performance of short-period reinforced masonry buildings. The study considered differences in archetype configurations compared with those of previous FEMA P-695 collapse evaluations and compared modeled "baseline" collapse performance to observed earthquake data. Baseline models considered the results of other parametric studies and incorporated a best estimate for each parameter to provide an overall best estimate of the simulated response of short-period reinforced masonry buildings.

Displacement Capacity Parametric Study: investigated the effects of collapse displacement capacity in a system on response behavior and collapse performance. Variations in the collapse displacement capacity in a system were represented by different modeling assumptions of post-capping residual strength. Comparison of response and collapse results of the archetype models with different collapse displacement capacities to results of corresponding baseline configuration archetype models provided the basis for evaluating the effects of displacement capacity.

Soil-Structure Interaction (SSI) and Foundation Flexibility Parametric Study: investigated SSI inertial and kinematic effects and foundation flexibility on response behavior and collapse performance. SSI inertial effects were modeled with a distributed set of discrete nonlinear soil springs

and dashpots below flexible foundation elements. SSI kinematic effects were evaluated by modifying the frequency content of ground-motion records (filtered records) used for response history analysis. Comparison of response and collapse results of archetype models with nonlinear soil springs, dashpots, and flexible foundation elements analyzed using filtered records to the results of corresponding baseline configuration archetype models on fixed bases (i.e., rigid foundations) analyzed using unfiltered records provided the basis for evaluating the effects of SSI and foundation flexibility.

Slab-Induced Wall Coupling Parametric Study: investigated the effects of slab-induced coupling of walls on response behavior and collapse performance. Typical design practice assumes that floor systems are effectively pin connected to walls, meaning that the floor system provides kinematic compatibility between the shear walls without inducing flexural coupling action. However, in reality, floor slabs and beams provide some additional lateral capacity to shear walls through flexural coupling. Comparison of response and collapse results of archetype models with pin-connected shear walls to results of corresponding baseline configuration archetype models with flexural-coupled shear walls provided the basis for evaluating the effects of slab-induced wall coupling.

Coupling of Flanged Walls Parametric Study: investigated the effects of coupling of flanged walls on response behavior and collapse performance. Although reinforced masonry design standards provide guidance to account for the behavior of flanged walls, in practice, designers prefer to ignore the intersecting wall effects and, instead, design the in-plane walls in each direction independently. Comparison of response and collapse results of archetype models designed without coupling of flanged walls (and modeled as acting independently) to results of corresponding baseline configuration archetype models designed with flanged walls that acted together provided the basis for evaluating the effects of coupling of flanged walls.

Due to budget and time constraints, not all reinforced masonry archetype buildings were designed, modeled, and analyzed. Table 1-2 lists the names of the archetype models for which parametric studies were completed. A total of 20 computationally efficient frame models were developed for three parametric studies (each archetype analyzed for the displacement capacity parametric study and the SSI and foundation flexibility parametric study had two variations). Although they were not all analyzed, the designs for all the baseline configuration archetype buildings were completed, and details for these designs are provided in the report. The COM occupancy was prioritized over the RES occupancy because it was anticipated that the latter typically have so much masonry wall that archetypes would need to have

heights outside the short-period range before they would experience significant cracking and yielding for study. The COM occupancy was prioritized over the BOX occupancy because the large diaphragms of the latter might put the buildings outside the short-period range. The high-seismic ground-motion level was prioritized over the moderate ground-motion level because previous FEMA P-695 studies have shown that high-seismic collapse probabilities tend to be larger, all else equal, and because high-seismic ground motion best represents strong ground motions of major earthquakes at sites not close to fault rupture. The very high-seismic ground-motion level was prioritized over the moderate ground-motion level in order to investigate the effects of unlikely but possible very strong ground motions, such as those near a fault rupture.

Table 1-2 Reinforced Masonry Building Archetypes Developed for the Parametric Studies

Archetype ID	No. of Stories	(1) Baseline Configuration	(2) Displ. Capacity	(3) Soil-Structure Interaction and Foundation Flexibility	(4) Slab-Induced Wall Coupling	(5) Coupling of Flanged Walls
Commercial Buildings: High Seismic						
COM1	1	COM1B	COM1B-DC	-	-	-
COM2	2	COM2B	COM2B-DC	COM2B2-SS	-	-
COM3	4	COM3B	COM3B-DC	-	-	-
Commercial Buildings: Very High Seismic						
COM4	1	COM4B	COM4B-DC	-	-	-
COM5	2	COM5B	COM5B-DC	-	-	-
COM6	4	COM6B	COMB6B-DC	-	-	-

1.3 Organization and Content

This report describes an investigation of the response behavior and collapse performance of short-period reinforced masonry buildings. It presents historical data on earthquake performance, typical configurations of reinforced masonry construction, development of archetype designs and numerical models, results from parametric analytical studies, solutions to the short-period building seismic performance paradox, and recommendations for seismic design, engineering practice, and future research.

Chapter 2 identifies potential sources of earthquake data, describes methods for evaluation of response behavior and collapse performance using these data, presents observations of short-period reinforced masonry building performance in past earthquakes, and establishes benchmarks of collapse performance for comparison with parametric study results.

Chapter 3 discusses factors influencing the performance of short-period reinforced masonry buildings, identifies common building types in terms of use (occupancy) and structural configuration, defines representative building archetypes and their associated design criteria, and describes the design of these archetypes.

Chapter 4 describes the methods used to develop numerical models of short-period reinforced masonry archetypes, including their calibration and validation with experimental data, and provides a detailed description of the parametric studies.

Chapter 5 summarizes the analytical results for each of the parametric studies on short-period reinforced masonry buildings.

Chapter 6 presents key findings, conclusions, and recommendations related to short-period reinforced masonry buildings.

Appendix A provides additional archetype design details that are not included in Chapter 3, including the designs of all baseline models (even those that were not analyzed).

Appendix B presents detailed information about the calibration process for the numerical models of short-period reinforced masonry archetypes.

Appendix C presents a brief introduction of SSI theory followed by a detailed description of the means and methods used in modeling the effects of SSI and foundation flexibility for this study.

Appendix D describes the organization and content of peak response quantities from each archetype that have been archived for further study and future use.

References and a list of project participants are provided at the end of this report.

Chapter 2

Observed Response and Performance Benchmarks

2.1 Introduction

This chapter summarizes the observed damage and collapse of modern short-period reinforced masonry buildings in past earthquakes, presents key results from shake-table tests, and describes the performance benchmarks used in this study for comparison with baseline archetype model results.

2.2 Observed Damage and Collapse of Modern Short-Period Reinforced Masonry Buildings in Past Earthquakes

The literature on the performance of short-period reinforced masonry buildings in earthquakes is limited and not sufficient to develop a quantitative measure of collapse failure rates. This is due, in part, to the relatively small population of all short-period buildings that are constructed of reinforced masonry and the relatively good performance of modern reinforced masonry buildings in past earthquakes. Still, only a small number of modern reinforced masonry buildings have been "tested" by very strong (e.g., MCE_R or greater) ground motions.

The development of shear cracks in reinforced masonry walls due to strong earthquake ground shaking has been widely observed, and in some cases, walls have "failed," but there are no reported collapses of modern reinforced masonry buildings in the United States due to in-plane failure of shear walls, and there are no reported instances of out-of-plane failure of reinforced masonry walls without diaphragm connection failure. This contrasts with the common observation of the failure of unreinforced masonry building walls, which tend to collapse out-of-plane after sustaining in-plane damage.

A summary of reinforced masonry damage patterns and statistics from the 1987 Whittier earthquake, the 1994 Northridge earthquake, and the 2011 Christchurch, New Zealand earthquake follows.

2.2.1 Reinforced Masonry Building Damage in the 1987 Whittier Earthquake

After the 1987 Whittier earthquake, a comprehensive survey of 50 reinforced masonry buildings and 38 unreinforced masonry (URM) buildings was made in downtown Whittier (Table 2, Hart et al., 1988), the area of strongest ground motion intensity (MMI VIII). Damage data were never published, but anecdotal information suggests that few, if any, of the 50 reinforced masonry buildings had significant structural damage.

A strong-motion instrument located in the basement of a 10-story building in downtown Whittier (Bright Avenue) close to the masonry building survey area recorded a peak ground acceleration of 0.63g (Figure 4, Brady et al., 1988) and a peak response spectral acceleration of about 1.8g at short periods (Figure 10, Wald, et al., 1988), which are approximately the same as the MCE_R ground motions required by ASCE/SEI 7-10 for this site. However, the 1987 Whittier earthquake was only a magnitude 5.9 event, the duration of strong shaking was short (i.e., only about 10–15 seconds), and the frequency content of ground motions at periods of one second and longer was very low (e.g., response spectral acceleration of the Bright Avenue records was less than 0.2g at a period of one second). The low level of ground motions at periods of one second and longer implies a peak displacement response of short-period buildings of not more than about 2 inches, which could not cause collapse even if the spectral accelerations at short periods were strong enough to have caused damage (e.g., cracking of reinforced masonry walls).

2.2.2 Reinforced Masonry Building Damage in the 1994 Northridge Earthquake

After the 1994 Northridge earthquake, a reconnaissance team surveyed approximately 140 masonry buildings in the greater Los Angeles area (TMS, 1994). The executive summary of the TMS reconnaissance report provides the following general description of reinforced masonry building performance.

> "Throughout Los Angeles there are many reinforced masonry schools, post offices, fire stations, and police stations. Most of these buildings showed little apparent structural damage and continued operating after the earthquake. In the greater Los Angeles area, and particularly in the epicentral region, very little distress was shown by modern one-story reinforced masonry or by multistory reinforced bearing-wall buildings. In contrast, un-retrofitted URM buildings generally had more extensive wall damage. In general, masonry structures, built since the 1950s, that were engineered, grouted,

reinforced, and inspected in accordance with then-current building codes, experienced little damage in the earthquake."

Many post-earthquake safety assessments use the guidelines provided in ATC-20, *Procedures for Postearthquake Safety Evaluation of Buildings* (ATC, 1989; 2005). The ATC-20 safety assessment procedure is a rapid evaluation tool that focuses on the integrity of the structural system. Inspectors are instructed to affix a placard (colored tag) on an inspected structure, according to the following guidelines:

- **Inspected Placard (green tag).** No apparent hazard found, although repairs may be required. Original lateral load capacity not significantly decreased. No restriction on use or occupancy.
- **Restricted Use Placard (yellow tag).** Dangerous condition believed to be present. Entry by owner permitted only for emergency purposes and only at own risk. No usage on a continuous basis. Entry by public not permitted. Possible major aftershock hazard.
- **Unsafe Placard (red tag).** Extreme hazard, may collapse. Imminent danger of collapse from aftershock. Unsafe for occupancy or entry, except by authorities.

The 140 reinforced masonry buildings surveyed after the 1994 Northridge earthquake represent only a fraction of all reinforced masonry buildings in the area of strongest ground motions, although the total number of reinforced masonry buildings is not known. For reference, post-earthquake safety evaluations of 114,039 potentially damaged buildings included 10,393 commercial and industrial buildings, of which 637 (6.1 percent) were deemed unsafe and assigned a red tag (Table 4-2, OES, 1995). Those safety inspections included 3,068 "Class C" structures having exterior walls of brick, concrete block, or poured-in-place concrete (e.g., tilt-up buildings), of which 277 (9 percent) were assigned a red tag (Table 4-3, OES, 1995). Here, "Class C" structures included unreinforced masonry buildings that were much more vulnerable to earthquake damage than reinforced masonry buildings. Only a fraction of all buildings was safety inspected, and red tag percentages based on the number of inspected buildings, rather than the total number of buildings in the affected area, represent an upper bound on observed damage.

More meaningful estimates of red tag percentages are shown in Figure 2-1 for wood buildings and for other (non-wood) buildings for each of five MMI regions (V–IX). Here, the red tag percentage is the ratio of the number of buildings assigned a red tag (Table 4-3, OES, 1995) to the number of

buildings in the MMI region of interest (Table 6, Kircher et al., 2006). Red tag percentages are plotted as a function of the average value of 0.3-second response spectral acceleration of the MMI region of interest (Table 6, Kircher et al., 2006). Non-wood buildings include three primary construction classes: (1) steel frame; (2) concrete frame; and (3) brick, block, or poured-in-place concrete. Non-wood construction classes are grouped together since the red tag percentages could not be reliably estimated for individual construction classes (other than wood). For example, although brick, block, and poured-in-place concrete (Class C) buildings are the most common non-wood building type, they represent only about 3.5 percent of all buildings in Los Angeles County (Table 4-2, OES, 1995). The red tag percentages shown in Figure 2-1 should be considered an upper bound on red tag rates for reinforced masonry buildings since brick, concrete block, and poured-in-place concrete (Class C) buildings also include unreinforced masonry and tilt-up buildings, which were much more vulnerable to damage in the 1994 Northridge earthquake.

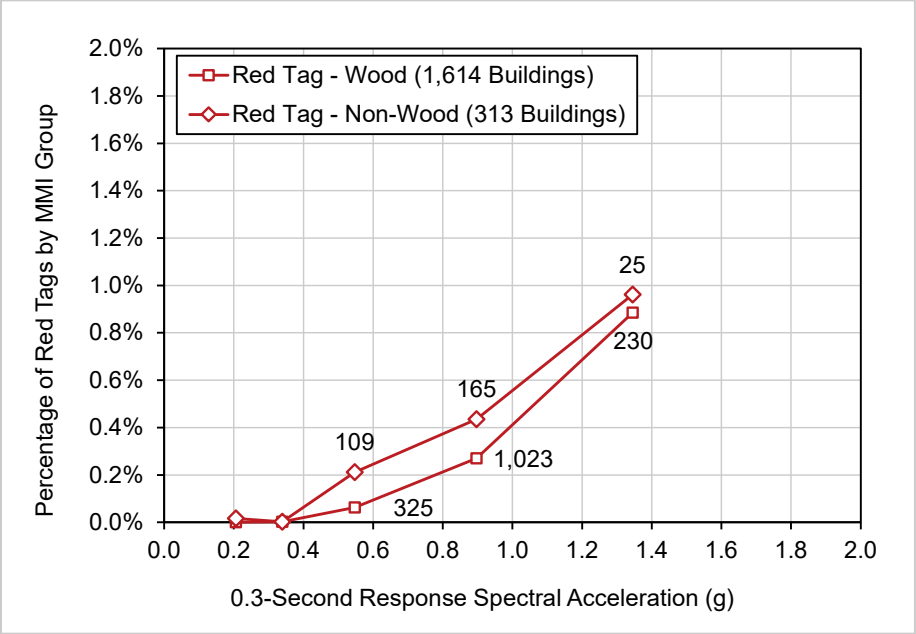

Figure 2-1 Percentage of wood and non-wood buildings assigned a red tag as a function of 0.3-second response spectral acceleration for five MMI regions (V–IX) based on post-earthquake safety inspections following the 1994 Northridge earthquake.

As shown in Figure 2-1, red tag percentages are quite low, less than 1 percent, even for the MMI IX region (e.g., average 0.3-second response spectral acceleration of 1.35g). The number of buildings assigned a red tag is shown in the figure for MMI regions VII, VIII, and IX. For example, only 25 of the 313 non-wood buildings assigned a red tag are in the MMI IX

region, most of which were either unreinforced masonry or tilt-up buildings that sustained out-of-plane wall failures. Qualitatively, non-wood buildings have similar trends and values of red tag percentages as wood buildings (e.g., about 1 percent for the MMI IX region), and reinforced masonry buildings appear to have performed somewhat better, on average, than wood and other construction classes (although the paucity of data precludes reliable quantification of this observation).

2.2.3 Reinforced Masonry Building Damage in the 2011 Christchurch Earthquake

After the February 22, 2011, Christchurch earthquake, an international team of researchers was deployed to document the observed earthquake damage to masonry buildings and to churches (Dizhur, 2011). The study focused on investigating commonly encountered failure patterns and collapse mechanisms. External evaluations of 342 reinforced concrete masonry buildings with solid-wall construction located within the Central Business District of Christchurch found the majority of these buildings (83 percent) had little or no damage, 15 percent had moderate damage, and only 5 percent had severe damage. Diagonal in-plane shear cracking was the most common failure mode (64 percent), including both step-pattern cracking along the head and bed mortar joints and diagonal cracking through masonry blocks. Vertical cracking of the block was also commonly observed (20 percent), followed less frequently by horizontal cracking along bed joints and spalling of the block. In contrast to the relatively good performance of reinforced masonry buildings, almost 200 unreinforced masonry buildings were demolished in the first five months following the earthquake (approximately 85 percent of all buildings demolished during this time), and of those that remained, few were in a usable condition (Dizhur, 2011).

2.3 Observed Performance in Shake-Table Tests

Although the number of reinforced masonry shake-table tests is limited, those that have been performed provide valuable insights into their response behavior and failure modes. The test results provide a basis to validate the numerical modeling of nonlinear dynamic response described in Chapter 4.

Full-scale shake-table tests of two-story and three-story reinforced masonry buildings at the University of California, San Diego, suggest that shear failure of first-story walls is the likely collapse failure mode of reinforced masonry buildings (Ahmadi et al., 2015; Mavros et al., 2016; Stavridis et al., 2016). The structures tested did not collapse; however, damage to first-story shear walls was more severe and extensive than the damage to shear walls at upper floors.

More recent shake-table tests of two single-story reinforced masonry coupled T-wall structures, also at the University of California, San Diego, show the test structures withstanding very large story drifts without collapse (Cheng et al., 2020). After being subjected to a series of earthquake ground motions of increasing intensities, the first test structure developed severe shear cracks in the webs of the walls. The maximum story drift reached during the shaking was 2.5 percent. Afterwards, the structure was subjected to a static-pull test to a maximum story drift ratio of 16 percent, at which point the lateral resistance dropped to 5 percent of the peak value, but the test structure remained standing. The second structure was tested with earthquake ground motions to the verge of collapse with the maximum story drift reaching 13 percent, at which the structure was still able to carry the gravity load without collapse (see Figure 4-19). Again, the T-walls developed diagonal cracks with severe masonry spalling.

2.4 Collapse Failure Modes and Target Collapse Rates of Reinforced Masonry Buildings

Observations of reinforced masonry building performance in past earthquakes is limited and not sufficient to develop a quantitative measure of collapse failure rates. Qualitatively, however, collapse performance of modern short-period reinforced masonry buildings appears to be similar to that of wood buildings.

As shown in Figure 2-1, non-wood building red tag damage data are sparse but suggest that reinforced masonry buildings have collapse rates that are no larger than that of wood buildings, for which data are more reliable for generating collapse statistics. Hence, for the purposes of this study, benchmark target collapse rates for modeled performance of reinforced masonry buildings are assumed to be the following:

- **One-Story Buildings.** 1 percent (0 percent to 2 percent) probability of collapse given MCE_R ground motions of S_{MS} = 1.5g; and
- **Two-or-More-Story Buildings.** 2.5 percent (0 percent to 5 percent) probability of collapse given MCE_R ground motions of S_{MS} = 1.5g.

Benchmark MCE_R collapse probabilities represent building collapse that includes both partial collapse and full collapse of the building structure, consistent with the ASCE/SEI 7-10 and FEMA P-695 definition of collapse. The higher benchmark MCE_R collapse probabilities for buildings two stories or more in height are based on an observed first-story failure mechanism of wood light-frame buildings and may not be applicable to other collapse failure modes (e.g., foundation rocking) of reinforced masonry buildings, which have not been observed.

Chapter 3

Development of Building Archetype Configurations and Designs

3.1 Introduction

This chapter describes the rationale for selecting the occupancy, height, and seismic design criteria for the reinforced masonry archetypes used for this study. It presents reinforced masonry building characteristics used in other relevant studies and highlights key aspects of this study's archetype configurations and detailed designs.

An important consideration in the design of archetype structures is to establish the age and historic design approach that is appropriate to represent the population of buildings that are the focus of the study. The variation in masonry building designs among the stock of existing reinforced masonry buildings is very broad. It was determined that the geometric configuration of the archetypes was the critical factor that would most directly affect the behavior and probability of collapse and that the use of current codes and materials would lead to archetype designs that would adequately represent that behavior. Similarly, the existing reinforced masonry building stock includes a broad variety of walls perforated by windows and doors, creating numerous configurations of pier shapes and sizes with both shear-dominated and flexure-dominated behavior. In this study, all walls were solid and unperforated with geometries that were intended to produce a range of shear-dominated and flexure-dominated behavior. Finally, the archetypes were expected to exhibit failure modes indicative of the primary structural system response and not of secondary load paths, such as the out-of-plane connection of diaphragms to walls.

The information presented in this chapter provides the basis for the numerical models described in Chapter 4 and used to predict the seismic collapse performance of the archetypes. Additional design details are provided in Appendix A.

3.2 Factors Influencing Building Performance

This section presents factors that were expected to influence the seismic response and performance of reinforced masonry buildings and thus were considered in the design of the archetypes.

3.2.1 Seismic Design Level

This study focused on the performance of short-period reinforced masonry buildings in locations of high seismicity. This study defined "high-seismic" demand to be a location where the MCE_R ground motion is characterized by a mapped short-period spectral response acceleration (S_S) of 1.5g. For ordinary soil profiles, this corresponded to a short-period MCE_R spectral response acceleration adjusted for site class effects (S_{MS}) of 1.5g. This level of seismicity placed ordinary occupancy buildings in Seismic Design Category (SDC) D in the 2015 IBC and ASCE/SEI 7-10.

To capture a range of seismic hazard levels, archetype designs were also prepared for 50 percent of the basic value (termed "moderate seismic" in this study) and 150 percent of the basic value (termed "very high seismic" in this study). S_{MS} = 0.75g is the threshold between SDC C and SDC D, so the design rules for SDC C were applied in the moderate-seismic designs in this study. S_{MS} = 2.25g is high enough that the mapped one-second MCE_R spectral response acceleration, S_1, will often place the building into SDC E, so the rules for SDC E were applied to the very high-seismic designs in this study.

3.2.2 Occupancy and Architectural Influence on Structure Configuration

Masonry buildings have the important characteristic that the structural configuration is often established by nonstructural criteria set by the building architect, not the engineer. These criteria include the building envelope shape, the fire-rating or fire-separation requirements, the acoustic rating, material durability, aesthetics, building occupancy, and building program. The structural configuration of the building—and thus the primary seismic-force-resisting system—may be beyond the control of the structural engineer.

Section 7.3 of TMS 402/602, *Building Code Requirements and Specification for Masonry Structures* (TMS, 2013), defines "participating" and "nonparticipating" elements of the seismic-force-resisting system. Nonparticipating walls must be explicitly isolated in their own plane from the seismic-force-resisting system; if not, they must be treated as participating. It is generally simpler and more cost-effective to detail most walls as participating. This characteristic often results in buildings that have stiffness

and strength that exceed the demand, often at the expense of ductility. In other words, many masonry buildings can be expected to exhibit only minor nonlinear behavior under design-level ground motions. For the same reasons, some buildings may exhibit nonlinear behavior, but with a shear-dominated response rather than the code-intended flexure-dominated ductile response. This situation is represented in the chosen archetypes, especially in the residential and retail (i.e., "big box") archetypes, which have more walls (length and number) participating in the seismic-force-resisting system than would be necessary to meet structural design demands.

3.2.3 Reinforced Masonry Design and Construction Practice

Masonry design and construction practice varies widely across the United States and evolved significantly during the twentieth century. The practice of reinforcing masonry began with early innovators in the 1920s, ultimately leading to the introduction of reinforced masonry to the building codes in the 1950s. Ongoing research and code development, particularly since the mid-1970s, has contributed to the steady evolution of design practice. The use of reinforcement in masonry, which started in the West and progressed eastward, is now widespread in the country. When modern reinforced masonry was first developed in the United States, multi-wythe systems—in which two wythes of solid-unit clay-brick masonry were connected by a reinforced and grouted space between them—were common. Over time, this system has been almost entirely replaced in common practice by hollow-unit masonry with reinforcement placed in the grout-filled cores of the units. Clay brick masonry is often used as a nonstructural veneer rather than as a structural material.

Geographic location strongly influences construction practices. The use of reinforced masonry evolved more quickly in the western United States than in the East. Even today, there are differences around the country as local craftsmen set the standards of practice. For example, fully grouted reinforced masonry is relatively common on the West Coast but less common in the Midwest and East Coast, where partial grouting is the preferred practice. Archetypes in this study are all fully grouted both to represent common practice in areas of high-seismic hazard and to allow the use of past experimental and numerical studies, which are more numerous for fully grouted than partially grouted systems, in the development of this study's numerical models.

Variation in design practice is another variable. Even within the context of current design practice, the building code for masonry, TMS 402/602, accommodates a wide range of design and construction practice across the

United States, including *allowable stress* design and *strength design* for both reinforced and unreinforced masonry. TMS 402/602 also allows *empirical design* rules with limited application and recently introduced *limit design* provisions.

Because of this variability, the same building design problem may result in very different solutions depending on the designer's location and choice among several code-sanctioned design methods. This study focused on seismic-force-resisting systems common in high-seismic areas in the western United States, specifically: loadbearing, fully grouted, reinforced hollow-unit concrete masonry with cantilevered shear walls. Masonry walls are generally identified either as perforated, with regular or irregular openings, or as cantilevered. All the walls in this study were the cantilever type. Nominal 8-inch thick walls were used in all archetypes wherever possible, although 12-inch walls were required in one case. The chosen design process for the archetypes was intended to represent typical practice exercised in areas of significant seismicity using the normal standard of care for the referenced codes and, inherently, the associated time of practice. The strength design provisions of the 2013 version of TMS 402/602 were used. Regardless of Seismic Design Category, all walls were designed as "special reinforced masonry shear walls" per ASCE/SEI 7-10 with a response modification coefficient (R) equal to 5.

As special reinforced masonry shear wall buildings, the archetypes lent themselves to the application of the design principles and procedures described in NIST GCR 14-917-31, *Seismic Design of Special Reinforced Masonry Shear Walls: A Guide for Practicing Engineers* (NIST, 2014). That document discusses, among other things, the restrictions on vertical reinforcement, requirements for boundary elements, and the influence of flanged walls on design. The archetype configurations in this study were chosen to ensure that special boundary elements per the provisions of TMS 402/602 were not required.

The type of structural diaphragm used in short-period reinforced masonry buildings is similarly dependent on local practice, occupancy, fire rating requirements, and cost. Their influence on collapse performance is primarily seen in how forces are distributed to vertical elements, and in the out-of-plane forces imposed on masonry walls by the diaphragms, especially for flexible diaphragms. The archetypes in this study are all biaxially symmetric (or very nearly so), so the distribution of seismic forces to each line of resistance is relatively insensitive to diaphragm type. As described below, archetype floor diaphragms were rigid, and roof diaphragms were relatively flexible.

Residential and retail archetypes in this study were expected to exhibit behavior driven entirely by the geometry imposed on the design by architectural constraints. The commercial archetypes were expected to have a reasonable amount of wall necessary to meet an architectural demand for openness, while meeting all structural code requirements. As such, the residential and retail archetypes were expected to represent buildings with significant overstrength, and the commercial archetypes less so.

3.2.4 Site Class and Foundation Systems

The foundation system and its connectivity and interaction with the ground have long been identified as a possible source for explaining performance under seismic loads that is different than would be predicted by numerical models that ignore any such flexibility or energy dissipation. Accordingly, this study included a parametric study regarding the effects of soil-structure interaction (SSI) and foundation flexibility, comparing building response on sites with stiff soil and soft soil. Unique designs were prepared for each site using different allowable soil bearing pressures and moduli of subgrade reaction. Both sites were characterized as Site Class D.

There is also often an association between site characteristics and foundation type. Typically, piles or caissons are used with soft soil, and shallow spread footings are used with firmer sites. Exceptions include "poor" sites with soft soils, liquefaction potential, or expansive soil. For the purposes of this study, a shallow spread-footing foundation with a slab-on-grade was selected for both stiff and soft soil sites. Interior columns bear on isolated spread footings, and exterior walls bear on continuous stem walls supported on continuous strip footings around the building perimeter. A slab-on-grade bears on the interior isolated footings and was bound by the stem walls. The selected foundation system was representative of typical systems and appropriate for studying the inclusion or exclusion of foundation flexibility in response prediction.

Details of the soil properties and designs are documented in Section 3.4.4 and Appendix A.

3.2.5 Architectural and Nonstructural Components

The effects of architectural and nonstructural components on the behavior of reinforced masonry buildings is generally assumed to be small, because the mass and stiffness of these components are usually small relative to the properties of the structural masonry itself. As discussed previously, masonry walls often serve both an architectural and structural purpose; in this context, "architectural and nonstructural components" are intended to include non-

masonry partition walls or building envelope systems, drywall, stucco, or similar lightweight finishes. Such architectural and nonstructural components were not included in this study.

3.2.6 Behavior of Reinforced Masonry Walls under Seismic Loads

At the most basic level, the behavior of reinforced masonry shear walls under seismic loads can be characterized in one of two fundamental categories (NIST, 2014):

- *Flexure-dominated walls* are walls whose behavior is dominated by flexure, with reliable ductility and inelastic displacement capacity.
- *Shear-dominated walls* are walls whose behavior, often for reasons beyond the control of the structural designer, is dominated by shear, with limited ductility capacity.

It is the intent of the building code to encourage flexure-dominated behavior, but it is unrealistic to assume that all masonry elements will do so. Different structural elements in the archetypes were expected to exhibit both behaviors.

3.3 Building Type Considerations for Development of Archetypes

This section describes considerations in the selection of occupancies, heights, and configurations for the archetypes, which were meant to broadly represent common reinforced masonry shear wall building types and expected structural behaviors routinely encountered in practice. The section begins with a summary of reinforced masonry building characteristics used in other relevant studies.

3.3.1 FEMA Model Building Types

In selecting the archetypes, previous studies using masonry structures were considered. One possibility for this study would have been to simply reuse the archetypes chosen for previous studies; ultimately, it was determined that the previous archetypes would not capture the behavior relevant to the short-period building seismic performance paradox. The previous studies and their relevance to this study are briefly described here.

FEMA Model Building Types (MBTs) define different types of structural systems in terms that are believed useful for characterizing seismic performance. These designations have been used extensively in FEMA publications, such as FEMA 547, *Techniques for the Seismic Rehabilitation of Existing Buildings* (FEMA, 2006), and FEMA P-154, *Rapid Visual Screening of Buildings for Potential Seismic Hazards: A Handbook* (FEMA, 2015a).

A list of FEMA MBTs from FEMA P-154 is shown in Table 3-1. The FEMA MBTs included two reinforced masonry building types: RM1 (reinforced masonry buildings with flexible diaphragms), and RM2 (reinforced masonry buildings with stiff diaphragms). Both FEMA reinforced masonry MBTs were represented in the archetypes for this study, but the characterization of the two categories was not sufficient to describe the variations in occupancy, building height, and configuration that are important to this study. Instead, archetypes were developed for three common occupancies, with varying heights appropriate to those occupancies.

Table 3-1 FEMA Model Building Types

Designation	Description
W1	Light wood frame single- or multiple-family dwellings of one or more stories in height
W1A	Light wood frame multi-unit, multi-story residential buildings with plan areas on each floor of greater than 3,000 square feet
W2	Wood frame commercial and industrial buildings with a floor area larger than 5,000 square feet
S1	Steel moment-resisting frame
S2	Braced steel frame
S3	Light metal frame
S4	Steel frame with cast-in-place concrete shear walls
S5	Steel frame with unreinforced masonry infill walls
C1	Concrete moment-resisting frame
C2	Concrete shear wall
C3	Concrete frame with unreinforced masonry infill walls
PC1	Tilt-up construction
PC2	Precast concrete frames
RM1	Reinforced masonry with flexible floor and roof diaphragms
RM2	Reinforced masonry with rigid floor and roof diaphragms
URM	Unreinforced masonry bearing-wall buildings
MH	Manufactured housing

NIST GCR 10-917-8, *Evaluation of the FEMA P-695 Methodology for Quantification of Building Seismic Performance Factors* (NIST, 2010), selected 40 representative masonry archetypes to evaluate the FEMA P-695 methodology. The archetypes had two plan configurations based on two common occupancies:

- retail occupancy: one-story with 12-foot roof height (see Figure 3-1), and
- residential occupancy: multi-story with 10-foot floor-to-floor height, with archetypes for two, four, eight, and twelve stories (see Figure 3-2 and Figure 3-3).

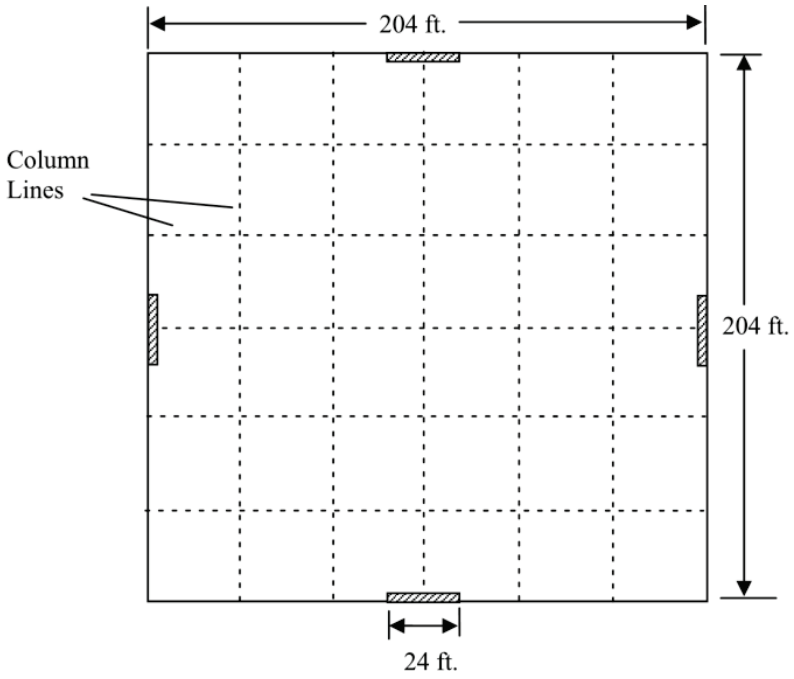

Figure 3-1 Reinforced masonry retail occupancy building from NIST GCR 10-917-8—plan view.

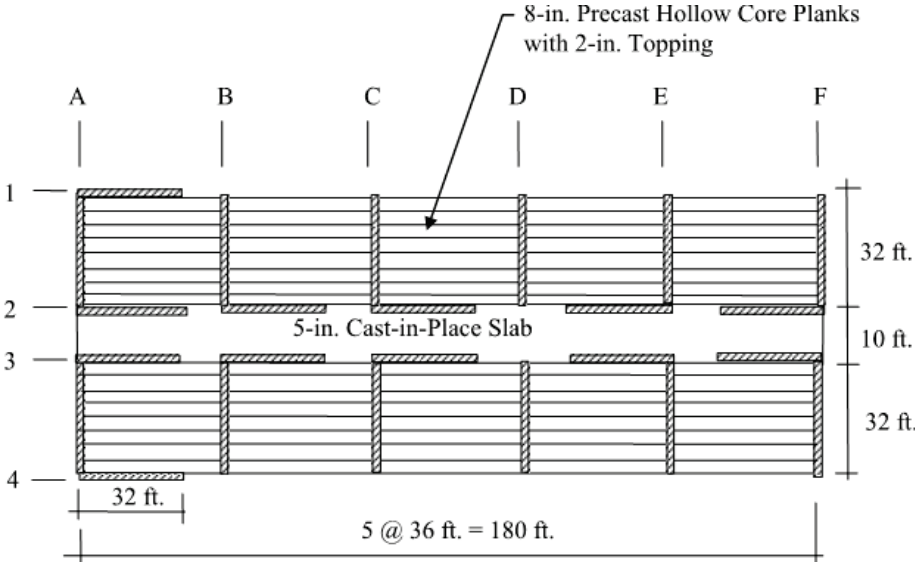

Figure 3-2 Reinforced masonry residential occupancy building from NIST GCR 10-917-8—plan view.

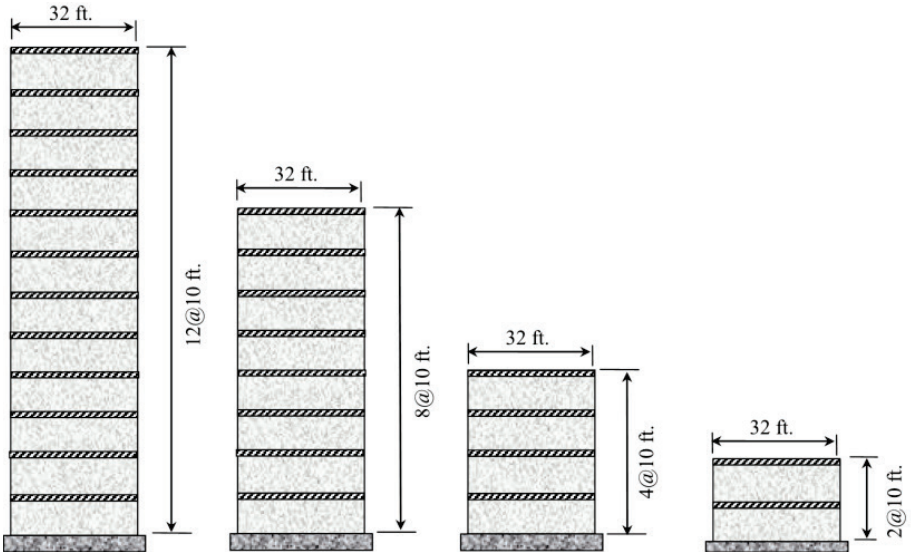

Figure 3-3 Reinforced masonry residential occupancy building from NIST GCR 10-917-8—elevation view.

3.3.2 Building Occupancy

The following limitations were imposed to bound the variables in the NIST study:

- all walls were cantilevered (not perforated) with rectangular cross sections,
- flanged-wall behavior was not considered, and
- coupling between walls was not considered.

Within these limitations, the following variables were explicitly considered by the NIST study:

- special versus ordinary detailing,
- fully grouted versus partially grouted construction,
- seismic design category,
- level of seismic design loading,
- level of gravity load,
- number of stories,
- building period (short and long), and
- wall aspect ratio.

The archetypes from the NIST study were an important reference, but there are several differences in the chosen archetypes for this study. For example,

the scope of this study was explicitly limited to short-period structures, and this study did not include partially grouted structures or ordinary shear wall detailing.

In the NIST study, the retail occupancy building (Figure 3-1) was 204 feet square. However, only one 24-foot segment of exterior wall centered on each elevation was considered as a participating structural element and was optimized for strength relative to the seismic design load. Structural walls had aspect ratios ranging between 0.5 and 1. Because it was a goal of this study to consider elements of short-period building construction that may participate in the seismic-force-resisting system, even if they are not explicitly necessary, all exterior masonry walls were assumed to be *participating* elements as defined by TMS 402/602.

The residential archetype in the NIST study was nearly duplicated in this study, with an identical plan layout but the exclusion of exterior longitudinal walls, which were considered unrealistic elements for a residential occupancy. However, in this study, the design considered flanged walls in accordance with the recommendations in TMS 402/602, rather than considering each wall as an independent rectangular cantilever wall in the design. Coupling between shear walls due to beam or slab bending was not explicitly included in the design for either study.

The NIST study did not include a structure like the commercial archetype chosen for this study, with flanged walls on the building perimeter.

Finally, while the NIST archetypes included two-, four-, eight-, and twelve-story versions, this study was limited to one-, two-, and four-story versions because of the focus on short-period structures.

Short-period reinforced masonry building archetypes were developed for three common occupancies:

- commercial office buildings (COM),
- multi-family residential and hotel buildings (RES), and
- retail, industrial, and warehouse buildings (BOX).

These are described in the following sections.

Another common occupancy for masonry buildings is schools, which are often characterized by long exterior walls perforated by windows and doors and relatively solid interior separation walls. This occupancy was not included in the study because its behavior was expected to be captured by the other three building types.

3.3.3 Commercial Buildings (COM)

The use of reinforced masonry in commercial buildings is common in a variety of building configurations (Figure 3-4). For the purposes of this study, the commercial building archetype was assumed to support an architectural program with an open interior for maximum occupant flexibility and with all structural walls on the building exterior. Because windows are also valuable for prime office space, the exterior walls were optimized to be the minimum length necessary to meet code requirements for the seismic-force-resisting system.

Figure 3-4 Typical reinforced masonry commercial office building (photo credit: FEMA P-749, Chapter 4, Figure 23).

3.3.4 Multi-Family Residential and Hotel Buildings (RES)

The use of reinforced masonry as the primary structural system for single-family homes is rare, and the occupancy is not included in this study. In contrast, reinforced masonry is common in multi-family residential construction, because, in addition to its structural role, the masonry walls can provide fire and acoustic separation between units and egress corridors (Figure 3-5). Low- to mid-rise hotel structures using reinforced masonry party and corridor walls with precast hollow-core concrete diaphragms are common. Although designs were prepared for this archetype, numerical analyses were not ultimately conducted as part of this study.

Figure 3-5 Typical reinforced masonry multi-family residential building (photo credit: G. Kingsley).

3.3.5 Retail, Industrial, and Warehouse Buildings (BOX)

Among the most common reinforced masonry building types in the United States is the single-story retail or warehouse structure, often referred to as "big box" retail (Figure 3-6). These structures are characterized by large plan dimensions with reinforced masonry walls defining the entire exterior envelope and seismic-force-resisting system. The interior structure is often composed of steel columns with open-webbed steel joists and joist girders, with a corrugated metal deck or panelized wood diaphragm. The diaphragm is flexible relative to the masonry walls. Although designs were prepared for this archetype, numerical analyses were not ultimately conducted as part of this study.

Figure 3-6 Typical "big box" retail construction (photo credit: G. Kingsley).

3.4 Archetype Design Criteria and Configurations

This section documents the criteria for designing the archetype reinforced masonry buildings and the basic configurations that were used for this study. Detailed documentation of the designs for each archetype are provided in Appendix A.

3.4.1 Applicable Codes and Standards

Design loads were based on design requirements of ASCE/SEI 7-10. Design strength, performance, and detailing were established in accordance with masonry design standards in TMS 402 and construction specifications in TMS 602. As stated previously, the archetypes were designed in accordance with the strength design method, as opposed to the allowable-stress, empirical, or limit-design methods, all of which are allowed by the code.

3.4.2 Gravity Loads

Archetype design dead and live loads are summarized in Table 3-2. The weight of all walls, except those of the exterior, was averaged across the floor plate, and a portion was assigned to the roof for the determination of seismic loads. The interior wall dead load value used was 15 pounds per square foot (psf) distributed uniformly over each story.

Table 3-2 Gravity Loads used for Design of Reinforced Masonry Building Archetypes

Building Type	Floor Live Load (psf)	Partition Load (psf)	Floor Dead Load (psf)	Roof Dead Load (psf)	Exterior Wall Dead Load (psf)
COM	50	15	80	20	20
RES	40	15	100	90	10
BOX	100	-	n/a	20	34

3.4.3 Seismic Loads and Design Criteria

Archetype designs were developed for three different seismic criteria summarized in Table 3-3. The mapped MCE_R spectral response acceleration at a period of 1 second (S_1), the short-period site coefficient (F_a), the short-period design spectral response acceleration (S_{DS}), and the other listed parameters, all previously defined, were calculated in accordance with ASCE/SEI 7-10 requirements for the equivalent-lateral-force (ELF) method. All designs were based on Risk Category II and a response modification factor (R) of 5 for Special Reinforced Masonry Shear Walls. Table 3-4 summarizes the basic seismic design criteria for the archetypes.

Table 3-3 Seismic Loads Used for Design of Reinforced Masonry Archetypes

Building Type	Seismic Design Level	Seismic Design Category (SDC)	MCE_R Ground Motion Definition				
			S_1 (g)	S_S (g)	F_a	S_{MS} (g)	S_{DS} (g)
COM, RES, and BOX	Very High	E	0.90	2.25	1.0	2.25	1.5
	High	D	0.60	1.50	1.0	1.50	1.0
	Moderate	C	0.132	0.55	1.36	0.75	0.5

Table 3-4 Seismic Design Criteria used for Design of Reinforced Masonry Archetypes

Base Archetype ID	No. of Stories	Seismic Design Criteria			
		SDC	S_{MS} (g)	T^* (sec)	C_s (g)
Commercial Buildings: High Seismic					
COM1	1	D	1.5	0.25	0.20
COM2	2	D	1.5	0.30	0.20
COM3	4	D	1.5	0.51	0.20
Commercial Buildings: Very High Seismic					
COM4	1	E	2.25	0.25	0.30
COM5	2	E	2.25	0.30	0.30
COM6	4	E	2.25	0.51	0.30
Commercial Buildings: Moderate Seismic					
COM7	1	C	0.75	0.25	0.10
COM8	2	C	0.75	0.33	0.10
COM9	4	C	0.75	0.55	0.10
Multi-Family Residential/Hotel Buildings: High Seismic					
RES1	4	D	1.5	0.51	0.20
Multi-Family Residential/Hotel Buildings: Very High Seismic					
RES2	4	E	2.25	0.51	0.30
Multi-Family Residential/Hotel Buildings: Moderate Seismic					
RES3	4	C	0.75	0.55	0.10
Retail/Industrial/Warehouse Buildings: High Seismic					
BOX1	1	D	1.5	0.30	0.20
Retail/Industrial/Warehouse Buildings: Very High Seismic					
BOX2	1	E	2.25	0.30	0.30
Retail/Industrial/Warehouse Buildings: Moderate Seismic					
BOX3	1	C	0.75	0.33	0.10

* $T = C_u T_a \geq 0.25$ seconds, in accordance with the analysis requirements of FEMA P-695, where the values of the parameters C_u and T_a are specified by ASCE/SEI 7-10. However, as is described in Section A.2.5, the archetypes were designed using T_a.

3.4.4 Foundation Design Criteria

Soil properties were assumed to represent typical West Coast sites, which are described in detail in Appendix C. Assumed site-specific properties of soils are summarized in Table 3-5. For the SSI and foundation flexibility study only, a soft soil profile was assumed, with a lower bearing pressure. Both stiff and soft soil sites were characterized as Site Class D.

Table 3-5 Foundation Criteria used for Design of Reinforced Masonry Building Archetypes

Material	Properties
Assumed Site Class	D
Allowable Soil Bearing Pressure (stiff soil)	3000 psf
Allowable Soil Bearing Pressure (soft soil)	1500 psf
Modulus of subgrade reaction (stiff soil)	129 kip / cu ft
Modulus of subgrade reaction (soft soil)	60 kip / cu ft
Minimum Footing Depth	12 in

3.4.5 Archetype Height

Commercial buildings with heights of one story, two stories, and four stories are common, so the selected reinforced masonry commercial building archetypes included all three.

Historically, and in current practice, buildings with residential occupancies shorter than four or five stories would typically be wood light-framed where permitted by code. Accordingly, only one height—four stories—was designed for the reinforced masonry residential archetypes.

The retail archetype, representing a typical "big box" store, was also self-limiting in that reinforced masonry structures of that type rarely exceed one story. Therefore, only one height—one story—was designed for the reinforced masonry retail archetypes.

3.5 Commercial Building Archetypes (COM)

Plan dimensions of 48 feet × 96 feet were selected for the commercial building archetypes. One-story, two-story, and four-story archetypes were designed. In each, the ground floor was a slab-on-grade, and elevated floors, if any, were composite steel framing with concrete on metal deck spanning between beams, which in turn were supported on girders and columns or walls. This floor system provided a relatively stiff diaphragm. In accordance with common practice, the roof was un-topped steel deck supported by open-web steel joists and wide-flange perimeter beams. This

roof system provided a relatively flexible diaphragm. Figure 3-7 shows an isometric view of the two-story commercial archetype.

The selection of this configuration was motivated in part by the desire to represent structural walls that, based on their aspect ratios and relatively light gravity loads, were expected to be flexure dominated and well aligned with the code intent for special reinforced masonry shear walls.

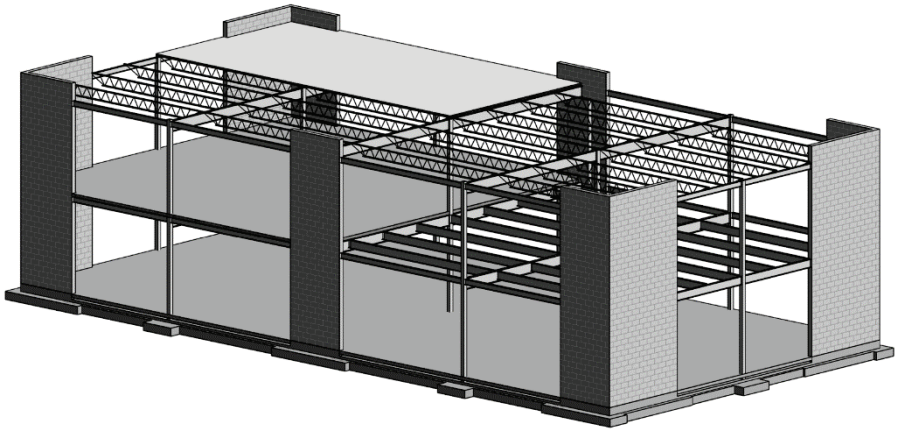

Figure 3-7 Isometric view of the two-story commercial archetype (COM2).

In this archetype, as with the others, the reinforced masonry walls served as gravity-load-carrying elements, as well as elements of the seismic-force-resisting system. Floor beams and girders transferred gravity loads through bearing plates on masonry pilasters built into the walls. For the purposes of design, it was assumed, as is common practice, that the floor system was effectively pin-connected to the walls, meaning that it provided kinematic compatibility between the shear walls without inducing flexural-coupling action.

The archetypes also included flanged walls, which are common in practice. TMS 402/602 provides guidance to account for the behavior of flanged walls, and this guidance was followed explicitly in the design of the archetypes. In practice, anecdotal experience suggests that many designers prefer to ignore the intersecting-wall effects and design the in-plane walls in each direction independently. Designs that incorporate flanged-wall behavior can be challenging, considering the need to adhere to maximum reinforcement limits and competing demands for a single flanged wall element that must meet code requirements for design forces in two orthogonal directions. In some cases, provisions of the TMS 402 code that allow maximum reinforcement requirements to be bypassed under certain conditions were invoked (NIST, 2014). These conditions are specifically identified for the commercial archetypes in Appendix A.

The building envelope was assumed to be a combination of glazing and cold-formed steel framing with a relatively light exterior skin (e.g., stucco, cement board, or metal panel) applied to the exterior of the masonry walls. Buildings of this type may also have a heavier brick masonry veneer, but lighter materials are generally less expensive, and more common, and so were chosen for the archetype.

3.5.1 Commercial Building Parametric Designs

Several parametric studies were considered to study the influence of design and analysis choices on the modeled numerical results; ultimately, two were executed: displacement capacity and SSI and foundation flexibility.

The displacement capacity study investigated the effects on response behavior and collapse performance of collapse displacement capacity in a system. It was not necessary to alter the archetype designs for this study.

The SSI and foundation flexibility study investigated SSI inertial and kinematic effects and foundation flexibility on response behavior and collapse performance. The archetypes for the SSI and foundation flexibility parametric study were based on two designs, one for sites with relatively stiff soils (allowable bearing pressure = 3,000 psf) and one for sites with soft soils (allowable bearing pressure = 1,500 psf). The ELF seismic-design forces were not altered, only the allowable soil bearing pressure, so the resulting design changed only the footing dimensions and reinforcing.

3.6 Multi-Family Residential Archetypes (RES)

The multi-family residential masonry archetype (Figure 3-8) was 74 feet × 180 feet in plan, with structural party walls and corridor walls. Shear-dominated behavior was expected based on the aspect ratios, axial loading, and large flanges of these walls.

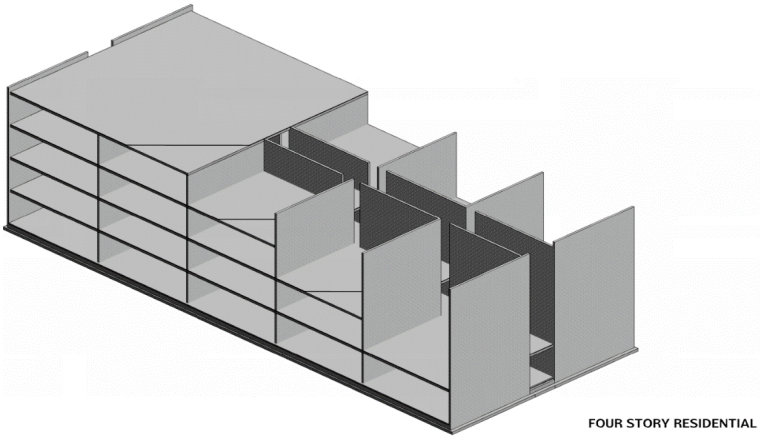

Figure 3-8 Isometric view of the four-story residentail archetype (RES1).

The floor system chosen for the archetype consisted of 8-inch precast hollow-core planks with a 2-inch minimum normal-weight concrete topping. This system was chosen based on its appropriateness for residential applications (e.g., acoustic properties, vibration, thin cross-section), based on its use in previous numerical modeling studies (NIST, 2010) and on its use in previous experimental studies available for calibration of numerical models (Mavros et al., 2016). The planks were single span, bearing on the party walls and exterior walls. At corridor walls, the planks were designed not to bear directly on the walls, but the concrete topping slabs and reinforcement provided shear connection from floors to walls. The topped precast system provided rigid floor diaphragms. Structural designers would generally assume that this floor system provides little or no flexural coupling between the shear walls. This was assumed in the design, despite experimental tests showing that coupling effects can be significant (Seible et al., 1991).

The significant flanges were considered in the design of the masonry structural walls. Each L-shaped wall was designed for ground motions in the two directions and balanced to work in both. Designs for the baseline archetypes were developed, and no additional designs were developed to support parametric studies for the multi-family residential archetypes. Only commercial building archetypes were designed, modeled, and analyzed.

3.7 Retail, Industrial, and Warehouse Archetypes (BOX)

The plan dimensions were chosen to be double the plan dimensions of the commercial archetypes, or 96 feet × 182 feet. The building was single story with a height of 24 feet to the roof plane. In accordance with common practice for structures of this type in the western United States, the roof was designed as a panelized wood system with prefabricated panels of plywood on wood joists supported on bar joists and joist girders supported on columns and walls (Lawson, 2013). The roof was a low-slope gable form.

The walls were tall and slender, with few openings that were expected to have little or no influence on the behavior. Control-joint spacing was approximately 24 feet on center, resulting in shear-wall segments with a shear span-to-depth ratio of approximately 1.

This building type and occupancy are so common that it was considered relevant to the study; however, it is recognized that the size and flexibility of the wood diaphragm would result in a structure that would not fit the description of a short-period structure, as defined in this study.

Designs for the baseline archetypes were developed, and no additional designs were developed to support parametric studies for the retail,

industrial, and warehouse archetypes. Only commercial building archetypes were designed, modeled, and analyzed.

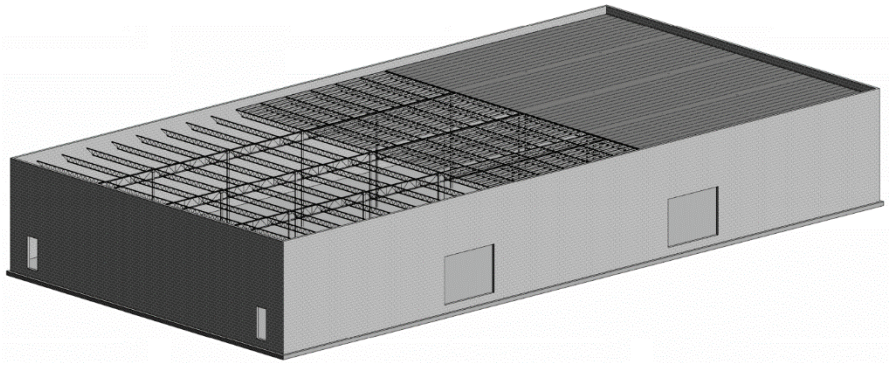

Figure 3-9 Isometric view of the BOX archetype (BOX1).

Chapter 4

Numerical Modeling for Parametric Studies

4.1 Introduction

Numerical parametric studies were conducted to evaluate the collapse probabilities for the commercial building archetypes whose design details are presented in Chapter 3 and Appendix A. They include one-story, two-story, and four-story archetypes designed for high-seismic (COM1, COM2, and COM3) and very high-seismic (COM4, COM5, and COM6) regions. The numerical studies also included investigations into the effects of varied assumptions for displacement capacity and soil-structure interaction (SSI) and foundation flexibility.

To assess collapse probabilities, incremental dynamic analyses (IDAs) were performed following the FEMA P-695 procedure. The IDAs were conducted with simplified frame models, which were calibrated with numerical results from detailed finite-element analyses. The detailed finite-element models used could capture different failure mechanisms of reinforced masonry wall systems, as well as the associated strength degradation. This chapter presents the modeling approach and assumptions, including key features of the models, as well as the calibration and validation of the refined and simplified models with experimental and numerical data.

4.2 Background and Modeling Methods

4.2.1 Behavior of Reinforced Masonry Shear Walls

The modeling of the inelastic response of reinforced masonry wall systems to static and dynamic loading is a challenging endeavor. Wall components in a reinforced masonry wall system can exhibit different failure mechanisms, depending on the axial load exerted on the wall, the reinforcement details, and the wall aspect ratio. Slender cantilever walls are expected to have relatively ductile flexure-dominated behavior, whereas wall components with a low shear-span ratio tend to exhibit brittle shear-dominated behavior characterized by diagonal cracking. Walls with very low shear-span ratios can develop base sliding in lieu of diagonal cracking. Although special reinforced masonry walls complying to ASCE/SEI 7 and TMS 402/602 are expected to have

ductile behavior dominated by flexure, this is not always guaranteed either by codes and standards or by design practice (NIST, 2014). This is especially true for short-period masonry buildings, which may have walls with low shear-span ratios. Moreover, a wall system can behave very differently from what was assumed in the design process because the design might not have fully accounted for the interaction of the wall components with other elements in the structural system. For example, the designer may underestimate the coupling moments exerted by horizontal diaphragms on structural walls, and thereby overestimate the shear-span ratio of the walls. This could result in walls whose behavior would be dominated by shear rather than flexure, as shown in a study by Stavridis et al. (2016). Furthermore, the coupling forces exerted by horizontal diaphragms or beams and the axial restraints exerted by walls whose webs are perpendicular to the direction of the seismic action can influence the axial forces developed in the walls parallel to the seismic action, thereby changing their strength and behavior.

The flexural behavior of a reinforced masonry wall depends on several factors. Because most reinforced masonry walls do not have confined boundary elements, a flexure-dominated wall can exhibit severe toe crushing, followed by the buckling of the exposed vertical reinforcing bars, as shown in Figure 4-1. Toe crushing may jeopardize the effectiveness of the vertical bars if they are lap-spliced to dowel bars at the wall base. After a buckled bar has been subjected to a few cycles of straightening and bending as the wall is displaced back and forth, bar fracture may soon follow due to low-cycle fatigue. This will lead to severe strength degradation in the wall. For a given displacement level, the extent of toe crushing depends on the axial compressive load, the amount of vertical reinforcement, and the shear-span ratio.

The strength and behavior of a wall dominated by diagonal shear cracks, as shown in Figure 4-2, depend on the shear-span ratio, the strength of the masonry, the aggregate-interlock action along the cracks, the amount of the shear reinforcement, and the applied axial load. The vertical reinforcement may also contribute to the shear resistance through dowel action. However, this contribution is normally small compared to that provided by the horizontal reinforcement, unless the top of the wall is so restrained in the vertical direction that diagonal tension can develop in the vertical reinforcement crossing the diagonal cracks as the cracks open.

A wall may also develop base sliding. In that case, the resistance is provided by shear friction, as well as the dowel action of the vertical reinforcement, depending on the magnitude of the axial compressive load on the wall and the amount of clamping force developed by the vertical reinforcement.

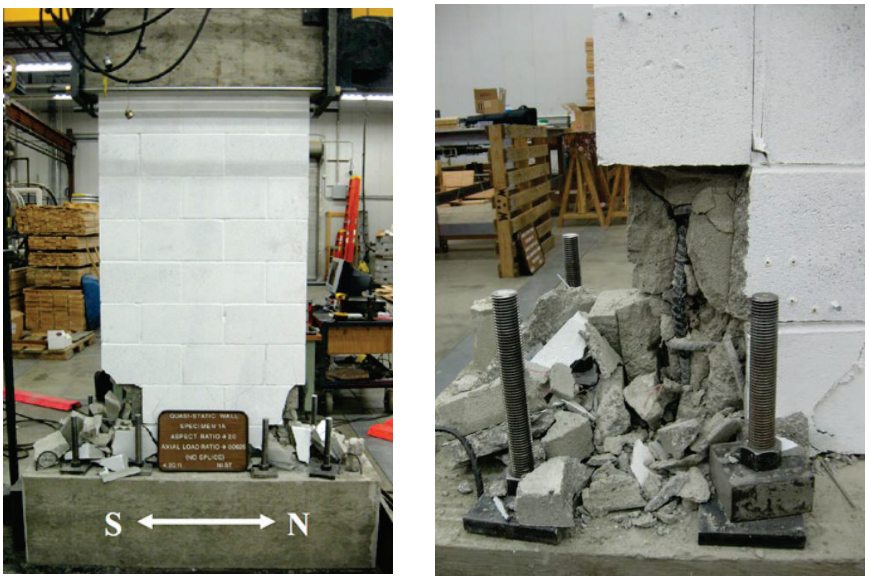

Figure 4-1 Crushing and bar buckling in a flexure-dominated wall (Wall WSU-W-1A tested by Sherman, 2011).

Figure 4-2 Failure of a shear-dominated wall (Wall UT-PBS-02 tested by Ahmadi, 2012).

Ideally, a numerical model used to simulate the inelastic behavior and assess the collapse potential of a reinforced masonry building must be capable of capturing the aforementioned failure mechanisms and the system effects that may influence the strength and ultimate behavior of the wall system. In particular, the model should have sufficient sophistication to accurately describe the physical mechanisms that govern the inelastic behavior,

accounting for the influence of the wall geometry, reinforcement details, and boundary conditions on the failure mechanisms, which determine the strength and displacement capacity of a wall.

4.2.2 Overview of Modeling Methods

Different modeling approaches, ranging from simplified macro-element models to refined finite-element models, have been used to analyze the behavior of reinforced masonry buildings. Macro-element models cannot predict the physical mechanisms that develop in a masonry wall system, but rather they describe the load-displacement relations of the wall components or system with phenomenological hysteresis laws that have to be calibrated with experimental data or numerical results from refined finite-element models. To select appropriate experimental data for model calibration, the failure mechanisms of the walls have to be known *a priori*.

Depending on the level of sophistication, refined finite-element models can describe various physical mechanisms that govern the inelastic behavior of a wall. For refined finite-element analysis of 3D reinforced masonry structures, Mavros (2015) used shell elements with smeared-crack material models and cohesive-crack interface elements to simulate the crushing and cracking behavior of masonry. These models also incorporated additional elements to simulate the bond-slip behavior and dowel actions of reinforcing bars, which can have a significant influence on the inelastic behavior of a wall whether it is dominated by flexure, shear, or base sliding. The models, however, did not account for bar buckling and fracture. Because of this, the models tended to overestimate the residual strength of a wall after severe damage. The models also did not account for the geometric nonlinearity, which could be important for modeling behavior of a structure near collapse. Other than that, the models were able to adequately predict the failure mechanisms and inelastic behavior of masonry walls. Nevertheless, in spite of their predictive capability, one main drawback of refined finite-element models is that they demand significant computational resources, and therefore they are not practical for high-volume numerical simulations like incremental dynamic analysis.

To attain computational efficiency, while not completely forgoing the physics of the problem, frame models have been used to represent masonry wall systems. In these models, beam-column line elements are used to model the vertical and horizontal wall components, and the panel zones connecting the wall components and the cross-sectional lengths of the walls are idealized as rigid end zones in the beam elements, as shown by the examples presented in Figure 4-3.

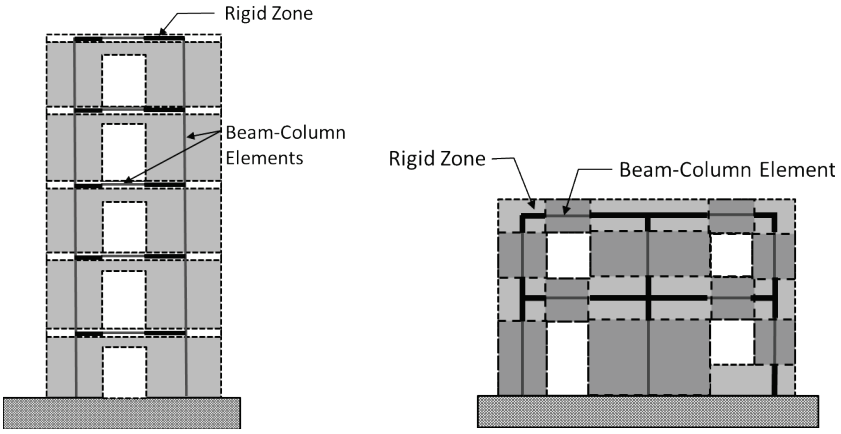

Figure 4-3 Frame models for masonry wall systems.

Beam-column elements with a fiber-section discretization can accurately capture the inelastic flexural behavior of a reinforced masonry wall, including the axial load-moment interaction, as long as appropriate material models are used to describe the behavior of masonry and steel reinforcement, accounting for bar buckling and fracture, and an accurate estimation is made for the effective plastic-hinge length of the wall (NIST, 2017). Such models have been extended to simulate the inelastic shear behavior of reinforced concrete or masonry members (e.g., Petrangeli et al., 1999; Rose, 2001; Marini and Spacone, 2006; Jiang and Kurama, 2010; Massone et al., 2009; Kolozvari et al., 2014; Peruch et al., 2019). However, the shear stress-shear deformation laws used in these models are either empirical without predictive capabilities or not sufficiently reliable and robust for the analysis of a wall system.

Beam-truss models have also been used to analyze reinforced masonry and concrete shear walls (Moharrami et al., 2015; Lu et al., 2016; Lu and Panagiotou, 2013; 2016). These models can capture the flexural and shear behavior of walls. Although they are computationally more efficient than refined finite-element models, they require more simplifying assumptions and, therefore, may not be as realistic as finite-element models.

4.2.3 Adopted Modeling Approach

Considering the pros and cons of various modeling methods and the need for a computationally efficient, yet-accurate method for incremental dynamic analysis, a two-pronged approach was adopted to assess the collapse potential of the reinforced masonry building archetypes. First, for each building archetype, a refined finite-element model was developed. The model was able to capture both the flexural and the shear behavior of the walls. Dynamic response-history analyses were performed with the model using three sets of bi-directional ground motion records that had different

response spectrum characteristics and time-history profiles. The numerical results obtained were used to calibrate a computationally efficient frame model suitable for incremental dynamic analysis. Because the refined models showed that diagonal shear cracking played a significant role in the inelastic behavior of the bottom-story walls, a macro-element model was used to represent the behavior of each of these walls in the simplified frame models. Each macro-element consisted of a rigid bar with rotational springs at one or both ends. The nonlinear behavior of the rotational springs was described by a phenomenological hysteretic law, which was calibrated with the results of the refined finite-element analyses. Walls in the upper stories of the archetypes suffered light or no damage. They were, therefore, modeled with linearly elastic beam-column elements.

The refined finite-element modeling method used was an extension of the scheme used by Mavros (2015). It was able to capture the response of a reinforced masonry building in the large-displacement regime up to the point of collapse. The modeling method also was able to capture the local damage behavior and failure mechanisms of a wall in a detailed manner, including the degradation of the bond and dowel resistance developed by the reinforcing bars and bar buckling and fracture. A detailed description of the modeling scheme and material models is presented in Koutras (2019). The refined models were built with shell and beam elements with geometric nonlinearity to account for P-delta effects. An element removal strategy (for crushed masonry and fractured bars) was introduced to enhance the robustness of the numerical computation and the accuracy of the model when the structure approached collapse. The modeling scheme was validated by experimental data. Details of the refined and simplified models follow.

4.3 Refined Finite-Element Modeling

4.3.1 Overview of Modeling Approach

Figure 4-4 shows the refined finite-element model developed in this study for a two-story commercial building archetype. It is representative of the refined models developed for all the archetypes. The analyses were conducted with the commercial software LS-DYNA (LSTC, 2018). Custom material models were implemented in the software to meet the special modeling needs to capture the various failure mechanisms. A smeared-crack material law was implemented in the shell elements to describe the crushing and cracking behavior of the masonry walls and horizontal concrete diaphragms. For masonry walls in the bottom story, where significant diagonal shear cracks might develop, cohesive crack interface elements were introduced to represent cracks in a discrete fashion, and to model sliding along crack surfaces and

joints. The reinforcement in these walls was modeled with beam elements to allow the simulation of bar buckling. The bars were connected to the shell elements with interface elements to simulate bond slip and dowel actions. For walls in the upper stories, where no significant damage was expected, the nonlinear behavior was modeled in a coarser manner, in which only smeared-crack shell elements were used and the reinforcement was modeled in a smeared fashion with a bi-linear material law.

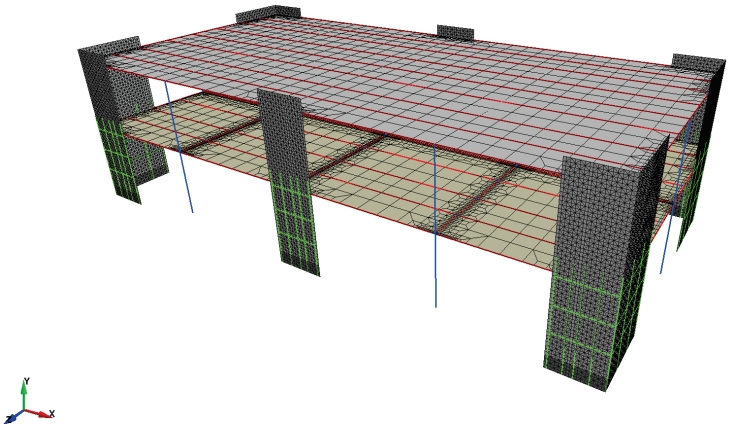

Figure 4-4 Refined finite-element model for a two-story reinforced masonry commercial building archetype.

The steel beams in the floor and roof systems and the steel columns in the gravity frames were represented by beam-column elements with fiber sections and a bi-linear material law. Zero-length springs were used to connect the steel beams to the columns and masonry walls.

4.3.2 Detailed Modeling of Reinforced Masonry Walls

For modeling the bottom-story walls, which might develop significant diagonal cracking, four types of elements were used. Smeared-crack shell elements and cohesive-crack zero-thickness interface elements were used for modeling the behavior of masonry, beam elements for modeling the horizontal and vertical reinforcing bars, and additional interface elements for modeling the bond-slip and dowel-action behaviors of reinforcing bars. The discretization scheme for a typical wall is shown in Figure 4-5. The placement of cohesive-crack interface elements at a 45-degree angle was used to represent diagonal shear cracks in a discrete fashion, preventing possible stress locking that could be introduced by smeared-crack elements (Rots, 1988; Lotfi and Shing, 1991). The horizontal cohesive-crack interface elements were to allow an accurate simulation of sliding along a crack surface or joint. The beam elements representing the reinforcing bars were connected to the shell elements through interface elements to allow the

simulation of bond slip and dowel actions. The beam elements had a steel material law that accounted for low-cycle fatigue and bar fracture. The material models adopted for these elements are described in the next section.

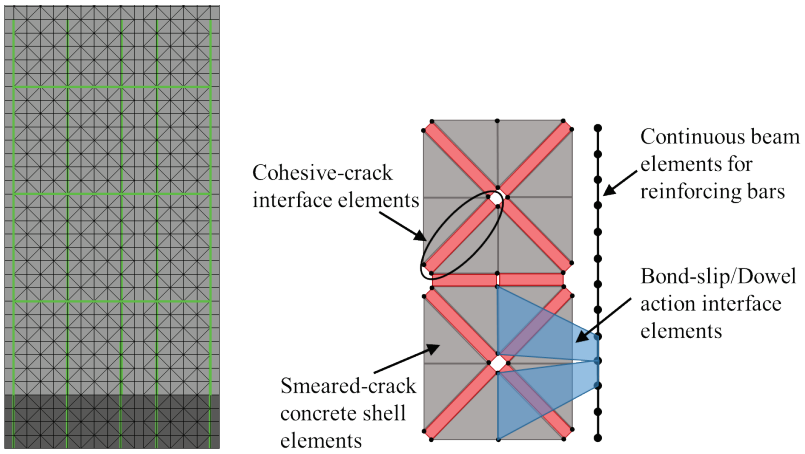

Figure 4-5 Detailed modeling of reinforced masonry walls with finite elements.

4.3.3 Smeared-Crack Shell Elements

The cross section of each shell element was discretized into three layers of masonry or concrete to simulate the out-of-plane bending behavior of a wall or that of a horizontal diaphragm. A smeared-crack material model was used to simulate the compressive behavior, as well as tensile cracking of the material in an efficient fashion. The smeared-crack model adopted a simple and robust orthotropic material law. As shown in Figure 4-6, before cracking, the axes of orthotropy were aligned with the directions of the principal strains. Cracking initiated when the maximum principal stress reached the tensile strength of the material. Beyond that point, the axes of orthotropy remained fixed, with directions parallel and perpendicular to the direction of the first crack, as illustrated in Figure 4-6. Shear strain and shear stress could develop along the crack since the axes of orthotropy would not necessarily coincide with the directions of the principal strains after the development of the crack. After this point, the shear stress was related to the shear strain with an elastic-perfectly plastic material law, with the initial yield strength assumed to be 50 percent of the tensile strength, f_t. Another crack could develop in the direction perpendicular to the first crack when the tensile stress parallel to the first crack exceeded the tensile strength.

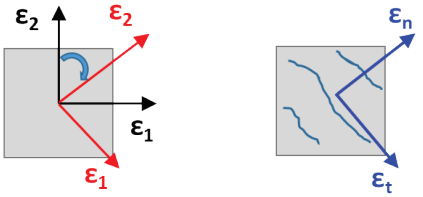

Axes of orthotropy rotate together with the axes of principal strains

Axes of orthotropy remain fixed, parallel and normal to the direction of the first crack.

(a) Before cracking (b) After cracking

Figure 4-6 Axes of orthotropy of the smeared model before and after cracking.

The uniaxial stress-strain law for tension and compression in each of the orthotropic directions is shown in Figure 4-7. After crack initiation, the stress-strain relation for the tension regime assumed an exponential function to represent strain softening and a reduced elastic stiffness for unloading and reloading. The reduced stiffness allowed complete crack closure upon unloading. In the first compressive loading cycle, the material response was linearly elastic until it reached the stress level, f_o; after that, it was described by a parabolic function to represent strain hardening and a linear function with a negative slope to represent post-peak strain softening. Unloading in compression followed the initial stiffness until reaching zero stress. The stress remained zero upon the further decrement of the compressive strain until the strain reached zero. After that point, tensile stress might develop.

The residual plastic strain in compression was denoted by ε_{pl}, which was calculated during each unloading in the compression regime. Reloading in compression followed the same path, and compressive stress developed when the compressive strain exceeded ε_{pl}. Interaction of the compressive responses in the two orthotropic directions was modeled in a simple and efficient manner by assuming that the residual plastic strain, ε_{pl}, was isotropic and equal to the larger of the two developed in these directions. When the compressive strain exceeded ε_0, the tensile strength and shear strength were reduced in the same proportion as the decrement of the compressive resistance with respect to the peak. The material was considered completely crushed when the compressive strain in any of the two directions reached ε_u. The shell element was removed when this condition occurred at all sampling points. This material model was implemented as a user-defined material in LS-DYNA. Although similar material laws were available in LS-DYNA, they did not allow the element removal strategy used in this study, which required the material law to pass information to the adjacent interface elements.

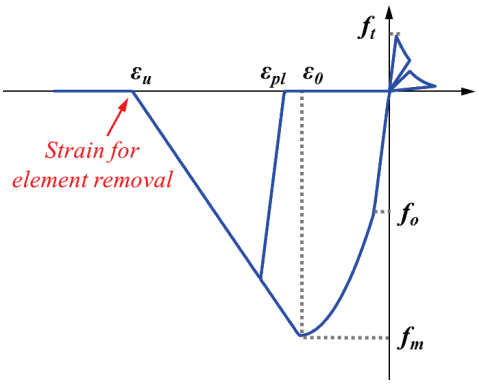

Figure 4-7 Uniaxial stress-strain relation for the orthotropic model for masonry and concrete; the relation shown is for a material first loaded in tension.

4.3.4 Cohesive-Crack Interface Elements

Figure 4-8 shows the cohesive-crack interface model used to simulate shear and flexural cracks in a wall in a discrete fashion. The interface elements had zero-thickness and were compatible with the shell elements in that the interface could have a distributed normal stress developed over the area to resist the out-of-plane bending moment developed by a shell element. A 3D plasticity model was used to simulate mixed-mode (mode I, II, and III) fracture, crack opening and closing, and relative shear sliding in the interface. Failure was governed by a yield surface that had the shape of a hyperboloid, as shown in Figure 4-8(b), and damage in shear and tension was modeled with a set of softening rules that governed the evolution of the yield surface. The model could simulate reversible joint dilatation due to the wedging action of the asperities, and irreversible joint compaction due to damage induced by cyclic shear reversals under compression. The cohesive-crack material law was based on the work of Kottari (2016), which is an extension of the two-dimensional cohesive crack law of Koutromanos and Shing (2012). The material model was implemented as a user-defined material in LS-DYNA. Each interface element had four Gauss integration points.

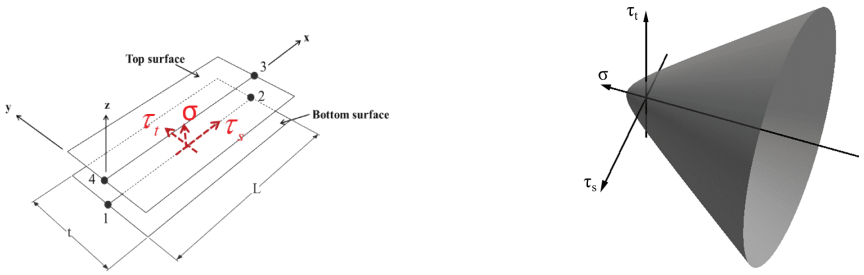

(a) Interface element configuration

(b) Yield surface for mixed-mode fracture

Figure 4-8 Cohesive-crack interface element.

4.3.5 Beam Elements for Steel Reinforcement

The beam elements used to model reinforcing bars had the Hughes-Liu beam-element formulation (LSTC, 2018). It accounted for geometric nonlinearity. Although beam elements were computationally more demanding than truss elements, they could describe bar buckling and dowel actions. The uniaxial material law of Kim and Koutromanos (2016) was implemented to model the cyclic behavior of steel. The responses of the model under a monotonically increasing displacement and cyclic loading are shown in Figure 4-9. The material model also accounted for bar fracture due to low-cyclic fatigue. Fracture was triggered when a scalar damage parameter, which was based on the cumulative plastic work related to the tensile stress, exceeded a critical value. The model had been calibrated and used by Moharrami and Koutromanos (2017) for structural collapse simulations. The beam element was removed as soon as fracture was detected at any point at a beam cross section.

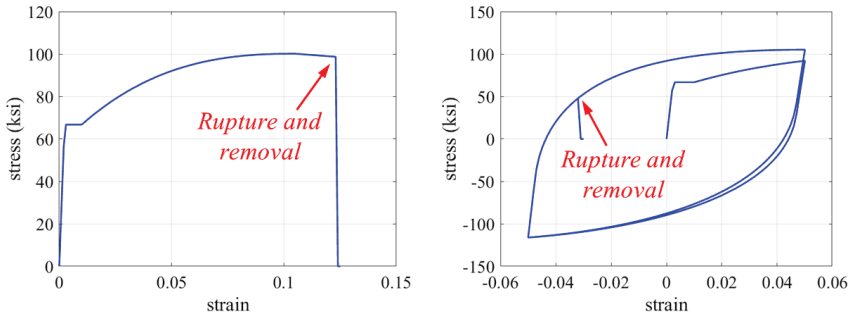

Figure 4-9 Steel material model for reinforcing bars (Kim and Koutromanos, 2016).

4.3.6 Bond-Slip and Dowel-Action Interface Elements

The beam elements representing the reinforcement were attached to the masonry shell elements through interface elements that simulated bond slip and dowel actions, as shown in Figure 4-10. The relative displacement of the interface consisted of three components: (1) the relative shear displacement (slip), $\tilde{u}$, between the bar and the masonry along the axial direction of the bar; (2) the relative displacements $\tilde{v}$ and $\tilde{w}$ that were normal to the slip, representing the deformation of the masonry adjacent to the bar and any gap created by the dowel action of the bar; and (3) the relative twist between the masonry and the bar, as depicted in Figure 4-10. This third component was restrained by a torsional stiffness as discussed later. To account for large rigid-body rotations, the local coordinate system of the element was constantly updated so that the x axis always remained parallel to the masonry side, and the y and z axes were determined from the averaged respective rotations of the nodes on the masonry side (Crisfield, 1990).

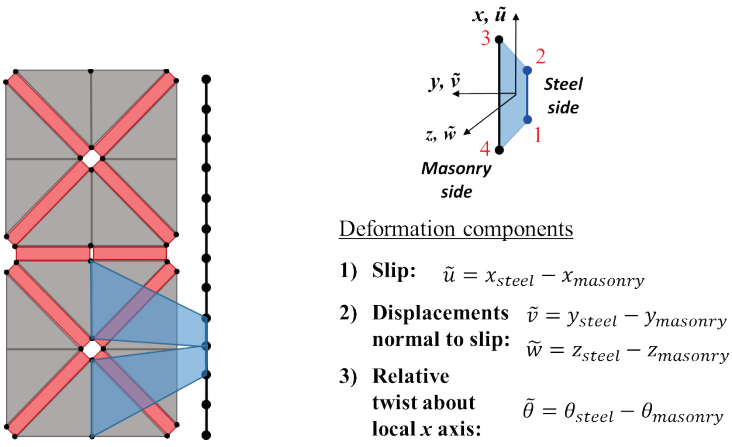

(a) Connectivity (b) Deformation components

Figure 4-10 Bond-slip and dowel-action interface elements connecting bars to masonry.

Bar slip was modeled with the bond-slip law developed by Murcia-Delso and Shing (2014) for reinforced concrete. The monotonic and cyclic behaviors of the bond-slip model are shown in Figure 4-11. The bond strength was specified as a function of the compressive strength of the grout, and the model accounted for the degradation of bond resistance as the gap between the bar and the surrounding grout or concrete increased. The masonry behavior in dowel actions along each of the local coordinates *y* and *z* was represented by a simple uniaxial material law, which is shown in Figure 4-12. The behavior along each direction was assumed to be independent of the other. Under monotonic loading, the material behavior was initially elastic-perfectly plastic. Beyond a certain deformation, the model showed a post-peak softening behavior described by a linear function until a specified residual strength was reached, as shown in Figure 4-12(a). Unloading occurred with a stiffness higher than the initial stiffness. After the stress reached zero, it remained zero upon further decrement in deformation. The deformation at which the stress reached zero represented a gap. The gap generated this way could only increase in each loading direction and could be different in the positive and negative directions. Reloading followed the initial stiffness once the gap was closed. The initial stiffness and yield strength were determined with the dowel law proposed by Dulacska (1972) for reinforced concrete. The calibration was performed with a simple model consisting of a dowel bar embedded in masonry, which was subjected to increasing shear displacement along a frictionless joint, as shown in Figure 4-12(b). The slope of the linear softening branch was determined in an *ad hoc* manner by matching results of reinforced masonry wall analyses to quasi-static wall test data, as presented in a following section. Using Dulacska's formula, the dowel strength, P_{max}, was calculated as a function of

the compressive strength of the grout, the diameter of the bar, the yield strength of the bar, and the angle of the crack plane with respect to the direction of the bar. The crack angle was assumed to be 45 degrees to model the dowel resistance of the bars at locations adjacent to diagonal cracks.

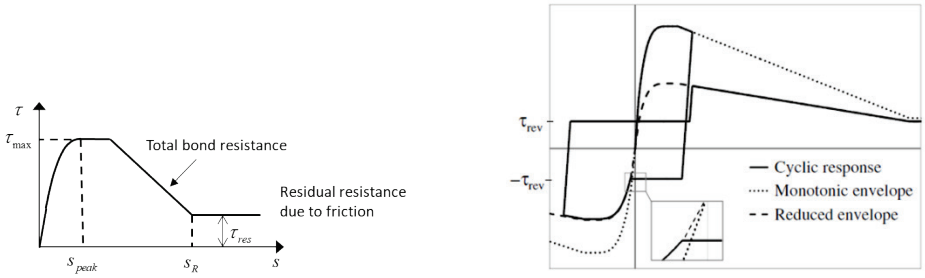

(a) Monotonic response (b) Cyclic response

Figure 4-11 Monotonic and cyclic behaviors of bond-slip model (Murcia-Delso and Shing, 2014).

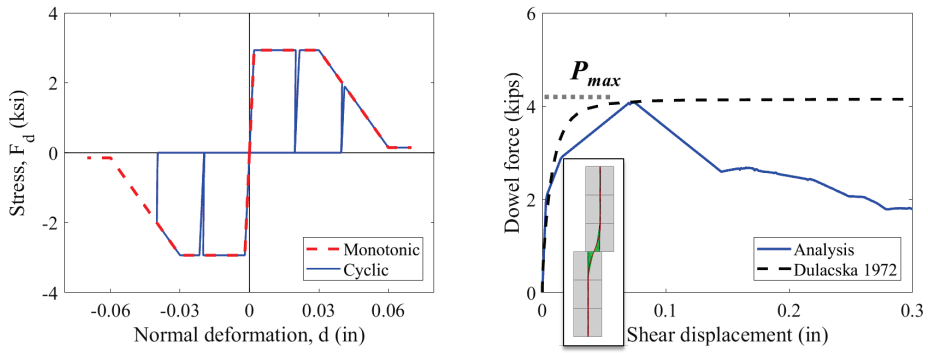

(a) Stress-deformation relation (b) Calibration of model

Figure 4-12 Monotonic and cyclic behaviors of dowel-action model.

The reduction of the bond and dowel resistances due to the compressive crushing of the surrounding masonry was modeled with a strength-reduction factor, k. The factor was equal to one before the onset of crushing of masonry (i.e., when the maximum compressive strain had not exceeded ε_o) and was reduced to a residual value k_{res} when the maximum masonry compressive strain reached ε_u, as shown in Figure 4-13. The compressive strain developed in the surrounding masonry was estimated by assuming that it was equal to the axial compressive strain developed at the masonry side of the interface element.

A bi-linear material law was introduced to restrain the spinning of the bar with respect to the masonry. The interface element was implemented as a user-defined element in LS-DYNA using the formulation proposed by Kottari et al. (2017), which allowed the connection of beam elements to larger shell elements.

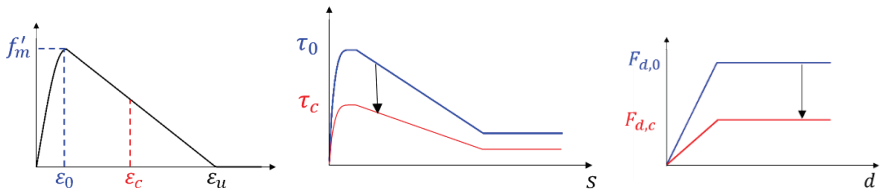

(a) Masonry crushing

(b) Degradation of bond strength

(c) Degradation of dowel strength

$$\tau_c = k(\varepsilon_c)\tau_0 \tag{5-1}$$

$$F_{d,c} = k(\varepsilon_c)F_{d,0} \tag{5-2}$$

$$k(\varepsilon_c) = \left[1 + \frac{\varepsilon_c - \varepsilon_0}{\varepsilon_u - \varepsilon_0}\left(k_{res} - 1\right)\right] \tag{5-3}$$

Figure 4-13 Degradation of bond and dowel strengths caused by masonry crushing.

4.3.7 Element Removal Scheme

An element removal scheme was introduced to remove elements whose material reached the failure point. The process was triggered by either masonry crushing or bar fracture. When a masonry shell element reached the crushing condition, the shell element was removed, all the adjacent cohesive interface elements were removed, and all the bond-slip/dowel-action interface elements connected to the shell element were removed. When a beam element reached fracture, the beam element was removed, and the adjacent bond-slip/dowel-action interface element was removed. To do this, a non-local scheme was implemented to inform neighboring elements when an element reached the failure point.

This scheme helped to prevent numerical problems that could be introduced by severe element distortion and unrestrained degrees of freedom when a shell or beam element reached the failure point. This scheme also eliminated undesired spurious resistance introduced by the remaining cohesive-crack or bond-slip/dowel-action interface elements after the shell or beam element was removed.

4.3.8 Calibration and Validation with Experimental Data

The finite-element modeling scheme was validated with experimental data from quasi-static tests of reinforced masonry wall segments and shake-table tests of two masonry wall structures. The material models for the smeared-crack shell elements, cohesive crack interface elements, and bond-slip and dowel-action interface elements had a number of parameters to be calibrated. However, the values of many of these parameters were not available from the experimental studies, which typically provided only the compressive

strengths of the masonry materials and the yield and tensile strengths of the steel reinforcement. Hence, material parameters, such as the compressive and tensile fracture energies of the masonry, the parameters governing the stiffness and strength of the dowel-action interface, and the bond strength and bond deterioration for the bond-slip law, had to be calibrated based on information provided in the literature, as well as the observed response of the wall specimens in the experiments.

The calibrated models were used for the analyses of the building archetypes, as will be discussed later. For the analyses of the wall tests and the building archetypes, the values of the material parameters were either kept constant or specified as functions of the material strengths in a consistent fashion.

For the smeared-crack model, the modulus of elasticity of masonry was assumed to be 667 times the masonry compressive strength, f'_m. It was found to provide a better correlation with the wall test data than the value of $900f'_m$, as recommend in TMS 402. The masonry strain at the peak compressive strength was set to -0.003 based on the prism test data of Atkinson and Kingsley (1985). The fracture energy dissipation in compression was controlled by the ultimate strain, ε_u, at which the compressive resistance of masonry was completely exhausted (see Figure 4-7). The fracture energy that could be dissipated in each shell element must be a function of the element size with respect to the expected plastic-hinge height of the wall to ensure the objectivity of the numerical results. This is due to the artificial plastic strain localization phenomenon that can be exhibited by a finite-element model (Bažant and Oh, 1983). In this study, the value of ε_u was specified to be -0.035, which was found to be satisfactory for all the cases considered.

Quasi-Static Wall Segment Tests

To demonstrate the capability of the refined modeling scheme to capture the inelastic response and associated failure mechanisms of reinforced masonry shear walls, four quasi-static tests conducted on wall segments were considered. Two of them had flexure-dominated walls, and the other two had shear-dominated walls. The material parameters were determined with the approach described above. The material strengths are based on the data provided in the test reports.

Figure 4-14 and Figure 4-15 compare the experimental and numerical results for flexure-dominated walls tested by Kapoi (2012) and Sherman (2011), respectively. Both walls had the same dimensions and similar reinforcement details. The wall in Figure 4-14 had five #4 vertical bars and nine #4 horizontal bars, whereas the wall in Figure 4-15 had five #6 vertical bars and

the same horizontal reinforcement. Both walls were subjected to a constant axial compressive load of 48 kips. The failure behavior of the wall in Figure 4-15 is shown in Figure 4-1.

Figure 4-14 and Figure 4-15 show that the finite-element models were able to adequately capture the lateral strengths, hysteretic responses, and failure mechanism of the walls. However, the extent of toe crushing along the height of the walls was underestimated by the models, as shown by the extent of element removals in the figures. In the analyses, compressive softening was localized in a single row of shell elements, leading to unloading in the elements above, whereas crushing was more spread into the upper courses in the actual tests. This strain localization was a numerical artifact, as discussed above.

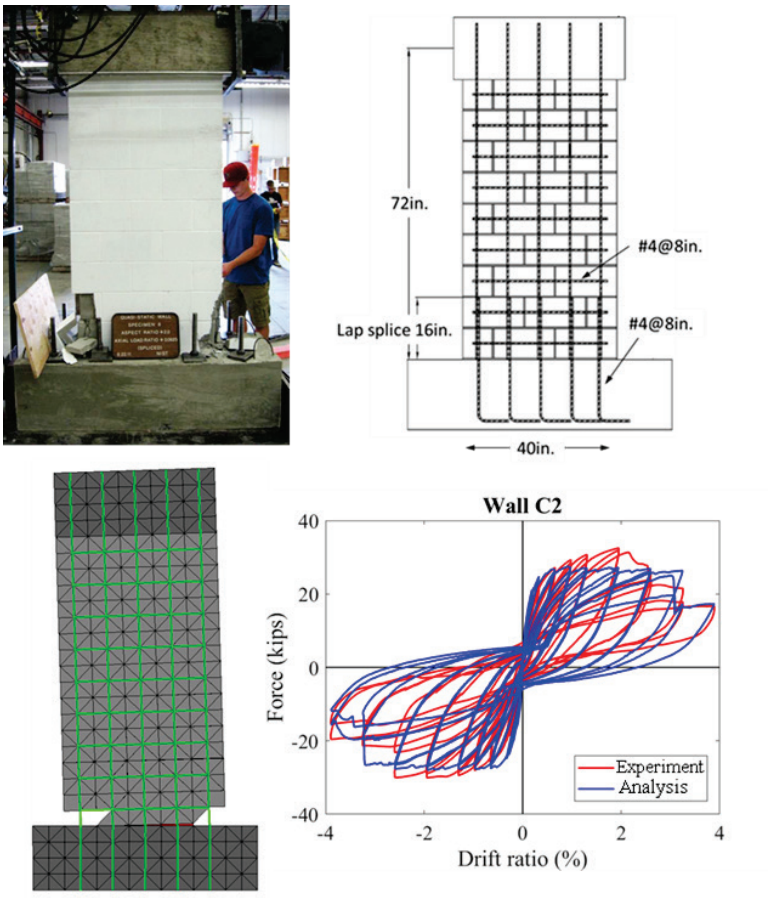

Figure 4-14 Flexure-dominated wall tested by Kapoi (2012).

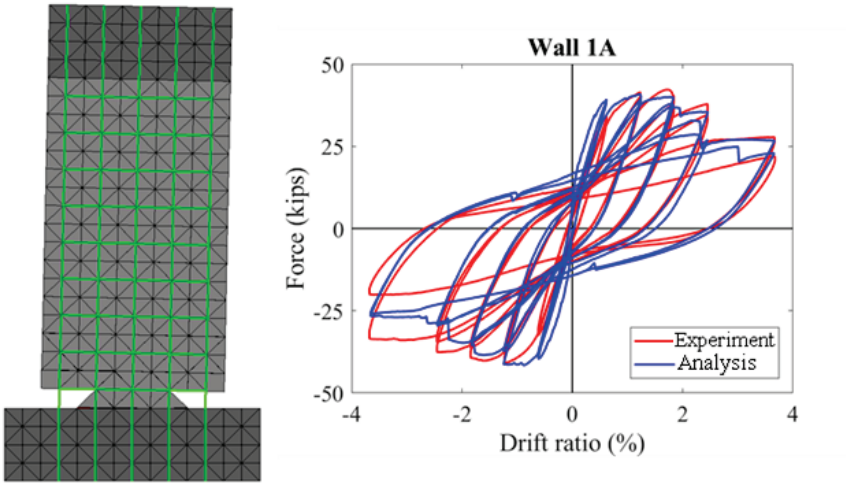

Figure 4-15 Flexure-dominated wall tested by Sherman (2011).

The two shear-dominated walls modeled here were tested by Voon and Ingham (2006) and Ahmadi (2012), respectively. One had horizontal reinforcement and the other did not. As shown in Figure 4-16 and Figure 4-17, the finite-element models were able to reproduce the hysteretic responses and failure mechanism well.

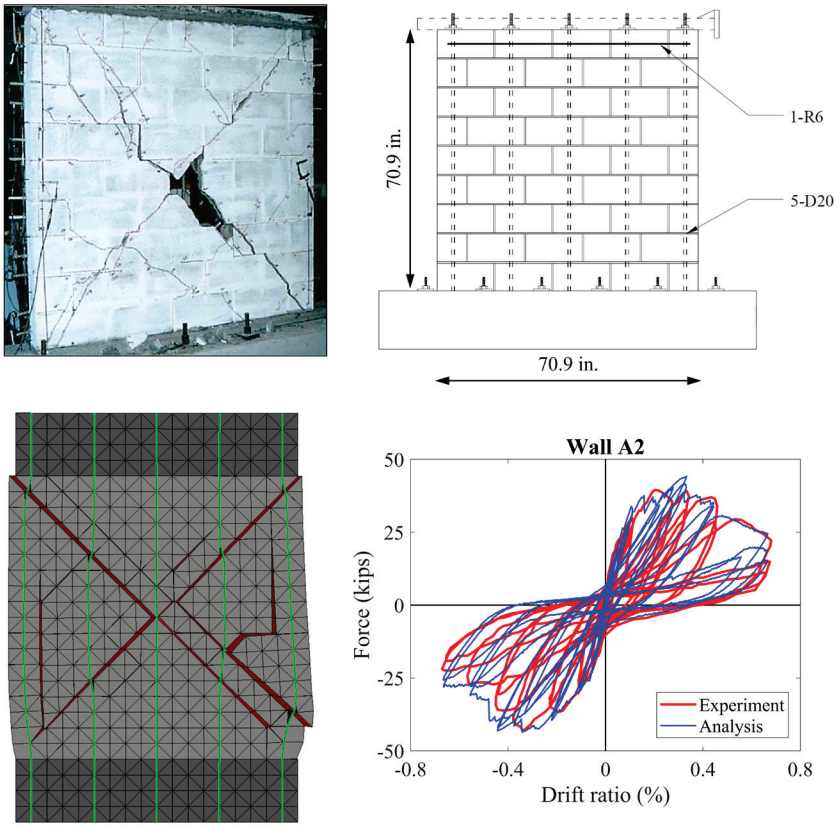

Figure 4-16 Shear-dominated wall tested by Voon and Ingham (2006).

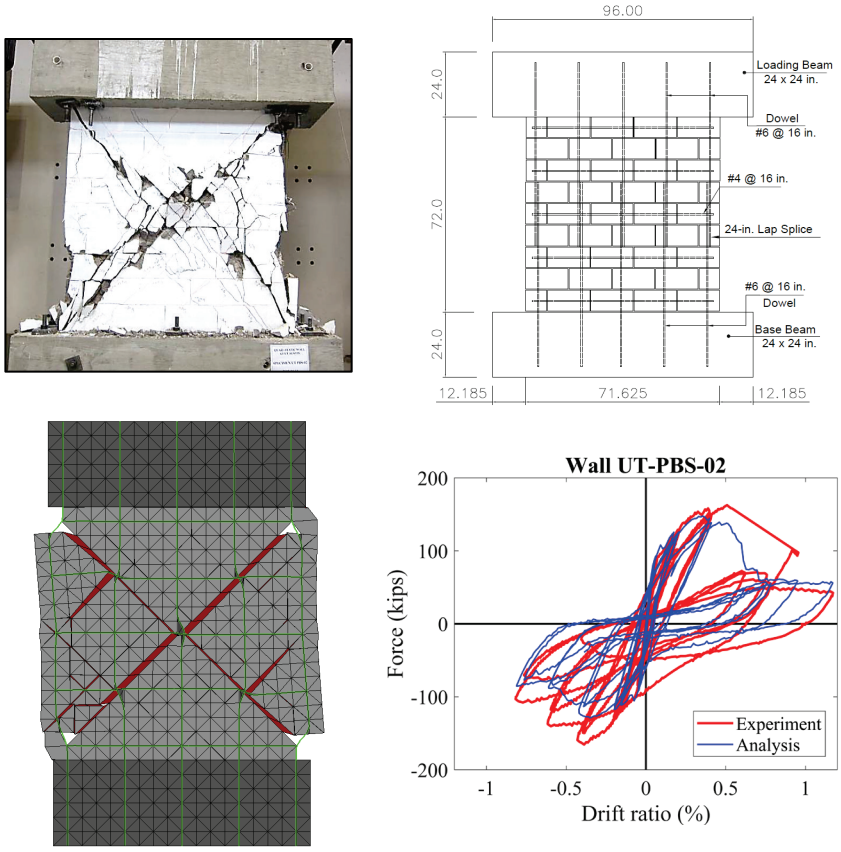

Figure 4-17 Shear-dominated wall (UT-PBS-02) tested by Ahmadi (2012).

Shake-Table Test of a Two-Story Building

To validate the ability of the modeling scheme to simulate the dynamic response of a masonry building, a two-story reinforced masonry wall structure tested by Mavros et al. (2016) on a shake table, as shown in Figure 4-18, was analyzed. Uni-directional ground motions were applied in the test series. The structure had two short masonry piers in the bottom story developing diagonal shear cracks during the test, whereas the slender pier had flexure-dominated behavior. The model was subjected to a sequence of ground motions from the tests. The numerical results are compared to the test results in Figure 4-18 for the last ground motion in the experiment, which was at the level of the maximum considered earthquake.

Shake-Table Test of a Wall Structure to Near Collapse

The ability of the refined modeling scheme to capture the behavior of a masonry wall system at the verge of collapse was validated with the shake-table tests of two single-story masonry structures (Cheng et al., 2020). Each structure had two coupled T-walls as the seismic-force-resisting system, and the second structure had six rectangular walls perpendicular to the direction

of shaking. Each was subjected to a sequence of uni-directional ground motions. As shown in Figure 4-19, the second structure sustained a story drift of 13 percent without collapse, and the failure of the two T-walls was governed by diagonal shear cracks. The severely damaged structure was still able to carry the gravity load after the test. The other structure exhibited similar performance. A refined finite-element model was developed to simulate the shake-table tests. Figure 4-19 compares the base shear-vs.-the story-drift hysteresis curves obtained from the last test and the model. It also shows the numerically obtained failure pattern. The model was able to predict the lateral resistance, load degradation, and failure mechanism of the structure well.

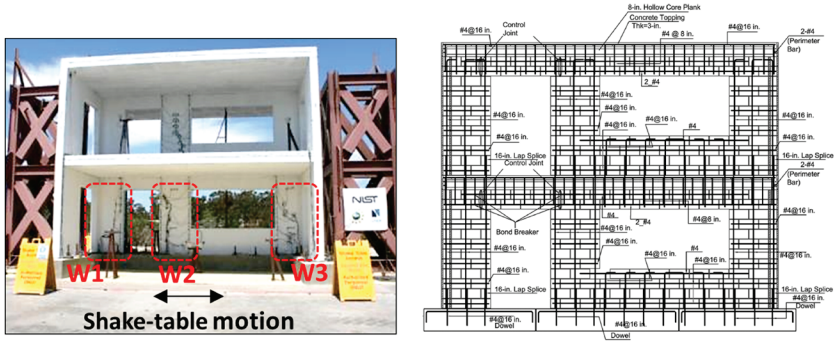

Test configuration and reinforcement details

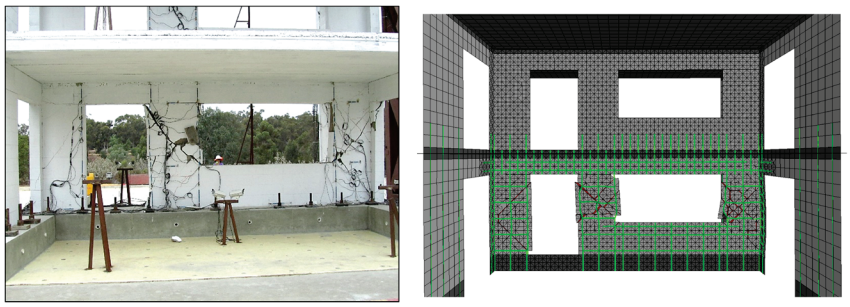

Damage in structure and model after the sequence of motions (deformations magnified by 3)

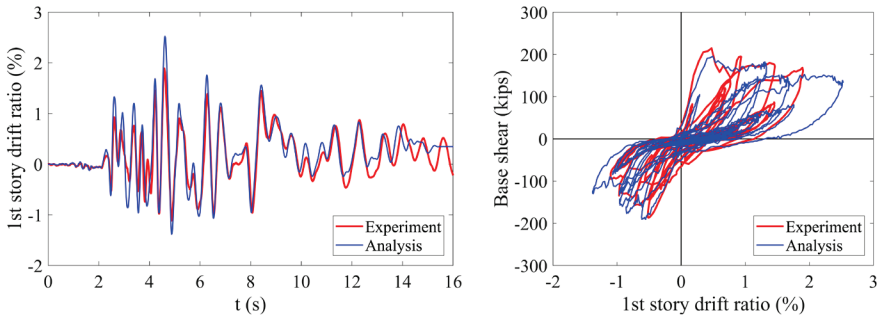

Comparison of experimental and numerical response in the final motion

Figure 4-18 Two-story reinforced masonry wall structure tested by Mavros et al. (2016).

Damage after Rinaldi 130% (final motion)

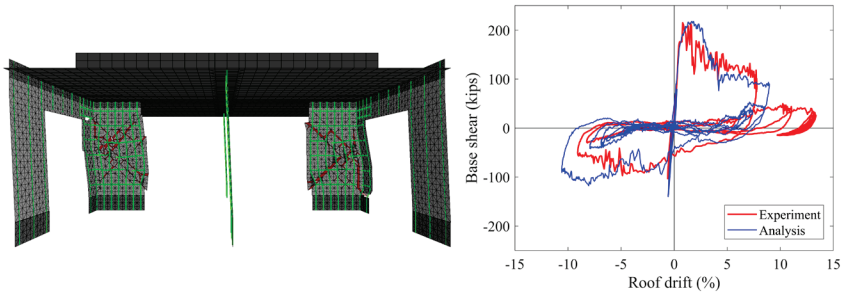

Analysis of the test sequence: Numerical results for Rinaldi 130%

Figure 4-19 Reinforced masonry wall system tested to near collapse on a shake table (Cheng et al., 2020).

4.4 Overview of Archetypes Considered for Parametric Studies

Six commercial building archetypes, COM1 through COM6, whose designs are discussed and presented in Chapter 3 and Appendix A, were selected for parametric studies. Their configurations and seismic-design criteria are summarized in Table 4-1.

Archetypes COM1, COM2, and COM3 have one, two, and four stories, respectively, and were designed for a high-seismic intensity (S_{MS} = 1.5g). COM4, COM5, and COM6 have the same number of stories as COM1, COM2, and COM3, respectively, but were designed for a very high-seismic intensity (S_{MS} = 2.25g). Except for COM4, the latter group had more reinforcement in the walls, and COM6 had a larger total wall cross-sectional area than COM3. The walls in COM1 and COM4 had identical designs with the reinforcement governed by the minimum prescriptive requirements of the code, but COM4 had a stronger roof diaphragm. The roof system of the archetypes consisted of a corrugated steel deck on steel joists, and the floor diaphragms were constructed of concrete slabs cast on corrugated steel pans supported on steel beams and joists. The gravity loads were carried by the walls and steel columns.

A refined finite-element model was developed for each archetype. Each refined model was then used to calibrate a simplified frame model, which in turn was used for incremental dynamic analysis to calculate a collapse fragility curve.

Table 4-1 Commercial Reinforced Masonry Building Archetypes and Seismic-Design Criteria

Archetype ID	Configuration			Seismic-Design Criteria			
	No. of Stories	h_r (feet)	W (kips)	S_{MS} (g)	T_a[1] (sec)	$T=C_uT_a \geq$ 0.25 sec[2]	C_s (g)
Commercial Buildings: High Seismic							
COM1	1	12	258	1.5	0.13	0.25	0.20
COM2	2	24	762	1.5	0.22	0.30	0.20
COM3	4	48	1899	1.5	0.37	0.51	0.20
Commercial Buildings: Very High Seismic							
COM4	1	12	258	2.25	0.13	0.25	0.30
COM5	2	24	762	2.25	0.22	0.30	0.30
COM6	4	48	2419	2.25	0.37	0.51	0.30

[1] Building period calculated with ASCE/SEI 7-10 Equation 12.8-7, which was used in archetype design.

[2] Building period used in incremental dynamic analyses to determine collapse performance. $T = C_uT_a \geq 0.25$ seconds, in accordance with the requirements of FEMA P-695, where the values of the parameters C_u and T_a are specified by ASCE/SEI 7-10.

4.5 Refined Finite-Element Models for the Archetypes

The configurations of the refined finite-element models developed for the six archetypes are shown in Figure 4-20 (where the wall reinforcement shown for the two-story case represents that of COM5).

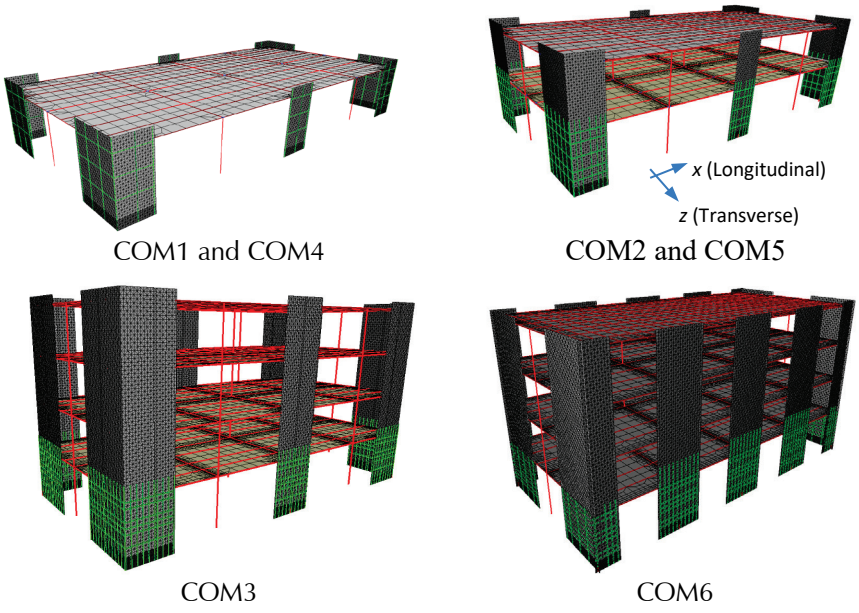

Figure 4-20 Finite-element models for commercial building archetypes.

In the refined finite-element models, the footings underneath the walls were modeled with vertically oriented elastic shell elements, whose bottom nodes were prevented from translations and out-of-plane rotations. In developing the refined models, different modeling schemes were tried. For all the archetypes, it was found that damage was localized in the bottom-story walls of the buildings. The upper-story walls experienced only mild cracking and yielding, if any, of the reinforcement. The collapse of the buildings was eventually governed by wall failures occurring in the bottom stories. For this reason, only the bottom-story walls were modeled with the detailed scheme described in Section 4.3.2. The upper-story walls were modeled in a less-refined fashion for the sake of computational efficiency, with only smeared-crack shell elements and smeared reinforcement, which was described by a bi-linear material law. This was deemed sufficient to capture the mild damage developed in the upper stories without affecting the failure mechanisms of the building archetypes. The lap splices for the vertical reinforcement in the walls were not modeled.

The steel columns and beams in the gravity-frame systems were modeled with displacement-based beam-column elements having a fiber-section discretization and a bi-linear material law. Each column had eight elements per story. Similar discretization was used for the beams. The columns were assumed to be hinge-connected at their bases. The beams at each floor were connected with clip angles to the columns and to the webs of the other beams running in the orthogonal direction. These connections did not provide much moment or axial-force restraint to the ends of the connected beams. This did not allow the development of strong composite action between the beams and the floor slabs at the locations of the connections. To represent this situation, the beams under the floor slabs in the two- and four-story archetypes were connected to the supporting beams and the columns with zero-length springs that did not transmit moments or axial forces but exerted strong translational restraint in the vertical and lateral directions. Beams were connected to the walls in the same way. The beams for the roof decks had regular hinge connections, except for the beam elements representing the joists, which were connected to the supporting beams without the axial restraint. The modeling of the horizontal diaphragms and the aforementioned connection details are further described in the following section.

For the analysis, the weight of each archetype was based on the following load combination: $1.05D + 0.25L$ (with D and L being the dead and live loads, respectively), according to the FEMA P-695 procedure. This resulted in a total building (excluding the foundation) weight of 274 kips for COM1 and COM4, 870 kips for COM2 and COM5, 2,200 kips for COM3, and

2,720 kips for COM6. The mass was distributed among the nodes according to the mass density of the elements.

4.5.1 Modeling of Horizontal Diaphragms

The floor and roof diaphragms were modeled with nonlinear shell and beam elements. Each floor diaphragm had a concrete slab cast on a corrugated steel pan with 2-inch ribs running along the transverse direction (z direction) of the buildings (see Figure 4-20 for the coordinate system). The distance from the top surface of the concrete slab to the top of the ribs was 3 inches, and the slab contained temperature and shrinkage steel running perpendicular to the ribs. To simplify modeling, the ribs were not explicitly represented. The slab was assumed to have a uniform thickness of 4 inches, including the concrete topping, and a 0.0474-inch-thick bottom layer representing the steel pan. The steel layer was set to act only along the direction of the ribs. The steel beams supporting the slabs were modeled with fiber-section beam elements with a bi-linear material law. The centroids of the beam and shell elements were offset vertically to represent the bending stiffness and capacity of the composite section correctly.

The finite-element discretization of a floor diaphragm is shown in Figure 4-21. As shown in the figure, at each beam-to-column connection beneath the slab, stiff beam elements were used to represent the offset between the centerline of the column and the end of the beam for a clip-angle connection. The offset was assumed to be 6 inches. Since the clip-angle connections were not able to transmit axial forces or moments, the bending resistance of the floor system in this region was provided by the slab only. Hence, the beams were connected to the columns with zero-length springs that did not transmit moments or axial forces but provided strong translational restraints in the vertical and lateral directions. Furthermore, the shell elements were not connected to the beam elements within this region. To capture the bending behavior of the slab in this region accurately, a fine discretization with 2-inch-wide shell elements was used. The same scheme was used to model the connections between the beams along the longitudinal direction of the building and the webs of the beams along the transverse direction. Away from these connections, a coarser mesh with the element dimension of 36 inches was used.

For all the archetypes, the roof diaphragm was a light-corrugated steel deck with 1.5-inch ribs, as shown in Figure 4-22, running along the transverse direction (z direction) of the buildings. The deck panels were stitched together with fasteners and are supported on steel joists. Experimental studies by Tremblay et al. (2004) showed that the in-plane shear stiffness and

strength of metal decks greatly depends on the stiffness and strength of the panel-to-panel side-lap connections and deck-to-frame connections. The same pattern of deck-to-frame welds was used for all the archetypes, but two types of side-lap connections were specified. Archetypes COM1 and COM2 have screws spaced at 12-inches on center along the side laps, whereas the rest have spot welds spaced at 9-inches on center.

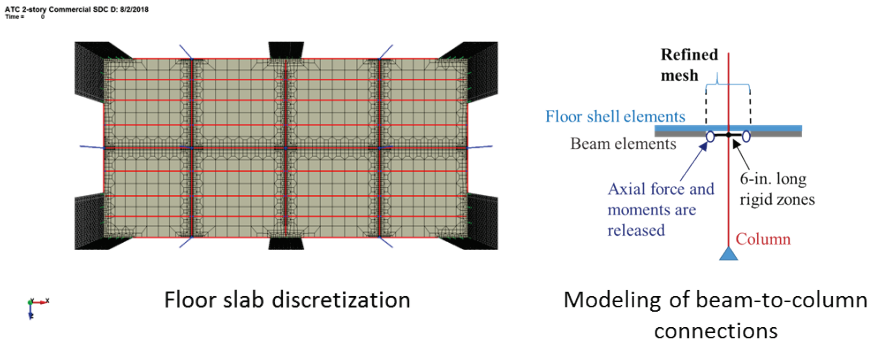

Figure 4-21 Modeling of floor diaphragms.

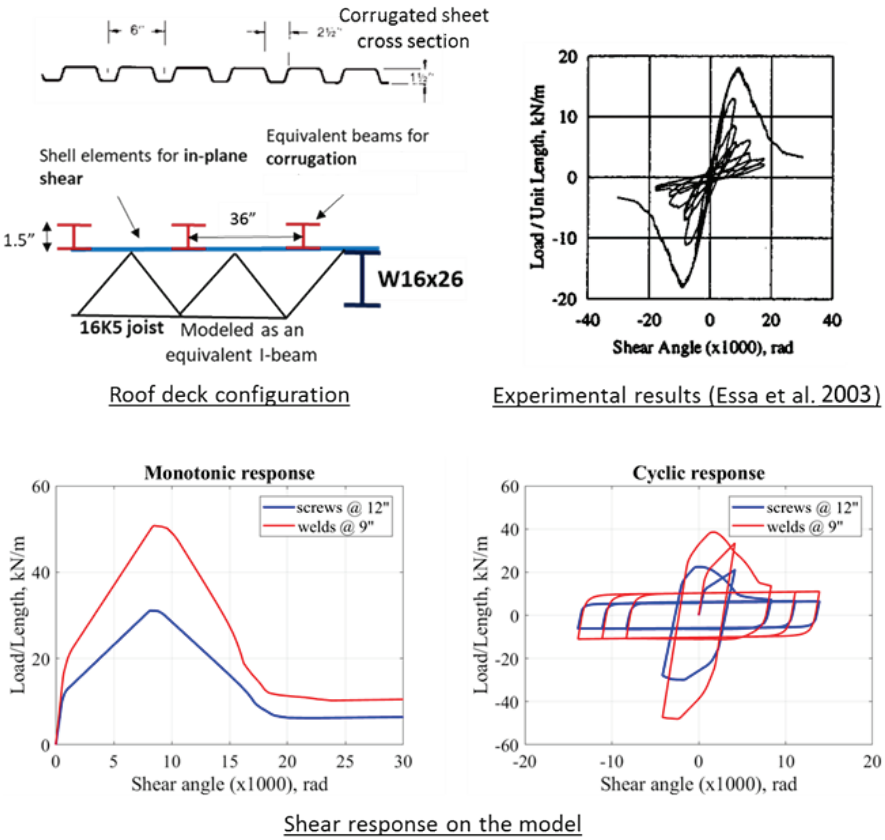

Figure 4-22 Modeling of roof diaphragm.

As shown in Figure 4-22, for the corrugated panels, beam elements with a fiber-section discretization were used to simulate the bending stiffness of the ribs, and shell elements were used to provide the in-plane resistance. Both had nonlinear material laws. The beam elements were oriented along the transverse direction of the building with a spacing of 36 inches. Each beam had an I-shaped cross section that represented the bending stiffness of the ribs over a 36-inch-wide panel. The beam elements were 36-inches long. To ensure that no additional in-plane shear resistance was introduced by the bending of the beams, the moments at the ends of each beam element about the axis perpendicular to the deck were released. The shell elements had dimensions of 36 inches × 36 inches and had common nodes with the beam elements.

The nonlinear in-plane shear response of the shell elements representing the roof deck was calibrated with experimental data. The calibration accounted for both the behavior of the panel and that of the side-lap connectors. The material law for shear assumed that the panel was elastic up to 40 percent of the peak strength, had linear hardening afterwards until the peak strength was reached, and had linear softening after the peak until a constant residual strength equal to 20 percent of the peak was reached. The initial stiffness and peak strength were estimated based on the guidelines of the *Steel Deck Institute Diaphragm Design Manual* (Luttrell, 1995). The rest of the parameters were determined with the test data of Tremblay et al. (2004) and Essa et al. (2003) on roof-deck diaphragms with fasteners similar to those used for the building archetypes. It was assumed that the peak strength occurred at a shear angle of 0.008 radians, and the residual strength was reached at a shear angle of 0.20 radians. The same deformation limits were used for both diaphragm types based on the data of Essa et al. (2003). Figure 4-22 shows the shear responses of the decks tested by Essa et al. (2003) under monotonic and cyclic loads with screw fasteners. The roof diaphragms of the archetypes with screw fasteners were modeled as stronger than the diaphragms tested by Essa et al. (2003) because the former have a thicker steel panel (0.0474 inches versus 0.0295 inches) and have panel-to-frame welds located in every flute rather than every other flute. Figure 4-22 also shows the response of the model under monotonic and cyclic loading for a deck panel that had the same configuration as that tested by Essa et al. (2003) but had the side laps connected with the screw or weld fasteners specified for the archetypes.

The shell elements representing the roof and floor diaphragms were directly connected to the shell elements representing the walls. Due to the large variation in the type and detailing of connectors in practice, the flexibility

and possible failure of the diaphragm-to-wall connections were not considered in the model. For the roof diaphragms, which were connected to the walls with welds, the failure of the deck panels was expected to precede that of the connectors. Therefore, modeling the nonlinear behavior of the roof diaphragm-to-wall connectors would have been redundant and was omitted. Within a 6-inch wide region next to each wall, the diaphragms were modeled with elastic shell elements to account for the wall thickness and the strengthening provided by the steel angle along the edge of the slab.

4.5.2 Calibration of Material Models

The values of the material parameters for the archetype models were determined with the guidelines developed in the validation studies as discussed in Section 4.3.8. Expected strengths were used for the masonry and reinforcing steel. The compressive strength of masonry, f'_m, was assumed to be 3,125 psi for COM6 and 2,500 psi for the other archetypes. These values were 1.25 times the respective nominal strengths specified for the design, as recommended in a prior study (NIST, 2010). The compressive behavior of masonry was determined in the way consistent with the validation studies. The ultimate compressive strain, ε_u, (see Figure 4-7) was assumed to be -0.047 for the one- and two-story archetypes, and -0.035 for the four-story archetypes, because the latter had a larger element size (8 inches versus 6 inches). The values of ε_u were determined according to the size of the shell elements used in the respective archetype models in order to have consistent fracture energy dissipation in the expected plastic-hinge zone, whose height was assumed to be 20 percent of the wall height in the bottom story. The tensile strength of masonry was assumed to be 10 percent of f'_m.

For the steel reinforcement, the expected yield and tensile strengths were taken to be 1.13 times the nominal strengths, based on the data provided by Nowak et al. (2008), resulting in an expected yield strength of 68 ksi and an expected tensile strength of 102 ksi. The values of the material parameters for the cohesive crack interface elements were determined with the guidelines from the validation studies. For the calculation of the bond and dowel strengths for the bond-slip/dowel-action interface elements, the compressive strength of the grout was used. The grout strength was assumed to be 4,375 psi for COM6 and 3,500 psi for the other archetypes. These values were based on the data reported by Mavros et al. (2016) and Stavridis et al. (2016) for masonry with comparable compressive strengths.

4.5.3 Pushover Analyses of Archetype Models

Pushover analyses were performed for each refined finite-element archetype model. In these analyses, a lateral load was applied at each level of the archetype in proportion to the product of the mass lumped at that level, including the tributary mass of the walls, and the fundamental modal displacement, as recommended in ASCE/SEI 41-13, *Seismic Evaluation and Retrofit of Existing Buildings* (ASCE, 2014). The fundamental mode shape was assumed to be linear, close to that obtained from the eigenvalue analysis. Analyses were conducted for both the longitudinal and transverse directions of each archetype.

Results of the pushover analyses performed on the archetypes are shown in Figure 4-23 and Figure 4-24. They are presented as the base shear plotted against the first-story and roof drift ratios, respectively. The roof drift ratio is the roof displacement divided by the building height. As expected, the base-shear capacity increases with the number of stories. The pushover curves show that the lateral deformations of the multi-story archetypes tended to concentrate at the bottom stories after the peak base shears had been reached, forming weak-story mechanisms. The four-story archetypes appeared to have less story-drift capacities than the two-story archetypes, and the one-story archetypes had the highest story-drift capacities. For the four-story archetypes, COM6 showed a more ductile behavior than COM3 up to a drift ratio of 9 percent. This was likely due to its having a larger total wall cross-sectional area. The failure mode for COM3 is illustrated in the deformed finite-element mesh in Figure 4-25. Failure was dominated by diagonal shear cracks developed in the bottom-story walls. On the other hand, COM6 showed a more flexure-dominated behavior in the pushover analyses.

4.5.4 Eigenvalue Analyses of Archetype Models

Eigenvalue analyses were performed with the refined finite-element models to identify the natural periods and mode shapes. Vibration modes that mainly engaged the vertical deflection of the roof diaphragm and only minimally engaged the lateral deformation of the walls were ignored. The natural periods for the first three modes of the archetypes are presented in Table 4-2. The corresponding mode shapes for COM2 are presented in Figure 4-26. The first and second modes of COM2 and COM5 corresponded to the response in the transverse direction (z direction), and the third mode corresponded to that in the longitudinal direction (x direction). The second mode in the transverse direction was dominated by the in-plane bending of the roof diaphragm, as shown in Figure 4-26. For COM3 and COM6, the first mode corresponded to the response in the longitudinal direction, and the third mode was dominated by torsion.

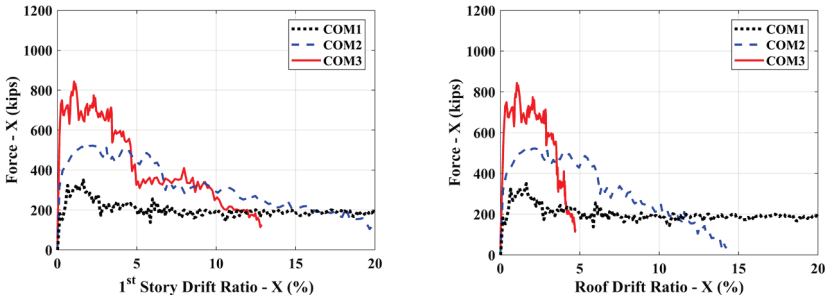

Longitudinal direction

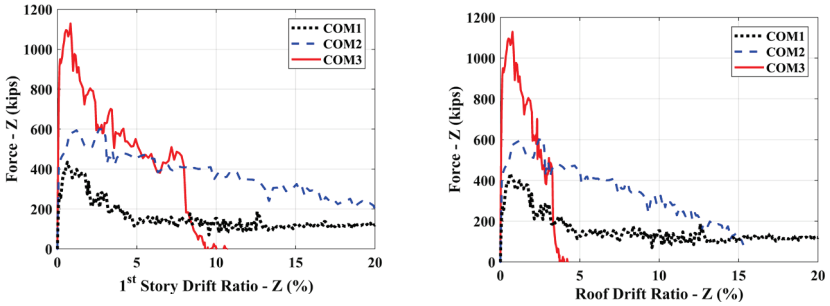

Transverse direction

Figure 4-23 Base shear-vs.-story-drift ratio curves for high-seismic archetypes.

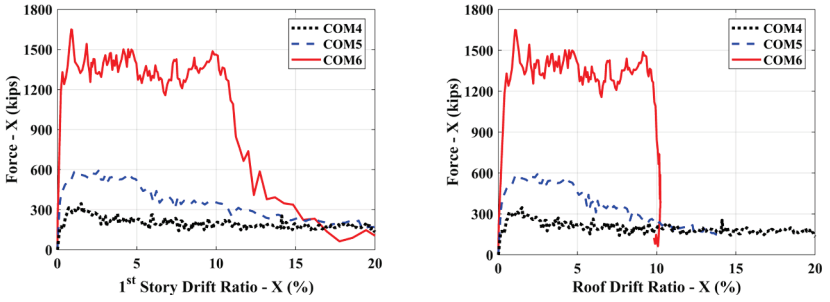

Longitudinal direction

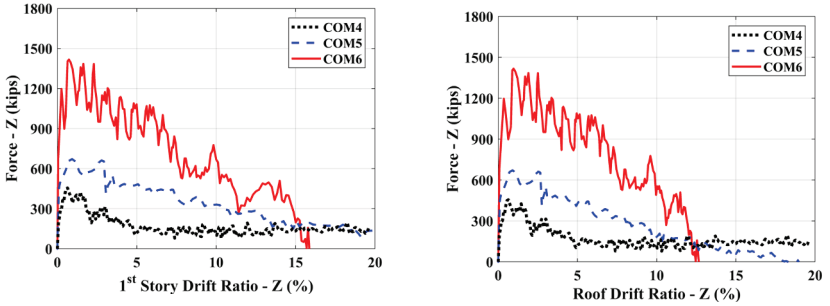

Transverse direction

Figure 4-24 Base shear-vs.-story-drift ratio curves for very high-seismic archetypes.

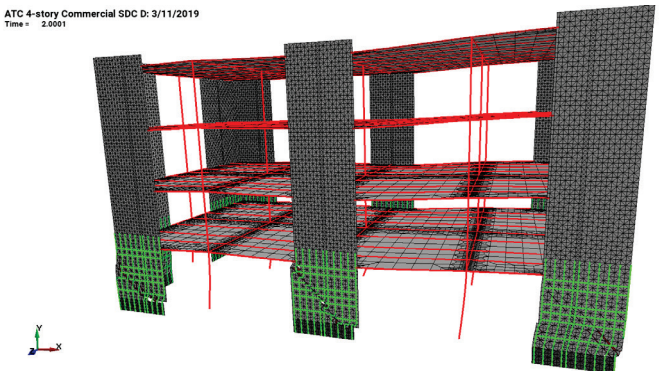

Figure 4-25 Deformed finite-element mesh for COM3 from pushover analysis.

Table 4-2 Natural Periods for the First Three Modes of the Building Archetypes from Refined Finite-Element Models

Archetype ID	No. of Stories	Natural Period (sec)*		
		1st mode	2nd mode	3rd mode
Commercial Buildings: High Seismic				
COM1	1	0.164 (T)	0.096 (L)	0.081 (TO)
COM2	2	0.206 (T)	0.190 (T)	0.180 (L)
COM3	4	0.333 (L)	0.294 (T)	0.168 (TO)
Commercial Buildings: Very High Seismic				
COM4	1	0.149 (T)	0.091 (L)	0.074 (TO)
COM5	2	0.197 (T)	0.187 (T)	0.177 (L)
COM6	4	0.282 (L)	0.259 (T)	0.166 (TO)

* T: transverse direction; L: longitudinal direction; TO: torsional

4.5.5 Response-History Analyses of Archetype Models

Nonlinear response-history analyses were performed with the refined models using three sets of ground motion records selected from the FEMA P-695 database. Each record has two components of horizontal ground acceleration. The three records have different characteristics in terms of spectral shapes and durations of strong motion. Figure 4-27 shows the ground-acceleration time histories and acceleration response spectra for these records, as well as the MCE_R spectrum for the high-seismic site. Each record was scaled to two intensity levels to cover a range of response amplitudes.

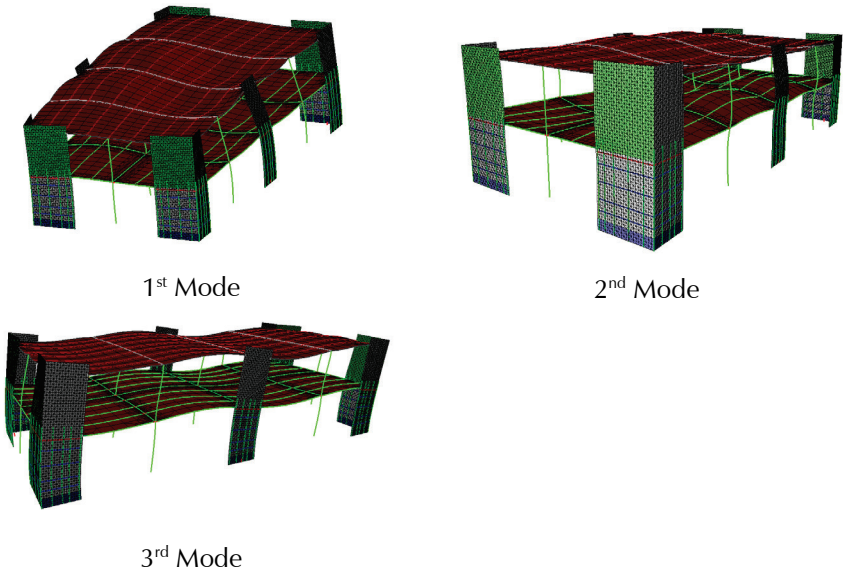

Figure 4-26 Mode shapes for the first three modes of the refined finite-element model of COM2.

Rayleigh damping was used in the response-history analyses, with damping equal to 0.1 percent of the critical for the first and fifth significant modes that engaged the lateral deformation of the archetypes. The initial stiffness of the elements was used to calculate the damping matrix. However, for the cohesive crack interface elements, the coefficient for the stiffness proportional damping component was two orders of magnitude smaller compared to that for the shell elements. The damping was activated only after cracking occurred to suppress the high-frequency response triggered by cracking but not to interfere with crack initiation.

Results of the response-history analyses—including the story-drift histories, base-shear histories, base shear-vs.-first-story drift hysteresis curves, and the deformed meshes showing the failure mechanisms of the archetypes—are presented in Appendix B. For the one-story archetypes, the corner walls developed significant toe crushing and base sliding, whereas the behavior of the two middle walls was dominated by flexure. For the multiple-story archetypes, wall failure concentrated in the bottom stories, with only mild cracking and yielding of the vertical reinforcement occurring in the second stories. The bottom-story walls first developed flexural yielding, and many of the walls subsequently developed severe diagonal cracks, as well as crushing at the bases. This was due to the influence of the horizontal diaphragms at the second floors, which restrained the rotation at the tops of the bottom-story walls, thereby reducing the effective shear-span ratios of the walls. Despite the shear-dominated behavior, the drift ratios reached in the first stories at which the base shears dropped to zero were 10 percent or more

for all cases. However, for the same archetype model, the failure mechanism of the walls varied depending on the ground motion and, in some cases, differed from that in the pushover analysis.

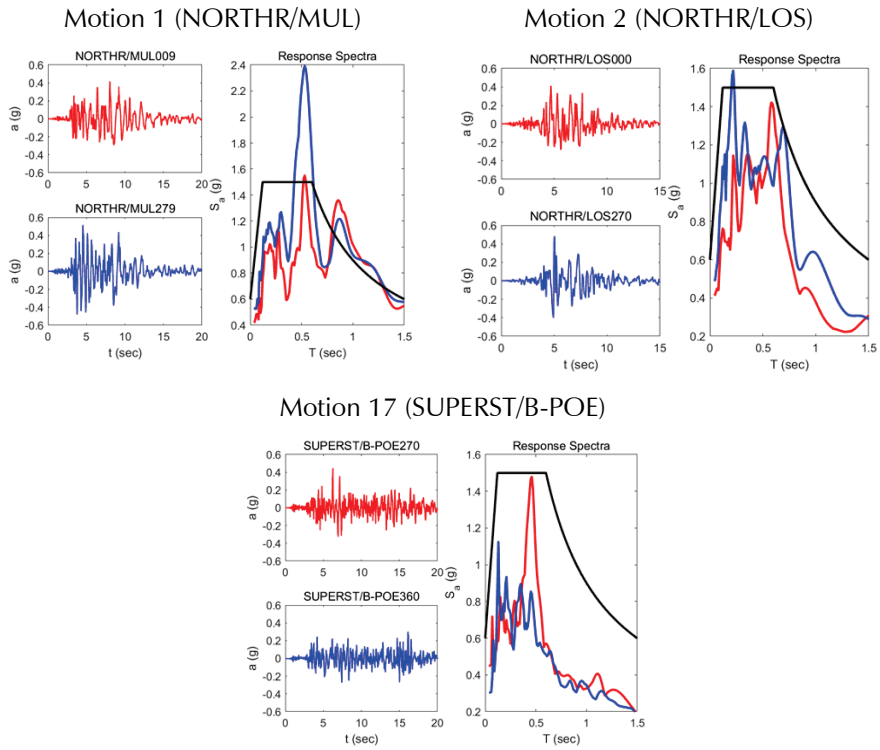

Figure 4-27 Earthquake ground-motion records used for response-history analyses (records shown are unscaled; MCE_R spectrum is the black solid line).

4.6 Simplified Frame Models used for Parametric Studies

4.6.1 Model Description

Computationally efficient, simplified frame models were used for incremental dynamic analyses (IDAs) based on the FEMA P-695 procedures, as is described in more detail in Section 4.8. The models were calibrated with the results of the nonlinear response-history analyses conducted with the refined finite-element models. The IDAs were performed with the software platform OpenSees (Mazzoni et al., 2006).

Figure 4-28 shows the frame model developed for the two-story archetypes (COM2 and COM5). It is representative of the simplified models developed for all the building archetypes. The refined finite-element analyses showed that major damage always concentrated in the first-story walls. For COM2 and COM5, these walls deformed in double curvature with a mixed flexural-shear behavior that was eventually dominated by shear. Hence, in the simplified models, the walls in the second stories were modeled with elastic

beam-column elements for the sake of computational efficiency. They were rigidly connected to the perimeter beams of the horizonal diaphragms. To model the inelastic response of the L-shaped walls in the first stories, each wall was represented by a rigid bar with two rotational springs at each end. One pair of top and bottom springs were used to model the wall behavior along each direction of the archetype. Figure 4-29 shows the macro-element model with one pair of rotational springs. The moment-vs.-rotation relation for each spring was represented by a phenomenological hysteretic law. The hysteretic law was calibrated to reproduce the lateral load-vs.-lateral displacement response of each wall, as well as the maximum moment developed at the wall base in the refined finite-element analyses. An accurate representation of the base moment was important for modeling the soil-structure interaction phenomenon, which was investigated as part of one parametric study. For the rectangular walls, the out-of-plane bending resistance was ignored. For the one-story and four-story archetypes, the macro-element model for each of the first-story walls had a hinge at the top. This was done because these walls tended to deform with a single curvature, and the introduction of a top spring would have created difficulties in the calibration process. For these models, the perimeter beams at the first floors were stiffened to reduce the rigid-body rotations of the second-story walls and to represent the initial stiffnesses of the second stories correctly.

Force-based beam-column elements with a fiber-section discretization and a bi-linear material law were used to model the steel columns in the first story. Each column was represented by one force-based element with a hinge at the base. Since the refined finite-element analyses showed that the steel columns in the second story and above remained practically elastic all the time, these columns were modeled with elastic beam-column elements.

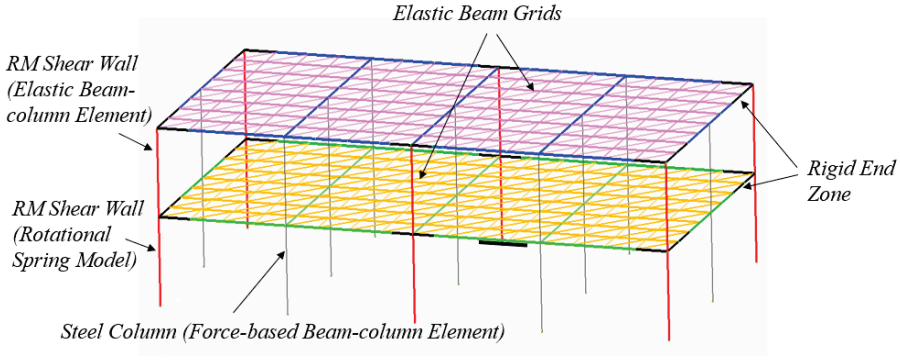

Figure 4-28 Frame model with OpenSees for COM2 and COM5.

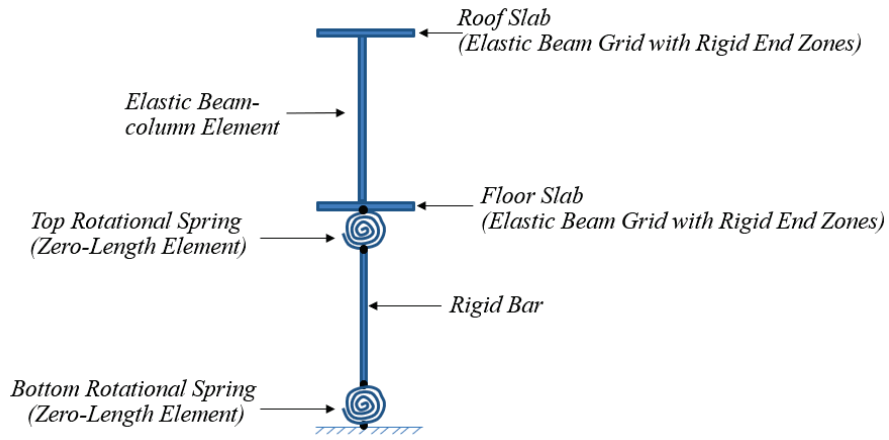

Figure 4-29 Modeling of a first-story wall for COM2 and COM5.

As shown in Figure 4-28, the horizontal diaphragms were represented by a grillage model using linearly elastic beam elements and diagonal truss bars. The stiffnesses of the beam elements and truss bars were assigned to match the elastic in-plane stiffness of the diaphragms of the refined finite-element models as closely as possible. Rigid end zones were introduced in the perimeter beams to represent the horizontal dimensions of the walls. The beams were connected to the columns with hinges. The nonlinear behavior of the horizontal diaphragms was ignored in the simplified models. This was based on the observation that the in-plane response of the diaphragms remained essentially linear in the refined finite-element models. Nevertheless, when the walls in the first story of the refined models experienced significant side-sway or vertical deformation, the diaphragms could exhibit significant nonlinear out-of-plane bending. The influence of this nonlinearity on the wall behavior and the building response was indirectly accounted for in the calibration of the macro-element models of the first-story walls.

4.6.2 Model Calibration

For the calibration of each simplified frame model, two sets of ground motion records (Motion 1 and Motion 2 shown in Figure 4-27) were used to determine the parameters of the hysteretic models, and the third set (Motion 17) was used to check the general validity of the calibration. For each set of records, the ground motions were scaled to two levels, the MCE_R level and a higher level. The simplified models calibrated in this way are referred to as the baseline models in the parametric studies. From here on, they are identified with a letter B after the respective archetype number. Their variants considered in the parametric studies are discussed in Section 4.7.

Figure 4-30 shows the plan view of the wall layouts for the archetypes. The L-shaped corner walls exhibited an asymmetric hysteretic response along each of the *x* and *z* directions, with the strong and weak directions depending on whether the flange was subjected to tension or compression. For the rectangular walls, the bending resistance to the out-of-plane deflection was ignored. A general hysteretic model in OpenSees was used to describe the behavior of the rotational springs representing the first-story walls. The hysteresis law was governed by five parameters, with two controlling the pinching of the hysteresis curves, one controlling the unloading stiffness, and the remaining two accounting for damage that was dependent on both the deformation amplitude and the cumulative plastic work. The values of these parameters were determined by matching the lateral load-vs.-lateral displacement hysteresis curves as closely as possible for the respective walls from the refined finite-element analyses. They were then further adjusted to improve the matching of the first-story drift histories and base shear-vs.-first-story drift hysteresis curves for the entire archetype. The rotational springs representing the walls that had the same dimensions and reinforcement details in the archetype had the same calibration, representing the average behavior of the wall group rather than that of a particular wall.

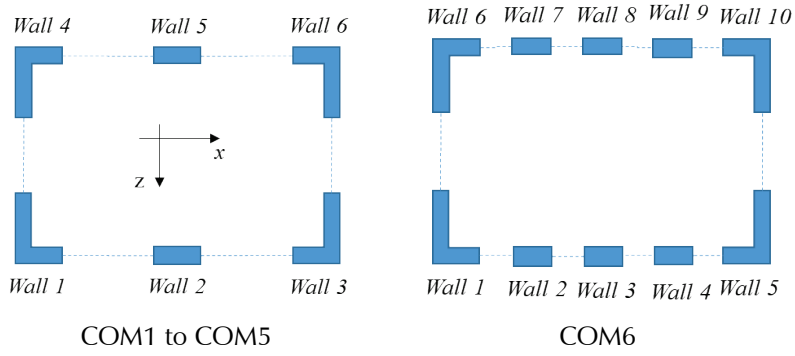

Figure 4-30 Plan view of wall layouts for commercial building archetypes.

The floor and roof mass was distributed among the nodes of the grillage model, and the wall mass was lumped at each end of the walls. The mass for the vertical and horizontal directions was the same. For the response-history analyses, Rayleigh damping was used with the damping ratio equal to one percent of the critical for the first and second modes. The initial stiffness of the model was used to calculate the damping matrix. Even though the damping ratio was different from that assumed for the refined finite-element models, it was found to provide a better match of the response histories. In Appendix B, the response histories and hysteresis curves from the simplified models are compared to those from the refined models for the three sets of ground-motion records.

4.6.3 Pushover Analyses of Baseline Models

Pushover analyses were performed with the simplified models using the same load distributions as those used in the refined finite-element analyses. For these analyses, the grillage model representing the horizontal diaphragms was assigned a very high in-plane stiffness so that the horizontal displacement at each floor was uniform. For each building archetype, two pushover analyses were conducted, one for each direction. In Figure 4-31, results of the pushover analyses for COM2B are compared to the pushover curves obtained with the refined finite-element model. The slopes of the rising branch of the pushover curves were well captured by the simplified model, but the refined model showed a substantially more gentle post-peak load degradation. This can be attributed to the fact that the simplified models were calibrated with the hysteresis curves from the response-history analyses of the refined models. The hysteretic response included the effects of cyclic displacement reversals, as well as the bi-axial deformations of the L-shaped walls, which caused more severe damage and load degradation than the uni-axial lateral loading in a pushover analysis. As shown in Figure 4-31, in an average sense, the slopes of the post-peak regime of the pushover curves from the simplified models match the envelopes of the hysteresis curves from the response-history analyses of the refined models.

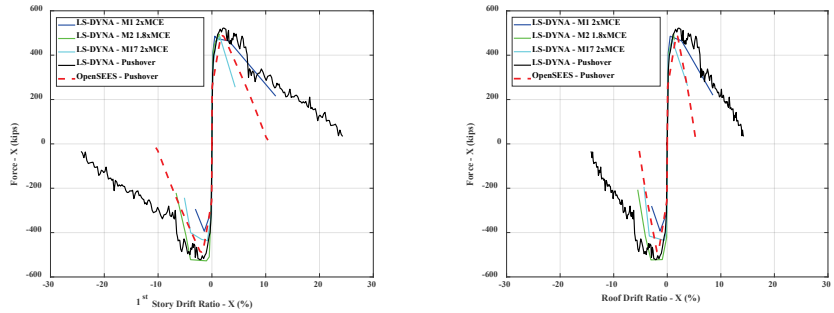

Longitudinal direction

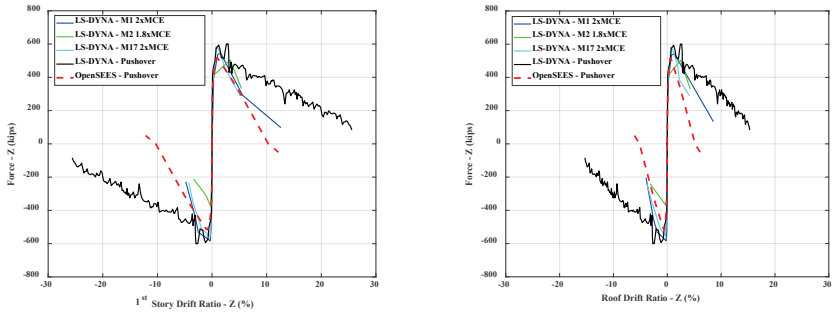

Transverse direction

Figure 4-31 Comparison of pushover analysis results from simplified (OpenSees) and refined finite-element (LS-DYNA) models for COM2B.

The data obtained from the pushover analyses were the maximum base shear strength (which is used to calculate the overstrength) and the ductility, which is needed in the FEMA P-695 methodology to calculate the spectral shape factor (*SSF*). Figure 4-32 illustrates how the maximum base shear strength, V_{max}, effective yield displacement, $\Delta_{y,eff}$ ($\delta_{y,eff}$ in Figure 4-32), and the displacement after 20 percent degradation from peak strength, $\Delta_{u,80}$ (δ_u in Figure 4-32), are calculated from the pushover curve (the displacements are typically expressed as drift ratios throughout this report). The overstrength factor, Ω, is then V_{max}/V_{design}, where V_{design} is the design base shear for the archetype, and the period-based ductility, μ_T, is $\Delta_{u,80}/\Delta_{y,eff}$.

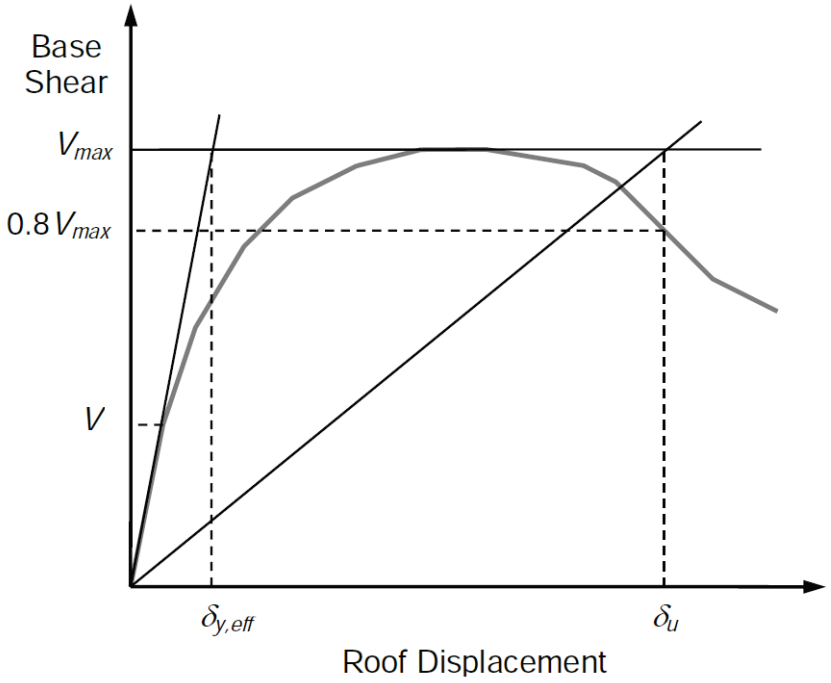

Figure 4-32 Idealized nonlinear static pushover curve (FEMA, 2009b).

4.6.4 Eigenvalue Analyses of Baseline Models

Eigenvalue analyses were conducted with the simplified frame models. The natural periods calculated for the first three modes of each archetype are shown in Table 4-3. Vibration modes dominated by the vertical deflection of the horizontal diaphragms are ignored. The fundamental periods of the simplified models matched those of the refined finite element models well. The mode shapes for the first three modes of COM2B are shown in Figure 4-33. For the one-story and four-story archetypes, the first three modes of the two models match well. However, for the two-story archetypes, the second and third mode shapes of the two models do not match.

Table 4-3 Natural Periods for the First Three Modes of the Baseline Building Archetypes from Simplified Models

Baseline Archetype ID	No. of Stories	Natural Period (sec)*		
		1st mode	2nd mode	3rd mode
Commercial Buildings: High Seismic				
COM1B	1	0.148 (T)	0.130 (L)	0.078 (TO)
COM2B	2	0.202 (T)	0.177 (L)	0.108 (TO)
COM3B	4	0.378 (L)	0.235 (T)	0.165 (TO)
Commercial Buildings: Very High Seismic				
COM4B	1	0.152 (T)	0.136 (L)	0.082 (TO)
COM5B	2	0.194 (T)	0.172 (L)	0.108 (TO)
COM6B	4	0.255 (L)	0.249 (T)	0.166 (TO)

* T: transverse direction; L: longitudinal direction; TO: torsional

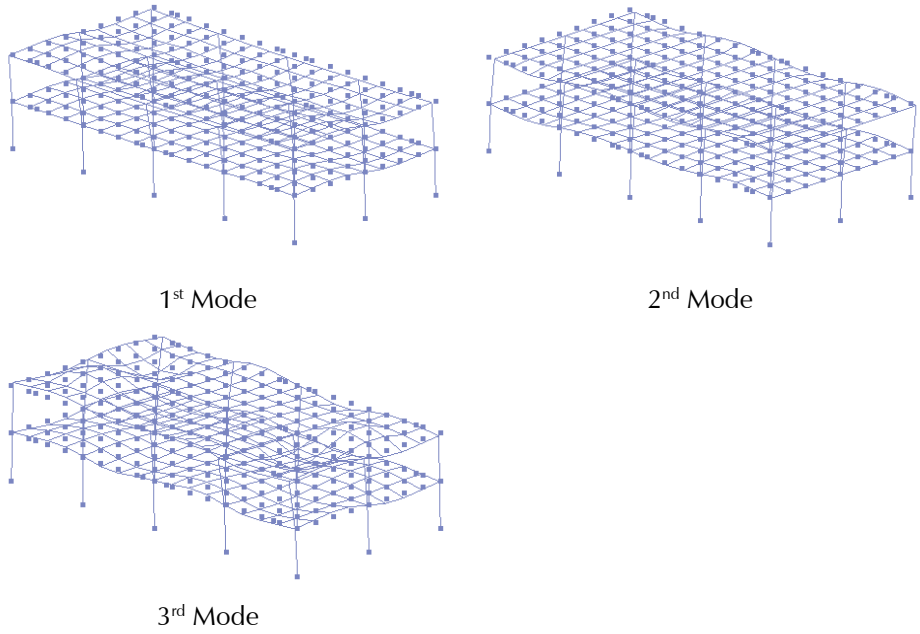

Figure 4-33 Mode shapes for the simplified model of COM2B.

4.7 Overview of Parametric Studies

This study investigated the collapse performance of short-period reinforced masonry archetypes, including a range of variations in building design and analysis that may affect collapse probability. Three parametric studies using the simplified frame models were investigated. These parametric studies included: (1) baseline configuration; (2) displacement capacity; and (3) soil-structure interaction (SSI) and foundation flexibility. These parametric studies are briefly described below, and Table 4-4 lists the names of the archetype models.

Table 4-4 Baseline and Variant Numerical Models for the Parametric Studies

No. of Modeled Archetypes	No. of Stories	Archetype ID		
		(1) Baseline Configuration	(2) Displacement Capacity	(3) Soil-Structure Interaction and Foundation Flexibility
Commercial Buildings: High Seismic				
3	1	COM1B	COM1B-DC(1,2)	-
5	2	COM2B	COM2B-DC(1,2)	COM2B-SS(1,2)
3	4	COM3B	COM3B-DC(1,2)	-
Commercial Buildings: Very High Seismic				
3	1	COM4B	COM4B-DC(1,2)	-
3	2	COM5B	COM5B-DC(1,2)	-
3	4	COM6B	COM6B-DC(1,2)	-

4.7.1 Baseline Configuration Parametric Study

Baseline archetypes of one, two, and four stories designed for high-seismic and very high-seismic ground motions were modeled to investigate response behavior and collapse performance. The baseline models were calibrated with results of response-history analyses performed on refined finite-element models without any modifications. The influence of fundamental period (or the number of stories), the ratio of the maximum base shear (V_{max}) to the seismic weight (W), and the ratio of V_{max} to the design base shear (i.e., the overstrength factor Ω) on collapse probability were investigated.

4.7.2 Displacement Capacity Parametric Study

The design of a masonry building, such as the number of walls, the geometric configuration of the walls, and the amount and spacing of the reinforcement, varies from one building to another depending on the architectural design and the preference of the engineer. Variations in the design may result in buildings with different displacement capacities, even though they have the same number of stories and functional characteristics. To investigate the influence of these variations on the collapse probability of a building, a parametric study focusing on displacement capacity was conducted. The displacement capacity was varied by changing the post-peak slope of the base shear-vs.-first-story drift curves for each baseline model. In general, increasing the steepness of the post-peak slope results in a smaller collapse displacement as determined by incremental dynamic analysis. Two variants were considered for each baseline archetype model. Variant COMXB-DC1

had the post-peak negative slope decreased by 30 percent with respect to the baseline model (less brittle), and COMXB-DC2 had the negative slope increased by 30 percent (more brittle). This range of variation was deemed reasonable by comparing the variations in the pushover analysis curves across the baseline models.

4.7.3 Soil-Structure Interaction and Foundation Flexibility Parametric Study

The influence of SSI and foundation flexibility on the collapse probability of the COM2B archetype was investigated. Two different sites were considered. One was a soft site with soil properties representative of those at the site class D/E boundary, and the other was a stiff site with soil properties representative of those at the site class C/D boundary. The design of the reinforced concrete foundations for the two sites is discussed in Chapter 3 and Appendix A. The stiff site variant model is designated as COM2B-SS1, and the soft site variant model is designated as COM2B-SS2. Additional modeling considerations for including SSI and foundation flexibility follow.

Special Modeling for SSI and Foundation Flexibility Analyses

Different foundation models were developed for the stiff and soft sites, with the plan view of the foundation model for the soft site shown in Figure 4-34. The foundation around the perimeter of the building was modeled with 1-foot-long displacement-based beam elements, which had fiber sections that accounted for material nonlinearity. The foundation underneath each wall was assumed to be rigid to compensate for the omission of the horizontal wall dimension, since each wall was represented by a line element. The mass of the foundation slab and grade beams was included. To capture inertial interaction, the properties of the soil were modeled with springs and dampers, which were placed at each node of the foundation model with a nodal spacing of 1 foot, as shown in Figure 4-35. There were three pairs of springs and dampers at each node aligned in the x, y, and z directions. The spring and the damper in each pair were parallel to one another and the spring had a bi-linear material law with a strain hardening ratio of 15 percent to account for passive soil pressure. Damping was assumed to be viscous, and the value of the damping coefficient was calculated from the damping ratio determined for the site using the formula recommended in NIST GCR 12-917-21, *Soil-Structure Interaction for Building Structures* (NIST, 2012b).

The vertical springs and dampers did not exert tension by using the model shown in Figure 4-35. In addition, a rotational spring was introduced at each node of the exterior foundation to account for the rotational resistance of the foundation strip about its long axis. This spring had an elastic-perfectly

plastic material law. The foundation of each interior column was assumed to have a zero dimension, and the soil resistance was modeled by five pairs of springs and dampers, all concentrated at the base of the column. Three of them were aligned along the *x*, *y*, and *z* directions, and two were rotational springs about the *x* and *z* axes. The properties of the soil strings and dampers and their derivations are presented in Appendix C. The capacities of the rotational springs for the exterior strip foundations in the model were equal to one-half of the values provided in Appendix C. This decision was based on the observation from the pushover analyses that the foundation slab exhibited significant uplift, causing it to lose contact with the soil springs at the corners of the building.

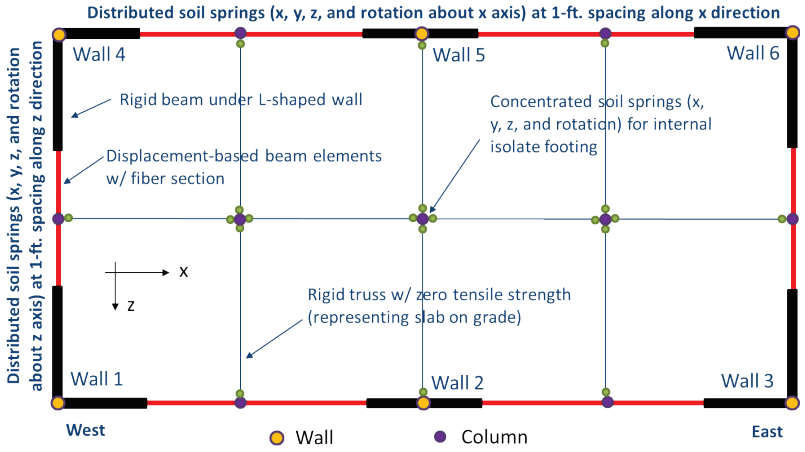

Figure 4-34 Foundation model for the soft site for SSI analyses.

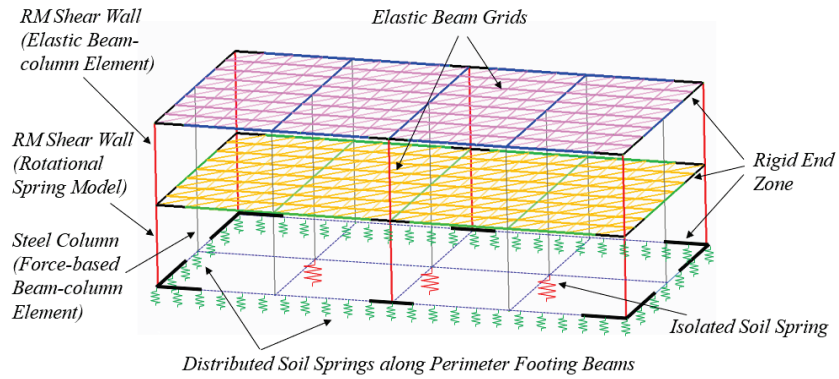

Modeling Scheme and Force-Displacement Relation for Vertical Soil Springs

Figure 4-35 Soil springs and dampers for SSI analyses.

The interior foundation slabs were connected to each other and to the exterior foundation with rigid links. The rigid links represented the slab-on-grade, which was not physically connected to the exterior or interior foundation. The links transmitted only axial compression, not tension or moment.

For the stiff site, the foundation was modeled in a similar way. However, since failure was expected to occur in the grade beams only, the foundation slabs underneath the walls and the exterior columns were assumed to be rigid, and the grade beams were modeled with displacement-based fiber-section beam elements, as shown in Figure 4-36. The soil springs and dampers were distributed along the exterior foundation slabs and grade beams with a 1-foot spacing. The properties of all the soil springs and dampers are given in Appendix C.

As discussed in Appendix C, to account for kinematic interaction, which includes the effects of base-slab averaging, the free-field ground motion records were filtered with a transfer function that was determined based on the site properties.

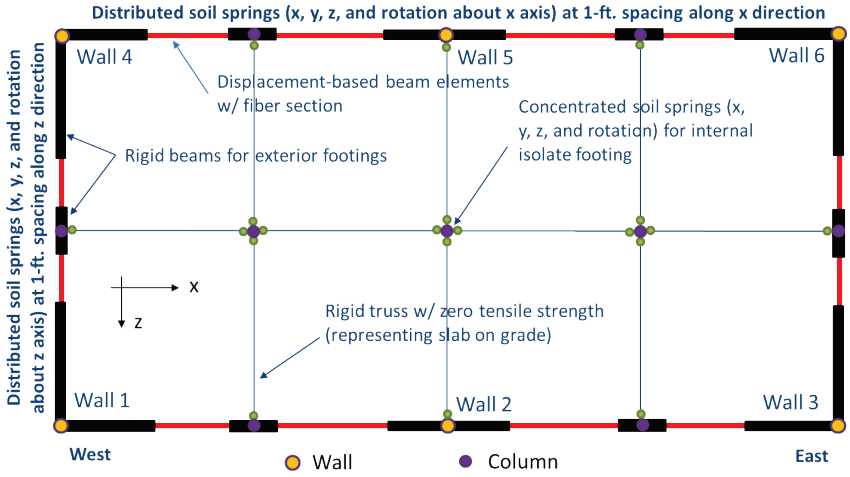

Figure 4-36 Foundation model for the stiff site for SSI analyses.

4.8 Incremental Dynamic Analyses and Peak Response Values

IDAs were conducted on all archetypes using the 22 sets of far-field ground-motion records from the FEMA P-695 database. Each set has two orthogonal horizontal ground-motion components. Each record set was applied to an archetype model twice, with the orientation of the two components rotated by 90 degrees in the second application. Hence, each archetype model was analyzed with 2 × 22 record sets. The acceleration response spectra for the 44 records (with 5 percent damping) are shown in Figure 4-37. The spectral curves shown have been scaled so that the median spectral intensity at the

period of 0.25 seconds corresponds to the MCE_R spectra level for high-seismic archetypes.

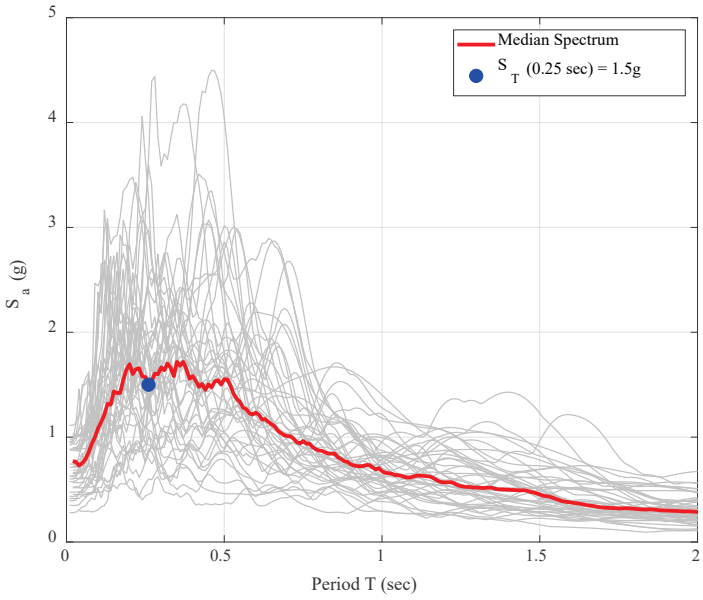

Figure 4-37 Acceleration response spectra for the 44 far-field ground motion records in FEMA P-695 database.

The records sets were scaled up simultaneously and gradually from a low-intensity level, with the median spectral intensity at the code-based period (T in Table 4-1) of the archetype increased in increments of 0.1g until all the records resulted in collapse. At each increment, the median spectral intensity (S_T) at period T (calculated with 5 percent damping) was plotted against the maximum first-story drift ratio (taken as the larger of the two orthogonal directions) induced by each set of ground-motion records. Since the response of all the archetypes was dominated by the weak first story, the first-story drift ratio was used for the IDA plots. Each curve represents the response to one ground-motion record set.

Figure 4-38 shows the IDA curves obtained for COM2B, the MCE_R spectral intensity, S_{MT}, for the design earthquake at period T, the median collapse spectral intensity, $S_{CT,raw}$, based on the raw data from the IDAs, and the adjusted median collapse intensity, $S_{CT,factored}$, which is equal to $1.2 \times SSF \times S_{CT,raw}$. The median collapse intensity ($S_{CT,raw}$) is defined as the median spectral intensity at which 50 percent of the 44 earthquake record sets results in collapse. The factor of 1.2 applied to the adjusted collapse intensity is recommended in the FEMA P-695 methodology if the value of $S_{CT,raw}$ is obtained from 3D nonlinear analyses using bi-axial ground-motions rather than 2D analyses. Previous studies have shown that the median collapse intensity resulting from 3D analyses is on average 20 percent less than that

from 2D analyses. Since the acceptance criteria in FEMA P-695 are largely calibrated with 2D analysis results, the factor of 1.2 is applied to 3D-analysis results to make the evaluation consistent. The spectral shape factor, *SSF*, is based on the observation that the shape of the response spectra of rare ground motions in California, such as the MCE_R-level ground motions, is more favorable (i.e., less damageable) to ductile structures, which is not necessarily reflected in the record sets. As described in FEMA P-695, the value of *SSF* is a function of the code-based fundamental period (T) and the period-based ductility (μ_T). For the baseline models, the values of *SSF* obtained varied from 1.18 to 1.33. However, the simplified models used in the pushover analyses underpredicted the roof drift capacity (but not $\delta_{y,eff}$), resulting in an under-prediction of values for the period-based ductility, μ_T, for the multi-story archetypes. For this reason, the value of *SSF* was taken to be 1.33, the upper-bound value recommended in FEMA P-695 for $T \leq 0.5$ sec, for all the archetype models.

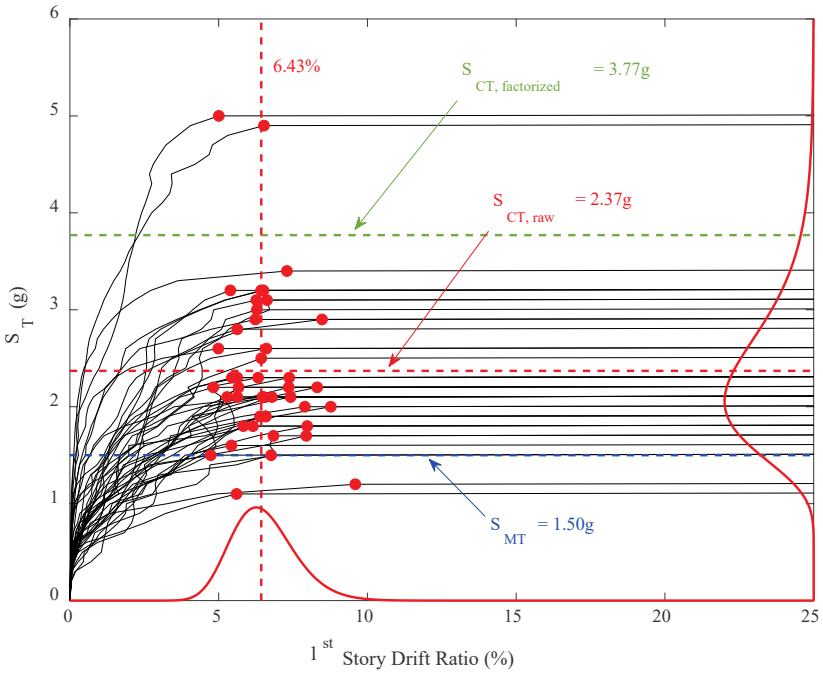

Figure 4-38 Incremental dynamic analysis results for COM2B. Red markers represent the incipient collapse points of individual ground motions. Vertical and horizontal red dashed lines show the lognormal fitted median incipient collapse drift ratio and $S_{CT,raw}$, respectively.

Incipient collapse was identified as the point (shown as red markers in Figure 4-38) on an IDA curve after which the story drift increased indefinitely with no further increase in S_T (i.e., the point after which the IDA curve goes flat) or when the first-story drift ratio reached 10 percent, whichever came first. The latter criterion took into account the rotational limit of the beam-to-

column connections of the steel gravity frame. This was determined from the data of Liu and Astaneh-Asl (2000; 2004) on tests of beam-to-column connections. However, the second criterion had no noticeable impact on the collapse probability because the first criterion was typically triggered. Figure 4-37 also shows the lognormal distributions for the incipient collapse drift ratios and incipient collapse spectral intensities. The median incipient collapse drift ratio for COM2B is 6.43 percent, as indicated by the vertical dashed line.

Figure 4-39 shows the collapse rates (collapse fraction) determined from the IDAs. For the IDA data shown, the spectral intensity was scaled by the factor of 1.2 to account for the 3D analyses. The collapse fragility curve shown in the figure is based on a lognormal distribution with the median collapse intensity equal to $S_{CT,factored}$ and the lognormal standard deviation, β, assumed to be 0.5. The β value accounts for the dispersion introduced by uncertainties in the record-to-record variability of the ground motions, design requirements, test data, and modeling. Prior studies (NIST, 2010) on similar building archetypes have indicated that 0.5 is a good estimate for the β value. The difference between the collapse fraction data points and the collapse fragility curve shown in the Figure 4-39 is largely due to the spectral shape factor (*SSF*), which was applied to the modified median spectral intensity $S_{CT,factored}$ to produce the fragility curve, but not to the collapse fraction data. The probability of collapse at the MCE_R ground-motion intensity $P[C|MCE_R]$ was determined directly from the collapse fragility curves.

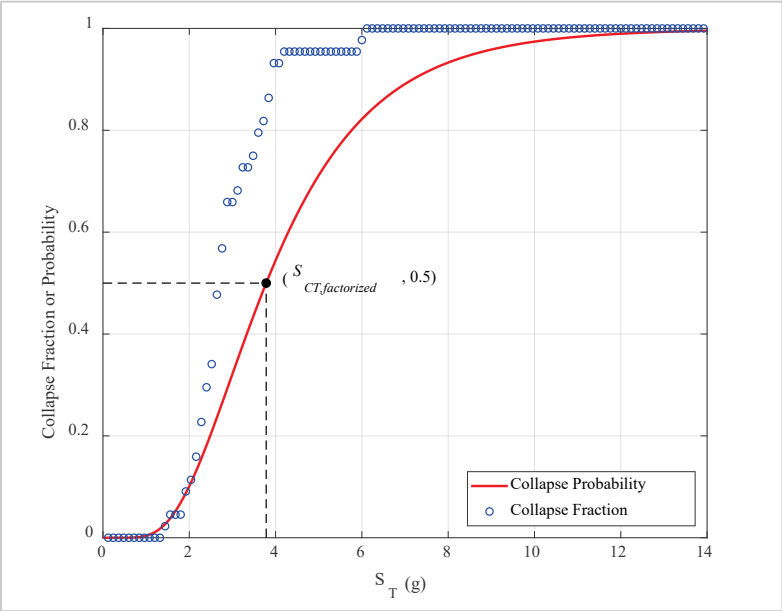

Figure 4-39 Collapse rates from IDA and derived collapse fragility curve for COM2B. S_T for the collapse fraction data has been scaled only by the factor of 1.2 for 3D analyses.

Per the FEMA P-695 methodology, when 3D analyses are performed, the collapse margin ratio (CMR_{3D}) is defined as $1.2 \times S_{CT,raw}/S_{MT}$, where S_{MT} is the MCE_R spectral intensity at the building period T. The adjusted collapse margin ratio ($ACMR$) is defined as $SSF \times CMR_{3D}$ (i.e., $S_{CT,factorized}/S_{MT}$). These values were computed for the building archetypes in this study.

Select response quantities obtained for each intensity stripe (at increments of 0.1g) were archived in a spreadsheet file. Table 4-5 summarizes the archived response quantities, which include the peak response quantities for each record set and for each response direction of an archetype model, the response statistics for the 2 × 22 ground motion record sets, and the collapse statistics. The file names are catalogued in Appendix D.

Table 4-5 Stripe Statistics Archived for Each Orthogonal Direction (Transverse and Longitudinal) of the Archetype Models

Statistic Type	Response Parameters	Statistic Values
Peak Relative Displacement	Peak Roof Relative Displacement Peak Roof Drift Ratio Peak 1st-Story Drift Ratio[5]	Median[1] Mean of Survivors[2] Overall Mean[3] Overall Beta[4] Minimum Maximum
Peak Relative Velocity	Peak Roof Relative Velocity Peak Floor Relative Velocity	
Peak Total Acceleration	Peak Roof Total Acceleration Peak Floor Total Acceleration	
Residual Relative Displacement	Residual Roof Displacement Residual Roof Drift Ratio Residual 1st-Story Drift Ratio[5]	
Collapse	Collapse Cases for 2 × 22 Record Sets	Number Percentage
	Individual Record Collapse Cases	Collapse (Yes/No) If No, Peak Roof Displacement If Yes, Peak Roof Displacement at Last Surviving Intensity; Floor Level Initiating Collapse and Collapse Direction.

[1] Median based on all 2 × 22 earthquake record sets; for non-surviving records (i.e., records causing collapse), they are calculated with the last values.

[2] Mean value for surviving earthquake records (i.e., records not causing collapse).

[3] Mean value for all 2 × 22 earthquake record sets; calculated with the last values for non-surviving records.

[4] The lognormal standard deviation for all 2 × 22 earthquake record sets; calculated with the last values for non-surviving records.

[5] Upper stories of the multi-story archetypes remain practically elastic and their drift ratios are mainly contributed by the rigid-body rotation of the walls above the bottom story. The rigid-body wall rotations are not accurately calculated with the simplified models, and the upper-story drift ratios are therefore not archived.

Chapter 5

Numerical Results of Parametric Studies

5.1 Introduction

This chapter presents results of three parametric studies performed for the commercial reinforced masonry building archetypes, whose baseline models are denoted as COM1B through COM6B. The probability of collapse was calculated for each baseline model and its variants considered in the parametric studies using the FEMA P-695 methodology, which consisted of pushover analyses and incremental dynamic analyses (IDAs). The analyses were conducted with the simplified frame models that were calibrated with refined finite-element models, as discussed in Chapter 4.

5.2 Baseline Configuration Parametric Study

This parametric study compares the performance of the baseline models by examining the pushover analysis curves, and the influence of several design variables and building characteristics on seismic performance. The variables considered include the period (or the number of stories) of the building, the maximum base shear strength of the pushover curve divided by the seismic weight of the building (V_{max}/W, referred to herein as the "normalized pushover strength"), the maximum base shear strength divided by the design base shear (Ω), and the level of the design earthquake.

5.2.1 Pushover and Incremental Dynamic Analyses

Pushover and incremental dynamic analyses were performed on the baseline models to provide the information required for calculating the collapse fragilities per the FEMA P-695 methodology. Figure 5-1 and Figure 5-2 show the base shear-vs.-drift ratio curves obtained from the pushover analyses of the baseline models designed for the high-seismic and very high-seismic sites, respectively, and Figure 5-3 shows the zoomed-in pushover curves for all the archetypes. The roof drift ratio is defined as the roof displacement divided by the building height, and the first-story drift ratio is the displacement of the first level divided by the story height. These curves represent the envelopes of the hysteretic response curves of the archetypes under bi-directional ground motions, rather than the true response under

monotonic loading, due to the way the simplified models were calibrated, as explained in Section 4.6. The figures show that the post-peak slopes of the pushover curves become steeper as the number of stories increases. This can be attributed to the higher axial compressive force and the higher amount of vertical reinforcement in the first-story walls of the taller buildings, which led to more severe masonry crushing in the first-story walls. The higher axial load also resulted in a more severe P-delta effect. Furthermore, because damage was localized in the first story for the multi-story archetypes, the base shear-vs.-roof drift ratio curves show much steeper post-peak slopes than the base shear-vs.-first-story drift ratio curves. However, the roof drift capacity of the multi-story archetypes was underpredicted by the simplified models, compared to that predicted by the refined models, due to the underestimation of the rigid-body rotation of the upper-story walls when damage developed in the bottom story. This, however, did not affect the reliability of the results because the nonlinear response of the bottom stories was well captured by the simplified models, as shown in Appendix B.

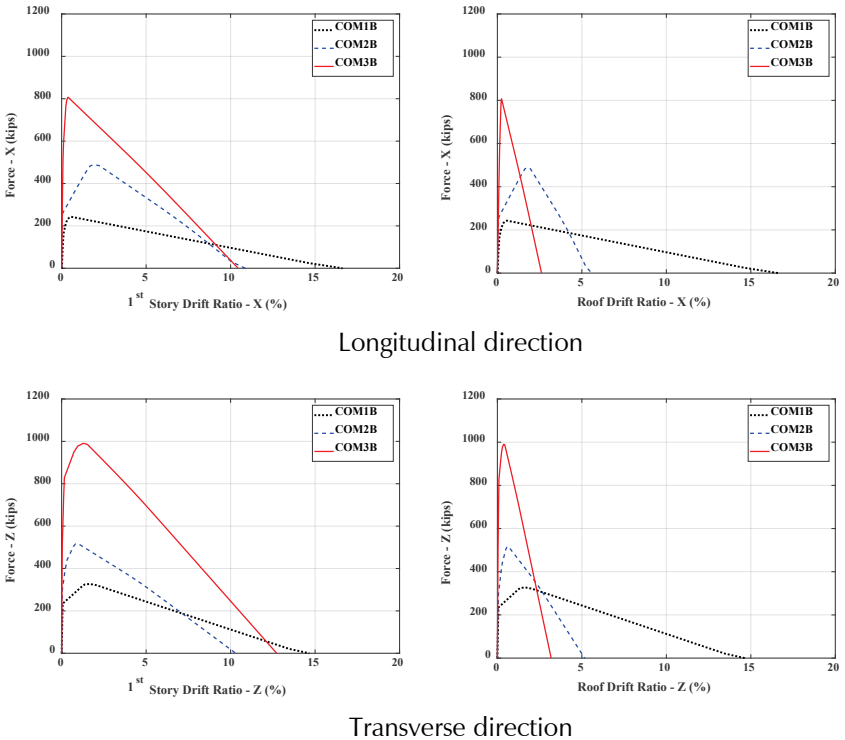

Figure 5-1 Pushover curves for high-seismic baseline models (COM1B, COM2B, and COM3B).

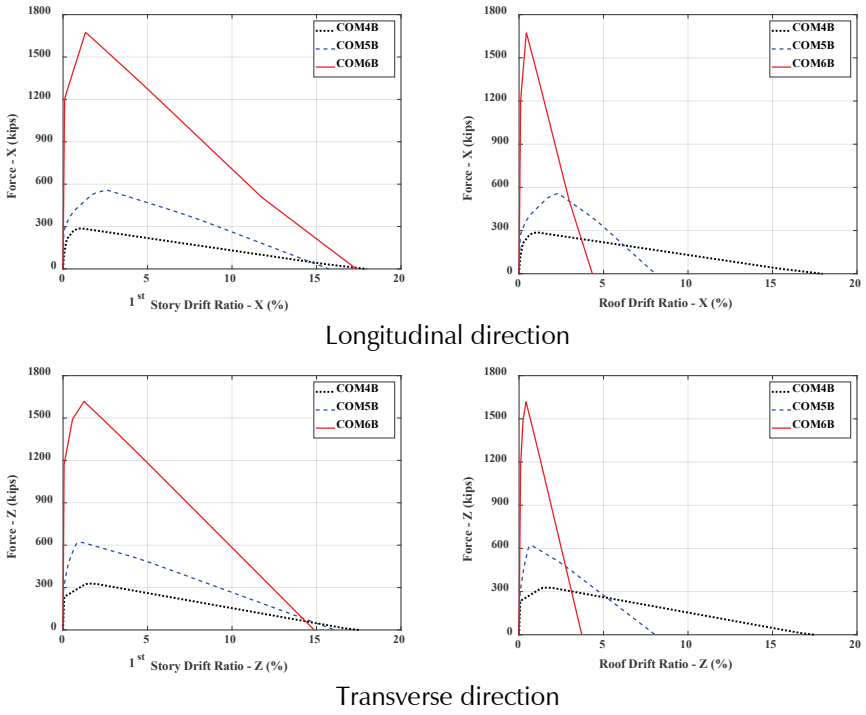

Figure 5-2 Pushover curves for very high-seismic baseline models (COM4B, COM5B, and COM6B).

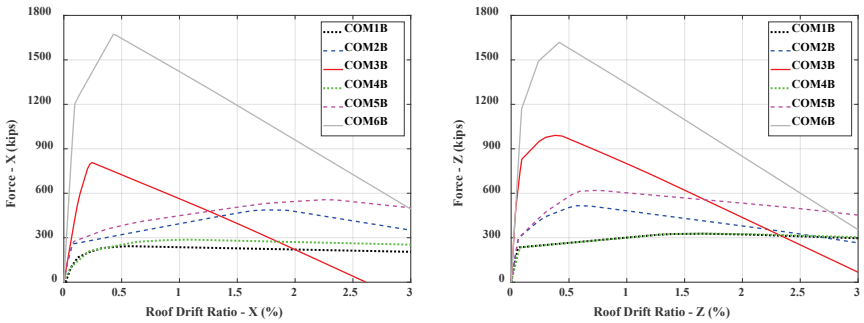

Figure 5-3 Zoomed-in pushover curves for all archetypes.

Figure 5-1 and Figure 5-2 show that COM5B (two-story, very high-seismic site) has a higher displacement capacity than COM2B (two-story, high-seismic site) even though the former has more vertical reinforcement. However, this difference in displacement capacity is less significant in the pushover analysis results from the refined finite-element models (as shown in Figure 4-23 and Figure 4-24) probably because the simplified models are calibrated with the hysteresis curves generated with bi-directional earthquake loading. If the behavior of a wall is governed by flexure, a higher amount of vertical reinforcement will lead to a smaller displacement capacity because it will cause more severe masonry toe crushing. However, this is not necessarily true for wall behavior dominated by diagonal shear or base sliding. For these cases, the higher amount of vertical reinforcement

provides more dowel resistance across diagonal shear cracks and horizontal base cracks. This could be the explanation for the higher displacement capacity of COM5B.

Figure 5-1 and Figure 5-2 also show that COM6B (four-story, very high-seismic site) has a higher displacement capacity than COM3B (four-story, high-seismic site). This can be largely attributed to the fact that COM6B has more wall cross-sectional area than COM3B.

Values of key parameters characterizing the pushover curves for each baseline model are presented in Table 5-1. In the table, the fundamental periods, T_1, were calculated from the eigenvalues analyses of the simplified models, $\Delta_{u,80}$ is the roof drift ratio at which the lateral resistance drops to 80 percent of the peak value, and $\Delta_{u,max}$ is the roof drift ratio at which the lateral resistance drops to zero. As mentioned previously, these roof drift values were under-predicted by the simplified models.

Table 5-1 Modal and Pushover Analysis Results of Baseline Archetype Models

Archetype ID	Transverse Direction				Longitudinal Direction			
	T_1 (sec)	V_{max}/W	$\Delta_{U,80}$ (in/in)	$\Delta_{U,max}$ (in/in)	T_1 (sec)	V_{max}/W	$\Delta_{U,80}$ (in/in)	$\Delta_{U,max}$ (in/in)
Commercial Buildings: High Seismic								
COM1B	0.148	1.27	0.043	0.146	0.130	0.95	0.038	0.166
COM2B	0.202	0.68	0.017	0.051	0.177	0.64	0.027	0.056
COM3B	0.235	0.52	0.010	0.032	0.378	0.43	0.007	0.026
Commercial Buildings: Very High Seismic								
COM4B	0.152	1.27	0.049	0. 175	0.136	1.11	0.044	0. 179
COM5B	0.194	0.81	0.025	0.081	0.172	0.73	0.037	0.081
COM6B	0.249	0.67	0.011	0.037	0.255	0.69	0.012	0.043

Table 5-1 shows that the ratio of V_{max} to W decreases with increasing number of stories, indicating that lower-rise archetypes have more reserve strength. The one-story archetypes have by far the largest V_{max}/W values because, as a result of the archetypes having configurations representative of actual buildings, they have a lot more walls than what is needed to resist code-specified seismic demands.

Table 5-2 shows the values of other parameters obtained from the pushover analyses. In this table, $V_{max,av}$ is the average of the maximum base shear strengths obtained for the two orthogonal directions of the archetype model, Ω is the overstrength factor based on $V_{max,av}$, and μ_T is the average of the period-based ductility values calculated for the two orthogonal directions.

The overstrength factor decreases as the number of stories increases, and the archetypes for the very high-seismic site have lower overstrength. As explained in Section 4.8, the simplified models underpredicted the value of μ_T and thereby the value of *SSF* for the multi-story archetypes. For this reason, *SSF* is taken to be 1.33, which is the upper-bound value according to FEMA P-695.

Table 5-2 Pushover and Collapse Analysis Results of Baseline Archetype Models

Archetype ID	Pushover Analysis			Collapse Analysis					
	$V_{max,av}/W$	Ω	μ_T	S_{CT}* (g)	CMR_{3D}	*SSF*	*ACMR*	P[CO | 0.5MCE$_R$] (%)	P[CO | MCE$_R$] (%)
Commercial Buildings: High Seismic									
COM1B	1.11	5.57	17.9	4.19	3.35	1.33	4.46	0.00	0.14
COM2B	0.66	3.29	8.52	2.37	1.90	1.33	2.52	0.07	3.22
COM3B	0.47	2.37	2.99	1.79	1.43	1.33	1.90	0.40	9.88
Commercial Buildings: Very High Seismic									
COM4B	1.19	3.98	18.9	4.54	2.42	1.33	1.90	0.01	0.97
COM5B	0.77	2.57	12.04	2.93	1.56	1.33	2.08	0.22	7.18
COM6B	0.68	2.26	4.25	2.73	1.46	1.33	1.94	0.35	9.36

* Without correction for 3D analysis (raw data)

Table 5-2 also shows the values of the median collapse intensity S_{CT} determined from the raw IDA data (equal to $S_{CT,raw}$ defined in Section 4.8) and the calculated collapse margin ratios. The collapse margin ratio (CMR_{3D}) is calculated as $1.2 \times S_{CT}/S_{MT}$, where S_{MT} is the MCE$_R$ spectral intensity at the design period of the archetype. The adjusted collapse margin ratio (*ACMR*) is calculated as $SSF \times CMR_{3D}$.

The collapse fraction data obtained from the IDAs and the lognormal collapse fragility curves derived from the IDA data for the high-seismic and very high-seismic archetypes are presented in Figure 5-4 and Figure 5-5, respectively. The dispersion factor, β, for these curves is assumed to be 0.5.

The collapse probabilities for the $0.5 \times$ MCE$_R$- and MCE$_R$-level ground motions are determined from the collapse fragility curve for each baseline model. As shown in Table 5-2, all the baseline models have collapse probabilities less than 10 percent for the MCE$_R$-level motion. The one-story archetypes have significantly lower probabilities of collapse. This applies to the entire spectral intensity range, as shown by the fragility curves in Figure 5-4 and Figure 5-5.

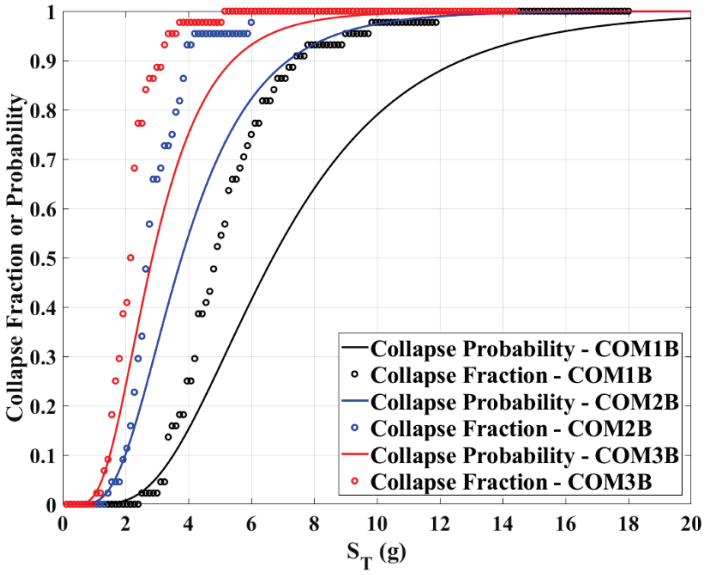

Figure 5-4 Collapse rates from IDA data and collapse fragility curves derived for high-seismic baseline models. S_T for the collapse fraction data has been scaled by 1.2, whereas that for the collapse probability curve has been scaled by $1.2 \times SSF$.

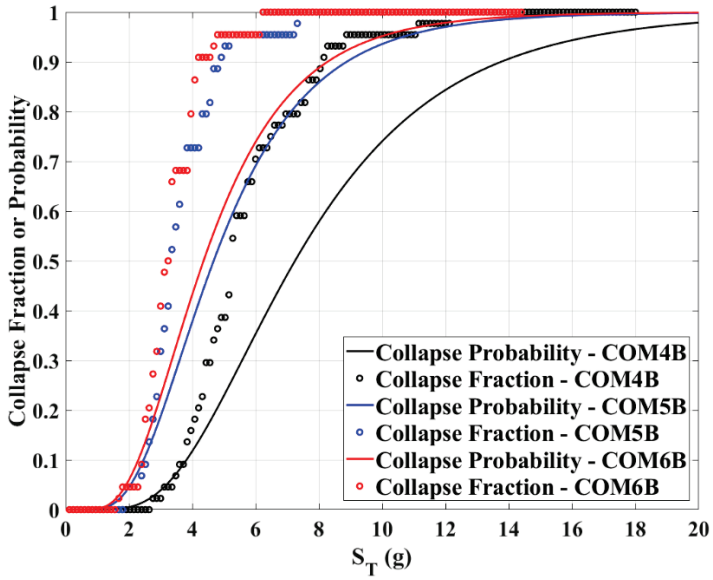

Figure 5-5 Collapse rates from IDA data and collapse fragility curves derived for very high-seismic baseline models. S_T for the collapse fraction data has been scaled by 1.2, whereas that for the collapse probability curve has been scaled by $1.2 \times SSF$.

Table 5-3 shows the median values of the peak roof drift, peak first-story drift, and response spectral intensity at incipient collapse, as well as the values of the lognormal standard deviation of these quantities. Consistent with the trend of the pushover curves shown in Figure 5-1 and Figure 5-2 and of the values of $\Delta_{u,max}$ shown in Table 5-1, the drift ratio at incipient collapse decreases as the number of stories increases. However, this trend is not as obvious for the very high-seismic cases. Furthermore, Table 5-3 shows that the spectral acceleration at incipient collapse decreases as the number of stories increases.

Table 5-3 Median and Lognormal Standard Deviation (β) Values of Peak Drift Ratio, First-Story Drift, and Response Spectral Acceleration at Incipient Collapse of Baseline Archetype Models

Archetype ID	Peak Drift Ratio at Incipient Collapse				Response Spectral Acceleration at Incipient Collapse S_T (g)	
	Roof		First Story			
	Median	β	Median	β	Median	β
Commercial Buildings: High Seismic						
COM1B	0.088	0.11	0.088	0.11	4.19	0.32
COM2B	0.035	0.16	0.064	0.16	2.37	0.30
COM3B	0.015	0.22	0.058	0.24	1.79	0.30
Commercial Buildings: Very High Seismic						
COM4B	0.092	0.07	0.092	0.07	4.54	0.32
COM5B	0.048	0.12	0.088	0.11	2.93	0.28
COM6B	0.021	0.11	0.084	0.12	2.73	0.27

5.2.2 Factors Influencing Probability of Collapse

Table 5-4 shows the collapse rates and the mean peak first-story drift ratios of the survivors for the 0.5 × MCE_R- and MCE_R-level ground motions based on the raw IDA data without applying the *SSF* or the 3D-analysis factor.

In Figure 5-6 through Figure 5-8, the probability of collapse for the MCE_R-level ground motions is plotted against the normalized pushover strength ($V_{max,av}/W$), the overstrength factor (Ω), and the calculated fundamental period (T_1), respectively. These figures show that the probability of collapse increases when the normalized pushover strength decreases or when the period increases (due to the increase of the number of stories). The clearest trend is the influence of the overstrength factor, as shown in Figure 5-7. The collapse probability increases as the value of Ω decreases. However, the relation between the collapse probability and Ω is not linear. There is a rapid increase in collapse probability when Ω drops below 2.5.

Table 5-4 **Collapse Rates of Baseline Archetype Models and Mean Peak First-Story Drift Ratios of Survivors at 50 Percent-of-MCE_R and MCE_R Ground-Motion Intensities**

Archetype ID	Collapse Rate at $0.5MCE_R$ (out of 44)*	Collapse Rate at MCE_R (out of 44)*	Mean Peak First-Story Drift Ratio of Survivors (%)			
			$0.5 \times MCE_R$		MCE_R	
			Trans. Direction	Long. Direction	Trans. Direction	Long. Direction
Commercial Buildings: High Seismic						
COM1B	0	0	0.09	0.13	0.30	0.58
COM2B	0	2	0.29	0.46	1.74	2.04
COM3B	0	6	0.50	1.05	2.17	2.71
Commercial Buildings: Very High Seismic						
COM4B	0	0	0.13	0.15	1.15	1.49
COM5B	0	2	0.70	0.94	3.30	3.85
COM6B	0	2	0.86	0.98	3.50	3.90

* The collapse rate is determined with the 1.2 factor applied to the MCE_R intensity to account for 3D analyses; however, this does not apply to other data in table.

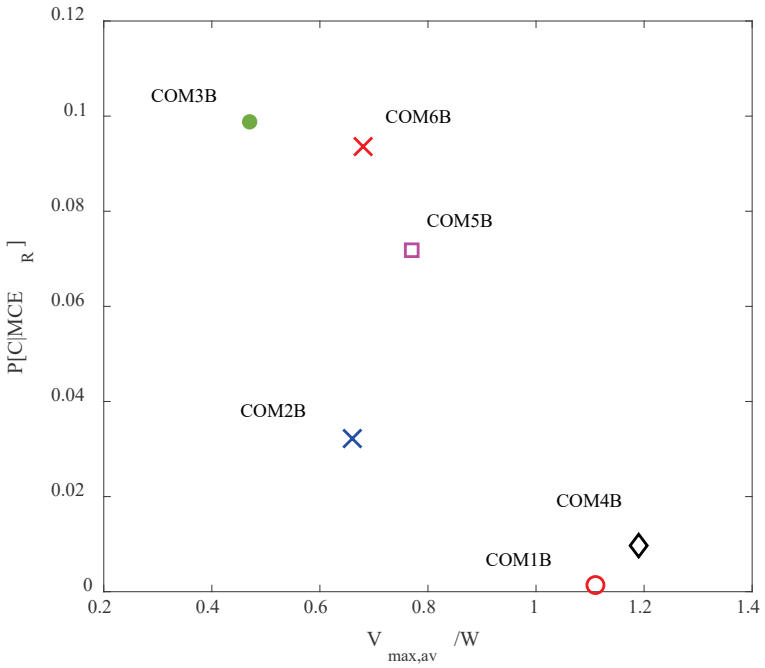

Figure 5-6 MCE_R collapse probability versus $V_{max,av}/W$ for the baseline models.

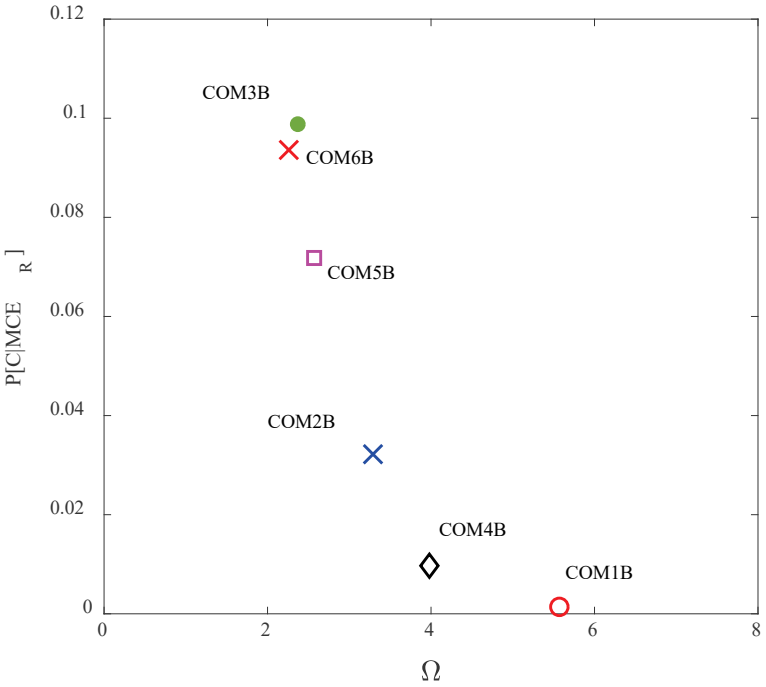

Figure 5-7 MCE_R collapse probability versus Ω for the baseline models.

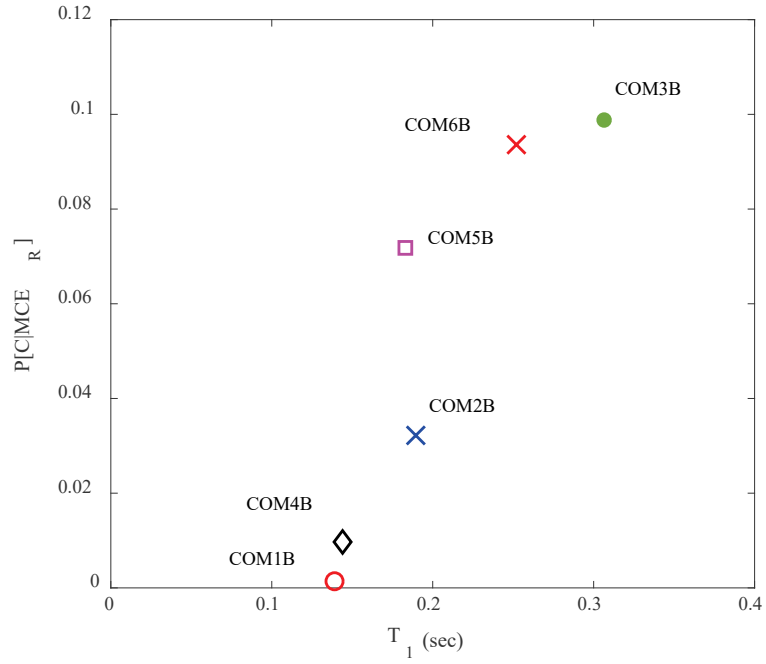

Figure 5-8 MCE_R collapse probability versus averaged fundamental period for the baseline models.

5.3 Displacement Capacity Parametric Study

This parametric study examines the influence of displacement capacity on collapse probability. In this study, the post-peak slopes of the base shear-vs.-first-story drift curves are varied. Two variants are considered for each baseline model COMXB. Model COMXB-DC1 has the post-peak negative slope decreased by 30 percent (more ductile), and COMXB-DC2 has the negative slope increased by 30 percent (less ductile).

The collapse fraction data and the collapse fragility curves derived for COM2B, COM2B-DC1, and COM2B-DC-2 are shown in Figure 5-9, and the collapse fragility curves for all the baseline models and their variants are shown collectively for the high-seismic and very high-seismic cases in Figure 5-10 and Figure 5-11, respectively.

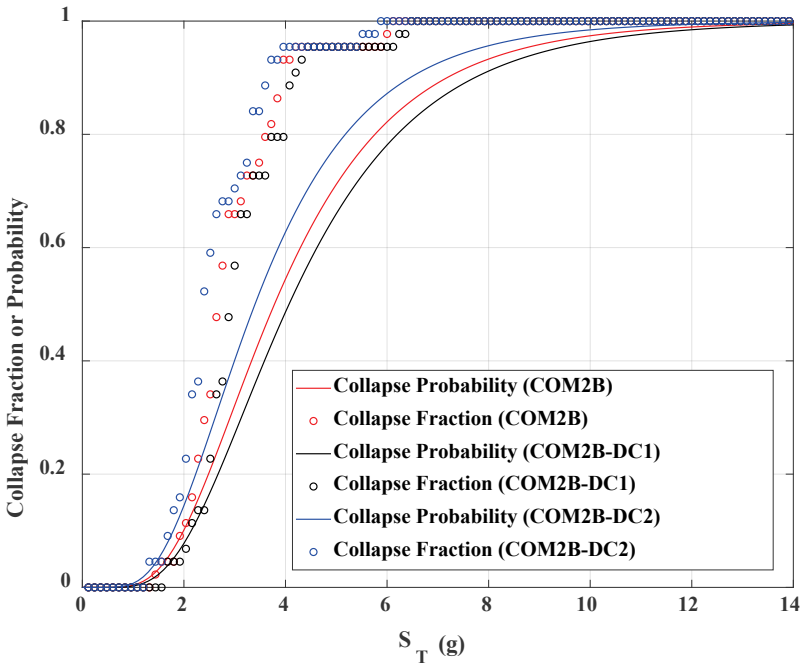

Figure 5-9 Collapse rates from IDA data and collapse fragility curves derived for COM2B, COM2B-DC1, and COM2B-DC2. S_T for the collapse fraction data has been scaled by 1.2, whereas that for the collapse probability curve has been scaled by $1.2 \times SSF$.

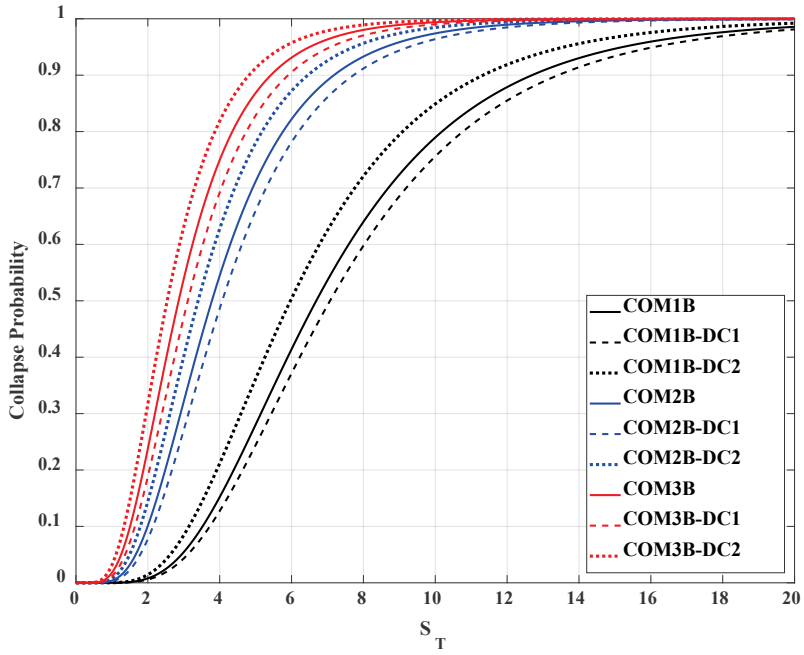

Figure 5-10 Collapse fragility curves for the displacement capacity parametric study for high-seismic archetypes.

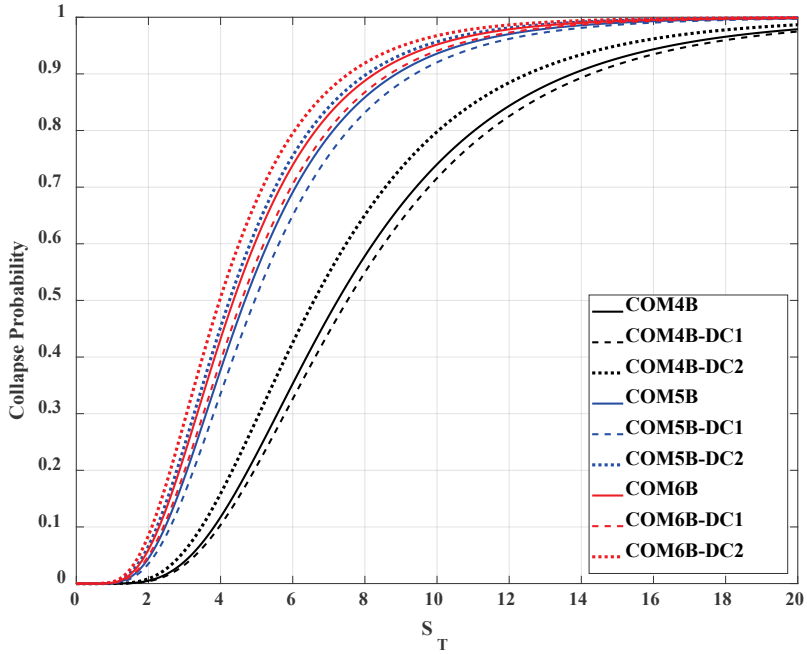

Figure 5-11 Collapse fragility curves for the displacement capacity parametric study for very high-seismic archetypes.

Table 5-5 summarizes the pushover analysis results obtained for the displacement capacity parametric study, and Table 5-6 shows the calculated collapse probabilities. The collapse probabilities vary in an expected manner, and the variation with respect to the change in displacement capacity

is not significant for any of the archetype models. Table 5-7 compares the mean and median values of the peak roof and first-story drift ratios, as well as the spectral intensities at incipient collapse. The mean and the median values are very close, and the mean and median peak first-story drift ratios at incipient collapse are all less than 10 percent. Incipient collapse is identified as the point on an IDA curve after which the curve goes flat or when the first-story drift ratio reaches 10 percent, whichever comes first. Hence, the archetypes that have the mean or median first-story incipient collapse drift ratios between 8 percent and 10 percent are more likely to have collapses triggered by the 10 percent drift limit. This occurs to archetypes that exhibit a more ductile behavior in the pushover analyses. For the high-seismic site, there is a clear trend that the drift ratio at incipient collapse decreases as the number of stories increases.

Table 5-5 Modal and Pushover Analysis Results of Displacement Capacity Parametric Study Archetype Models

Archetype ID	Transverse Direction				Longitudinal Direction			
	T_1 (sec)	V_{max}/W	$\Delta_{U,80}$ (in/in)	$\Delta_{U,max}$ (in/in)	T_1 (sec)	V_{max}/W	$\Delta_{U,80}$ (in/in)	$\Delta_{U,max}$ (in/in)
Commercial Buildings: High Seismic								
COM1B	0.148	1.27	0.043	0.146	0.130	0.95	0.038	0.166
COM1B-DC1	0.148	1.27	0.051	0.183	0.130	0.95	0.045	0.205
COM1B-DC2	0.148	1.27	0.034	0.107	0.130	0.95	0.028	0.123
COM2B	0.202	0.68	0.017	0.051	0.177	0.64	0.027	0.056
COM2B-DC1	0.202	0.68	0.020	0.064	0.177	0.64	0.031	0.067
COM2B-DC2	0.202	0.68	0.013	0.040	0.177	0.64	0.023	0.042
COM3B	0.235	0.52	0.010	0.032	0.378	0.43	0.007	0.026
COM3B-DC1	0.235	0.52	0.012	0.038	0.378	0.43	0.012	0.038
COM3B-DC2	0.235	0.52	0.008	0.024	0.378	0.43	0.006	0.020
Commercial Buildings: Very High Seismic								
COM4B	0.152	1.27	0.049	0. 175	0.136	1.11	0.044	0. 179
COM4B-DC1	0.152	1.27	0.058	0.217	0.136	1.11	0.052	0.223
COM4B-DC2	0.152	1.27	0.039	0.129	0.136	1.11	0.032	0.132
COM5B	0.194	0.81	0.025	0.081	0.172	0.73	0.037	0.081
COM5B-DC1	0.194	0.81	0.030	0.099	0.172	0.73	0.043	0.099
COM5B-DC2	0.194	0.81	0.019	0.059	0.172	0.73	0.031	0.061
COM6B	0.249	0.67	0.011	0.037	0.255	0.69	0.012	0.043
COM6B-DC1	0.249	0.67	0.013	0.045	0.255	0.69	0.014	0.052
COM6B-DC2	0.249	0.67	0.009	0.028	0.255	0.69	0.010	0.033

Table 5-6 Pushover and Collapse Analysis Results of Displacement Capacity Parametric Study Archetype Models

Archetype ID	Pushover Analysis			Collapse Analysis					
	$V_{max,av}/W$	Ω	μ_T	S_{CT}* (g)	CMR_{3D}	SSF	$ACMR$	P[CO| 0.5MCE$_R$] (%)	P[CO| MCE$_R$] (%)
Commercial Buildings: High Seismic									
COM1B	1.113	5.57	17.9	4.19	3.35	1.33	4.46	0.00	0.14
COM1B-DC1	1.113	5.57	21.2	4.43	3.54	1.33	4.71	0.00	0.10
COM1B-DC2	1.113	5.57	13.6	3.74	2.99	1.33	3.98	0.00	0.29
COM2B	0.659	3.29	8.516	2.37	1.90	1.33	2.52	0.07	3.22
COM2B-DC1	0.659	3.29	9.939	2.55	2.04	1.33	2.71	0.03	2.30
COM2B-DC2	0.659	3.29	7.072	2.13	1.70	1.33	2.27	0.14	5.09
COM3B	0.473	2.37	2.989	1.79	1.43	1.33	1.90	0.40	9.88
COM3B-DC1	0.473	2.37	4.050	1.95	1.56	1.33	2.07	0.24	7.22
COM3B-DC2	0.473	2.37	2.440	1.59	1.27	1.33	1.69	0.79	14.7
Commercial Buildings: Very High Seismic									
COM4B	1.193	3.98	18.9	4.54	2.42	1.33	1.90	0.01	0.97
COM4B-DC1	1.193	3.98	22.3	4.71	2.51	1.33	3.34	0.01	0.79
COM4B-DC2	1.193	3.98	14.4	4.13	2.20	1.33	2.93	0.02	1.58
COM5B	0.772	2.57	12.04	2.93	1.56	1.33	2.08	0.22	7.18
COM5B-DC1	0.772	2.57	14.09	3.10	1.65	1.33	2.20	0.15	5.75
COM5B-DC2	0.772	2.57	9.747	2.66	1.42	1.33	1.89	0.43	10.4
COM6B	0.679	2.26	4.246	2.73	1.46	1.33	1.94	0.35	9.36
COM6B-DC1	0.679	2.26	5.169	2.87	1.53	1.33	2.04	0.25	7.74
COM6B-DC2	0.679	2.26	3.692	2.49	1.33	1.33	1.77	0.58	12.7

* Without correction for 3D analysis (raw data)

Table 5-7 **Mean, Lognormal Standard Deviation (β), and median values of Peak Roof Drift, Peak First-Story Drift, and Response Spectral Acceleration at Incipient Collapse of Displacement Capacity Parametric Study Archetype Models**

Archetype ID	Peak Roof Drift at Incipient Collapse (%)			Peak First-Story Drift at Incipient Collapse (%)			Incipient Collapse S_T (g)[3]		
	Mean[1]	β	Median[2]	Mean[1]	β	Median[2]	Mean[1]	β	Median[2]
Commercial Buildings: High Seismic									
COM1B	8.87	0.11	8.82	8.87	0.11	8.82	4.41	0.32	4.19
COM1B-DC1	9.34	0.06	9.93	9.34	0.06	9.32	4.66	0.32	4.43
COM1B-DC2	7.34	0.19	7.22	7.34	0.19	7.22	3.96	0.34	3.73
COM2B	3.56	0.16	3.52	6.52	0.16	6.43	2.47	0.30	2.37
COM2B-DC1	4.21	0.16	4.16	7.86	0.17	7.76	2.65	0.28	2.55
COM2B-DC2	2.75	0.18	2.71	4.87	0.20	4.78	2.25	0.32	2.13
COM3B	1.56	0.22	1.52	6.00	0.24	5.83	1.87	0.30	1.79
COM3B-DC1	1.90	0.15	1.88	7.36	0.16	7.26	2.03	0.29	1.95
COM3B-DC2	1.17	0.21	1.14	4.39	0.24	4.28	1.67	0.31	1.59
Commercial Buildings: Very High Seismic									
COM4B	9.19	0.07	9.17	9.19	0.07	9.17	4.78	0.32	4.54
COM4B-DC1	9.43	0.07	9.40	9.43	0.07	9.40	4.96	0.32	4.71
COM4B-DC2	8.05	0.14	7.97	8.05	0.14	7.97	4.36	0.32	4.13
COM5B	4.78	0.12	4.75	8.87	0.11	8.82	3.06	0.28	2.93
COM5B-DC1	4.99	0.10	4.97	9.20	0.07	9.18	3.20	0.29	3.07
COM5B-DC2	4.04	0.18	3.98	7.45	0.18	7.34	2.78	0.30	2.66
COM6B	2.14	0.11	2.13	8.41	0.12	8.35	2.82	0.27	2.73
COM6B-DC1	2.29	0.11	2.28	8.98	0.11	8.93	2.97	0.26	2.87
COM6B-DC2	1.80	0.16	1.78	7.05	0.17	6.96	2.59	0.28	2.49

[1] Mean from raw data.

[2] Median from best-fit lognormal distribution curve.

[3] Without correction for 3D analyses (raw data).

Table 5-8 shows the collapse rates and the mean peak first-story drift ratios of the survivors for the 0.5 × MCE_R- and MCE_R-level ground motions based on the raw IDA data without applying the *SSF* or the 3D-analysis factor. In general, the collapse rate at MCE_R increases significantly as the displacement capacity is decreased by 30 percent (as shown by COMXB-DC2). Furthermore, the mean peak first-story drift ratio of survivors at MCE_R increases slightly as the displacement capacity increases.

Table 5-8 **Collapse Rates and Mean Peak First-Story Drift Ratios of Survivors at 50 Percent-of-MCE_R and MCE_R Ground-Motion Intensities of the Displacement Capacity Parametric Study Archetype Models**

Archetype ID	Collapse Rate at 0.5MCE_R (out of 44)*	Collapse Rate at MCE_R (out of 44)*	Mean Peak First-Story Drift Ratio of Survivors (%)			
			0.5 × MCE_R		MCE_R	
			Trans. Direction	Long. Direction	Trans. Direction	Long. Direction
Commercial Buildings: High Seismic						
COM1B	0	0	0.09	0.13	0.30	0.58
COM1B-DC1	0	0	0.09	0.13	0.30	0.58
COM1B-DC2	0	0	0.09	0.13	0.30	0.59
COM2B	0	2	0.29	0.46	1.74	2.04
COM2B-DC1	0	0	0.29	0.46	1.68	2.09
COM2B-DC2	0	2	0.29	0.46	1.66	1.75
COM3B	0	6	0.50	1.05	2.17	2.71
COM3B-DC1	0	4	0.50	1.03	2.33	2.86
COM3B-DC2	0	13	0.50	1.02	1.95	2.34
Commercial Buildings: Very High Seismic						
COM4B	0	0	0.13	0.15	1.15	1.49
COM4B-DC1	0	0	0.13	0.15	1.15	1.50
COM4B-DC2	0	0	0.13	0.15	1.17	1.51
COM5B	0	2	0.70	0.94	3.12	3.64
COM5B-DC1	0	2	0.70	0.94	3.19	3.67
COM5B-DC2	0	5	0.71	0.95	2.98	3.25
COM6B	0	2	0.86	0.98	3.36	3.67
COM6B-DC1	0	0	0.86	0.97	3.33	3.67
COM6B-DC2	0	7	0.87	0.99	3.07	3.28

* The collapse rate is determined with the 1.2 factor applied to the MCE_R intensity to account for 3D analyses; however, this does not apply to other data in table.

5.4 Soil-Structure Interaction and Foundation Flexibility Parametric Study

This parametric study examines the influence of soil-structure interaction (SSI) and foundation flexibility on the seismic performance of COM2B. Two site properties are considered. One is a stiff site that is at the site class C/D boundary (COM2B-SS1). The other is a soft site at the site class D/E boundary (COM2B-SS2). The modeling of the foundation and soil properties is discussed in Section 4.7.3, and the determination of the soil spring and damper properties is described in Appendix C. To account for

kinematic interaction (which includes the effects of base-slab averaging), the free-field ground-motion records were filtered with a transfer function determined for the respective site to obtain the input motions for the analyses. Incremental dynamic analyses were conducted for COM2B-SS2 with the original free-field motions and filtered motions to examine the influence of kinematic interaction.

In Figure 5-12, the pushover analysis curves obtained for the stiff and soft sites are compared to those for the baseline model. For the stiff site, the influence of the soil and foundation flexibility on the ascending branch of the pushover curves is negligible. Nevertheless, the post-peak slope of the pushover curve for the *x* direction for the stiff site is significantly more gentle than that for the baseline model. This is largely attributed to the rotation and flexural yielding of the foundation slab below the end walls (Wall 1 and Wall 3 as numbered in Figure 4-36), which resulted in a reduction of the plastic rotation demand on the bottom spring of the wall elements and thus delayed the inelastic softening behavior of the walls. The change of the rotation demand also slightly reduced the peak shear resistance of the walls, which depended on the moments developed in the top and bottom springs of each wall element.

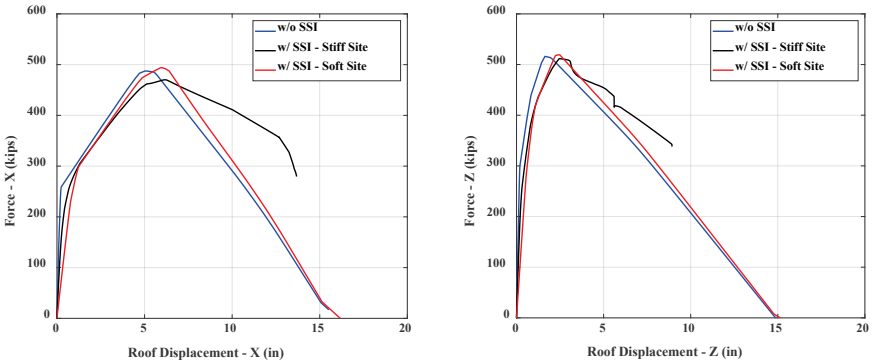

Figure 5-12 Pushover curves for COM2B with and without soil springs and dampers.

Figure 5-13 shows the vertical displacements of the foundations for the stiff and soft sites at the respective peak base shear. Because the stiff site had a smaller and weaker foundation, it had more significant foundation rotation and uplift. The stiffer soil also resulted in a more severe foundation edge uplift. For the soft site, the foundation rotation and uplift were significantly smaller because the foundation was larger and stronger. This resulted in only a small change in the post-peak slopes of the pushover curves.

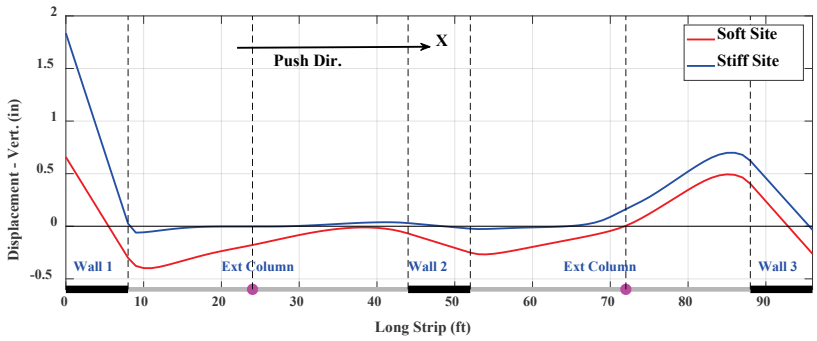

Figure 5-13 Vertical displacements of the foundations for the stiff and soft sites at the respective maximum base shear.

These results indicate that the pushover response was significantly affected by the flexural deformation and rotation of the foundation slab and less by the soil deformation. Figure 5-14 shows the forces developed in the vertical soil springs (which have a spacing of 1 foot) along the foundation strip in the longitudinal (x) direction of the building at the respective maximum base shear for both sites. The stiff site has zero force in the soil springs along a significant portion of the foundation due to the foundation uplift. For both the soft and stiff sites, the compressive forces developed in the soil springs are far below the bearing capacities. Because of the significant loss of soil contact for the stiff site, the foundation could slide under lateral earthquake forces. However, the influence of the soil-foundation contact condition on the horizontal (bearing or friction) resistance of the soil was not accounted for in the model.

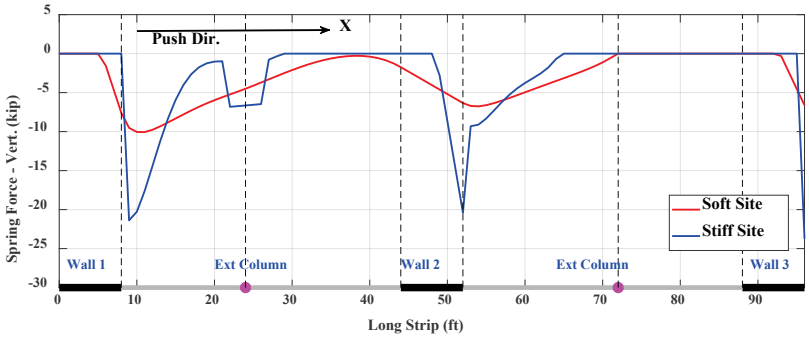

Figure 5-14 Forces in vertical soil springs for the stiff and soft sites at the respective maximum base shear.

The moments developed in the foundation slabs and grade beams at the respective maximum base shear are shown in Figure 5-15. Flexural yielding occurs in the foundation slabs or grade beams for both sites. To understand the interaction of the walls with the foundation slab and the underlying soil, and the resulting lateral load resisting mechanisms of the system, a U-shaped end segment of the foundation slab underneath Wall 1 and Wall 4 (the end walls on the windward side) for each site was isolated as a free body, as

depicted in Figure 5-16. The forces and moments shown in the figure are extracted from the pushover analyses at the respective maximum base shear. The moments and shear forces developed in the foundation slab, as well as the axial force exerted by the walls and the column on the foundation, counteracted the overturning moments exerted by the walls. Figure 5-15 also shows that the shear demand on the grade beam for the stiff site could be well beyond the shear strength of the beam (which has a cross-sectional dimension of 1 foot × 1 foot).

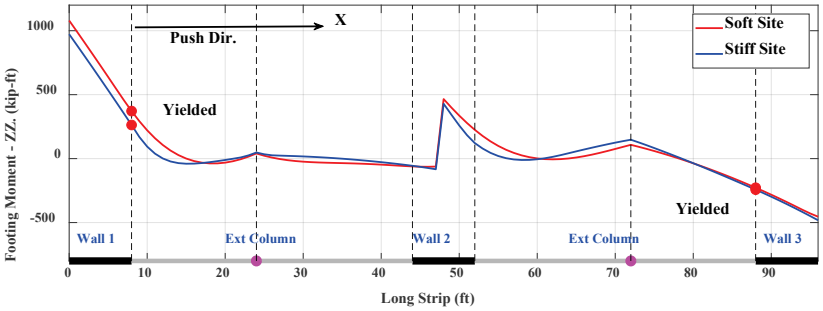

Figure 5-15 Moments in foundation slabs and grade beams for the stiff and soft sites at the respective maximum base shear.

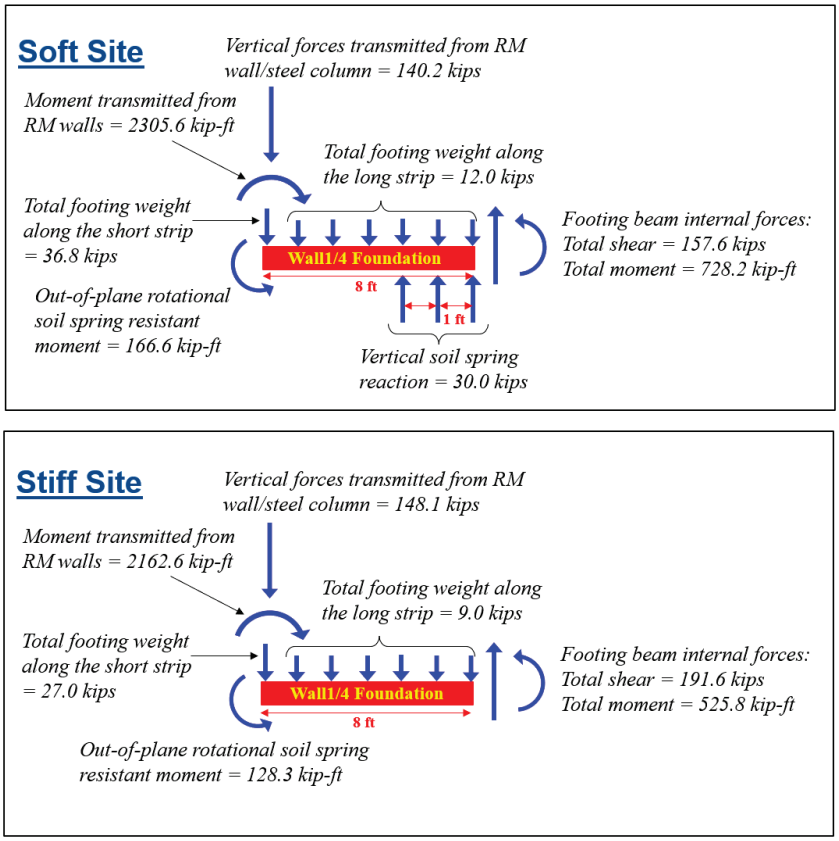

Figure 5-16 Resistance of foundation slabs to overturning moments of Wall 1 and Wall 4 for the stiff and soft sites at the respective maximum base shear.

The behavior of COM2B-SS1 (stiff site) was significantly influenced by the deformation of the foundation slab. Hence, it is uncertain if the simplified model calibrated with the refined finite-element model of a fixed-base building realistically represents the behavior of the walls sitting on a relatively flexible and weak foundation slab. In addition, the simplified foundation model does not capture the shear failure of the foundation slab or the shear resistance at the slab-soil interface when significant uplift occurs. The development of a detailed model to simulate these phenomena was outside the scope of this parametric study. For this reason, only COM2B-SS2, which has a stronger and stiffer foundation slab, is further considered for the collapse probability study.

Table 5-10 compares the fundamental periods and the key parameters of the pushover curves obtained for COM2B, COM2B-SS1, and COM2B-SS2. Model COM2B-SS2 has a significantly longer period than COM2B due to the soft soil.

Table 5-9 Modal and Pushover Analysis Results of the SSI and Foundation Flexibility Parametric Study Archetype Models

Archetype ID	Transverse Direction				Longitudinal Direction			
	T_1 (sec)	V_{max}/W	$\Delta_{U,80}$ (in/in)	$\Delta_{U,max}$ (in/in)	T_1 (sec)	V_{max}/W	$\Delta_{U,80}$ (in/in)	$\Delta_{U,max}$ (in/in)
Commercial Buildings: High Seismic								
COM2B	0.20	0.68	0.017	0.051	0.18	0.64	0.027	0.056
COM2B-SS1	0.24	0.67	0.022	-	0.27	0.62	0.041	-
COM2B-SS2	0.35	0.68	0.018	0.053	0.42	0.65	0.029	0.056

Table 5-10 Pushover and Collapse Analysis Results of SSI and Foundation Flexibility Parametric Study Archetype Models

Archetype ID	Pushover Analysis			Collapse Analysis					
	$V_{max,av}/W$	Ω	μ_T	S_{CT}[1] (g)	CMR_{3D}	SSF	$ACMR$	P[CO| 0.5MCE$_R$] (%)	P[CO| MCE$_R$] (%)
Commercial Buildings: High Seismic									
COM2B	0.66	3.29	8.516	2.37	1.90	1.33	2.52	0.07	3.22
COM2B-SS1[2]	0.64	3.22	9.469	-	-	-	-	-	-
COM2B-SS2 (Unfiltered)	0.67	3.33	9.172	2.35	1.88	1.33	2.50	0.07	3.34
COM2B-SS2 (Filtered)	0.67	3.33	9.172	2.36	1.89	1.33	2.51	0.07	3.28

[1] Without correction for 3D analysis (raw data).

[2] No incremental dynamic analysis performed.

Incremental dynamic analyses were performed on COM2B-SS2 with filtered and unfiltered ground-motion records. The filtered records account for kinematic interaction. Table 5-10 compares the numerical results obtained for COM2B and COM2B2-SS2. The influence of SSI and foundation flexibility on collapse probability is negligible; although it slightly increases the collapse probability. This can be explained by the shape of the median acceleration spectrum of the ground-motion records, as shown in Figure 4-37. The spectral curve has a plateau for the period range between 0.20 seconds and 0.35 seconds. Hence, the increase of the structural period from 0.20 seconds (for the fixed-based archetype) to 0.35 seconds (for the archetype on soft soil) does not change the spectral acceleration but may increase the spectral displacement. However, the influence may be diminished by the nonlinear response of the system. Figure 5-17 shows the plots of the median spectral intensity (S_T) against the resulting median maximum first-story drift ratio for COM2B and COM2B-SS2. The curves show a trend that is consistent with the above observation and suggest that the use of the filtered motions slightly increases the collapse spectral intensity compared to the unfiltered records. Figure 5-18 compares the collapse rates from the IDAs and the collapse fragility curves for COM2B and COM2B-SS2 (with and without filtered ground motions). The collapse fragility curves are indistinguishable.

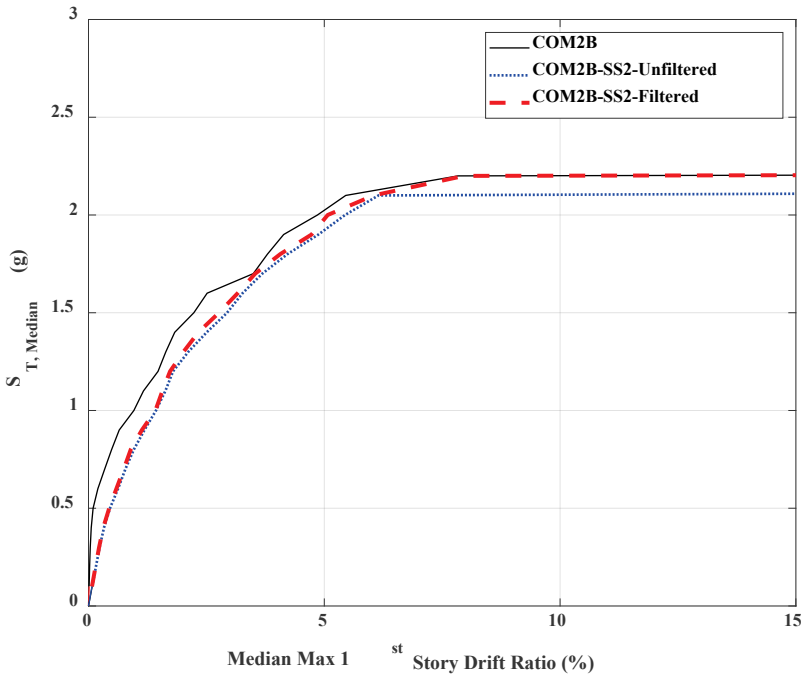

Figure 5-17 Median spectral intensity versus median maximum first-story drift.

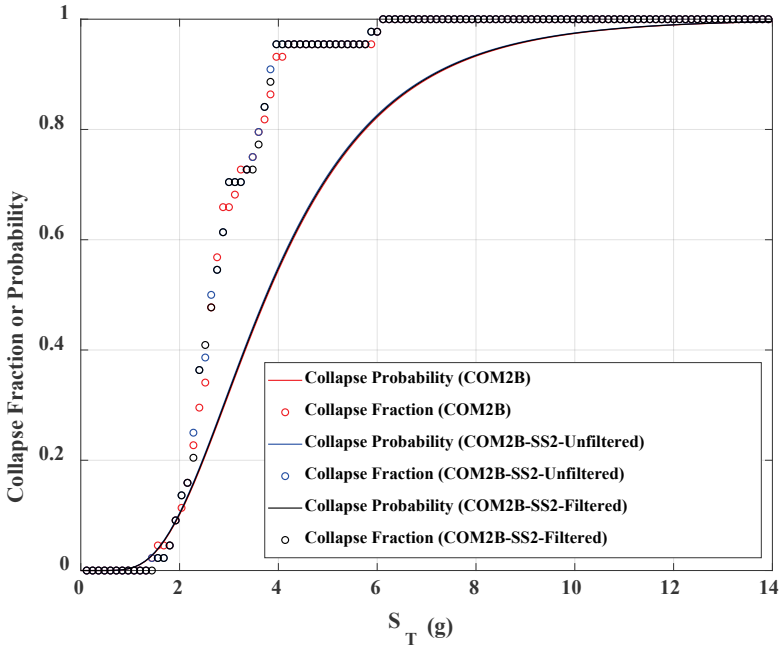

Figure 5-18 Collapse rates from IDA data and collapse fragility curves derived for COM2B and COM2B2-SS2. S_T for the collapse fraction data has been scaled by 1.2, whereas that for the collapse probability curve has been scaled by $1.2 \times SSF$.

Table 5-11 shows the median values of the peak roof drift, peak first-story drift, and response spectral intensity at incipient collapse, as well as the values of the lognormal standard deviation of these quantities, for the SSI and foundation flexibility parametric study. As shown, the inclusion of SSI and foundation flexibility in the analysis results in very small changes.

Table 5-11 Median and Lognormal Standard Deviation (β) Values of Peak Drift Ratio, First-Story Drift, and Response Spectral Acceleration at Incipient Collapse of the SSI and Foundation Flexibility Archetype Models

Archetype ID	Peak Drift Ratio at Incipient Collapse				Response Spectral Acceleration at Incipient Collapse S_T (g)	
	Roof		First Story			
	Median	β	Median	β	Median	β
COM2B	0.035	0.16	0.064	0.16	2.37	0.30
COM2B-SS2-Unfiltered	0.037	0.14	0.067	0.15	2.35	0.29
COM2B-SS2-Filtered	0.036	0.16	0.066	0.18	2.36	0.29

Table 5-12 shows the collapse rates and the mean peak first-story drift ratios of the survivors for the 0.5 × MCE_R- and MCE_R-level ground motions based on the raw IDA data without applying the *SSF* or the 3D-analysis factor. The inclusion of SSI and foundation flexibility reduces the collapse rate at MCE_R from two to one out of the suite of ground motions. However, the median collapse spectral intensities for COM2B and COM2B-SS2 are very close to each other, and because they use the same dispersion factor, β, their collapse fragility curves are nearly identical, as shown in Figure 5-18.

Table 5-12 Collapse Rates and Mean Peak First-Story Drift Ratios of Survivors at 50 Percent-of-MCE_R and MCE_R Ground-Motion Intensities of the SSI and Foundation Flexibility Parametric Study Archetype Models

Archetype ID	Collapse Rate at 0.5MCE_R (out of 44)*	Collapse Rate at MCE_R (out of 44)*	Mean Peak First-Story Drift Ratio of Survivors (%)			
			0.5 × MCE_R		MCE_R	
			Trans. Direction	Long. Direction	Trans. Direction	Long. Direction
Commercial Buildings: High Seismic						
COM2B	0	2	0.29	0.46	1.74	2.04
COM2B-SS2 (Unfiltered)	0	1	0.67	0.84	2.17	2.33
COM2B-SS2 (Filtered)	0	1	0.63	0.82	2.10	2.28

* The collapse rate is determined with the 1.2 factor applied to the MCE_R intensity to account for 3D analyses; however, this does not apply to other data in table.

Chapter 6

Findings, Conclusions, and Recommendations

6.1 Introduction

This chapter summarizes key findings, conclusions, and recommendations arising from the parametric studies conducted on reinforced masonry building archetypes. In preceding chapters, the following topics were addressed:

- establishing target collapse performance benchmarks for the numerical models of reinforced masonry buildings based on observations of collapse performance in past earthquakes and shake-table tests (Chapter 2);
- identifying representative building archetypes and developing detailed designs of these building archetypes according to current seismic-code requirements (Chapter 3);
- transforming the archetype designs into nonlinear numerical models, including variations on selected parameters in the models (Chapter 4); and
- conducting nonlinear pushover and incremental dynamic analyses with these numerical models to evaluate the relative importance of the modeling assumptions and parametric variations on the reliable calculation of response behavior and collapse performance (Chapter 5).

6.2 Key Findings of the Parametric Studies

Key findings of the parametric studies are summarized and discussed in the following sections. A table is provided with each parametric study, summarizing key archetype model properties (e.g., number of stories, first-mode period, T_1, overstrength, Ω, and normalized pushover strength, V_{max}/W) and key collapse results (e.g., roof and first-story drift ratios at the point of incipient collapse, the collapse margin ratio, CMR_{3D}, and the probability of collapse given MCE_R ground motions). The target range of benchmark collapse probabilities are also provided for comparison with the collapse probabilities of archetype models designed for high-seismic loads (S_{MS} =

1.5g). Values of first-mode period, overstrength, and normalized pushover strength in these tables represent the average value of these parameters in the two horizontal directions of response.

6.2.1 Baseline Configuration Parametric Study

This parametric study investigated the response behavior and collapse performance of the baseline archetype configurations. The baseline archetype configurations included variations in occupancy (COM, RES, BOX), height (one story, two stories, and four stories for COM and RES; one story for BOX), and seismic-design levels (moderate, high, and very high seismic). However, the parametric study was only completed for a subset of one-story, two-story and four-story COM archetype building configurations, and thus the conclusions presented in this section reflect this limited scope.

Baseline configuration models considered the results of other parametric studies and incorporated a best estimate for each parameter to provide an overall best estimate of the simulated response of short-period reinforced masonry buildings. Table 6-1 summarizes key model properties and collapse results for each of the six baseline archetypes.

Table 6-1 Summary of Key Model Properties and Collapse Results of Baseline Archetype Models

Archetype ID	Model Properties				Collapse Results				Benchmark Collapse Probability (%)
	No. of Stories	Period T_1 (sec)	Strength		Drift Ratio*		CMR_{3D}	P[COL | MCE_R] (%)	
			Ω	V_{max}/W	Roof	First Story			
High-Seismic (S_{MS} = 1.5g) Baseline Archetype Models									
COM1B	1	0.14	5.6	1.11	0.088	0.088	3.35	0.14	0 to 2
COM2B	2	0.19	3.3	0.66	0.035	0.064	1.90	3.2	0 to 5
COM3B	4	0.31	2.4	0.47	0.015	0.058	1.43	9.9	0 to 5
Very High-Seismic (S_{MS} = 2.25g) Baseline Archetype Models									
COM4B	1	0.14	4.0	1.19	0.092	0.092	2.42	1.0	NA
COM5B	2	0.18	2.6	0.77	0.048	0.088	1.56	7.2	NA
COM6B	4	0.25	2.3	0.68	0.021	0.084	1.46	9.4	NA

* Median drift ratio at incipient collapse.

The overall findings of the baseline parametric study include the following:

1. **Collapse Failure Mode.** Sidesway collapse of all baseline building archetype models was due to the formation of a weak-story mechanism in the first story, which is consistent with observed failure of reinforced masonry buildings tested on shake tables (Ahmadi et al., 2015; Mavros et al., 2016; Stavridis et al., 2016).

2. **Collapse Probabilities.** MCE_R collapse probabilities calculated for high-seismic one-story and two-story COM baseline archetype models (COM1B, COM2B) are consistent with benchmark collapse rates as shown in Table 6-1. The collapse probability of the high-seismic four-story COM baseline archetype model (COM3B) is approximately twice that of the benchmark (and about three times that of the two-story archetype model). The larger collapse probability of the four-story archetype model is consistent with the lower normalized pushover strength (V_{max}/W) and displacement capacity of this model (e.g., normalized pushover strength of the four-story archetype model is about 70 percent of that of the two-story archetype model).

   None of the MCE_R collapse probabilities of the very high-seismic COM baseline archetype models exceed the ASCE/SEI 7-10 collapse-safety objective of no-more-than 10 percent probability of collapse given MCE_R ground motions.

3. **Collapse Trend with Building Period.** The MCE_R probability of collapse of the baseline archetype models increases with archetype model period, T_1, all else being equal, as illustrated in Figure 6-1. This trend is most likely due to differences in building archetype model normalized pushover strength (V_{max}/W), which tends to decrease with period, and the P-delta effect, which becomes more critical with height (number of stories).

   For comparison purposes, horizontal lines are included in Figure 6-1 (and subsequent figures of this chapter that show the probability of collapse as a function of an archetype model parameter) to indicate: (1) the 2 percent benchmark collapse probability for one-story high-seismic archetype models; (2) the 5 percent benchmark collapse probability for two-story-and-taller high-seismic archetype models; and (3) the 10 percent collapse-safety objective of ASCE/SEI 7-10.

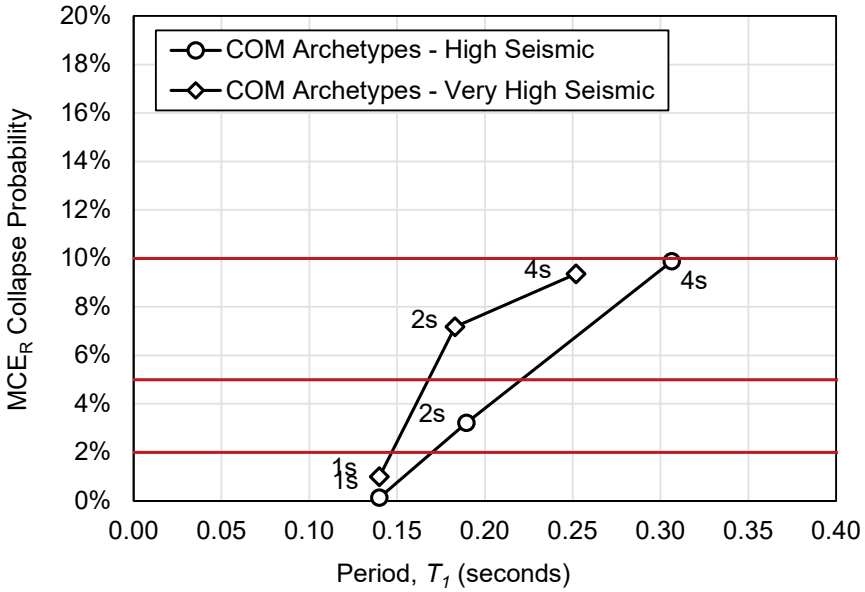

Figure 6-1 MCE$_R$ collapse probability of baseline archetype models plotted as a function of archetype model period (T_1), and benchmark (BM) values of high-seismic MCE$_R$ collapse probability and the MCE$_R$ collapse-safety objective of ASCE/SEI 7-10.

4. **Strength.** In general, collapse probability is strongly influenced by the archetype normalized pushover strength (V_{max}/W)—the stronger the archetype model, the better the collapse performance, all else being equal. The same trend is seen where collapse probability is expressed as a function of archetype model overstrength (Ω), which is the maximum base shear strength (V_{max}) of the model relative to the design seismic demand (V_{design}). Figure 6-2 shows MCE$_R$ collapse probabilities of the six COM baseline archetypes plotted as a function of average building archetype model overstrength (Ω), indicating the general trend of lower MCE$_R$ collapse probability with increased archetype model overstrength.

   As shown in Figure 6-2, high-seismic archetype models and very high-seismic archetype models have similar trends in collapse performance as a function of archetype model overstrength, such that where values of overstrength are about the same, values of probability of collapse are likewise about the same. For example, the four-story high-seismic archetype model and the four-story very high-seismic archetype model have about the same overstrength ($\Omega = 2.0$) and about the same MCE$_R$ probability of collapse of 10 percent).

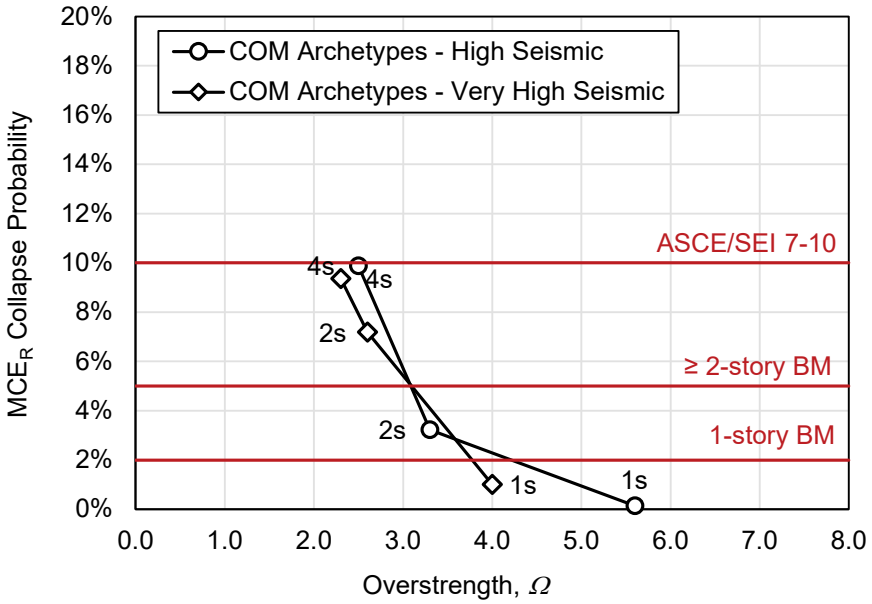

Figure 6-2 MCE_R collapse probabilities of baseline archetype models plotted as a function of average archetype model overstrength (Ω), and benchmark (BM) values of MCE_R collapse probability and the MCE_R collapse-safety objective of ASCE/SEI 7-10.

5. **Very High-Seismic Collapse Performance.** The probability of collapse of the one-story and two-story very high-seismic archetype models are larger than those of the corresponding high-seismic archetype models. This is consistent with the lower overstrength values of the former. Notably, all three very high-seismic archetypes have collapse probabilities less than the 10 percent collapse-safety objective of ASCE/SEI 7-10. The four-story very high-seismic archetype has a lot more wall cross-sectional area than the four-story high-seismic archetype, resulting in similar overstrength and collapse performance values for both archetypes.

   Collapse performance of very high-seismic designs was evaluated for MCE_R ground motions (S_{MS} = 2.25g) that represent a ground motion intensity typical of sites relatively close to active faults (an intensity 50 percent greater than that of high-seismic ground motions). The analysis was performed with ground motions recorded at far-field sites, but the amplitudes were scaled up based upon design as S_{MS} = 2.25g.

6.2.2 Displacement Capacity Parametric Study

The displacement capacity parametric study investigated the effects of varying the lateral displacement at which the archetype model lost its entire lateral resistance. As noted in the findings of the previous section, collapse was due

to the formation of a weak story at the first story in all cases. Therefore, the metric of interest is the displacement or drift ratio of the first story at the point of incipient collapse, after which the drift increased indefinitely in the IDA analysis per the FEMA P-695 collapse evaluation procedure. Collapse displacement capacity was investigated by varying the slope of the post-capping strength of COM building archetype models. Baseline building archetype models of one-story, two-story and four-story high-seismic COM buildings and one-story, two-story and four-story very high-seismic COM buildings were each modified to have two variants of post-capping strength slope (i.e., plus and minus 30 percent change in the slope). Key archetype model properties and collapse results are summarized in Table 6-2.

Table 6-2 Summary of Key Model Properties and Collapse Results of Displacement Capacity Parametric Study Archetype Models with Baseline, Enhanced (DC1) and Reduced (DC2) Post-Capping Strength

Reinforced-Masonry Building Archetype Model ID	Model Properties				Collapse Results				Benchmark Collapse Probability (%)
	No. of Stories	Period T_1 (sec)	Strength		Drift Ratio*		CMR_{3D}	P[COL | MCE_R] (%)	
			Ω	V_{max}/W	Roof	First Story			
High-Seismic (S_{MS} = 1.5g) Baseline Archetype Models									
COM1B-DC1	1	0.14	5.6	1.11	0.093	0.093	3.54	0.10	0 to 2
COM1B	1	0.14	5.6	1.11	0.088	0.088	3.35	0.14	0 to 2
COM1B-DC2	1	0.14	5.6	1.11	0.072	0.072	2.99	0.29	0 to 2
COM2B-DC1	2	0.19	3.3	0.66	0.042	0.078	2.04	2.3	0 to 5
COM2B	2	0.19	3.3	0.66	0.035	0.064	1.90	3.2	0 to 5
COM2B-DC2	2	0.19	3.3	0.66	0.027	0.048	1.70	5.1	0 to 5
COM3B-DC1	4	0.31	2.4	0.47	0.019	0.073	1.56	7.2	0 to 5
COM3B	4	0.31	2.4	0.47	0.015	0.058	1.43	9.9	0 to 5
COM3B-DC2	4	0.31	2.4	0.47	0.011	0.043	1.27	14.7	0 to 5
Very High-Seismic (S_{MS} = 2.25g) Baseline Archetype Models									
COM4B-DC1	1	0.14	4.0	1.19	0.094	0.094	2.51	0.8	NA
COM4B	1	0.14	4.0	1.19	0.092	0.092	2.42	1.0	NA
COM4B-DC2	1	0.14	4.0	1.19	0.080	0.080	2.20	1.6	NA
COM5B-DC1	2	0.18	2.6	0.77	0.050	0.092	1.65	5.8	NA
COM5B	2	0.18	2.6	0.77	0.048	0.088	1.56	7.2	NA
COM5B-DC2	2	0.18	2.6	0.77	0.040	0.073	1.42	10.4	NA
COM6B-DC1	4	0.25	2.3	0.68	0.023	0.089	1.53	7.7	NA
COM6B	4	0.25	2.3	0.68	0.021	0.084	1.46	9.4	NA
COM6B-DC2	4	0.25	2.3	0.68	0.018	0.070	1.33	12.7	NA

* Median drift ratio at incipient collapse.

In Table 6-2, archetype models labeled "DC1" have enhanced displacement capacity (flatter post-capping slope) and archetype models labeled "DC2" have reduced displacement capacity (steeper post-capping slope). In general, the flatter the slope of post-capping strength, the greater the incipient collapse drift ratio (and the lower the probability of collapse given MCE_R ground motions).

The overall findings of the parametric study of displacement capacity include the following:

1. **Collapse Probabilities.** In general, for a given archetype design, the probability of collapse decreases with the increase of post-capping displacement capacity. MCE_R collapse probabilities calculated for high-seismic one-story and two-story archetype models (COM1B and COM2B) are all consistent with benchmark collapse rates with only COM2B-DC2 slightly above the upper-bound value of 5 percent (Table 6-2), as illustrated in Figure 6-3.

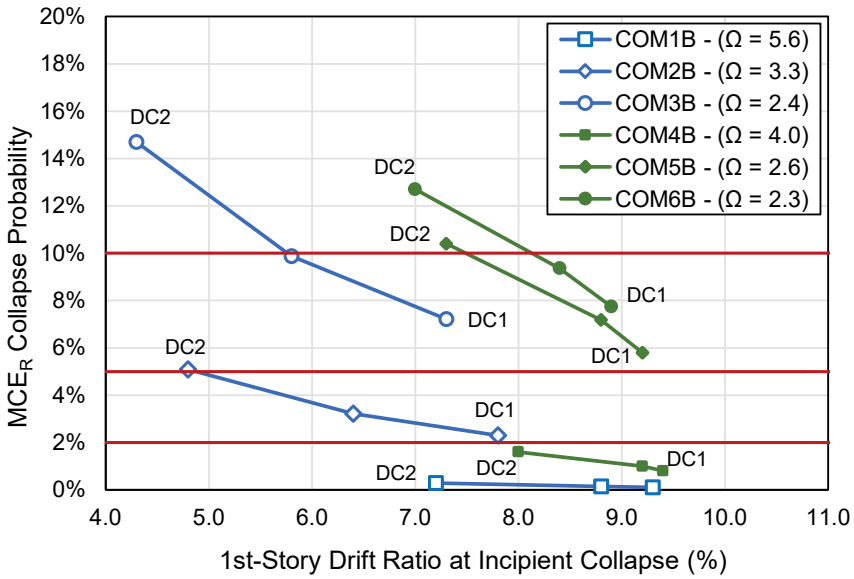

Figure 6-3 MCE_R collapse probability as a function of first-story drift ratio at incipient collapse of archetype models with varying amounts of post-capping displacement capacity, and benchmark (BM) values of MCE_R collapse probability and the MCE_R collapse-safety objective of ASCE/SEI 7-10. Archetype model overstrength (Ω) is shown in the legend.

2. **Correlation of the Collapse Margin Ratio with Post-Capping Displacement Capacity.** The collapse margin ratio (CMR_{3D}) is strongly correlated with the post-capping displacement capacity, as illustrated in Figure 6-4 by the plots of the CMR_{3D} parameter as a function of first-story drift ratio at incipient collapse. For a given archetype design, the greater the first-story drift ratio at incipient collapse, the larger the collapse margin ratio.

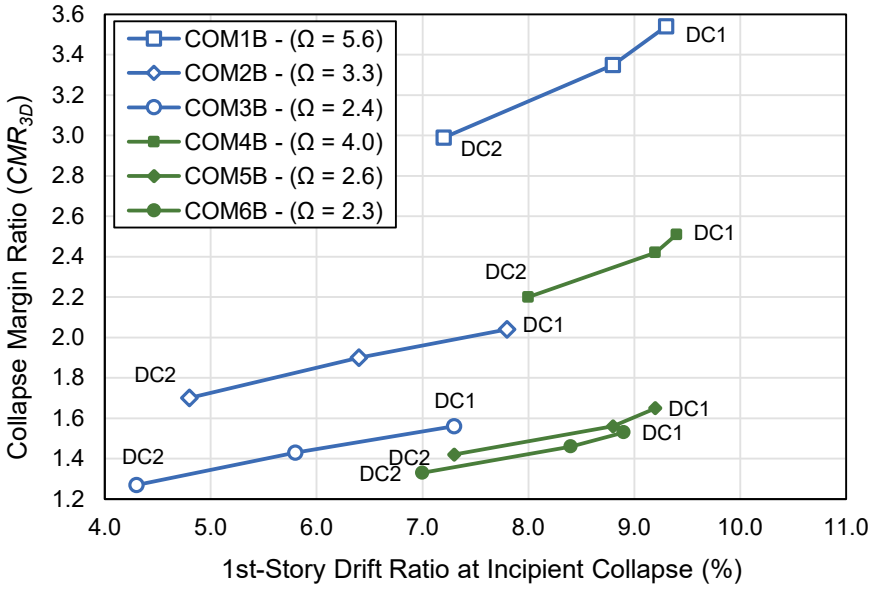

Figure 6-4 Collapse margin ratio (CMR_{3D}) as a function of first-story drift ratio at incipient collapse of archetype models with varying amounts of post-capping displacement capacity, and benchmark (BM) values of MCE_R collapse probability and the MCE_R collapse-safety objective of ASCE/SEI 7-10. Archetype model overstrength (Ω) is shown in the legend.

The related and more significant influence of archetype model strength (i.e., overstrength) on the collapse margin ratio is illustrated in Figure 6-4. The curves in Figure 6-4 show that for a given value of first-story drift ratio at incipient collapse, the collapse margin ratio varies roughly in proportion to archetype overstrength. For example, at a first-story drift ratio at incipient collapse of 9 percent, the collapse margin ratio of the COM4B archetype is about 50 percent greater than that of the COM5B archetype and, likewise, the overstrength of the COM4B archetype is about 50 percent greater than that of the COM5B archetype. The curves in Figure 6-4 also show a proportionally more modest increase in the collapse margin ratio with an increase in the first-story drift ratio at incipient collapse

6.2.3 *Soil-Structure Interaction (SSI) and Foundation Flexibility Parametric Study*

The soil-structure interaction (SSI) and foundation flexibility parametric study investigated the effects of SSI and foundation flexibility by: (1) modeling a distributed set of discrete nonlinear soil springs and dampers below flexible foundation elements; and (2) performing dynamic analysis with FEMA P-695 records filtered to reduce response at very short periods (i.e., due to kinematic interaction effects).

For this study, the two-story, high-seismic COM archetype was modeled with two variants of nonlinear soil springs and dampers representing: (1) stiff soil site conditions, i.e., v_{s30} = 360 m/s (COM2B-SS1); and (2) soft soil site conditions, i.e., v_{s30} = 180 m/s (COM2B-SS2). Pushover analyses were performed for both site conditions, although collapse evaluations were only performed for soft site conditions.

For the archetype model with nonlinear springs and dampers representing soft soil site conditions, collapse analyses were performed using earthquake records modified for kinematic interaction effects (i.e., filtered records), as well as the standard set of (unmodified) FEMA P-695 earthquake records.

Table 6-3 summarizes key model properties and collapse results for the two-story baseline archetype model (COMB2B) with a fixed base and variant archetype models with flexible foundations that incorporate SSI effects.

Table 6-3 Summary of Key Properties and Collapse Results of SSI and Foundation Flexibility Archetype Models with a Fixed Base and with Flexible Foundations that Incorporate SSI Effects

Reinforced-Masonry Building Archetype Model ID	Model Properties				Collapse Results				Benchmark Collapse Probability (%)
	No. of Stories	Period T_1 (sec)	Strength		Drift Ratio*		CMR_{3D}	P[COL | MCE_R] (%)	
			Ω	V_{max}/W	Roof	First Story			
High-Seismic (S_{MS} = 1.5g) Archetype Models									
COM2B	2	0.19	3.3	0.66	0.035	0.064	1.90	3.2	0 to 5
COM2B-SS1	2	0.26	3.2	0.65					
COM2B-SS2 (unfiltered)	2	0.39	3.3	0.67	0.037	0.067	1.88	3.3	0 to 5
COM2B-SS2 (filtered)	2	0.39	3.3	0.67	0.036	0.066	1.89	3.3	0 to 5

* Median drift ratio at incipient collapse.

The overall findings of the SSI and foundation flexibility parametric study include the following:

1. **Nonlinear Static (Pushover) Response.** The nonlinear static (pushover) curves of variant building archetype models representing stiff (SS1) and soft (SS2) site conditions were found to be qualitatively similar to the pushover curve of the baseline building archetype model with rigid, fixed-base foundations (e.g., see Figure 5-12). However, these two variant models were moderately to significantly more flexible at pushover displacements up to peak strength, and the soft site model showed a gentler post-capping slope compared to the fixed-based case. For the archetype models evaluated in this parametric study, the foundations had sufficient strength to develop yielding mechanisms and

induce failure of the reinforced masonry walls above. Other configurations of reinforced masonry buildings could conceivably have the opposite sequence of failure (i.e., failure of the foundation prior to the reinforced masonry wall above).

2. **Collapse Probabilities.** For the soft soil collapse analyses using FEMA P-695 records (1) without kinematic modification (SS2 unfiltered); and (2) with kinematic modification (SS2 filtered), the MCE_R collapse probabilities calculated for the variant building archetype models were found to be essentially the same as that of the baseline building archetype model with rigid, fixed-base foundations, as shown in Table 6-3. Although the analyses show no significant difference in collapse performance due to kinematic interaction effects (which includes the effects of base-slab averaging), the collapse probabilities could be appreciably different if foundation failure had occurred prior to failure of the reinforced masonry walls above.

6.3 Conclusions and Recommendations

Prior FEMA P-695 collapse performance studies on a variety of structural systems over a range of periods have suggested that, for systems with design periods less than about 0.5 seconds, the probability of collapse given MCE_R ground motions increases significantly as the design period decreases. Trends in observed earthquake damage of short-period buildings, however, do not support the high collapse probabilities predicted by numerical analysis. The apparent discrepancy between analytical prediction of collapse performance and the opinions and observations of structural engineers has been designated the *short-period building seismic performance paradox*.

With improved numerical modeling and representative reinforced masonry building archetypes, this study has shown that MCE_R collapse probabilities decrease as the design period decreases, which is a reversal of the trend observed in prior FEMA P-695 studies. Further, numerical analyses of short-period reinforced masonry buildings designed and evaluated for high-seismic loads (S_{MS} = 1.5g) resulted in low collapse probabilities for MCE_R ground motions, consistent with the collapse rates inferred by the observed performance of low-rise buildings in past earthquakes (e.g., red tag data from the 1994 Northridge earthquake). As a result, this study has solved the short-period building seismic performance paradox for reinforced masonry systems.

Numerical investigations conducted in this study provide valuable insights into the collapse performance of reinforced masonry buildings that should be of importance to seismic-code-development committees, engineering

practitioners, and researchers. In the sections that follow, results from this study are compared to prior FEMA P-695 studies on reinforced masonry building archetypes, and recommendations are provided in the following areas:

- Improved Seismic Design Codes and Standards
- Advanced Seismic Design and Analysis Practice
- Enhanced Modeling and Testing

6.3.1 Comparison with Prior FEMA P-695 Collapse Probability Studies

Key model properties and collapse results of prior studies of archetype models of reinforced masonry buildings, as reported in NIST GCR 10-917-8 and NIST GCR 12-917-20, are summarized in Table 6-4.

Table 6-4 Summary of Key Model Properties and Collapse Results of Archetype Models of Prior Studies of Special Reinforced Masonry Shear Wall Buildings Designed for High-Seismic Loads

Archetype ID	Model Properties					Collapse Results			
	No. of Stories	Period T (sec)	Period T_1 (sec)	Strength		Drift Ratio*		CMR	P[COL | MCE_R] (%)
				Ω	V_{max}/W	Roof	First Story		
NIST GCR 10-917-8: High-Gravity/High-Seismic (S_{MS} = 1.5 g) Archetype Models									
S1	1	0.25	0.10	1.84	0.37	-	-	0.52	79
S2	2	0.26	0.13	2.28	0.46	0.015	-	1.14	21
S3	4	0.45	0.21	1.87	0.37	-	-	1.55	8.4
PG-1S	*All*	*0.32*	*0.15*	*2.00*	*0.35*	-	-	*1.07*	*26*
NIST GCR 10-917-8: Low-Gravity/High-Seismic (S_{MS} = 1.5 g) Archetype Models									
S11	1	0.25	0.10	1.84	0.37	-	-	0.52	79
S12	2	0.26	0.13	1.82	0.36	-	-	1.71	5.9
S13	4	0.45	0.26	1.73	0.35	-	-	1.65	6.8
PG-5S	*All*	*0.32*	*0.16*	*1.80*	*0.36*	-	-	*1.29*	*15.3*
NIST GCR 12-917-20: R = 4/High-Seismic (S_{MS} = 1.5g) Archetype Models									
	1	0.25	0.11	2.04	0.51	0.014	0.014	1.00	35
	2	0.26	0.10	1.72	0.43	0.013	-	1.40	11.9
	4	0.45	0.16	1.82	0.46	0.028	-	2.40	1.4
PG-1s/2s	*1 & 2*	*0.26*	*0.11*	*1.86*	*0.47*	*0.014*	-	*1.20*	*21*
NIST GCR 12-917-20: R = 6/High-Seismic (S_{MS} = 1.5g) Archetype Models									
	1	0.25	0.11	1.93	0.32	0.014	0.014	0.80	48
	2	0.26	0.10	2.59	0.43	0.013	-	1.40	11.9
	4	0.45	0.16	2.27	0.38	0.028	-	2.40	1.4
PG-1s/2s	*1 & 2*	*0.26*	*0.11*	*2.26*	*0.38*	*0.014*	-	*1.10*	*24*

* Drift ratios of non-simulated failure modes (only reported by prior studies for certain archetype models).

Similar information in Table 6-1 through Table 6-3 of this chapter are reported in Table 6-4, noting the following differences:

- The design period, T, (as well as the model period, T_1) is reported (for comparison with collapse probabilities plotted in Figure 1-1 of this report).
- Collapse roof-drift ratios are based on non-simulated collapse failure modes (e.g., rupture or buckling of 30 percent or more of the flexural reinforcement), rather than on the results of incremental dynamic analysis (i.e., at the point of incipient collapse). Collapse roof-drift ratios were reported in the prior studies for only a few models.
- The collapse margin ratio, *CMR*, is based on incremental dynamic analysis of 2D analytical models. 2D (planar) models of walls were used in all prior studies of reinforced masonry building archetypes.

The NIST GCR 10-917-8 study evaluated collapse performance for one-story, two-story, four-story, eight-story and twelve-story heights of special and ordinary reinforced masonry building archetypes designed for two FEMA P-695 seismic levels, SDC D_{max} (S_{MS} = 1.5g) and SDC D_{min} (S_{MS} = 0.75g); only model properties and collapse results for one-story, two-story and four-story special reinforced masonry archetypes designed and evaluated for S_{MS} = 1.5g (i.e., high-seismic design level) are reported in Table 6-4. To determine how collapse margin ratios vary with design R values, the NIST GCR 12-917-20 study redesigned the one-story, two-story and four-story high-gravity load archetypes of the NIST GCR 10-917-8 study using R values of 1, 2, 4, and 8. Model properties and collapse results are reported in Table 6-4 for R = 4 and R = 6 designs of the NIST GCR 12-917-20 study, which bound the value of R = 5 used for design of the archetypes of this study (as described in Chapter 3).

Two collapse results plotted in Figure 1-1 of this report for short-period masonry archetypes represent the average values of the collapse probabilities of performance groups PG-1S and PG-5S of the NIST GCR 10-917-8 study (i.e., collapse probabilities of 15 percent and 26 percent, respectively, for an average design period of T = 0.32 seconds). The individual collapse probabilities for one-story, two-story and four-story archetype models that range from 6.8 percent and 8.4 percent for four-story archetype models to 79 percent for one-story archetype models are reported in Table 6-4.

The results of the NIST GCR 12-917-20 study show similar trends (although different values) of collapse probabilities for one-story and two-story archetype models, but significantly different and much lower collapse probabilities for the four-story archetype models (i.e., only 1.4 percent) than those of the NIST GCR 10-917-8 study. The explanation for differences in collapse probabilities of the two NIST studies and those of this study is

rooted in the differences in the strength and collapse displacement capacity of the archetype models, as discussed below for one-story, two-story and four-story archetype models.

Comparison of One-Story Archetype Model Properties and Collapse Performance. The probability of collapse of the COM1B archetype model of this study is less than 1 percent; whereas the collapse probabilities of one-story archetype models of prior studies is 35 percent to 79 percent. The strength of the COM1B model is about three times stronger than the strength of the models of prior studies (e.g., $\Omega = 5.6$ as compared to $\Omega = 1.84$ of Model S1 of the NIST GCR 10-917-8 study), and the collapse displacement capacity is about six times greater than collapse displacement capacity of the models of prior studies (e.g., 8.6 percent roof-drift ratio as compared to 1.4 percent roof-drift ratio of the NIST GCR 12-917-20 study).

Comparison of Two-Story Archetype Model Properties and Collapse Performance. The probability of collapse of the COM2B archetype model of this study is about 3 percent; whereas the collapse probabilities of two-story archetype models of prior studies is about 6 percent to 21 percent. The strength of the COM2B model of this study is about 1.5 times stronger than those of the prior studies (e.g., $\Omega = 3.3$ as compared to $\Omega = 2.28$ of Model S2 of the NIST GCR 10-917-8 study), and the collapse displacement capacity of the COM2B model is more than two times greater than those of prior studies (e.g., 3.5 percent roof-drift ratio as compared to 1.5 percent roof-drift ratio of Model S2 of the NIST GCR 10-917-8 study).

Comparison of Four-Story Archetype Model Properties and Collapse Performance. The probability of collapse of the COM3B archetype model of this study is about 10 percent; whereas the collapse probability of the four-story archetype model (S3) of the NIST CGR 10-917-8 study is similar but somewhat less, about 8 percent, and the collapse probabilities of the four-story archetype models of the NIST CGR 12-917-20 study are less than 2 percent. The COM3B archetype model has about the same strength as that of the S3 model of the NIST GCR 10-917-8 study (e.g., $\Omega = 2.4$ as compared to $\Omega = 1.87$). The COM3B archetype model has about the same strength as that of the four-story models of the NIST GCR 12-917-20 study (e.g., $\Omega = 2.4$ as compared to $\Omega = 1.82$ and $\Omega = 2.27$ of the $R = 4$ and $R = 6$ models, respectively) but only about one-half the collapse displacement capacity (e.g., 1.5 percent roof-drift ratio as compared to 2.8 percent roof-drift ratio of the prior models), which is consistent with the lower collapse probabilities of the four-story models of the NIST GCR 12-917-20 study.

The source of the strength discrepancies between the studies can be attributed primarily to different project objectives. In previous studies, archetypes were configured and optimized to provide the minimum seismic-force-resisting system necessary to meet the design seismic load demand (see Figure 3-1 of this study). In this study, archetypes were intended to represent typical building configurations. As a result, some archetypes exhibited significantly greater overstrength than previous studies, as described above. This result might reasonably be expected for:

- buildings with more wall than is structurally necessary as a result of architectural constraints,
- walls for which the minimum reinforcement requirement is greater than required to meet demand, and
- walls with relatively low seismic demand, such that small incremental changes in reinforcement size or spacing result in large relative changes in capacity.

All of these are common characteristics of short-period reinforced masonry buildings.

6.3.2 Recommendations for Improved Seismic Design Codes and Standards

This section describes topics and provides recommendations considered particularly relevant to seismic-code-development committees, including the Provisions Update Committee of the Building Seismic Safety Council, the ASCE/SEI 7 Seismic Subcommittee, the ASCE/SEI 41 Standards Committee, and the TMS 402/602 Standards Committee responsible for the development of TMS 402. Seismic-code committees have limited resources and any studies would, in most cases, require a funded project to develop the requisite technical basis of any proposals to improve existing codes or standards.

Deformation Compatibility of Components Not Part of the Seismic-Force-Resisting System. Consistent with shake-table and pull tests of full-scale test buildings described in Section 2.3, the nonlinear models of reinforced masonry building archetypes of this study have large drift displacement capacities (e.g., median first-story drift ratios as large as 10 percent at incipient collapse) that are significantly larger than those currently used for ASCE/SEI 7 to check deformation compatibility of components not part of the seismic-force-resisting system. This is of possible concern because the collapse probabilities determined by this project tacitly assume

that the gravity system can support gravity loads out to the drift at incipient collapse.

A study is recommended to determine whether current ASCE/SEI 7 provisions for deformation compatibility checks are adequate given the new drift information available from this project.

Seismic Retrofit of Existing Reinforced Masonry Buildings. Consistent with shake-table and pull tests of full-scale test buildings described in Section 2.3, the nonlinear models of reinforced masonry building archetypes of this study have large drift displacement capacities (e.g., median first-story drift ratios as large as 10 percent at incipient collapse). In contrast, the backbone curves of the nonlinear procedures of ASCE/SEI 41-17 (ASCE, 2017) have much more limited values of collapse drift displacements. For example, for walls controlled by shear, collapse is defined by drift ratios beyond 0.75 percent for evaluation of primary components and beyond 2.0 percent for evaluation of secondary components (Table 11-7).

It is recommended that the ASCE/SEI 41 Standards Committee update existing modeling parameters and acceptance criteria based on recent test data.

FEMA P-695 Seismic Criteria Update. The seismic criteria of FEMA P-695 are based on the "Zone 4" seismic criteria of the 1994 version of the *Uniform Building Code* (ICBO, 1994), as embodied in the deterministic-lower-limit seismic criteria of Section 21.2.2 of ASCE/SEI 7-05 (ASCE, 2005). The seismic criteria of FEMA P-695 are out-of-date with respect to the current seismic criteria of ASCE/SEI 7-16 (ASCE, 2016) and ASCE/SEI 7-22, as proposed. At short periods (i.e., the acceleration domain), the seismic criteria of FEMA P-695 are either the same as the deterministic lower limit of ASCE/SEI 7-16 or only about 10 percent less than those proposed for ASCE/SEI 7-22. In the velocity domain (i.e., periods greater than 1.0 seconds for Site Class D site conditions), the seismic criteria of FEMA P-695 are only about 60 percent of those of ASCE/SEI 7-16 (and somewhat less for ASCE/SEI 7-22, as proposed). Updating the seismic criteria of P-695 would not significantly affect the collapse evaluation of short-period building archetypes (and the findings of this study of reinforced masonry buildings) but could be of importance to the collapse evaluation of taller building archetypes with longer periods.

As per the original "Zone 4" approach of FEMA P-695, all of the ground motions represent "far-field" sites and purposely ignore higher levels of ground shaking typical of sites closer to the fault(s) governing site seismic

hazard. Accordingly, FEMA P-695 implicitly permits MCE_R collapse probabilities greater than 10 percent for structures at sites where ground motions are greater than those of the "far-field" SDC D_{max} seismic criteria; whereas, the 10 percent collapse objective of Section 1.3.1.3 (Performance-Based Procedures) and Section 12.2.1.1 (Alternate Structural Systems) of ASCE/SEI 7-16 applies to all sites, regardless of their proximity to fault rupture, noting that the commentary to Section 12.2.1.1 identifies FEMA P-695 as the preferred methodology for verifying compliance with the 10 percent collapse objective. As shown by comparison of the collapse performance of high-seismic and very high-seismic baseline archetype models of this study, very different conclusions could be reached if the MCE_R ground motions greater than those of the "far-field" SDC D_{max} of FEMA P-695 were required for collapse evaluation. The fundamental question is simply: does the 10 percent collapse-safety objective of ASCE/SEI 7-16 apply to buildings at all possible sites or only to those sites that are not "near-source"?

A study is recommended to determine what if any updates to FEMA P-695 should be made to: (1) incorporate current ASCE/SEI 7-16 and forthcoming ASCE/SEI 7-22 ground-motion criteria, and (2) address the apparent discrepancy between the acceptance criteria of FEMA P-695 and those of Section 12.2.1.1 of ASCE/SEI 7-16.

Effect of Overstrength. The conditions that result in overstrength for the walls of reinforced masonry buildings may also increase demand on adjacent elements, such as diaphragms or collectors. It may be relevant to code-writing committees that this common condition is not entirely consistent with the code intent for encouraging flexure-dominated behavior and capacity-based design.

6.3.3 Recommendations for Advanced Seismic Design and Analysis Practices

This section describes topics and provides recommendations considered particularly relevant to engineering practitioners, especially those who are interested in performance-based design of new reinforced masonry buildings or seismic retrofit of existing reinforced masonry buildings. The performance-based-design recommendations may not be practical for implementation by most practitioners and would likely require funded projects to fully develop the requisite methods.

Performance-Based Design Based on Pushover Strength. The archetype models, methods, and results of this study that better represent observed collapse performance may be of interest to practitioners for performance-based design of reinforced masonry buildings. The collapse analyses of

reinforced masonry building archetypes show a strong correlation between collapse performance and the strength of the archetype model, as determined by nonlinear (static) pushover analysis.

Additional study would be required to develop a complete performance-based design methodology for new buildings, or to augment the current performance-based methods of ASCE/SEI 41 for seismic retrofit of existing buildings.

Performance-Based-Design Criteria. The collapse results of baseline archetype models show strong trends of the combined influence of strength and displacement capacity on collapse performance. Such trends could be used to establish performance-based-design criteria for reinforced masonry buildings.

Additional study would be required to develop the relationship between the strength, displacement capacity, and collapse performance of reinforced masonry buildings considering differences in archetype configuration (e.g., multi-family dwellings), wall design (e.g., un-coupled flanged walls), and potential for uplift/rocking of foundations below tall walls, among other considerations.

Damage and Loss Estimation. The archetype models, methods, and results of this study that better represent observed collapse performance of reinforced masonry buildings may be of interest to practitioners developing estimates of earthquake damage and loss using, for example, the FEMA P-58 technology (FEMA, 2018), or other methods, such as those of the insurance industry. The probability of collapse is an important element of building damage and loss estimation and the improved models and methods of this study would provide a more reliable characterization of the earthquake collapse risk of reinforced masonry buildings.

Best-Practice Design Recommendations. The results of this study show that the following design considerations are relevant to MCE_R collapse performance.

- The building archetypes analyzed in this study, designed in accordance with TMS 402, resulted in good performance for both high-seismic and very high-seismic loads, achieving the target probability of collapse of 10 percent or less.
- Although collapse performance was good, behavior was not always consistent with code intent: shear-dominated behavior was common and damage was significant. Designers with performance objectives

requiring limited, repairable damage should consider additional measures to encourage flexure-dominate behavior.

- Shear Wall Design. The models in this study showed that significant nonlinear behavior was concentrated in the first story. It may therefore be appropriate to increase attention to the ductility of elements at the base of cantilever walls and perhaps relax requirements for upper levels with appropriate capacity-based design principals.
- Drift Capacity of the Gravity System Connections. Because this study showed that story drifts may be larger than expected, steel beam-column connections of the gravity system should have special detailing to avoid premature failure during large lateral displacements of reinforced masonry buildings (i.e., story drift ratios of up to 10 percent). Such detailing should include a minimum gap between the beam flange and column to avoid prying action on these connections.
- Minimum reinforcement requirements or architecturally stipulated wall configurations may result in unintended overstrength of reinforced masonry shear walls; as a result, foundations may uplift before walls can yield. In this case, foundations may require special design and detailing to accommodate rocking response of the walls above.
- Designers should understand the limitations of simplified analysis methods to represent complex behavior. For example, horizontal diaphragms may need to be modeled as both flexible and stiff to envelope the forces delivered to walls.

Best-Practice Analysis Recommendations. The results of this study show that where nonlinear models are used to evaluate the collapse potential of reinforced masonry buildings, to reliably calculate the behavior of structures and the probability of collapse, they should:

- incorporate 3D flange-web interaction (e.g., coupling of shear walls and floor slabs and beams),
- incorporate realistic collapse displacement capacity of the seismic-force-resisting system (i.e., backbone curves of ASCE/SEI 41 are too conservative), and
- explicitly model P-delta effects.

6.3.4 Recommendations for Enhanced Modeling and Testing

This section describes topics and provides recommendations considered particularly relevant to engineers and academics interested in research of reinforced masonry buildings. In this context, modeling recommendations

include the use of sophisticated nonlinear finite-element models, as well as simplified models, such as those described in Chapter 4 of this report, and testing recommendations include new experimental data that should be acquired through quasi-static and shake-table tests to fill the current knowledge gap and to further validate numerical models that can be used in research and practice.

6.3.4.1 Recommendations for Modeling

For performance-based design of reinforced masonry buildings, the ability to assess the damage states of a building subjected to different seismic-intensity levels and its vulnerability to collapse under an extreme seismic event is of critical importance. However, the analysis methods commonly used to study the behavior of and to design reinforced masonry buildings suffer from a number of shortcomings:

- Structural models used in design are often overly simplified, such as ignoring the coupling forces from horizontal diaphragms. This could result in modeled building behavior that is different from actual performance in an earthquake. For example, such models may predict wall behavior dominated by flexure, but diagonal shear may be the actual failure mechanism when the coupling forces come into play, as demonstrated by the behavior of the building archetypes considered in this study. Therefore, overly simplified models will not provide a reliable assessment of the strength and displacement capacity of a building, or good guidance for design.
- In spite of the shear-capacity design provisions in TMS 402, special reinforced masonry wall systems could still develop shear-dominated behavior when the shear-span ratios of the wall components are low. This could happen in buildings that have relatively strong horizontal diaphragms, perforated walls, or both. There is a lack of simple numerical tools to assess the seismic response of shear-dominated wall systems in a reliable manner.
- Phenomenological hysteretic models are sometimes used to predict the response of reinforced masonry wall systems dominated by shear. They are often calibrated with quasi-static test data obtained from planar wall specimens, ignoring wall flanges and other structural elements that are frequently present in a real building. Both the experimental data and refined finite-element analyses presented in Chapter 4 show that the displacement capacity of a reinforced masonry building with shear-dominated flanged walls can be far higher than that exhibited in planar wall-panel tests.

- In a seismic event, buildings are subjected to multi-axial ground motions. This study found that the response of a reinforced masonry flanged wall system subjected to bi-axial horizontal ground motions can be different from that developed in a uni-axial pushover analysis. Bi-axial earthquake ground motions will induce a more rapid post-peak load degradation. Hence, pushover analyses or cyclic analyses with uni-axial loading, as permitted by ASCE/SEI 41, may not adequately capture the behavior of a flanged-wall system under real earthquake conditions.

The following recommendations are provided to improve modeling methods.

Refined Finite-Element Modeling. Currently, refined finite-element modeling methods provide the most reliable and accurate means to evaluate and understand the seismic performance of reinforced masonry buildings up to large drift levels. These numerical models are able to capture both the flexure- and shear-dominated behaviors of walls. They are not only applicable to modeling reinforced masonry but also reinforced concrete shear wall systems. To capture detailed failure mechanisms and thereby the global behavior in a realistic manner, numerical models should account for masonry cracking and crushing, reinforcing bar buckling and fracture, and the bond slip and dowel action of the reinforcing bars. These mechanisms are responsible for the load degradation in the walls, as well as the residual strength when severe damage has developed.

For response-history analyses of building systems to be performed efficiently, simplifications are necessary, even for refined numerical models. To this end, masonry walls can be modeled with smeared-crack shell elements to simulate the cracking and crushing of masonry. However, these elements need to be supplemented with cohesive-crack interface elements to avoid stress-locking in smeared-crack elements, as explained in Chapter 4. This is especially important for modeling the behavior of diagonal shear cracks. The modeling of bond slip is important for capturing the behavior of reinforcing bars crossing discrete cracks and reducing the sensitivity of numerical results to the size of the shell elements to which the bar elements are connected. The dowel action of vertical reinforcing bars contributes to the lateral strength of a wall after the diagonal cracks have opened or horizontal cracks have developed. This resistance, even though small, may contribute a significant portion of the residual strength of a wall as the story drift increases. For computational efficiency, both the bond-slip behavior and dowel action can be modeled with double-node interface line elements using phenomenological interface laws. Normally, the modeling of the dowel action and the failure behavior of masonry requires different length scales. A relatively fine mesh is required for the bar elements and dowel-

interface elements. In this study, a special interface formulation (Kottari et al., 2017), as discussed in Chapter 4, was used for the bond-slip/dowel-action elements, which could be connected to larger shell elements.

To model the behavior of a wall system at incipient collapse, the inclusion of geometric nonlinearity is crucial. This will account for the P-delta effect, as well as the diagonal tension developed by the vertical reinforcing bars when the walls undergo large lateral drifts. Finally, for the numerical modeling scheme recommended here, the removal of elements that have lost their strength through crushing, cracking, or bar fracture is an important and necessary feature. This will not only enhance the robustness of the numerical computation, but also remove undesired restraints that could otherwise be introduced by the skeletons of the elements or the adjacent elements.

All the aforementioned features recommended for refined finite-element modeling have been implemented in LS-DYNA to carry out the analytical studies of reinforced masonry buildings. Only walls in the critical story (or stories) that develop the diagonal shear mechanism need to be modeled in detail, and the rest can be modeled with smeared-crack shell elements with smeared reinforcement alone. These modeling details can be found in Chapter 4. When other software is used, it is likely that only some of these modeling capabilities are available, and therefore, alternative but comparable modeling schemes must be developed to account for the failure mechanisms discussed above. Because of the large number of material parameters that need to be calibrated for nonlinear material models and the numerical artifacts, such as the strain localization and mesh-size sensitivity phenomena, which are inevitable in any computational model, a new model needs to be carefully calibrated with wall component tests and fully validated with experimental data including wall system tests.

Simplified Phenomenological Models. For incremental dynamic analysis (IDA), computationally efficient simplified numerical models must be employed. Refined finite-element models demand significant computational resources, and also require significant effort to develop and calibrate. Hence, they are not suitable for engineering practice. For simplification, a masonry wall system can be represented by a frame model, as was done in this study. Beam-column elements based on fiber-section idealization can simulate the flexural behavior of a reinforced masonry wall relatively well. However, to capture the load degradation of a flexure-dominated wall associated with the buckling and fracture of reinforcing bars, a suitable constitutive model that can indirectly account for these phenomena has to be used to represent the behavior of the bars (NIST, 2017), as discussed in Chapter 4. As to the modeling of the shear-dominated behavior of a masonry (or concrete) wall,

no reliable beam-column element is available. Most of the models for modeling shear are based on phenomenological hysteretic laws that do not provide any predictive capability or the ability to vary the shear strength as the axial load varies in an analysis.

When shear-dominated wall behavior is likely, any simplified model for a reinforced masonry building to be used for IDA or performance assessment has to be calibrated with a refined finite-element model of the entire building to capture the system effect, as well as the effect of bi-axial earthquake ground motions. The simplified model cannot be calibrated with quasi-static wall test data alone, which may not reflect the effects of the wall flange, wall loading condition in the structural system, or the history or direction of an earthquake ground motion. For calibration with a refined model, the use of three sets of bi-axial ground motion records that have distinct spectral and acceleration-history profiles is considered as the minimum. As was done in this study, two of the record sets are to be used to directly calibrate the model, and the third is to validate the calibration. If the validation is not satisfactory, then the whole process should be repeated to improve the calibration.

In the calibration process, response data on individual walls in the critical story (or stories) have to be extracted from the refined finite-element model. The basic data should include the shear force-vs.-story drift hysteresis curves, as well as the moment at the base of each wall. Because such data do not distinguish flexure response from shear response, and the response of a masonry wall can be a combination of both, calibration is a complicated process if the hysteresis model for shear is to be calibrated separately. For this reason, as discussed in Chapter 4, the two mechanisms were not distinguished in the simplified model adopted in this study. A rigid bar with a rotational spring at each end was used to represent the entire behavior of a wall, and the hysteresis curves of the springs were calibrated to match the story shear-vs.-story drift response curves, as well as the maximum moment developed at the wall base.

Areas for Future Improvement. The following is a list of specific areas for future improvement of numerical modeling of reinforced masonry.

- Even though the refined finite-element modeling scheme presented in Chapter 4 has been extensively verified, the numerical models have many material parameters to calibrate. It would be desirable to perform a systematic numerical parametric study to evaluate the sensitivity of the results to the modeling assumptions and material parameters to provide

insight into simplifying the modeling scheme and improving computational efficiency.

- The refined models developed for the building archetypes did not account for the nonlinear behavior and possible failure of the wall-to-horizontal diaphragm connections, which could affect the behavior of a wall system. The nonlinear behavior of wall-to-diaphragm connections should be examined in future studies. In such studies, different wall-to-diaphragm connection details should be considered and their impact on wall behavior investigated.
- Efforts should be devoted to the development of physics-based, computationally efficient beam-column elements to capture both the shear and flexural behaviors of reinforced masonry flanged walls subjected to large bi-axial drift levels. Such models should have the ability to capture the load degradation associated with the buckling and fracture of reinforcing bars, and the variation of the shear resistance with the axial load, as well as the influence of wall flanges and bi-axial loading on displacement capacity.
- The computational efficiency and accuracy of other simplified modeling approaches discussed in Chapter 4, such as truss models (Moharrami et al., 2015), should also be investigated.

6.3.4.2 Recommendations for Experimental Studies

Current assessment methodologies and tools for performance-based engineering, such as FEMA P-58 and ASCE/SEI 41, have relied on fragility data and pushover curves derived from quasi-static component tests. Numerical results from refined finite-element models and the shake-table test data used to validate these models, as presented in Chapter 4, show that these methodologies are overly conservative for the performance assessment of reinforced masonry buildings, especially with respect to the assessment of collapse probability. This can be largely attributed to the fact that the database was essentially based on planar wall tests without consideration of the flange effect.

Quasi-Static Tests of Flanged Walls. Since flanged walls are common in reinforced masonry buildings, and they can develop shear-dominated behavior in extreme earthquake events, more experimental data on such walls are needed. There is limited quasi-static test data available on reinforced masonry flanged walls with shear-dominated web behavior. Uni-axial and bi-axial (two horizontal directions) quasi-static tests would yield valuable data to help understand the shear behavior of these walls and for the calibration of numerical models.

Cyclic-Load Testing Protocol. For testing reinforced masonry shear walls with quasi-static loading, there is no standard loading protocol available. It has been generally recognized that the loading protocol developed in the Technical Coordinating Committee on Masonry Research (TCCMAR) program (Porter, 1987) for testing reinforced masonry shear walls can be overly demanding in terms of the number of gradually incremented loading and unloading cycles, compared to what would actually occur in a wall in a real seismic event. Commonly used loading protocols are typically defined in terms of displacement ductility levels, where displacement ductility is defined as the theoretically calculated lateral strength of the specimen divided by the yield displacement of an equivalent elastic-perfectly plastic system. The wall specimen is subject to two or three fully reversed displacement cycles at each ductility level until a significant load degradation is observed. However, these loading protocols tend to over-test the wall specimen. Hence, a study should be undertaken to review and update existing cyclic-load testing protocols to better reflect real earthquake loading conditions, considering potential differences in the frequency content and duration of earthquake ground motions and the benefits of defining the testing protocol in terms of displacement rather than displacement ductility. Furthermore, a bi-axial loading protocol should be developed for testing flanged walls. For this purpose, the first-floor response time histories of the archetype models archived in this project could be mined, and some high-intensity runs should be selected. It is also recommended that both the loading protocol and the testing apparatus be designed for testing wall specimens to a point of severe loading degradation in a safe manner to provide complete data to calibrate numerical models for collapse simulations.

Shake-Table Testing. Testing building systems to the verge of collapse on a shake table provides invaluable data to calibrate and validate numerical models. Such tests have been performed on reinforced masonry wall systems with uni-axial ground motions (Cheng et al, 2020). As mentioned previously, the refined finite-element analyses performed in this study have shown the important effect of bi-axial earthquake ground motions, which can induce more severe and rapid load degradation in building archetypes compared to uni-axial ground motion or pushover analysis. Currently, there are no experimental data available to confirm this observation or validate numerical models. Hence, it is recommended that bi-axial shake-table tests be performed to provide such data.

Appendix A
Archetype Design Criteria and Details

A.1 Introduction

Appendix A documents the material design criteria and structural design details for each of the archetypes in this study. Section A2 documents the design criteria for all the archetypes, and Section A3 through Section A5 show the designs for each archetype in plans, elevations, and details.

A.2 Design Criteria

A.2.1 Codes

Designs for the reinforced masonry building archetypes were based on design requirements of TMS 402-13 and construction specifications of TMS 602-13.

Design loads were based on design requirements of the 2015 IBC and, by reference, ASCE/SEI 7-10

A.2.2 Materials

Material properties are summarized in Table A-1.

Table A-1 Material Properties used for Design of Reinforced Masonry Building Archetypes

Material	Properties
Hollow Concrete Masonry Units	f'_m = 2,000 psi—ASTM C652 f'_m = 2,500 psi (COM 9 only)
Unit Sizes	8 in x 8 in x 16 in nominal (minimum), 12 in x 8 in x 16 in nominal (COM9 only)
Bond Pattern	Running Bond
Grout	Average Compressive Strength = 2000 psi—ASTM C476
Mortar	Type S Average Compressive Strength = 2000 psi—ASTM C270
Steel Reinforcing	F_y = 60 ksi—ASTM A615
Concrete	f'_c = 4.0 ksi—ASTM C150

A.2.3 Site-Specific Design Criteria

Soil properties were assumed to represent typical West Coast sites. The assumed site-specific soil properties are summarized in Table A-2. For the soil-structure interaction (SSI) and foundation flexibility parametric study only, a soft soil profile was assumed, with a lower bearing pressure. Both stiff and soft soil sites were characterized as Site Class D.

Table A-2 Site-Specific Design Criteria used for Design of Reinforced Masonry Building Archetypes

Material	Properties
Assumed Site Class	D
Allowable Soil Bearing Pressure (stiff soil)	3000 psf
Allowable Soil Bearing Pressure (soft soil)	1500 psf
Modulus of subgrade reaction (stiff soil)	129 kip / cu ft
Modulus of subgrade reaction (soft soil)	60 kip / cu ft
Minimum Footing Depth	12 in

A.2.4 Gravity Loads

Archetype design dead and live loads are summarized in Table A-3. The weight of all walls, except those of the exterior, was averaged across the floor plate, and a portion was assigned to the roof for the determination of seismic loads. The interior wall dead load used was 15 pounds per square foot (psf) distributed uniformly over each story.

Table A-3 Gravity Loads used for Design of Reinforced Masonry Building Archetypes

Building Type	Floor live load (psf)	Floor Dead Load (includes partitions) (psf)	Roof Dead Load (psf)	Exterior Wall Dead Load (psf)
COM	50	80	20	20
RES	40	100	90	10
BOX	100	n/a	20	34

A.2.5 Design Periods of Vibration

ASCE/SEI 7-10 allows several methods for calculating the period for masonry shear wall structures. The value of T_a calculated using ASCE/SEI 7 Equation 12.8-7 is used commonly in practice, whereas FEMA P-695 studies use $T = C_u T_a$ for design. The archetypes were designed using T_a, but, because the periods all fall in or very near the constant acceleration region of the design spectra, $T < T_s$, the design was unaffected by this choice. Table A-4 presents both periods of vibration for all archetypes.

Table A-4 Design Periods of Vibration for Reinforced Masonry Archetypes

Base Archetype ID	No. of Stories	SDC	C_t	h_n	C_u	T_a [(1)]	$T=C_uT_a$ [(2)]	T_s [(3)]
Commercial Buildings								
COM1	1	D	0.02	12	1.4	0.13	0.25	0.6
COM2	2	D	0.02	24	1.4	0.22	0.30	0.6
COM3	4	D	0.02	48	1.4	0.37	0.51	0.6
COM4	1	E	0.02	12	1.4	0.13	0.25	0.6
COM5	2	E	0.02	24	1.4	0.22	0.30	0.6
COM6	4	E	0.02	48	1.4	0.37	0.51	0.6
COM7	1	C	0.02	12	1.5	0.13	0.25	0.4
COM8	2	C	0.02	24	1.5	0.22	0.33	0.4
COM9	4	C	0.02	48	1.5	0.37	0.55	0.4
Residential Buildings								
RES1	4	D	0.02	48	1.4	0.37	0.51	0.6
RES2	4	E	0.02	48	1.4	0.37	0.51	0.6
RES3	4	C	0.02	48	1.5	0.37	0.55	0.4
Retail Buildings								
BOX1	1	D	0.02	24	1.4	0.22	0.30	0.6
BOX2	1	E	0.02	24	1.4	0.22	0.30	0.6
BOX3	1	C	0.02	24	1.5	0.22	0.33	0.4

(1) $T_a = C_t h_n^x$ ASCE/SEI 7-10, Section 12.8.2.1, Equation 12.8-7

(2) $T = C_u T_a \geq 0.25$ FEMA P-695, Equation 5-5

(3) $T_s = S_{D1} / S_{DS}$ ASCE/SEI 7-10, Section 11.4.5 upper boundary of plateau region of design response spectrum

A.2.6 Seismic Design Criteria

Archetype designs were developed for three different seismic criteria summarized in Table A-5. The mapped MCE_R spectral response acceleration at a period of 1 second (S_1), the short-period site coefficient (F_a), the short-period design spectral response acceleration (S_{DS}), and the other listed parameters, all previously defined, were calculated in accordance with ASCE/SEI 7-10 requirements for the equivalent-lateral-force (ELF) method. All designs were based on Risk Category II and $R = 5$ for Special Reinforced Masonry Shear Walls.

Table A-5 Seismic Criteria used for Design of Reinforced Masonry Archetypes

Building Type	Seismic Design Category (SDC)	MCE_R Ground Motions				Design Criteria	
		S_1 (g)	S_S (g)	F_a	S_{MS} (g)	S_{DS} (g)	C_s
COM, RES and BOX	E	0.90	2.25	1.0	2.25	1.5	0.30
	D	0.60	1.50	1.0	1.50	1.0	0.20
	C	0.13	0.55	1.36	0.75	0.5	0.10

A.2.7 Archetype Configurations

Key configuration and design criteria for the reinforced masonry building archetypes are summarized in Table A-6.

Table A-6 Summary of Short-Period Reinforced Masonry Building and Key Configuration and Design Criteria

Base Archetype ID	No. of Stories	Seismic Design Criteria			
		SDC	S_{MS} (g)	T^* (sec)	C_s (g)
Commercial Buildings: High Seismic					
COM1	1	D	1.5	0.25	0.20
COM2	2	D	1.5	0.30	0.20
COM3	4	D	1.5	0.51	0.20
Commercial Buildings: Very High Seismic					
COM4	1	E	2.25	0.25	0.30
COM5	2	E	2.25	0.30	0.30
COM6	4	E	2.25	0.51	0.30
Commercial Buildings: Moderate Seismic					
COM7	1	C	0.75	0.25	0.10
COM8	2	C	0.75	0.33	0.10
COM9	4	C	0.75	0.55	0.10
Residential Buildings: High Seismic					
RES1	4	D	1.5	0.51	0.20
Residential Buildings: Very High Seismic					
RES2	4	E	2.25	0.51	0.30
Residential Buildings: Moderate Seismic					
RES3	4	C	0.75	0.55	0.10
Box Retail Buildings: High Seismic					
BOX1	1	D	1.5	0.30	0.20
Box Retail Buildings: Very High Seismic					
BOX2	1	E	2.25	0.30	0.30
Box Retail Buildings: Moderate Seismic					
BOX3	1	C	0.75	0.33	0.10

* $T = C_u T_a \geq 0.25$ seconds, in accordance with the analysis requirements of FEMA P-695, where the values of the parameters C_u and T_a are specified by ASCE/SEI 7-10. However, as is described in Section A.2.5, the archetypes were designed using T_a.

A.3 Commercial Buildings (COM)

A.3.1 Structural Plans: Commercial Buildings

In the following sections, the structural designs for each of the commercial archetypes are documented, including plans, elevations, and details. The floor and roof framing are identical for all COM archetypes and are shown only once for the COM2 archetypes. The foundation designs are unique, but similar, and are indicated on a single plan (Figure A-3). Masonry reinforcement for all unique conditions are shown in wall elevation views. The structural designs for the baseline archetypes (e.g., COM2B) were identical to the designs for the variant archetypes (e.g., COM2B-DC), with the one exception being the foundation design for the COM2 archetype on a soft soil site for the SSI and foundation flexibility parametric study. Hence, plans, elevations, and details labeled with COMX should be assumed to apply to all variants, unless otherwise noted.

Selected design results for the individual walls of the high-seismic and very high-seismic commercial archetypes are tabulated in Table A-7. Design results for the moderate seismic archetypes are not provided because these archetypes were not ultimately included in the study. These results include:

- demand-to-capacity ratios (D/C) for strength,
- governing response (flexure or shear),
- comments indicating triggers for relevant code provisions in TMS 402,
- vertical and horizontal reinforcement, and
- the calculated drift ratio divided by the maximum allowed drift ratio.

The following definitions apply in Table A-7:

"D/C"	Demand-to-capacity ratio. In this context, the "demand" is the code-specified seismic load effect according to the equivalent-lateral-force procedure in ASCE/SEI 7, and the "capacity" is the governing limit state calculated in accordance with the ultimate-strength provisions of TMS 402.
"EW Straight Wall"	Refers to the straight walls oriented to carry shear in the East-West direction, centered on the North and South elevations.
"EW Flanged Wall"	Refers to the corner flanged wall, specifically the portion that is oriented to carry shear in the East-West

direction, and which appears on the North and South elevations.

"NS Flanged Wall" Refers to the corner flanged wall, specifically the portion that is oriented to carry shear in the North-South direction, and which appears in the East and West elevations.

Table A-7 Design Results for COM1, COM2, and COM3 Archetypes

Wall	D/C[1]	Criteria[2]	Comment	Reinforcement		Drift Ratio/ Max Drift Ratio
COM1: One Story, High Seismic (8" CMU, f'_m = 2000 psi)						
EW Straight Wall	0.34	Flexure	$V_n \geq 2.5V_u$[3]	Vertical: Horizontal:	#4 @32" #5 @ 32"	< 0.1
EW Flanged Wall	0.28	Flexure	$V_n \geq 2.5V_u$[3]	Vertical: Horizontal:	#4 @32" #5 @ 32"	
NS Flanged Wall	0.14	Flexure	$V_n \geq 2.5V_u$[3]	Vertical: Horizontal:	#5 @ 48" #5 @ 32"	
COM2: Two Story, High Seismic (8" CMU, f'_m = 2000 psi)						
EW Straight Wall	0.67	Flexure	$V_n \geq 2.5V_u$[3]	Vertical: Horizontal:	#5 @ 24" #5 @ 32"	0.16
EW Flanged Wall	0.69	Flexure	$V_n \geq 2.5V_u$[3]	Vertical: Horizontal:	#5 @ 24" #5 @ 32"	
NS Flanged Wall	0.71	Flexure	$V_n \geq 2.5V_u$[3]	Vertical: Horizontal:	#5 @ 32" #5 @ 32"	
COM3: Four Story, High Seismic (8" CMU, f'_m = 2000 psi)						
EW Straight Wall Base	1.02[5]	Flexure	$\rho/\rho_{max}=1.0$[4]	Vertical: Horizontal:	#6 @ 16" #4 @ 24"	0.71
EW Straight Wall Level 3	0.63	Flexure	-	Vertical: Horizontal:	#6 @ 32" #4 @ 24"	
EW Flanged Wall Base	1.02[5]	Flexure	$\rho/\rho_{max}=1.34$[4]	Vertical: Horizontal:	#5 @ 16" #4 @ 24"	
EW Flanged Wall Level 3	0.67	Flexure	-	Vertical: Horizontal:	#5 @ 32" #4 @ 24"	
NS Flanged Wall Base	0.97	Flexure	-	Vertical: Horizontal:	#5 @ 16" #4 @ 24"	
NS Flanged Wall Level 3	0.75	Flexure	$\rho/\rho_{max}=1.04$[4]	Vertical: Horizontal:	#5 @ 32" #4 @ 24"	

[1] D/C = Demand/Capacity ratio.

[2] Criteria indicates if the maximum demand/capacity ratio (D/C) resulted from combined flexure (with compression) or shear.

[3] TMS 402 §7.3.22.6.1.1 states V_n need not exceed $2.5V_u$. When this provision is invoked, shear-dominated behavior may result.

[4] TMS 402 §9.3.6.5 was invoked to allow exceedance of ρ_{max} by meeting checks for confinement.

[5] D/C ratio near or slightly > 1 accepted. Load combination including E_v governs.

Table A-8 Design Results for COM4, COM5, and COM6 Archetypes

Wall	D/C[1]	Criteria[2]	Comment	Reinforcement		Drift Ratio/ Max Drift Ratio
COM4: One Story, Very High Seismic (8" CMU, f'_m = 2000 psi)						
EW Straight Wall	0.52	Flexure	$V_n \geq 2.5V_u$[3]	Vertical: Horizontal:	#4 @32" #5 @ 32"	< 0.01
EW Flanged Wall	0.44	Flexure	$V_n \geq 2.5V_u$[3]	Vertical: Horizontal:	#4 @32" #5 @ 32"	
NS Flanged Wall	0.32	Flexure	$V_n \geq 2.5V_u$[3]	Vertical: Horizontal:	#5 @ 48″ #5 @ 32"	
COM5: Two Story, Very High Seismic (8" CMU, f'_m = 2000 psi)						
EW Straight Wall	0.87	Flexure	-	Vertical: Horizontal:	#5@16" #5 @ 32"	0.25
EW Flanged Wall	0.84	Flexure	-	Vertical: Horizontal:	#5 @ 16" #5 @ 32"	
NS Flanged Wall	0.91	Shear	-	Vertical: Horizontal:	#5 @ 24″ #5 @ 32"	
COM6: Four Story, Very High Seismic (12" CMU, f'_m = 2500 psi)						
EW Straight Wall Base	0.87	Flexure	-	Vertical: Horizontal:	#8 @ 16" #5 @ 24"	0.89
EW Straight Wall Level 3	0.75	Flexure	-	Vertical: Horizontal:	#6 @ 32" #5 @ 24"	
EW Flanged Wall Base	0.59	Flexure	-	Vertical: Horizontal:	#5 @ 24" #6 @ 16"	
EW Flanged Wall Level 3	0.24	Flexure	-	Vertical: Horizontal:	#5 @ 24" #6 @ 16"	
NS Flanged Wall Base	0.99	Shear	-	Vertical: Horizontal:	(2) #9 @ 48" #6 @ 16"	
NS Flanged Wall Level 3	0.67	Shear	$V_n \geq 2.5V_u$[3]	Vertical: Horizontal:	#8 @ 48" #6 @ 16"	

[1] D/C = Demand/Capacity ratio.

[2] Criteria indicates if the maximum demand/capacity ratio (D/C) resulted from combined flexure (with compression) or shear.

[3] TMS 402 §7.3.22.6.1.1 states V_n need not exceed $2.5V_u$. When this provision is invoked, shear dominated behavior may result.

[4] TMS 402 §9.3.6.5 was invoked to allow exceedance of ρ_{max} by meeting checks for confinement.

[5] D/C ratio near or slightly > 1 accepted. Load combination including E_v governs.

A.3.1.1 Single-Story Commercial Building Plans (COM1, COM4, COM7)

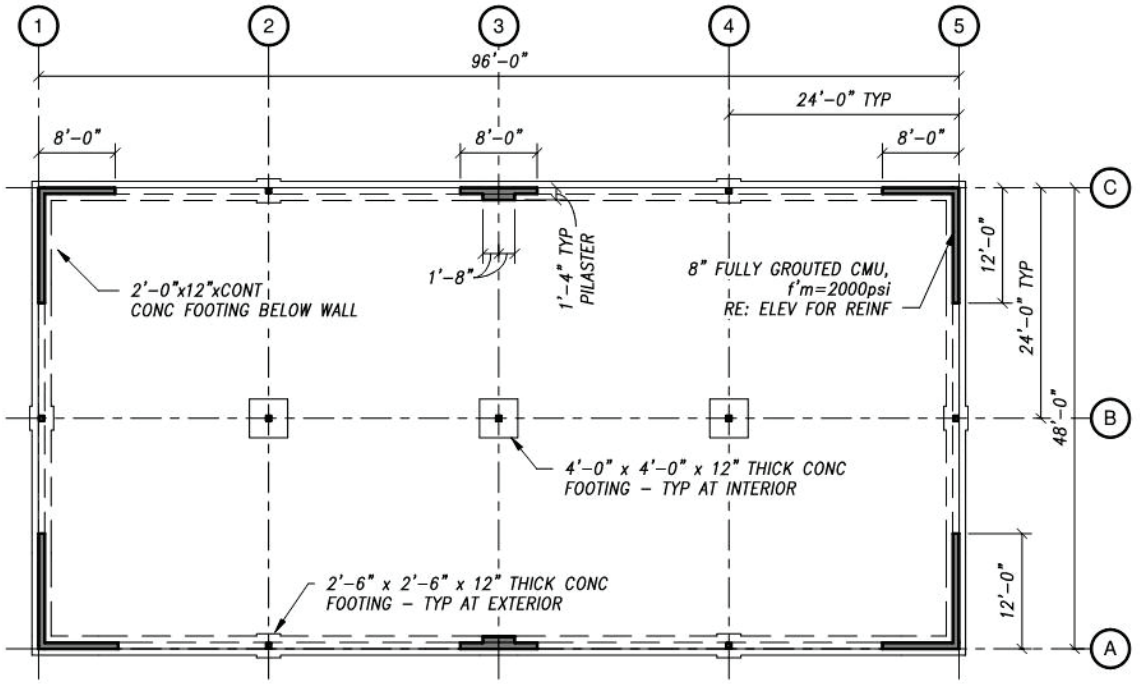

Figure A-1 Single-story commercial building foundation plan: COM1, COM4, COM7.

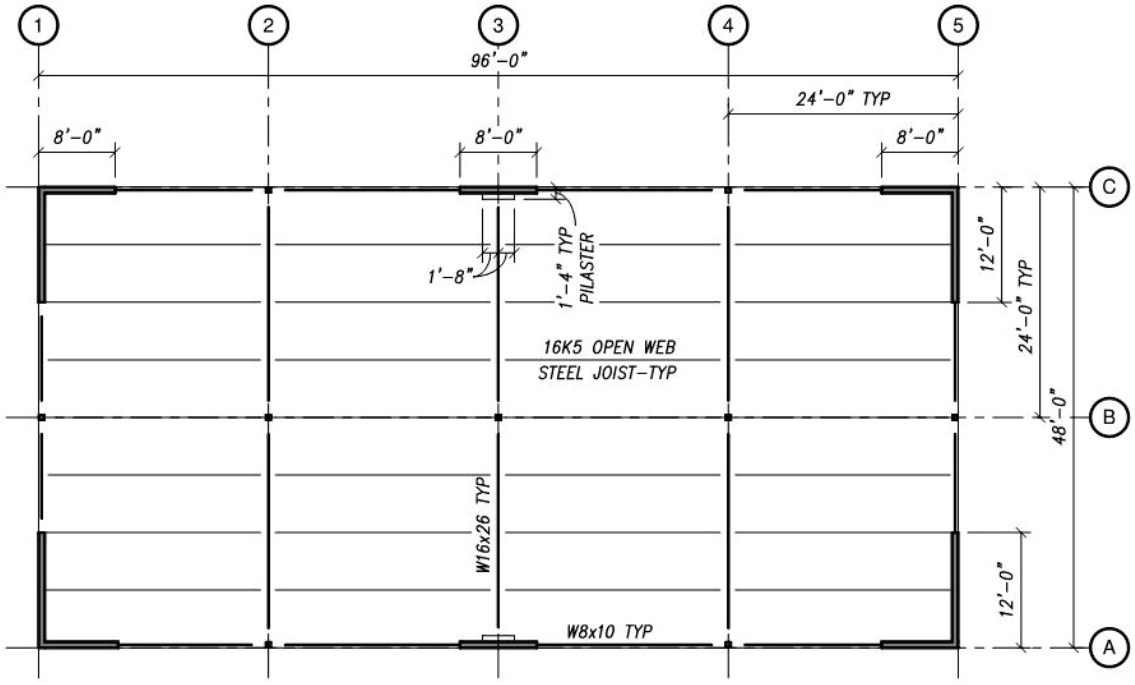

Figure A-2 Single-story commercial building roof framing plan: COM1, COM4, COM7.

A.3.1.2 Two-Story Commercial Building Plans (COM2, COM5, COM8)

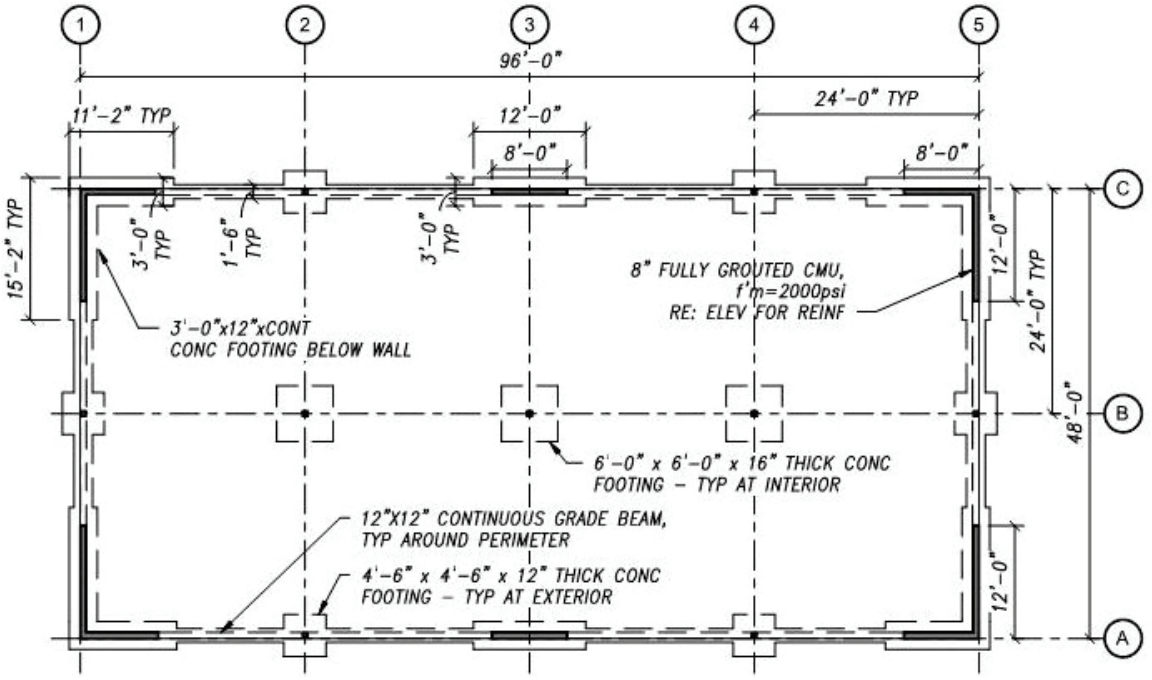

Figure A-3 Two-story commercial building foundation plan: COM2, COM5, COM8.

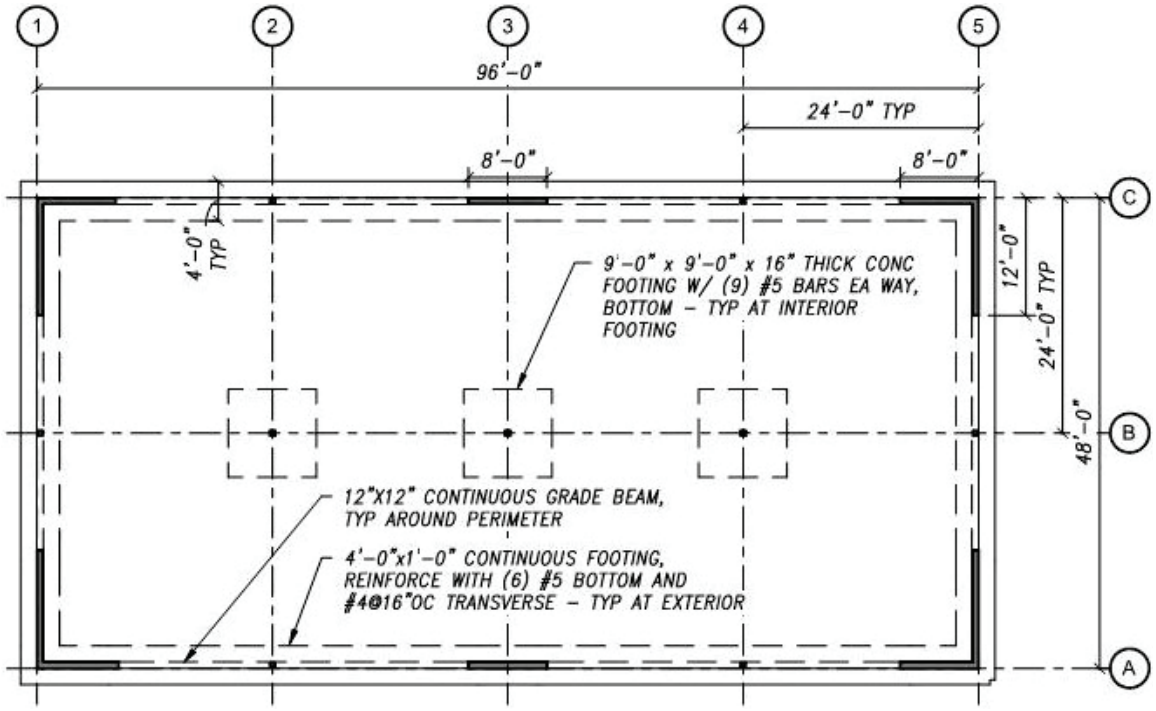

Figure A-4 Two-story commercial building foundation plan: COM2 archetype on soft soil.

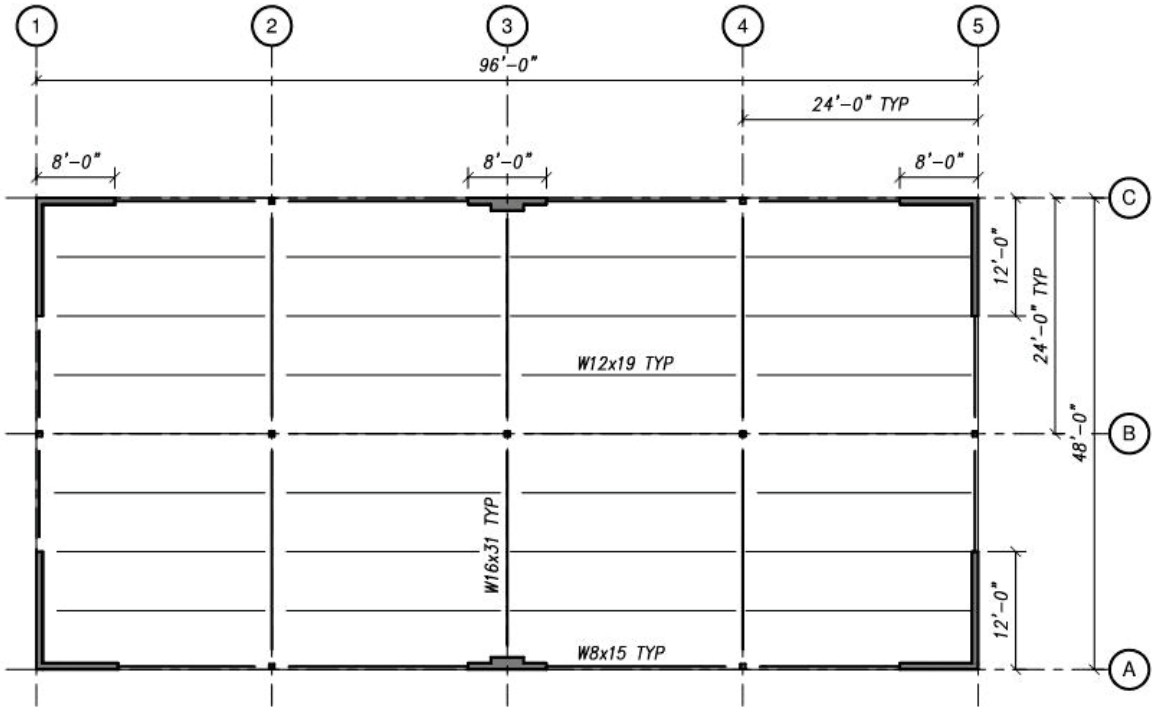

Figure A-5 Two-story commercial building typical framing plan: COM2, COM5, COM8.

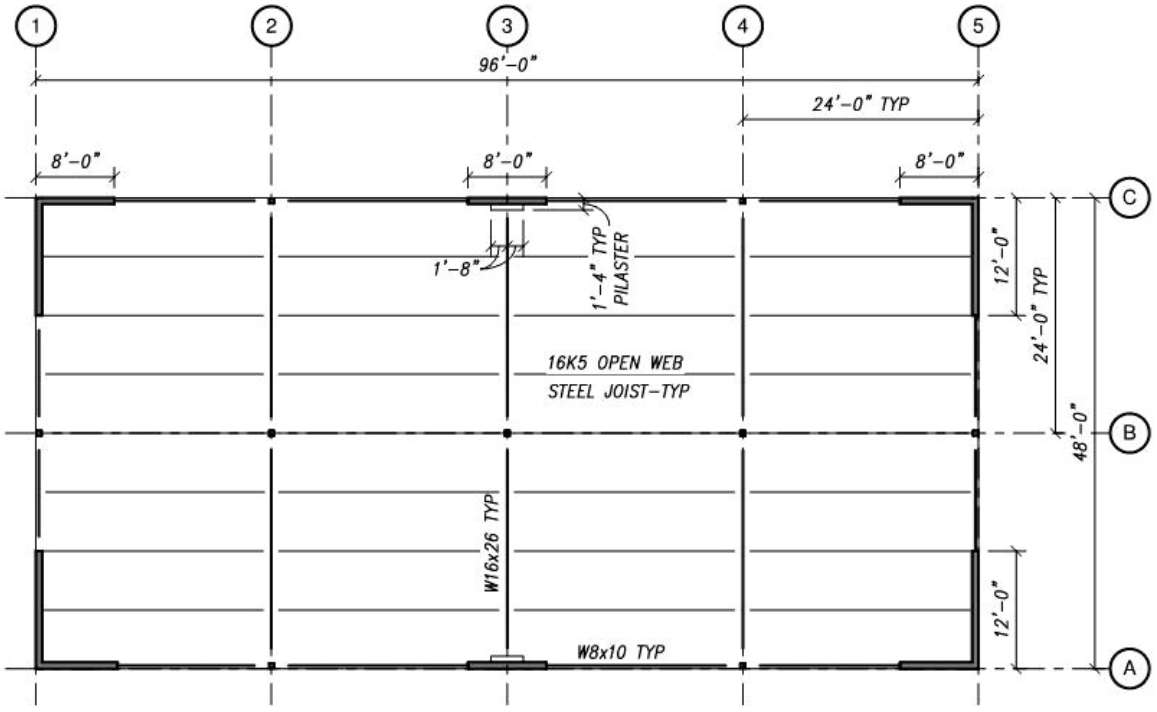

Figure A-6 Two-story commercial building roof framing plan: COM2, COM5, COM8.

A.3.1.3 Four-Story Commercial Building Plans (COM3)

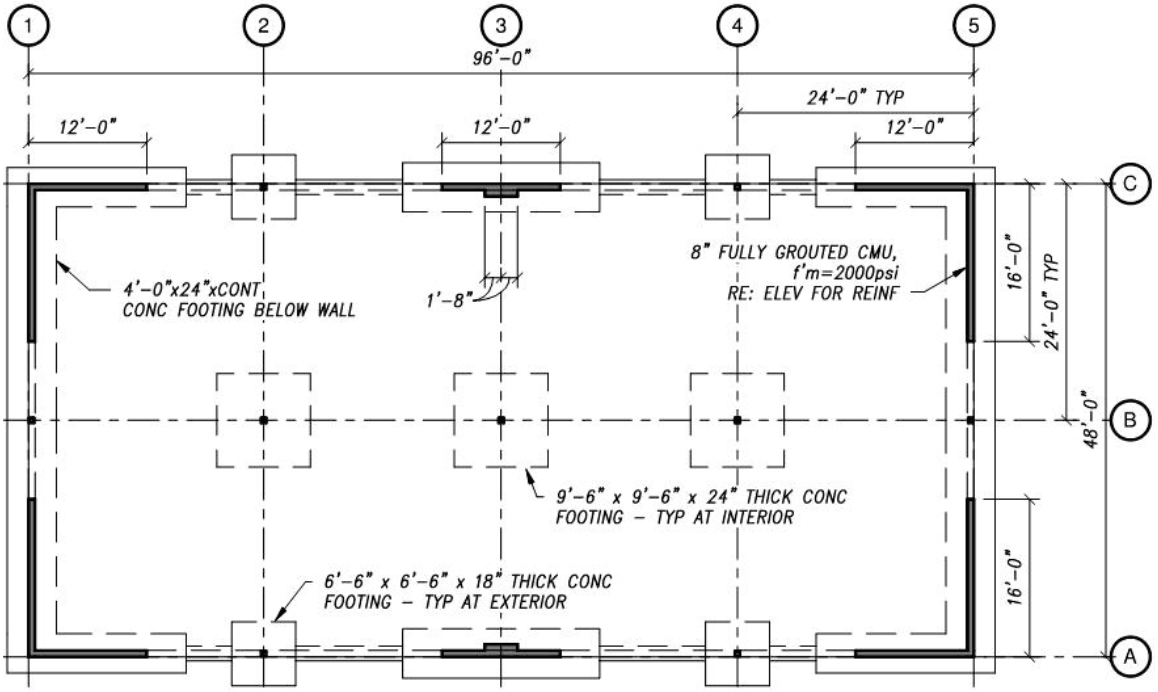

Figure A-7 Four-story commercial building foundation plan: COM3.

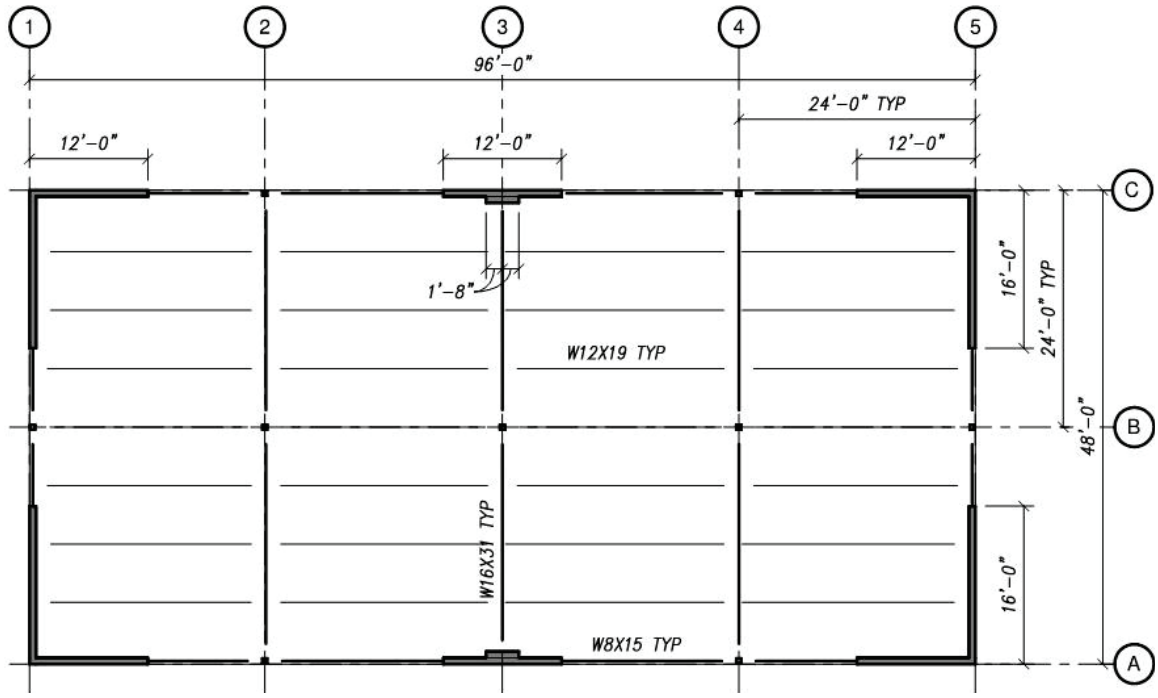

Figure A-8 Four-story commercial building typical framing plan: COM3.

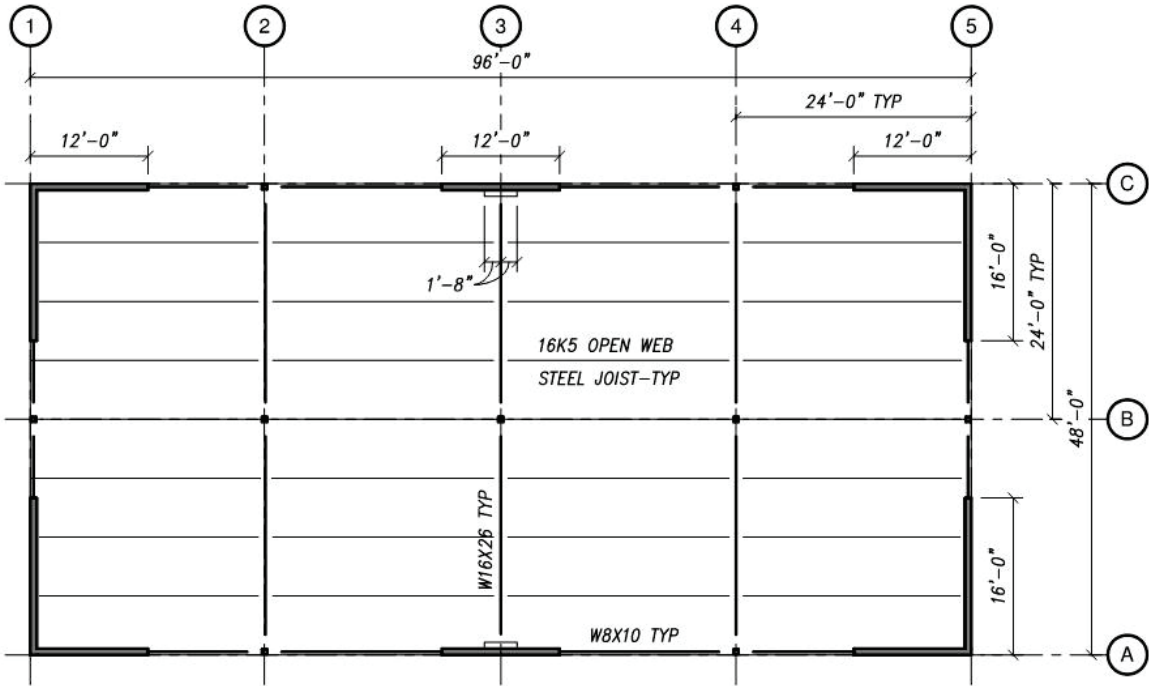

Figure A-9 Four-story commercial building roof framing plan: COM3.

A.3.1.4 Four-Story Commercial Building Plans (COM6)

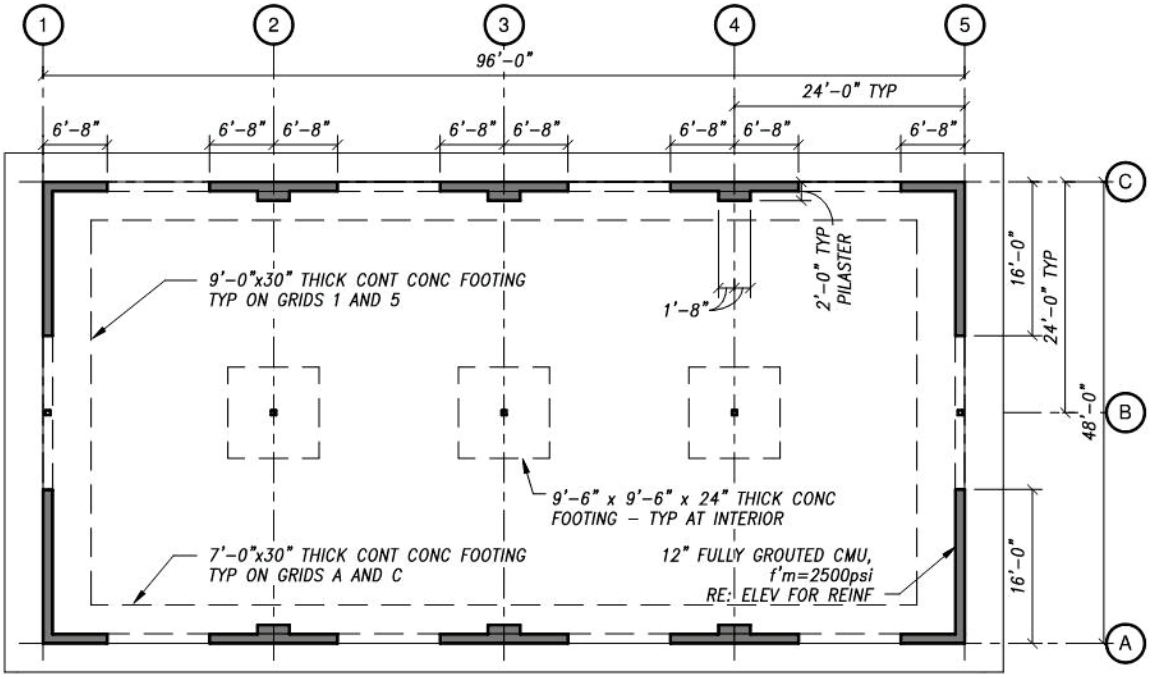

Figure A-10 Four-story commercial building foundation plan: COM6.

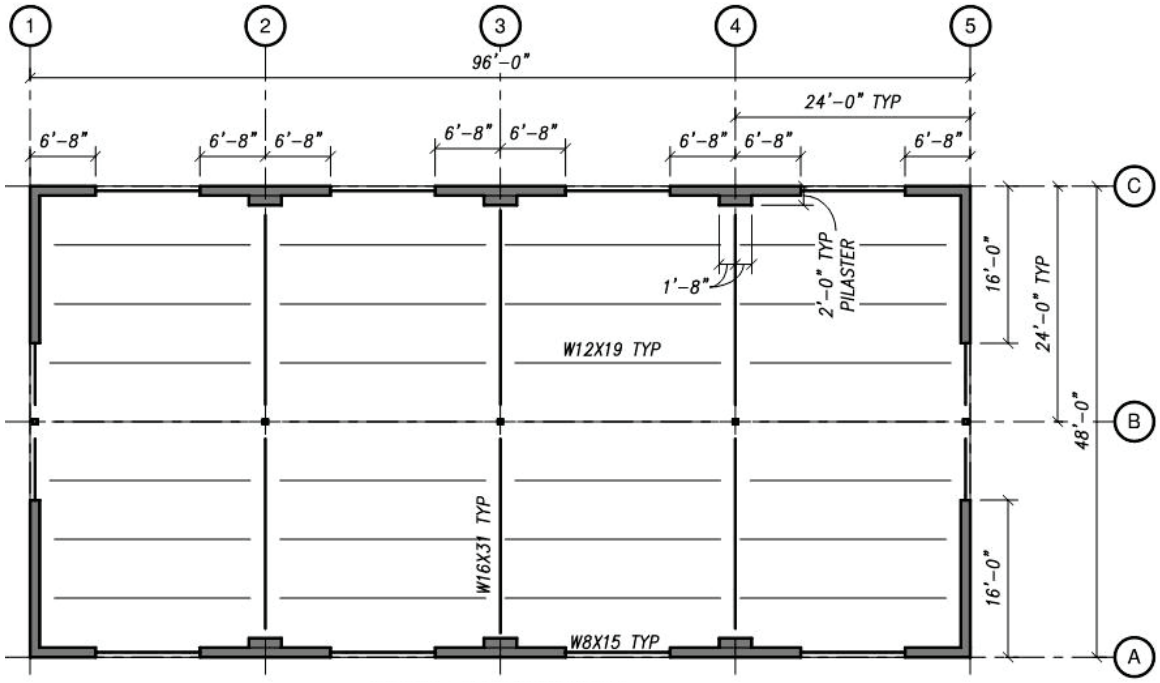

Figure A-11 Four-story commercial building typical framing plan: COM6.

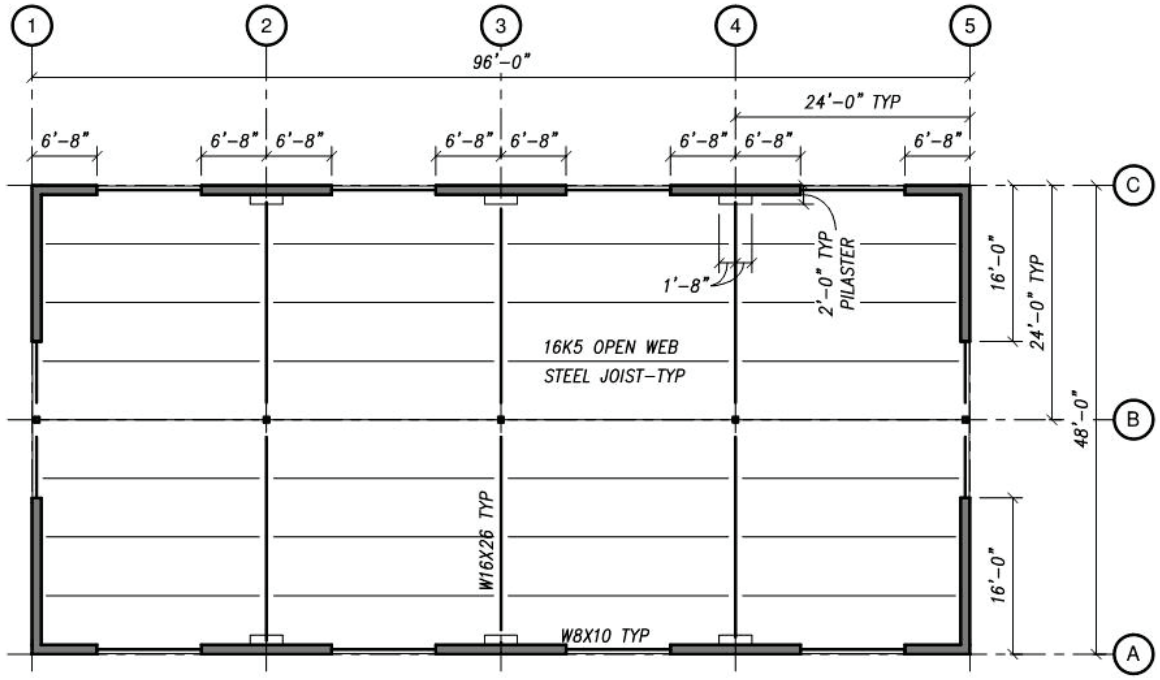

Figure A-12 Four-story commercial building roof framing plan: COM 6.

A.3.2 Structural Elevations: Commercial Buildings

A.3.2.1 Single-Story Commercial Building Elevations (COM1, COM4, COM7)

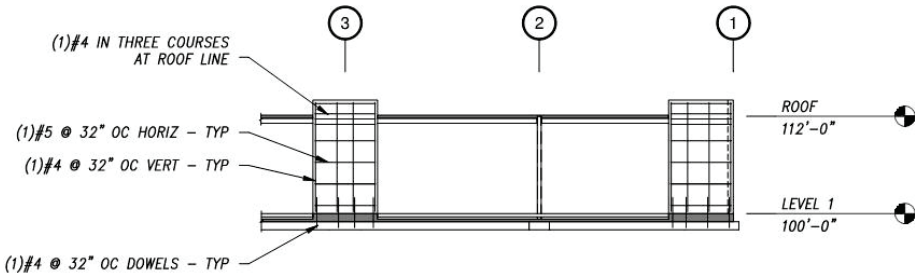

Figure A-13 Single-story commercial building North elevation: COM1, COM4, COM7.

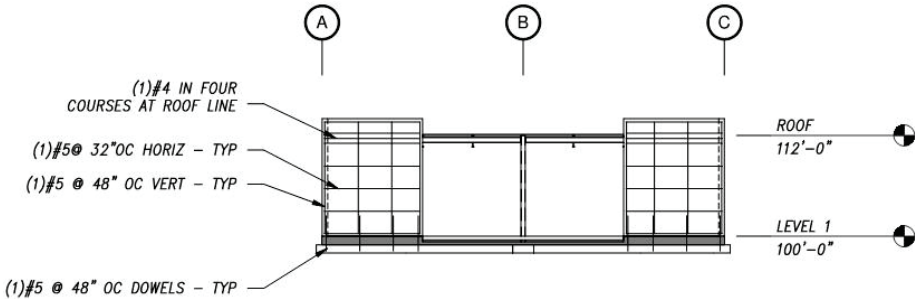

Figure A-14 Single-story commercial building East elevation: COM1, COM4, COM7.

A.3.2.2 Two-Story Commercial Building Elevations (COM2)

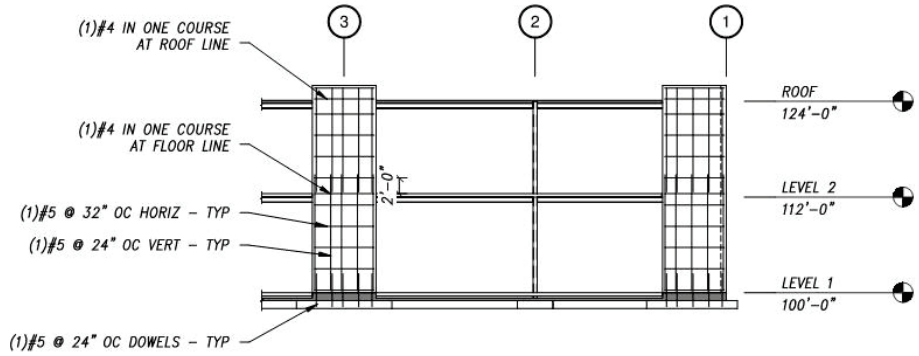

Figure A-15 Two-story commercial building North elevation: COM2.

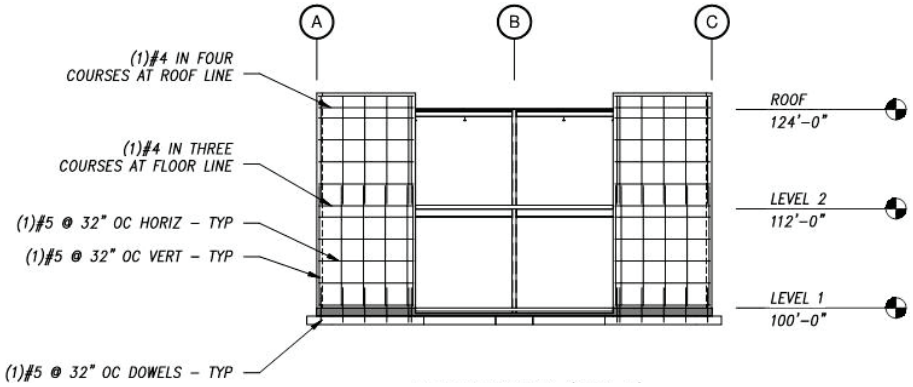

Figure A-16 Two-story commercial building East elevation: COM2.

A.3.2.3 Two-Story Commercial Building Elevations (COM5)

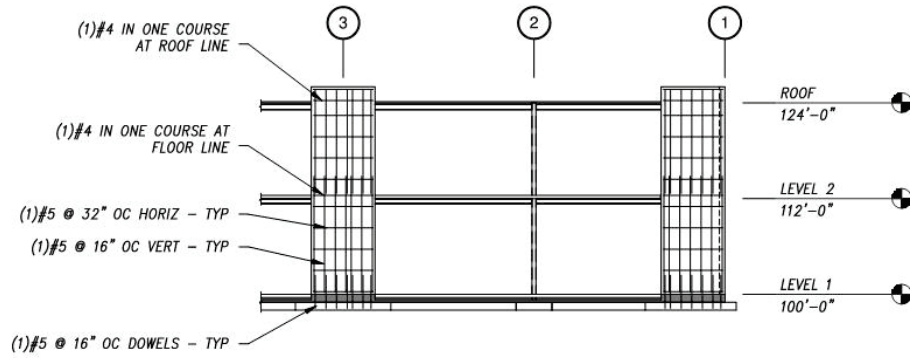

Figure A-17 Two-story commercial building North elevation: COM5.

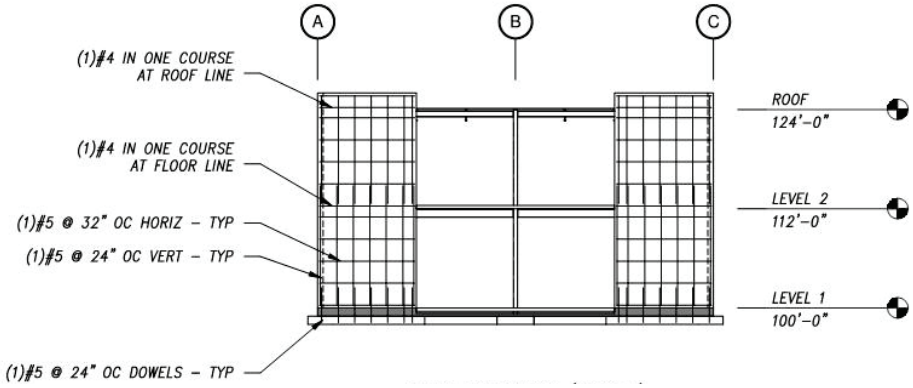

Figure A-18 Two-story commercial building East elevation: COM5.

A.3.2.4 Two-Story Commercial Building Elevations (COM8)

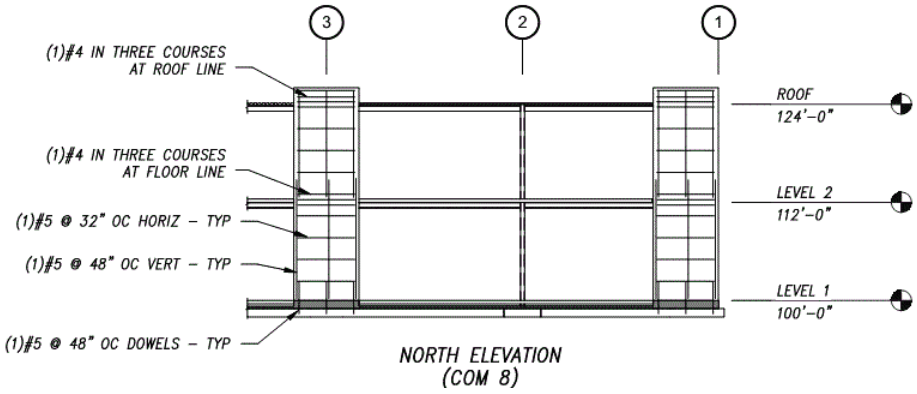

Figure A-19 Two-story commercial building North elevation: COM8.

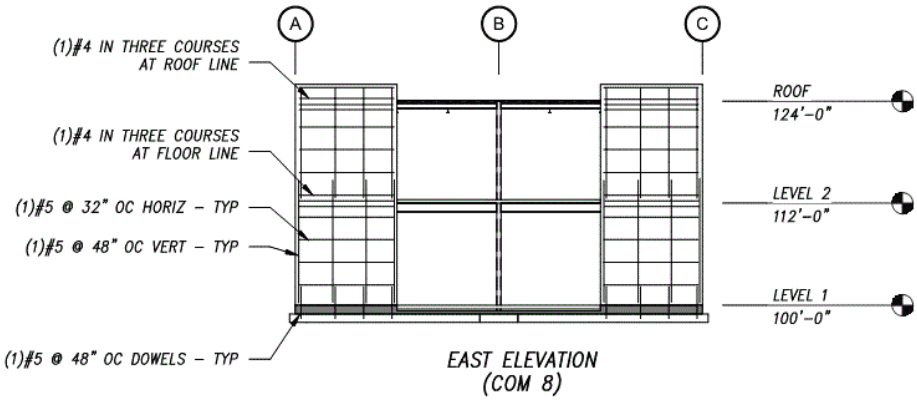

Figure A-20 Two-story commercial building East elevation: COM8.

A.3.2.5 Four-Story Commercial Building Elevations (COM3)

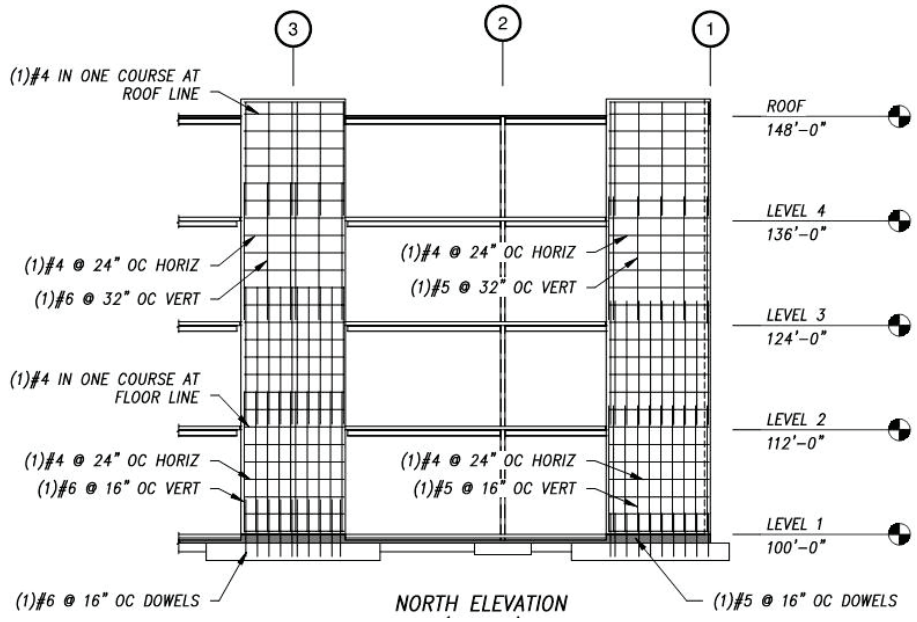

Figure A-21 Four-story commercial building North elevation: COM3.

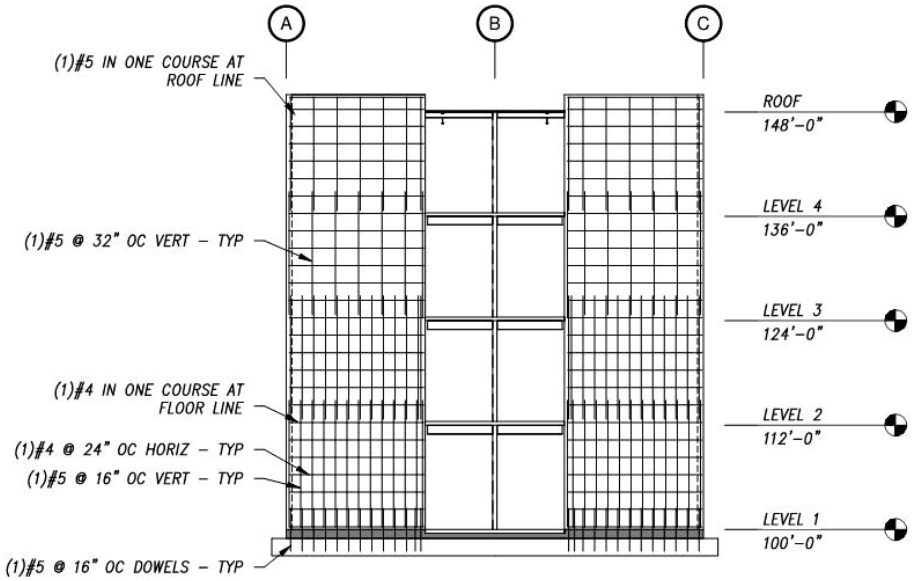

Figure A-22 Four-story commercial building East elevation: COM 3.

A.3.2.6 Four-Story Commercial Building Elevations (COM6)

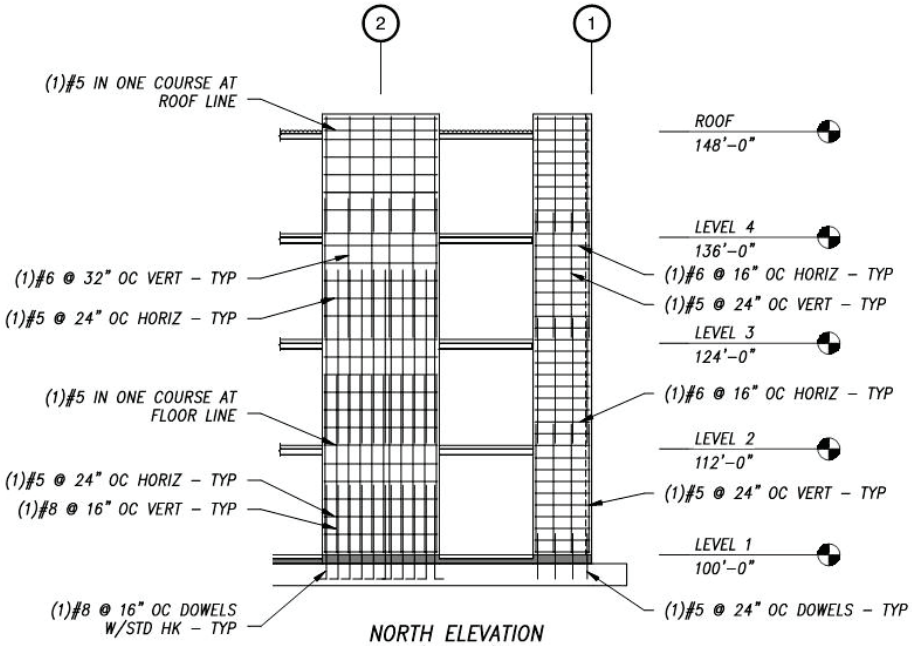

Figure A-23 Four-story commercial building North elevation: COM6.

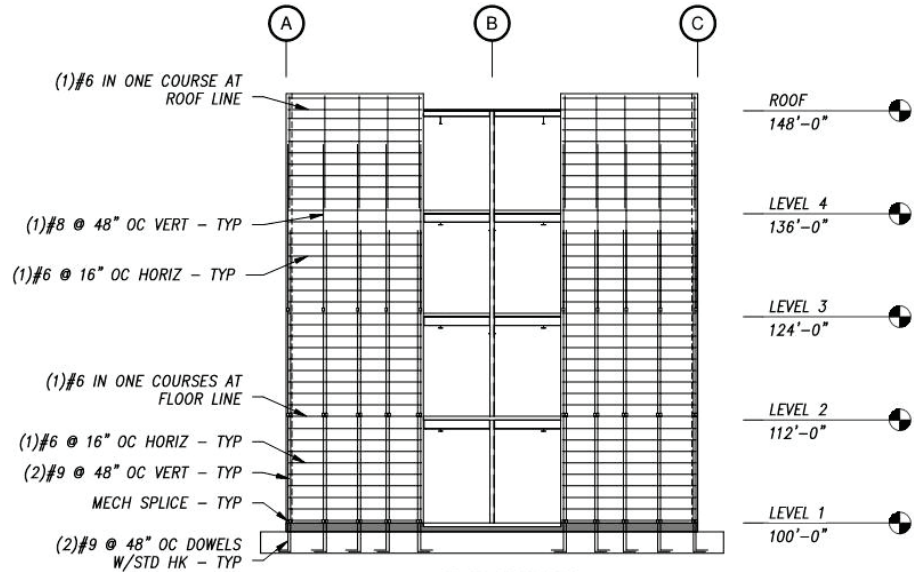

Figure A-24 Four-story commercial building East elevation: COM6.

A.3.2.7 Four-Story Commercial Building Elevations (COM9)

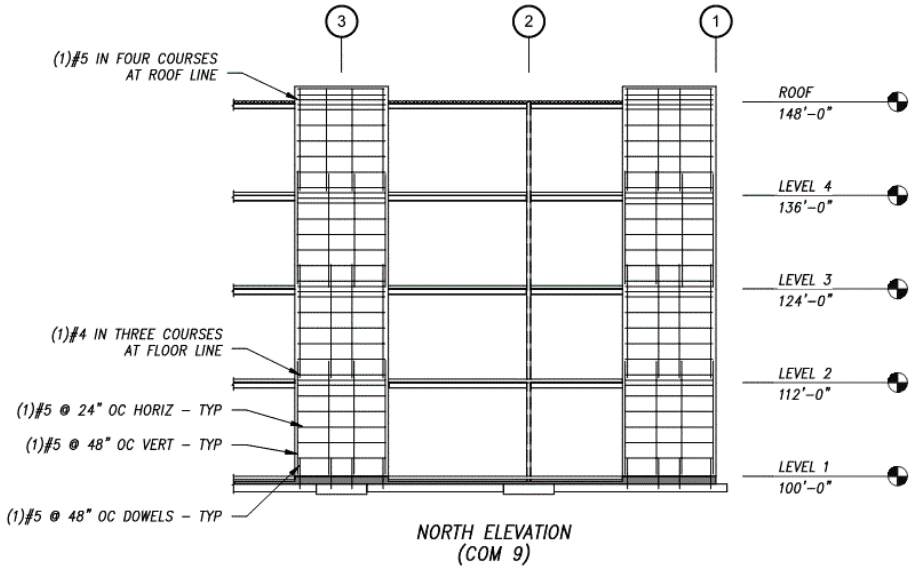

Figure A-25 Four-story commercial building North elevation: COM9.

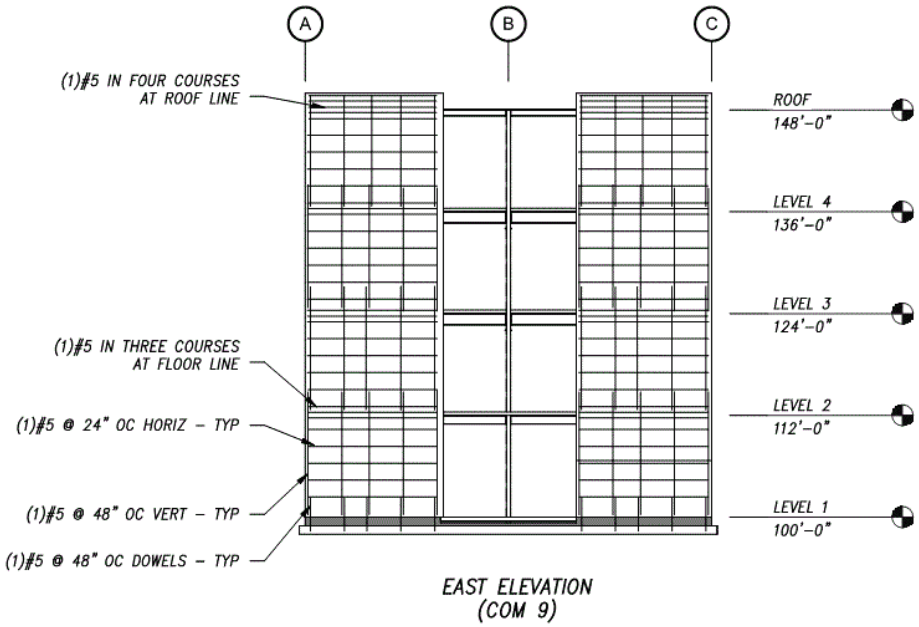

Figure A-26 Four-story commercial building East elevation: COM9.

A.3.3 Structural Details: Commercial Buildings

A.3.3.1 Foundation Details

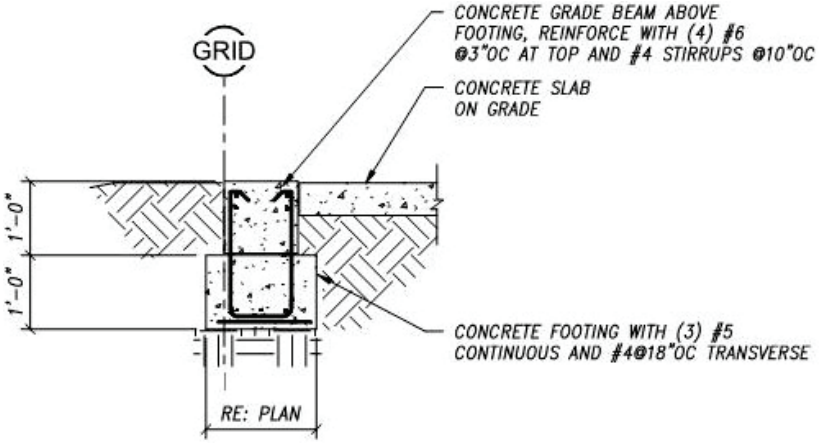

Figure A-27 Commercial building foundation detail.

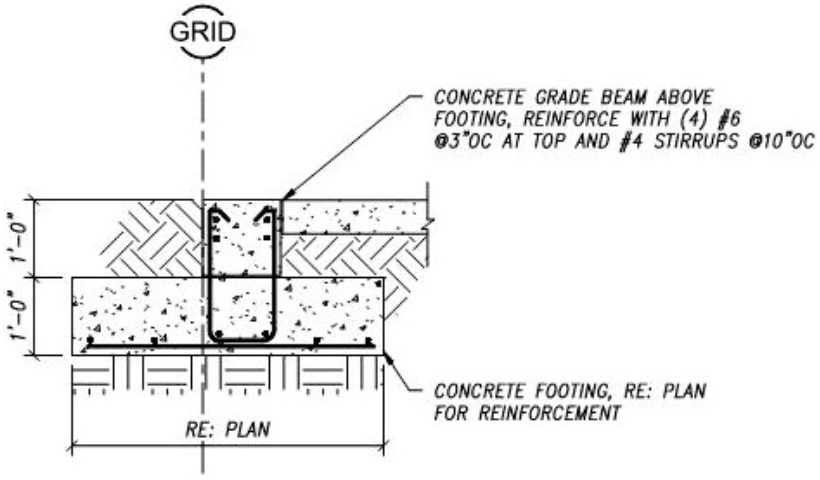

Figure A-28 Commercial building foundation detail for COM2 archetype on soft soil.

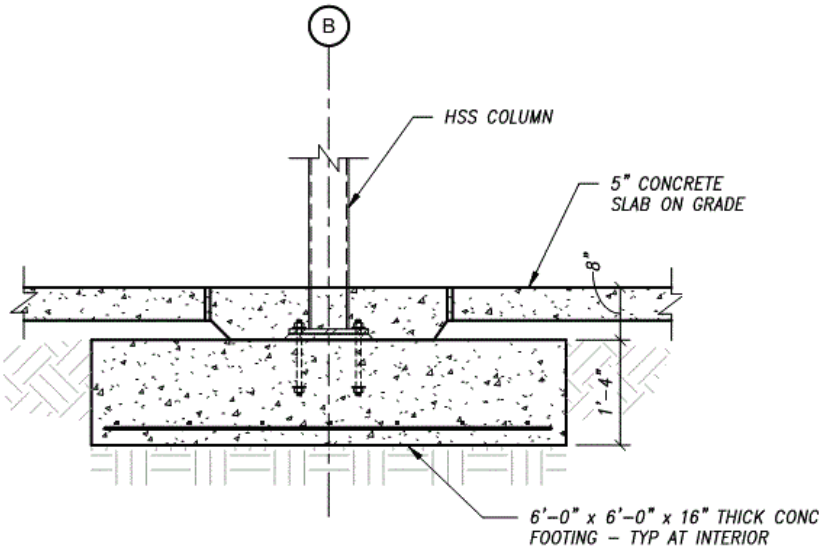

Figure A-29 Commercial building foundation detail.

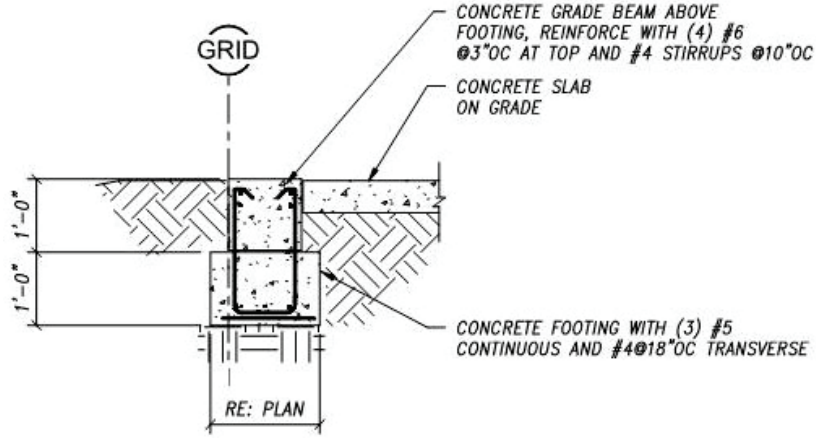

Figure A-30 Commercial building foundation detail at grade beam.

A.3.3.2 Framing Details

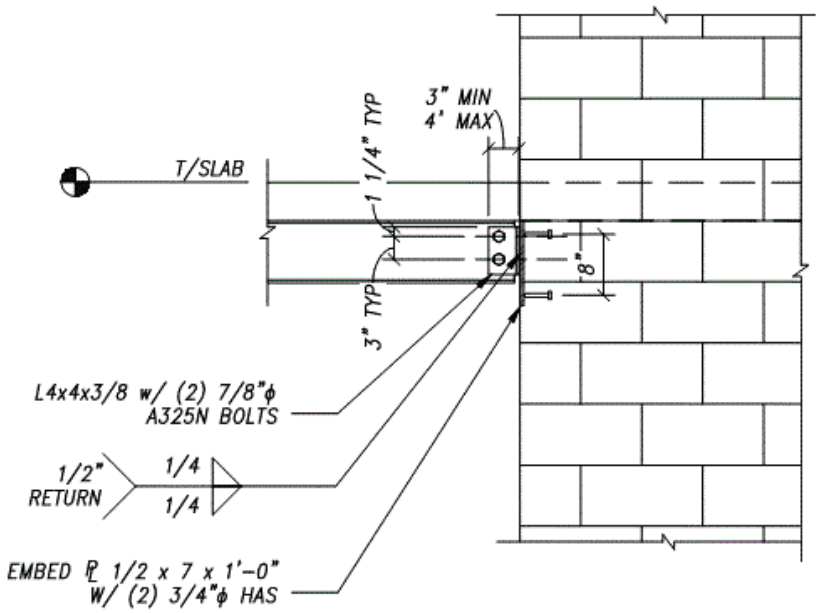

Figure A-31 Commercial building framing detail.

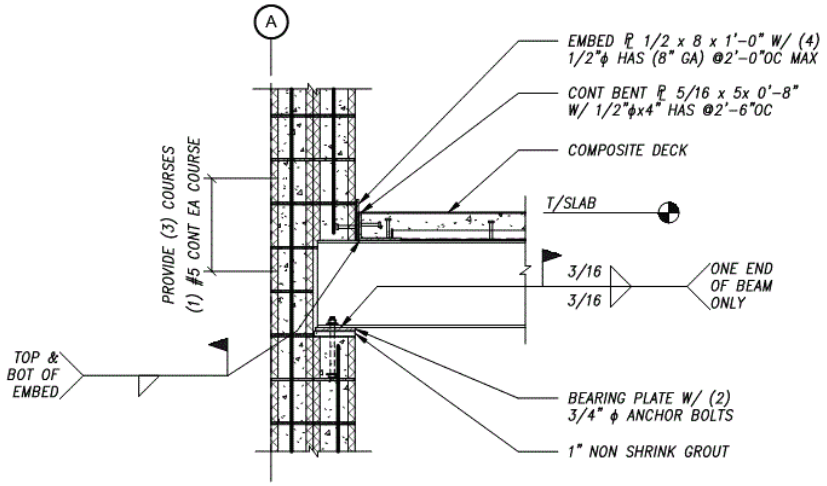

Figure A-32 Commercial building framing detail.

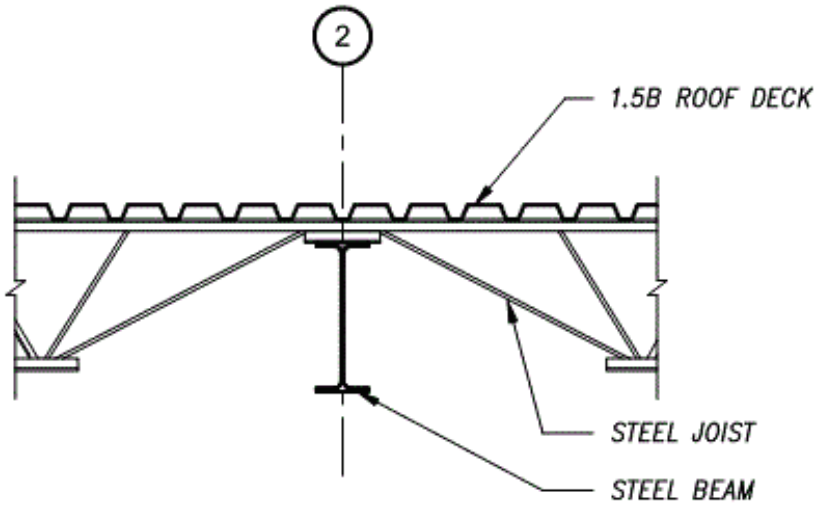

Figure A-33 Commercial building framing detail.

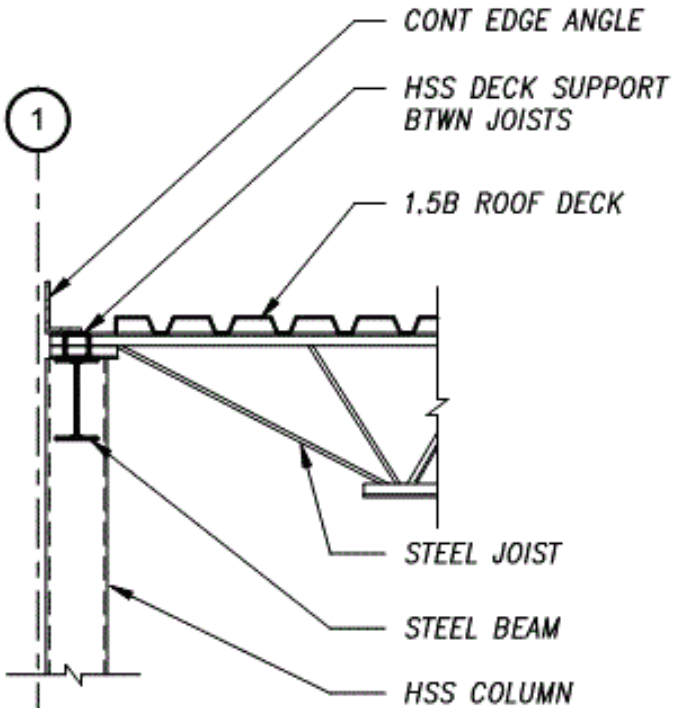

Figure A-34 Commercial building framing detail.

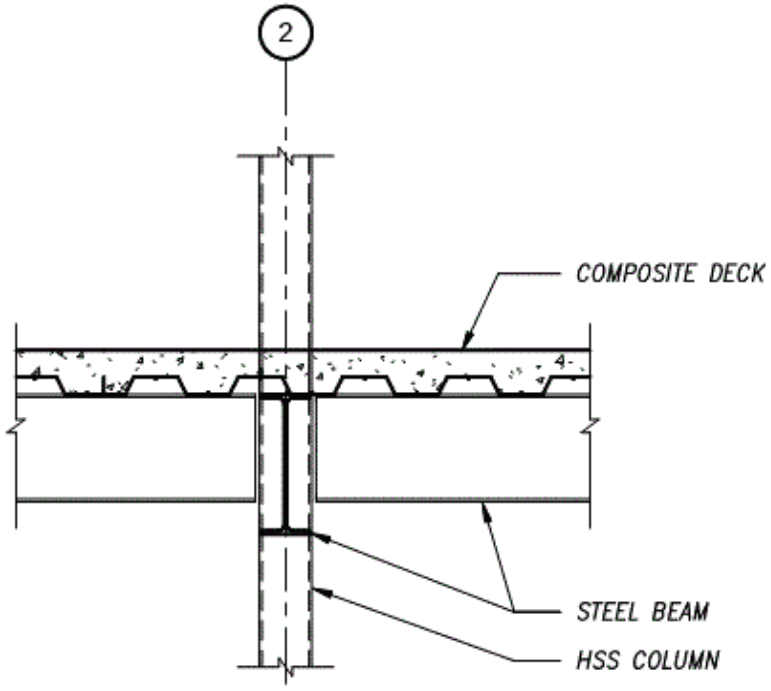

Figure A-35 Commercial building framing detail.

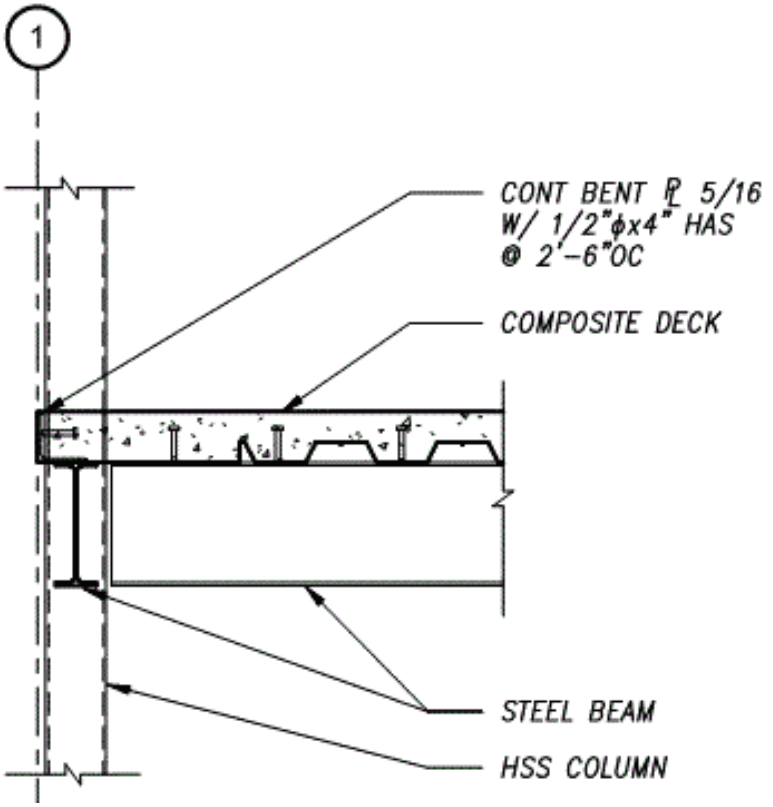

Figure A-36 Commercial building framing detail.

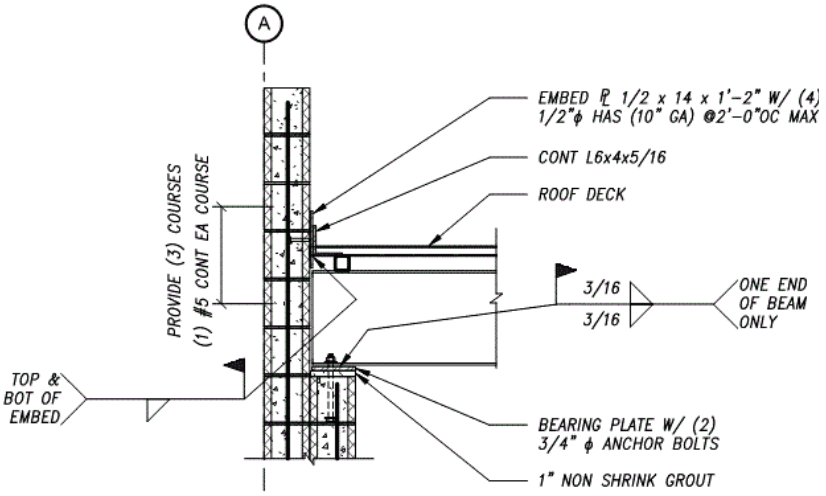

Figure A-37 Commercial building framing detail.

A.4 Multi-Family Residential and Hotel Buildings (RES)

A.4.1 Structural Plans: Residential Buildings

In the following sections, the structural designs for each of the multi-family residential and hotel archetypes are documented, including plans, elevations, and details. The floor and roof framing are identical for all archetypes and are shown only once for the RES1 archetype. The foundation designs are unique, but similar, and are tabulated on a single plan. Masonry reinforcement for all unique conditions are shown in wall elevation views.

A.4.1.1 Four-Story Residential Building Plans (RES1, RES2, RES3)

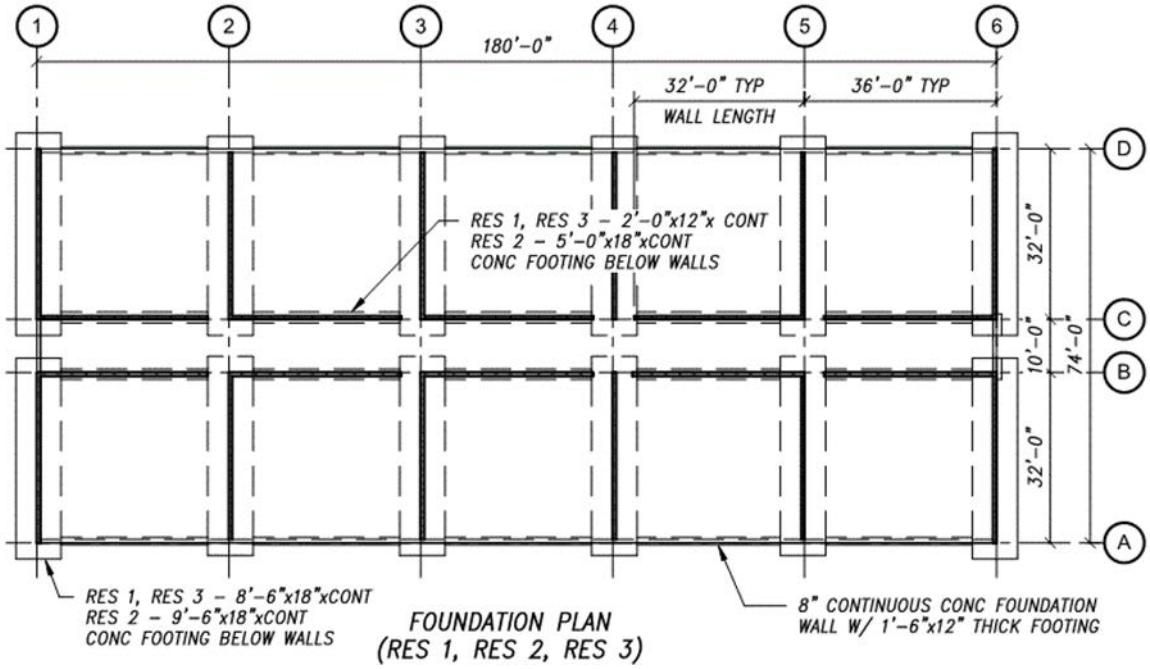

Figure A-38 Four-story residential building foundation configuration: RES1, RES2, RES3.

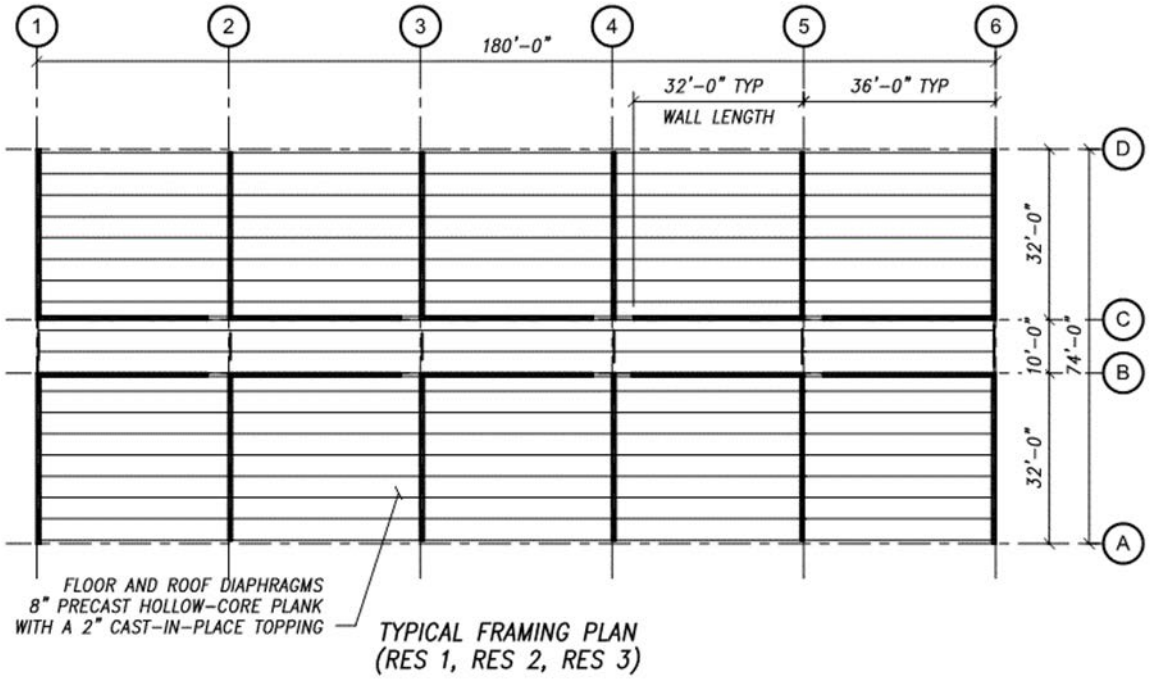

Figure A-39 Four-story residential building framing configuration: RES1, RES2, RES3.

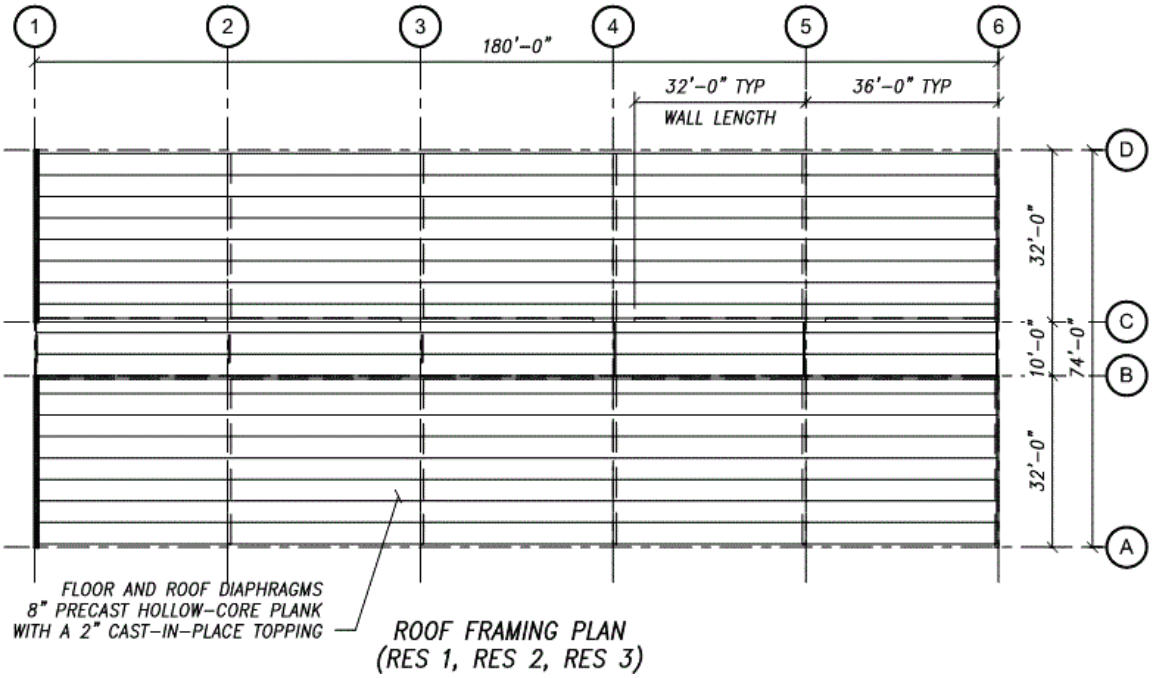

Figure A-40 Four-story residential building roof configuration: RES1, RES2, RES3.

A.4.2 Structural Elevations: Residential Buildings

A.4.2.1 Four-Story Residential Building Elevations (RES1, RES3)

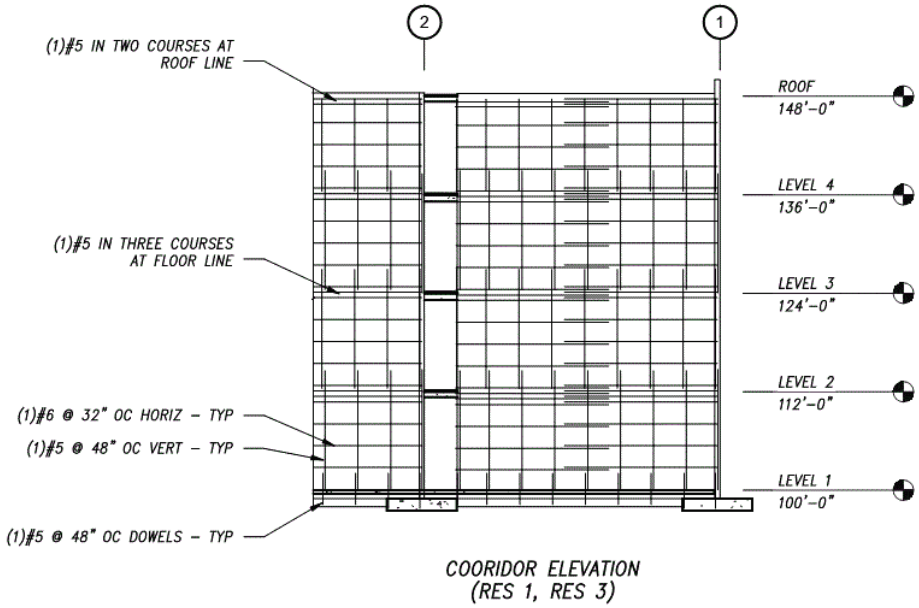

Figure A-41 Four-story residential building corridor elevation: RES1, RES3.

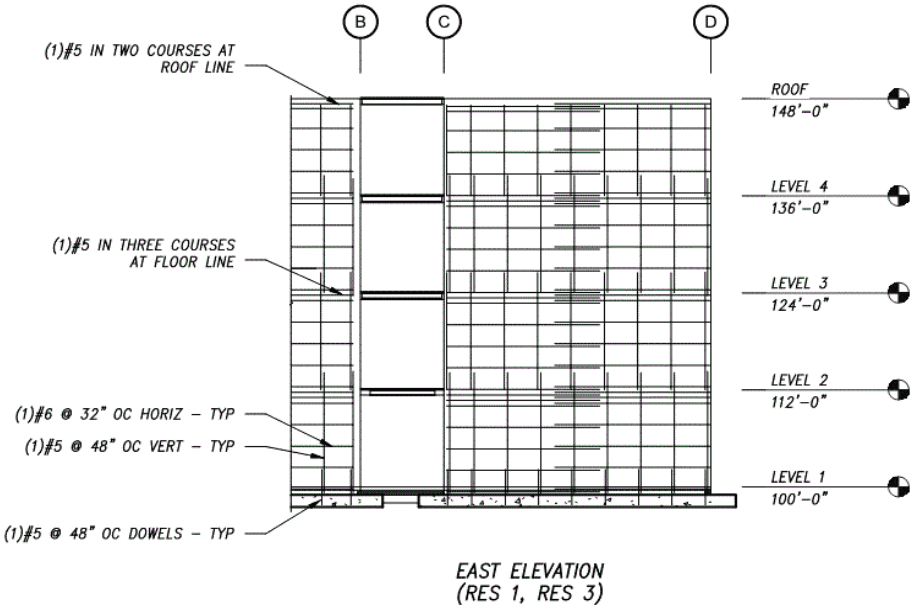

Figure A-42 Four-story residential building East elevation: RES1, RES3.

A.4.2.2 Four-Story Residential Building Elevations (RES 2)

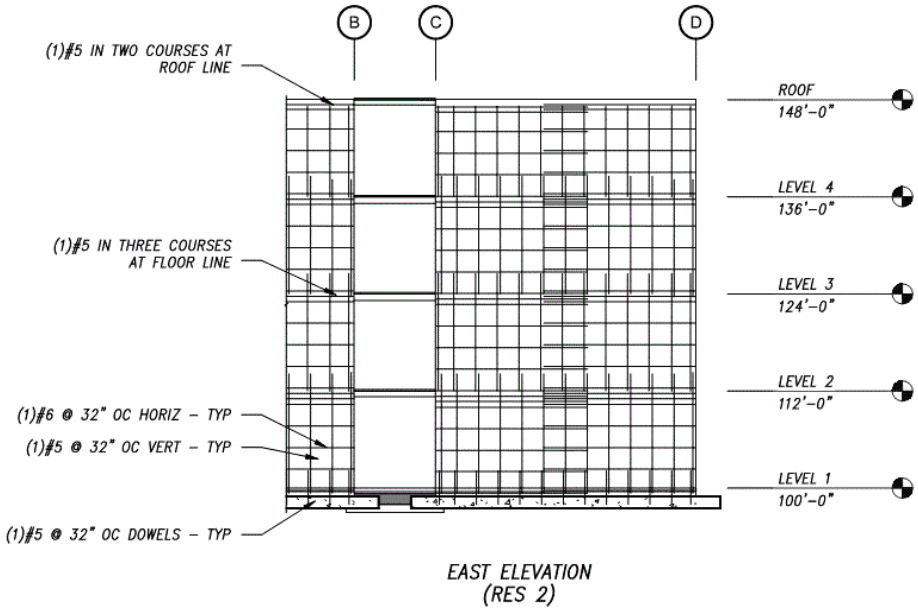

Figure A-43 Four-story residential building East elevation: RES2.

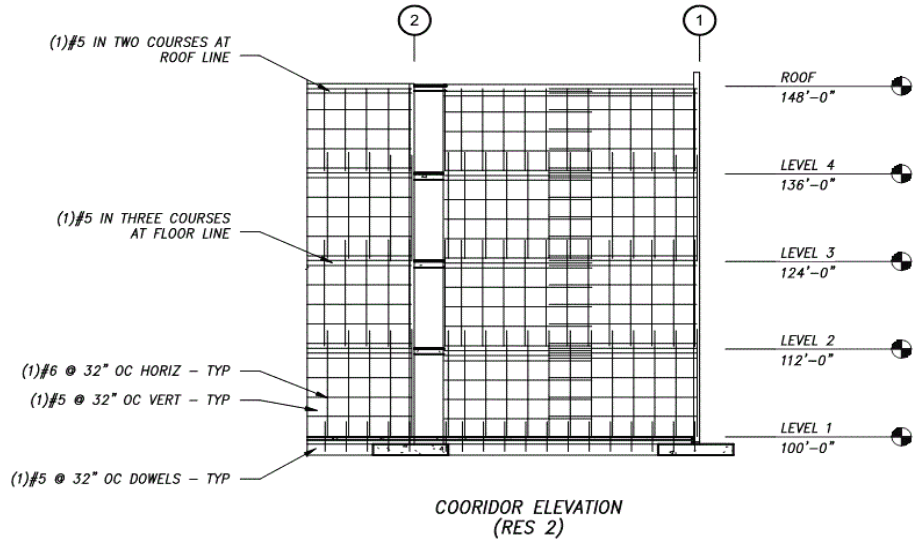

Figure A-44 Four-story residential building corridor elevation: RES2.

A.4.3 Structural Details: Residential Buildings

A.4.3.1 Foundation Details

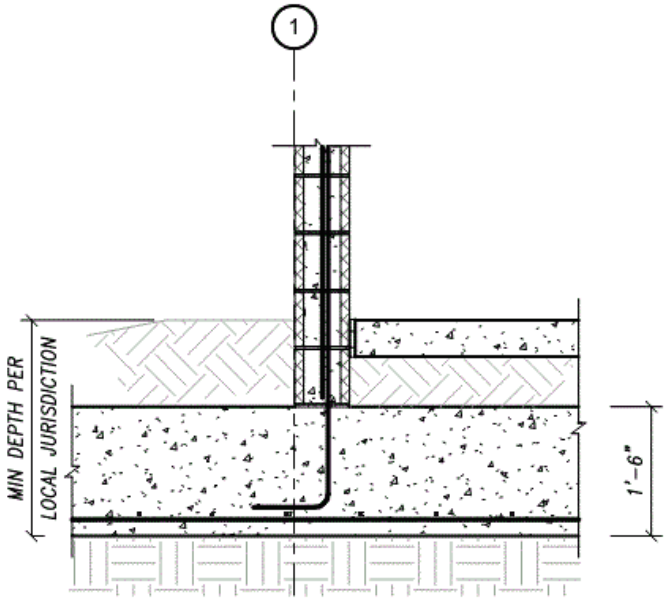

Figure A-45 Residential building foundation detail.

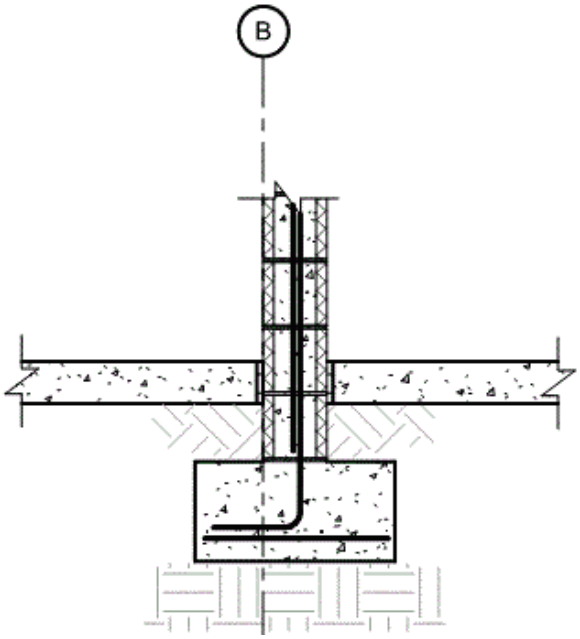

Figure A-46 Residential building foundation detail.

A.4.3.2 Framing Details

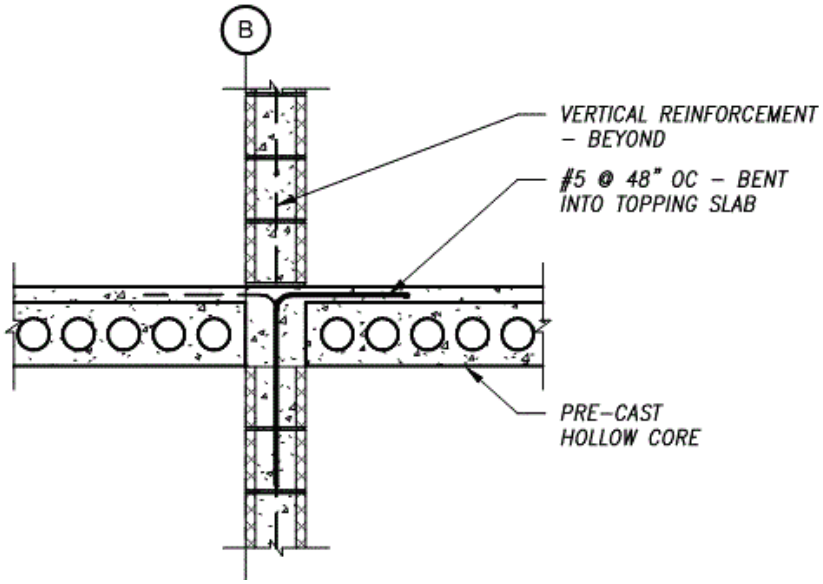

Figure A-47 Residential building framing detail.

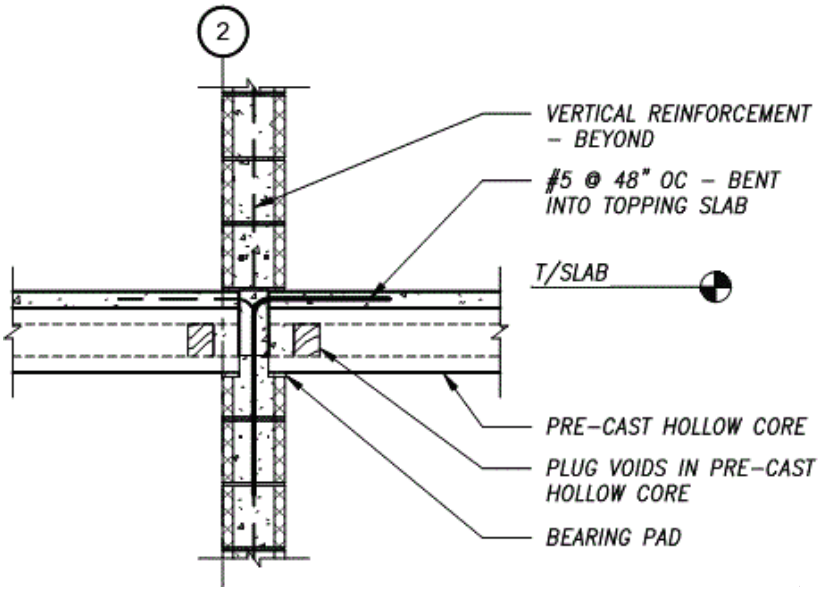

Figure A-48 Residential building framing detail.

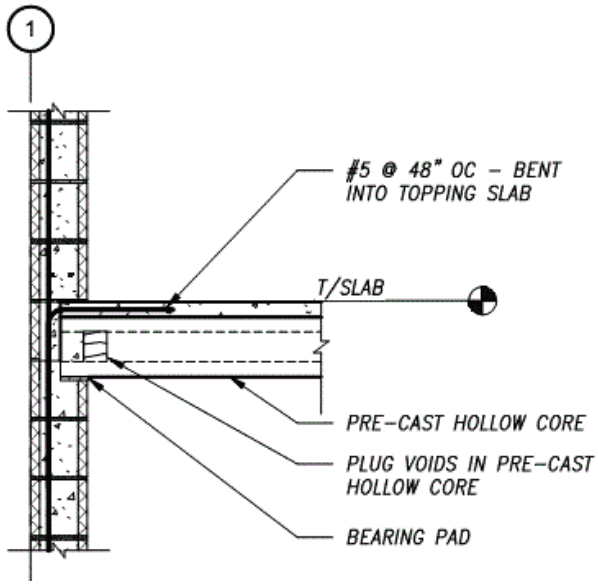

Figure A-49 Residential building framing detail.

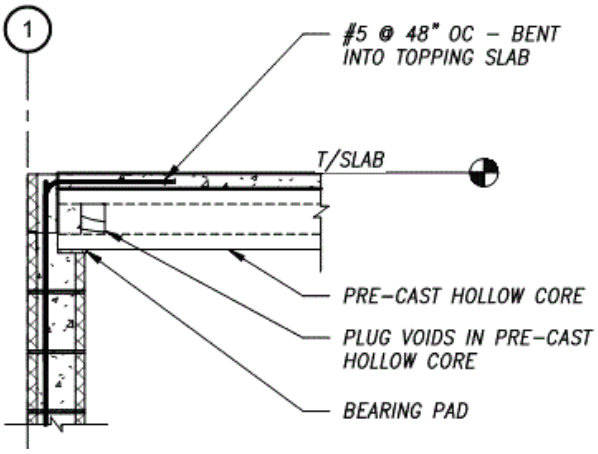

Figure A-50 Residential building framing detail.

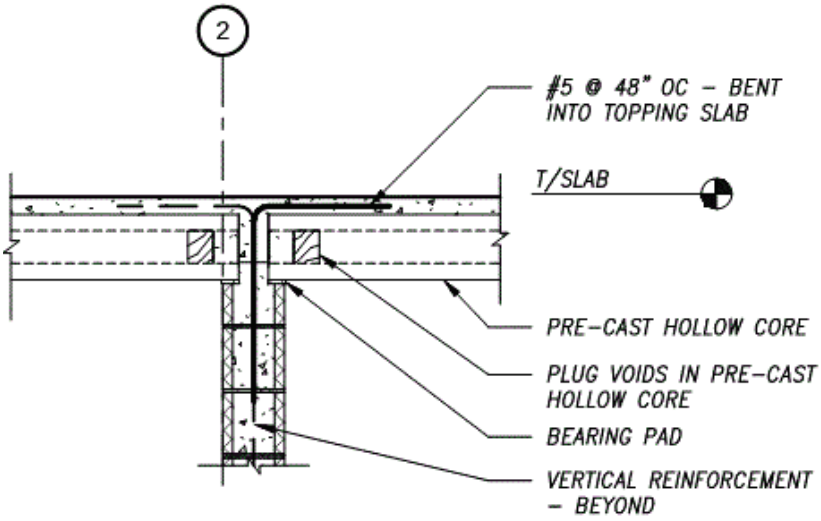

Figure A-51 Residential building framing detail.

A.5 Retail, Industrial, and Warehouse Buildings (BOX)

A.5.1 Structural Plans: Box Buildings

In the following sections, the structural designs for each of the retail, industrial, and warehouse archetypes are documented, including plans, elevations, and details. The floor and roof framing are identical for all archetypes and are shown only once for the BOX1 model. The foundation designs are unique, but similar, and are tabulated on a single plan. Masonry reinforcement for all unique conditions are shown in wall elevation views.

A.5.1.1 Building Plans (BOX1, BOX2, BOX3)

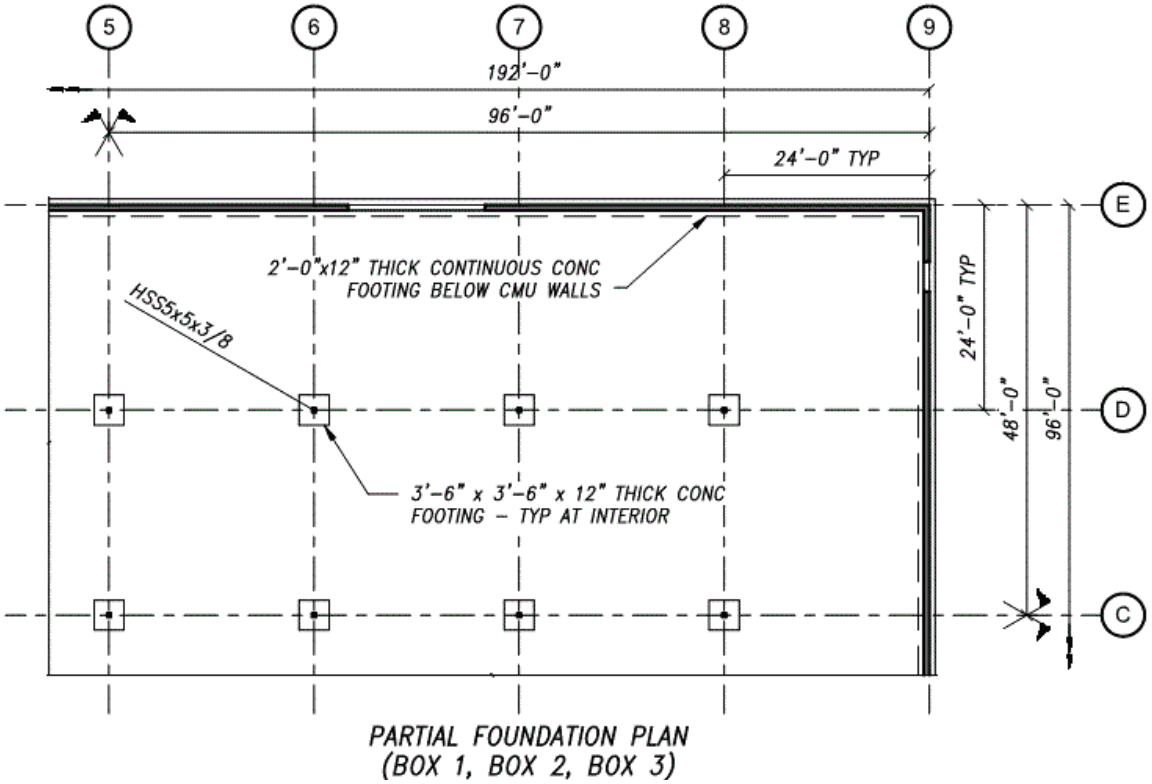

Figure A-52 Single-story retail/industrial/warehouse building foundation configuration: BOX1, BOX2, BOX3.

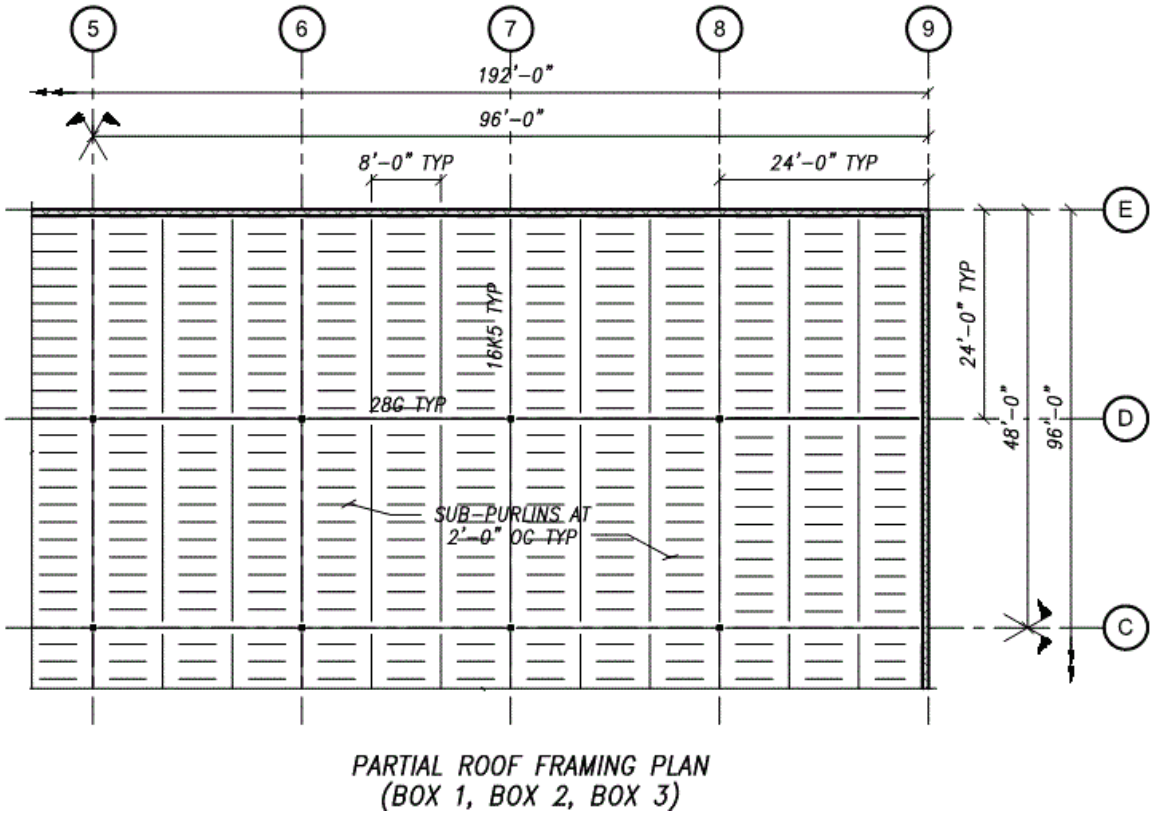

Figure A-53 Single-story retail/industrial/warehouse building roof framing configuration: BOX1, BOX2, BOX3.

A.5.2 Structural Elevations: Box Buildings

A.5.2.1 Building Elevations (BOX1)

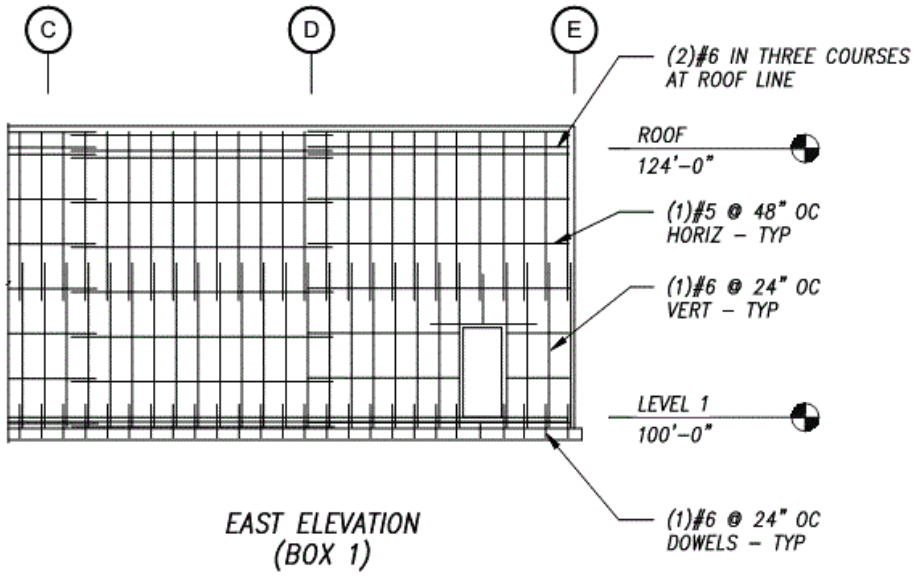

Figure A-54 Single-story retail/industrial/warehouse building East elevation: BOX1.

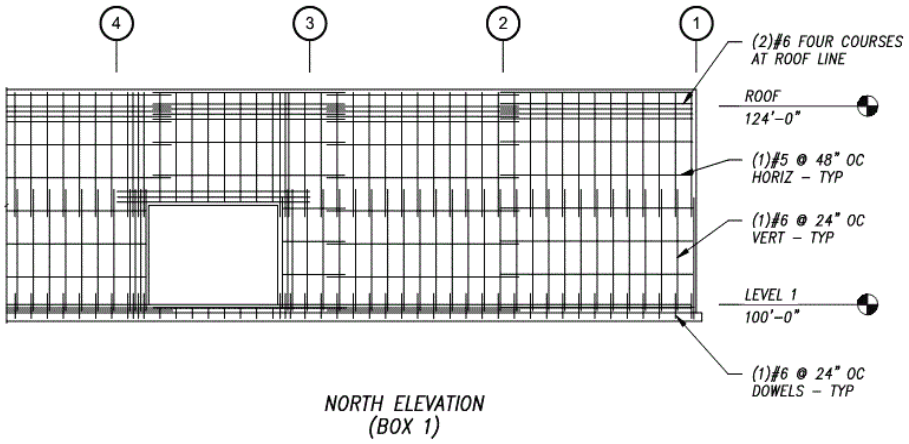

Figure A-55 Single-story retail/industrial/warehouse building North elevation: BOX1.

A.5.2.2 Building Elevations (BOX2)

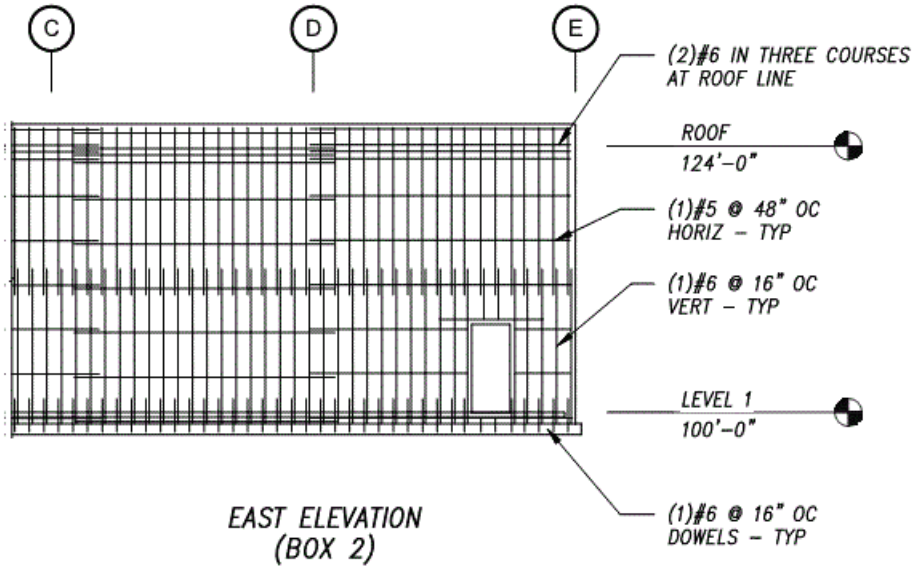

Figure A-56 Single-story retail/industrial/warehouse building East elevation: BOX 2.

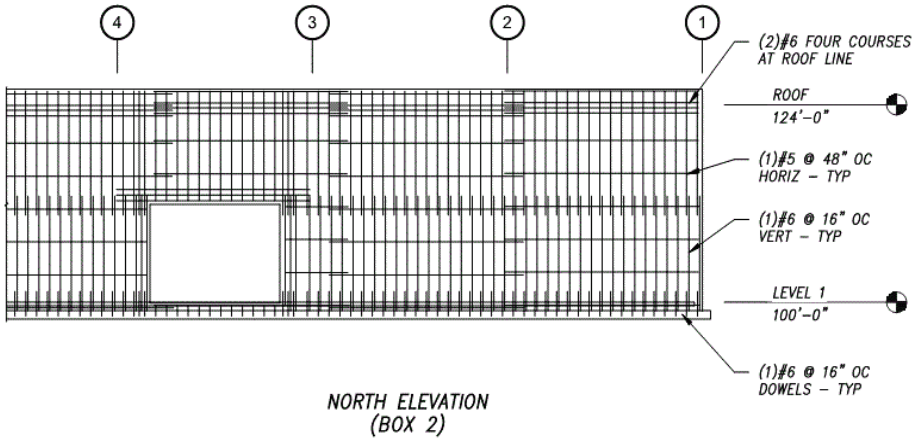

Figure A-57 Single-story retail/industrial/warehouse building North elevation: BOX2.

A.5.2.3 Building Elevations (BOX3)

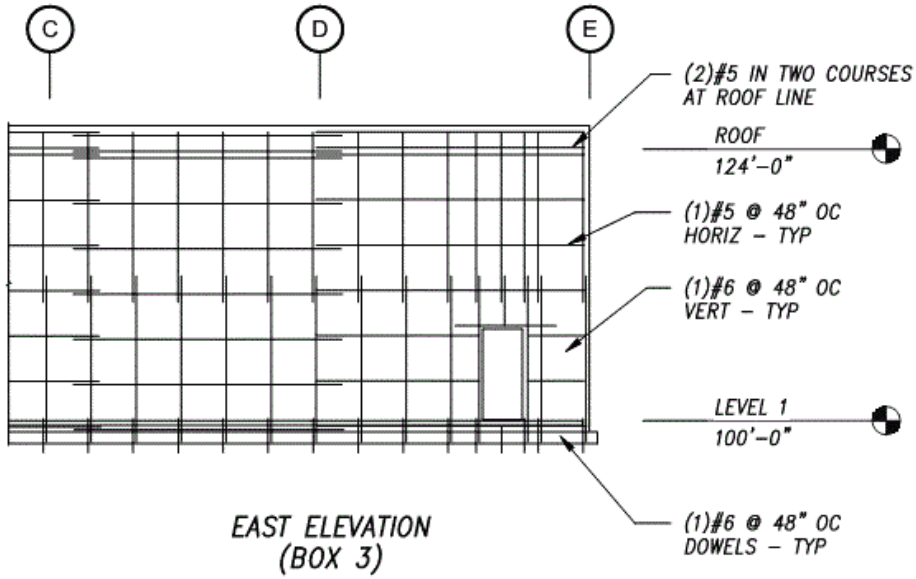

Figure A-58 Single-story retail/industrial/warehouse building East elevation: BOX3.

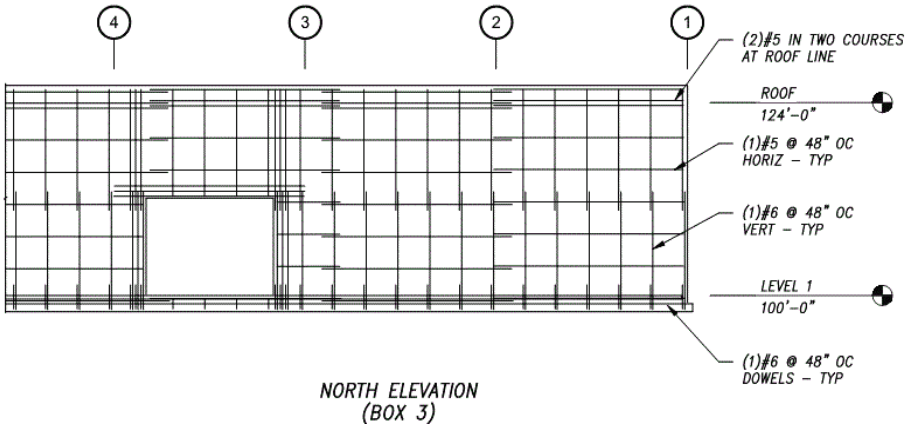

Figure A-59 Single-story retail/industrial/warehouse building North elevation: BOX3.

A.5.3 Structural Details: Box Buildings

A.5.3.1 Foundation Details

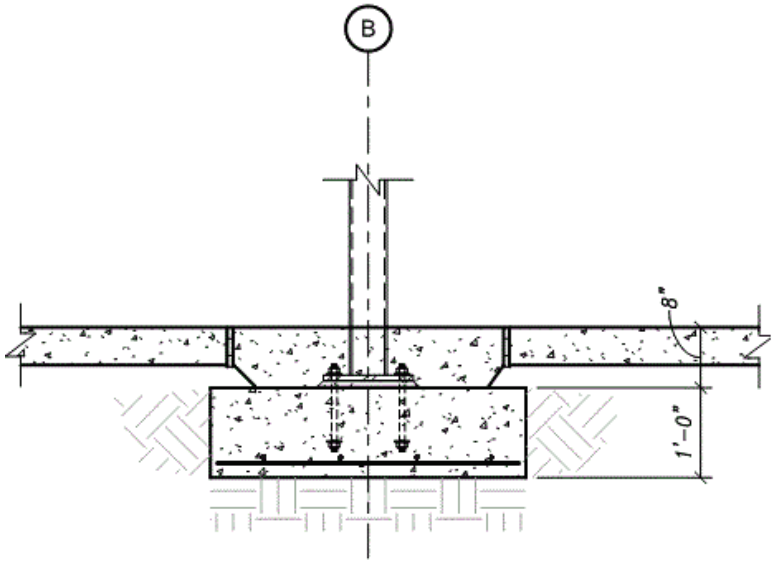

Figure A-60 Single-story retail/industrial/warehouse building foundation detail.

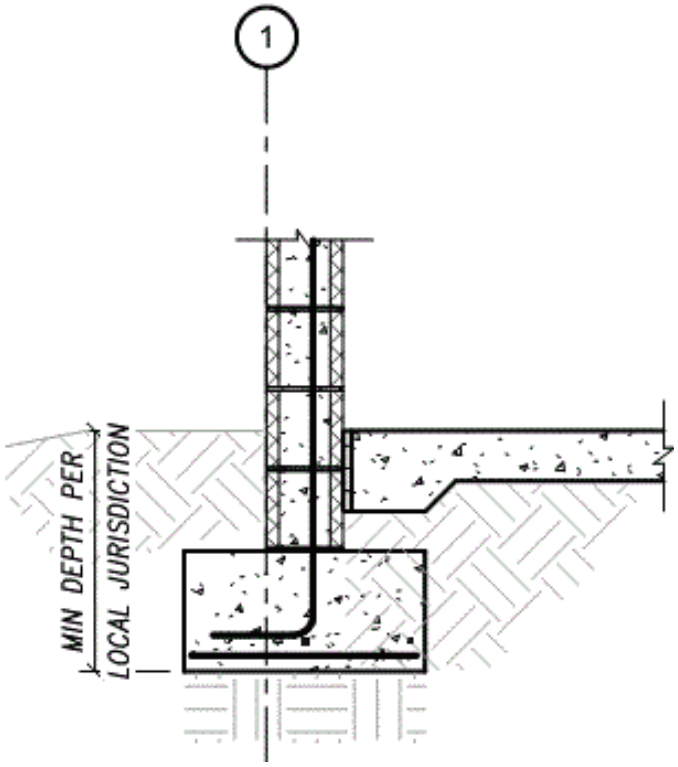

Figure A-61 Single-story retail/industrial/warehouse building foundation detail.

A.5.3.2 Framing Details

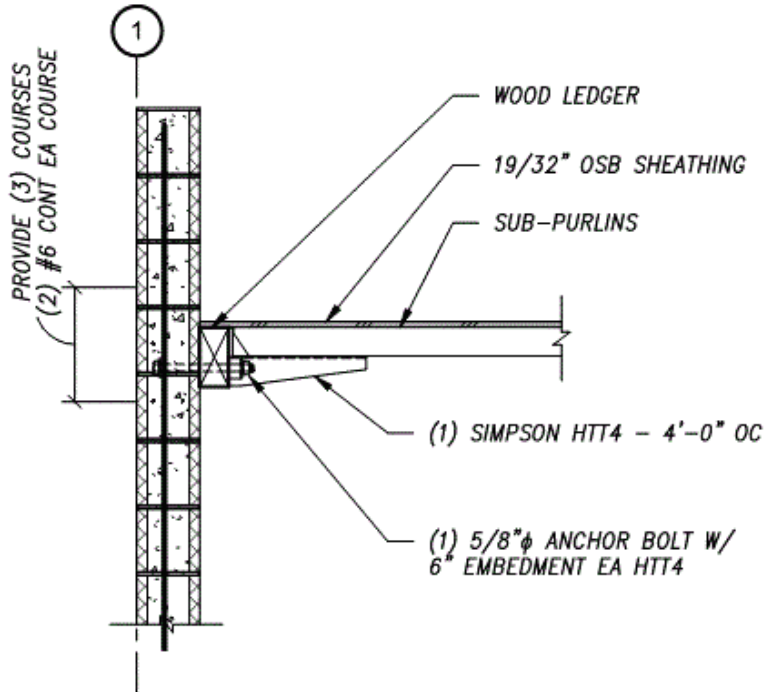

Figure A-62 Single-story retail/industrial/warehouse building framing detail.

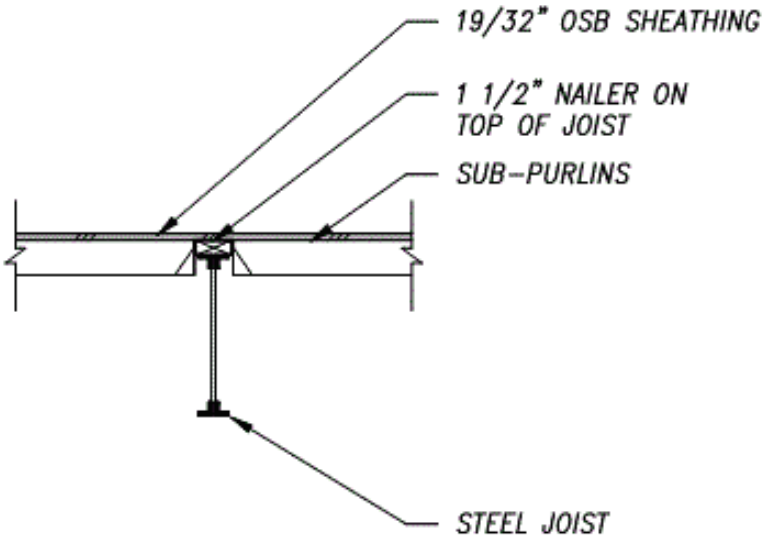

Figure A-63 Single-story retail/industrial/warehouse building framing detail.

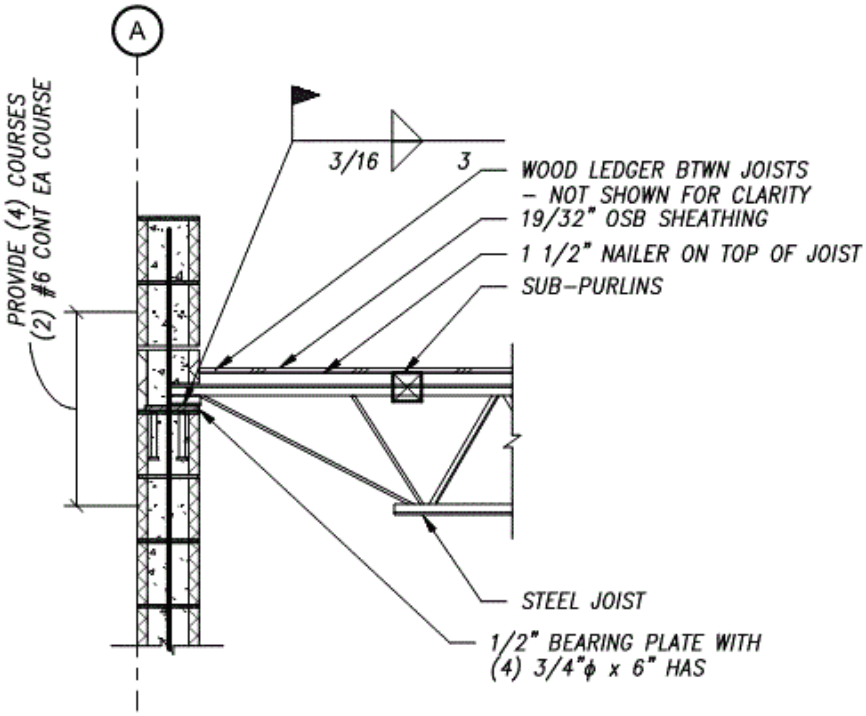

Figure A-64 Single-story retail/industrial/warehouse building framing detail.

Appendix B

Response-History Analysis Results Obtained with Refined and Simplified Numerical Models

This appendix presents numerical results generated for the calibration of the simplified frame models of the six commercial building archetypes, COM1 through COM6, with the refined finite-element models, as discussed in Chapter 4. The results include the response time histories and base shear-vs.-first-story drift hysteresis curves obtained with the refined finite-element models (using LS-DYNA) and simplified frame models (using OpenSees) for three sets of ground-motion records selected in the calibration process. The selected motions are Motion 1, Motion 2, and Motion 17 from the FEMA P-695 database. For these analyses, each record set was scaled to two intensity levels, the MCE_R level and a level beyond MCE_R. Deformed meshes of the refined finite-element models are also presented to illustrate the failure mechanisms of the archetypes.

As the following results show, for the multi-story archetypes, the upper-story drift histories obtained with the refined and the simplified models do not match well, especially for the four-story archetypes (COM3 and COM6). This is attributed to the deficiency of the simplified models in capturing the rigid-body rotation of the upper-story walls, which is the main source of story drifts occurring in the upper stories. Nevertheless, the good match of the base-shear time histories, the first-story drift histories, and the base shear-vs.-first-story drift hysteresis curves obtained with the two modeling approaches provides assurance that the incremental dynamic analysis results obtained with the simplified models are reliable. That is because collapse was always triggered by the story drifts concentrated in the first stories of the archetypes.

B.1 Archetype COM1

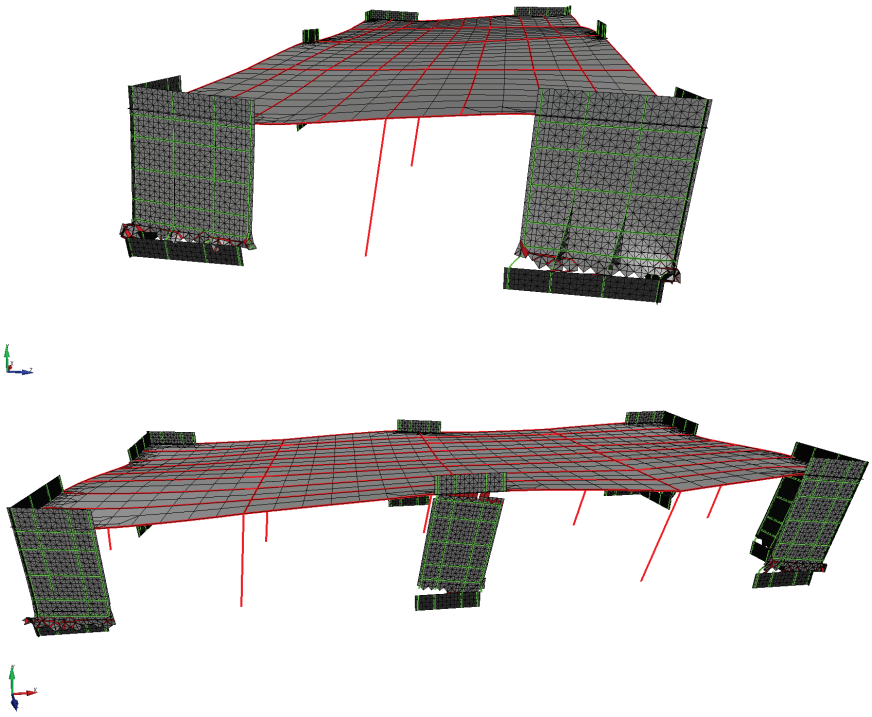

Figure B-1 Deformed meshes from refined model: COM1 (LS-DYNA) – Motion 1 ($3\times MCE_R$).

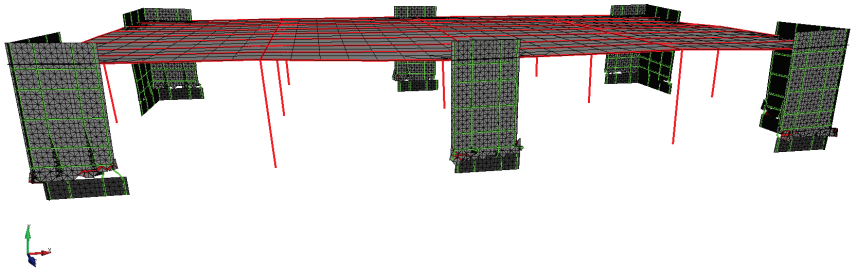

Figure B-2 Deformed meshes from refined model: COM1 (LS-DYNA) – Motion 2 ($2.7\times MCE_R$).

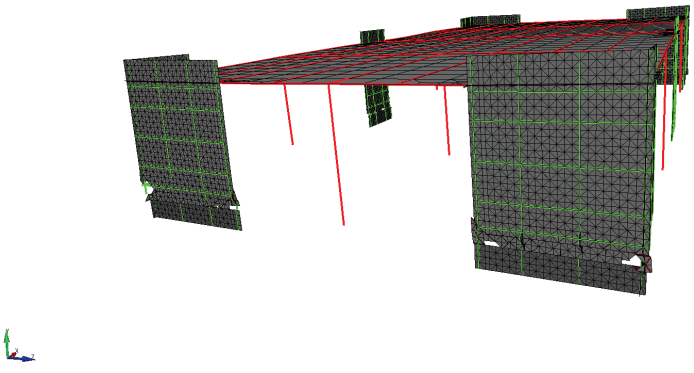

Figure B-3 Deformed meshes from refined model: COM1 (LS-DYNA) – Motion 17 ($3\times MCE_R$).

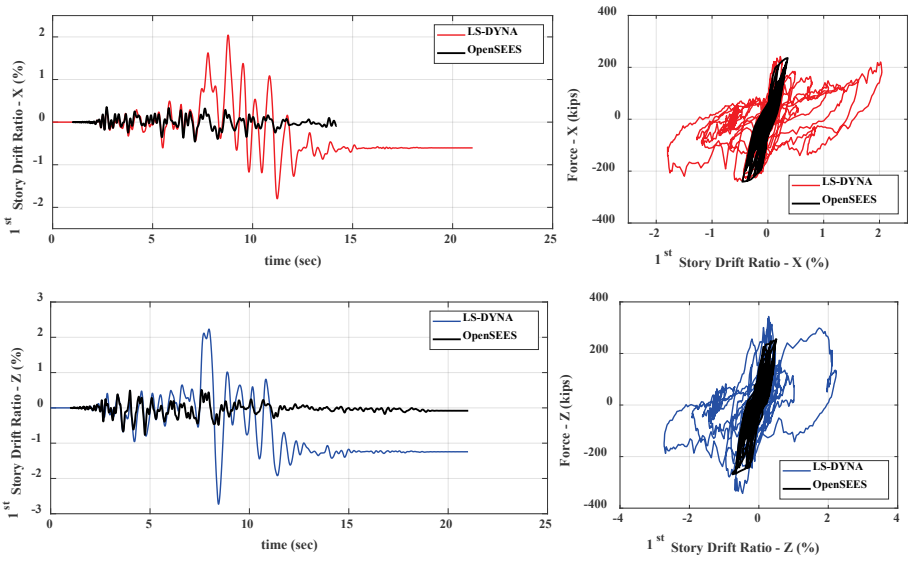

Figure B-4 Comparison of response histories for the first story: COM1 – Motion 1 ($1.5\times MCE_R$).

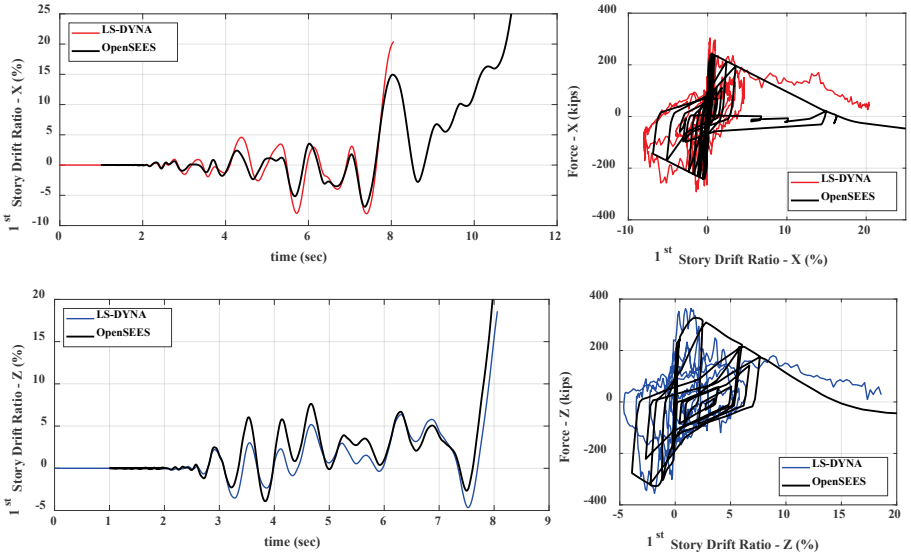

Figure B-5 Comparison of response histories for the first story: COM1 – Motion 1 ($3.0\times MCE_R$).

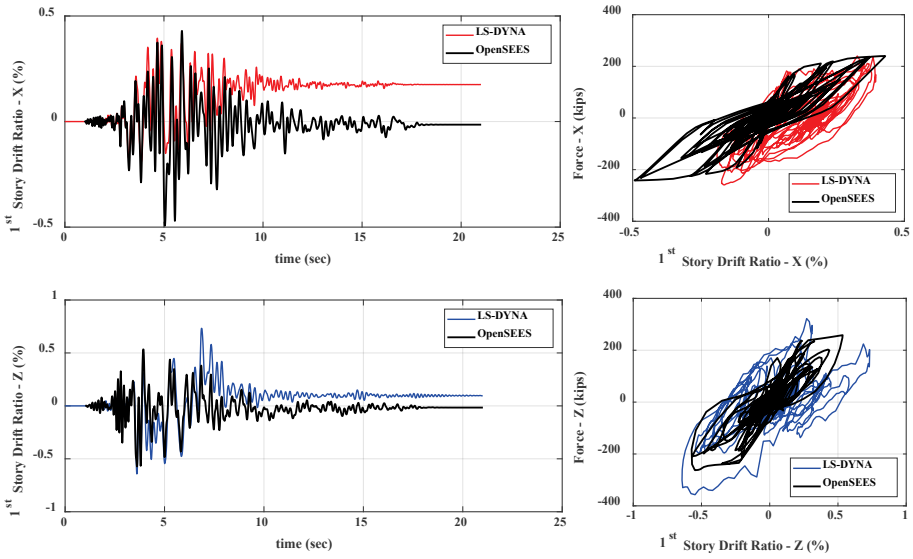

Figure B-6 Comparison of response histories for the first story: COM1 – Motion 2 ($1.5\times MCE_R$).

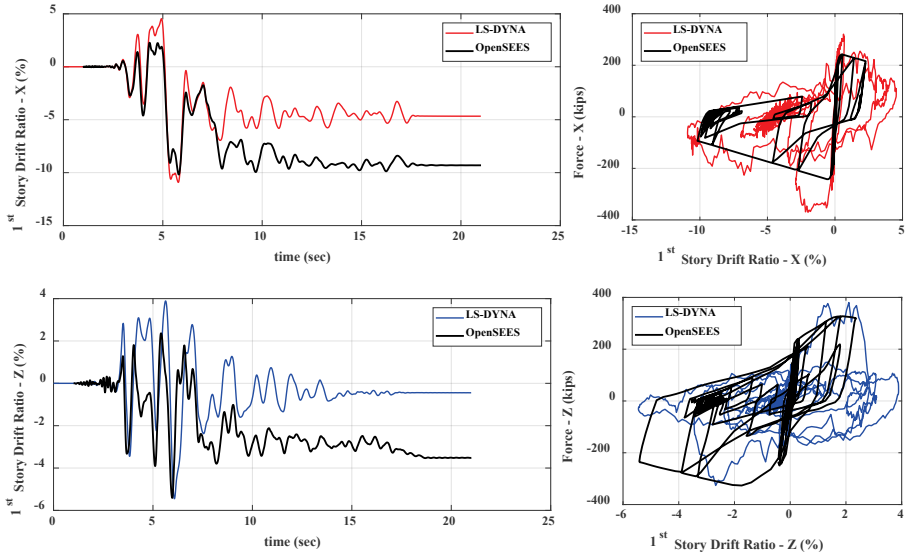

Figure B-7 Comparison of response histories for the first story: COM1 – Motion 2 ($2.7\times MCE_R$).

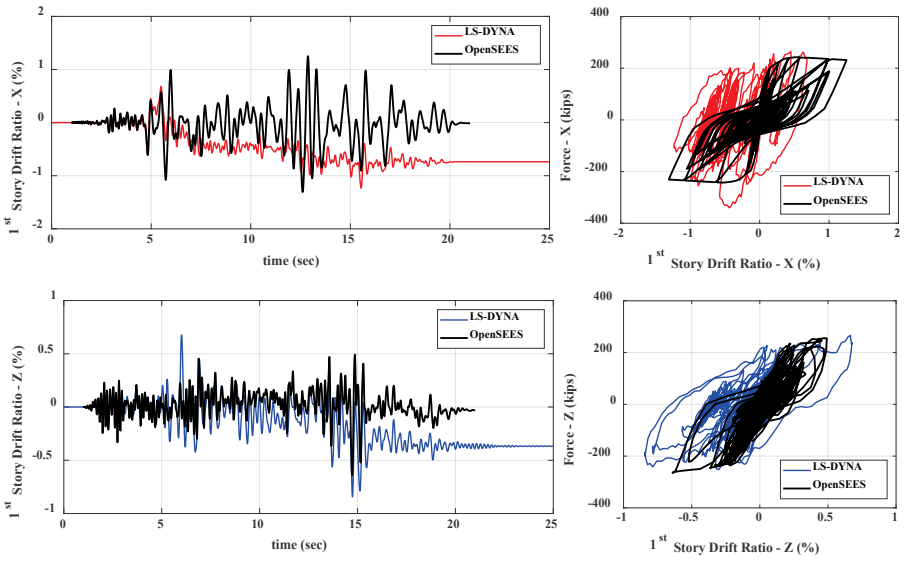

Figure B-8 Comparison of response histories for the first story: COM1 – Motion 17 ($1.5\times MCE_R$).

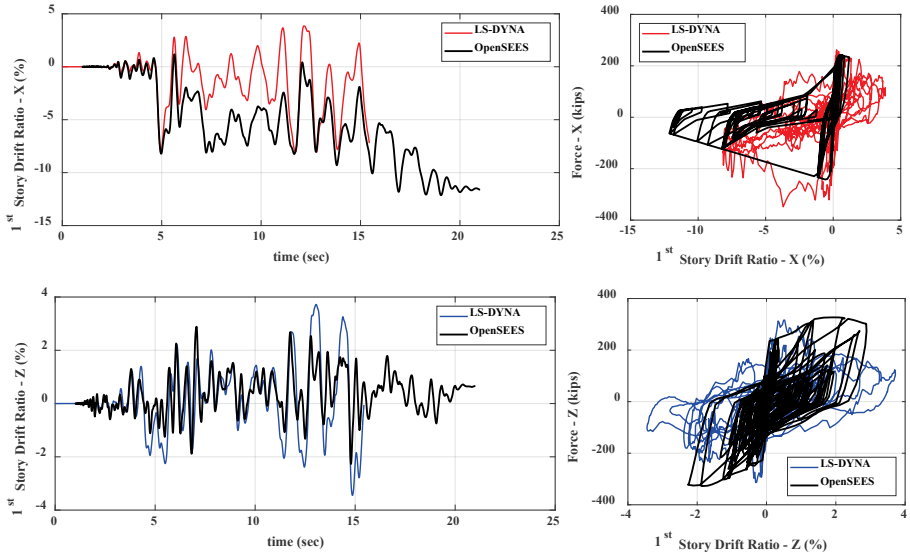

Figure B-9 Comparison of response histories for the first story: COM1 – Motion 17 ($3\times MCE_R$).

B.2 Archetype COM2

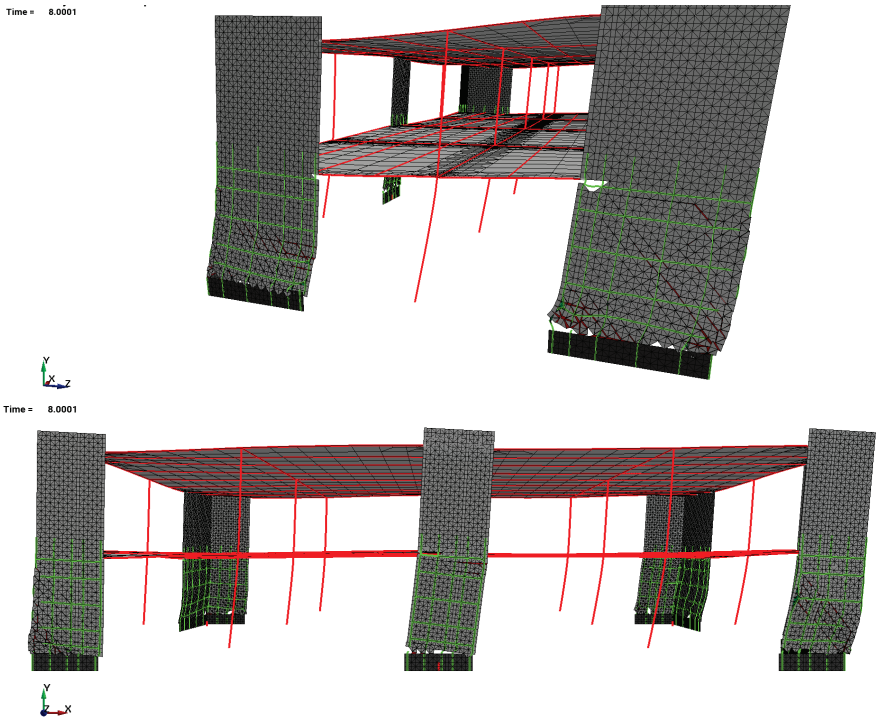

Figure B-10 Deformed meshes from refined model: COM2 (LS-DYNA) – Motion 1 ($2\times MCE_R$).

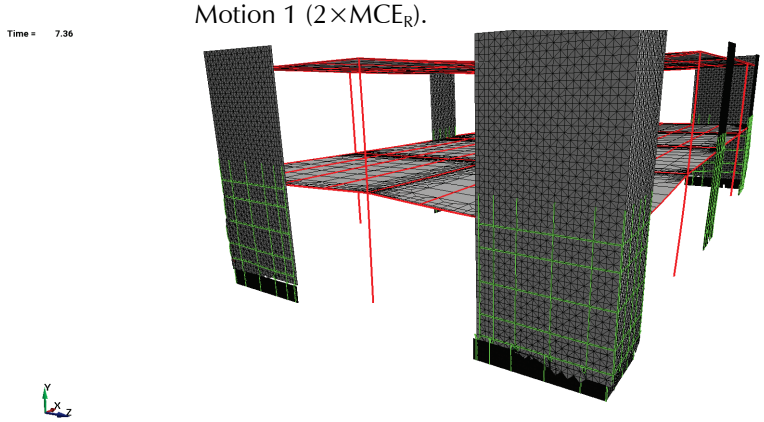

Figure B-11 Deformed meshes from refined model: COM2 (LS-DYNA) – Motion 2 ($2\times MCE_R$).

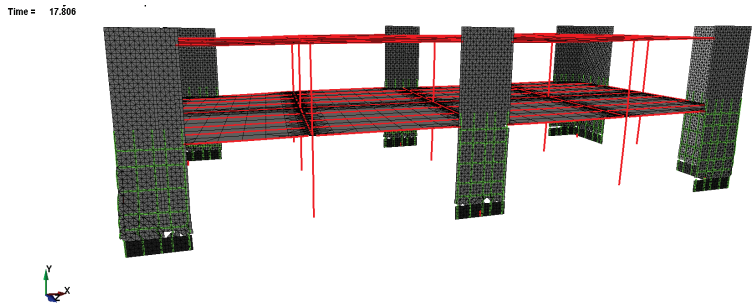

Figure B-12 Deformed meshes from refined model: COM2 (LS-DYNA) – Motion 17 ($2\times MCE_R$).

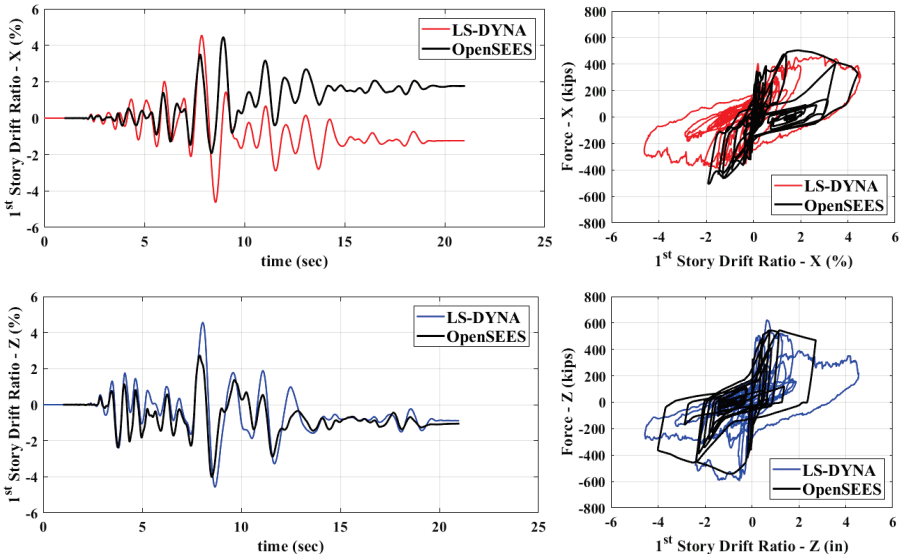

Figure B-13 Comparison of response histories for the first story: COM2 –- Motion 1 (MCE_R).

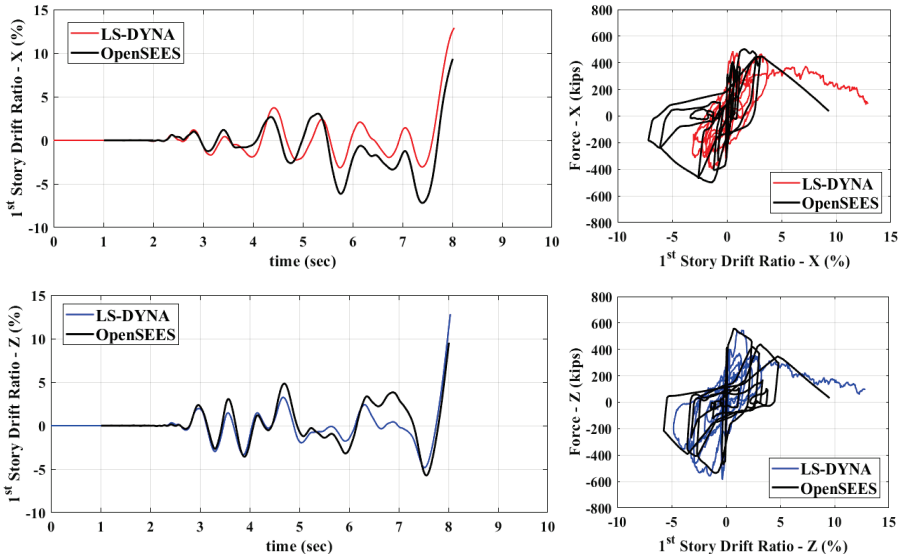

Figure B-14 Comparison of response histories for the first story: COM2 – Motion 1 ($2\times MCE_R$).

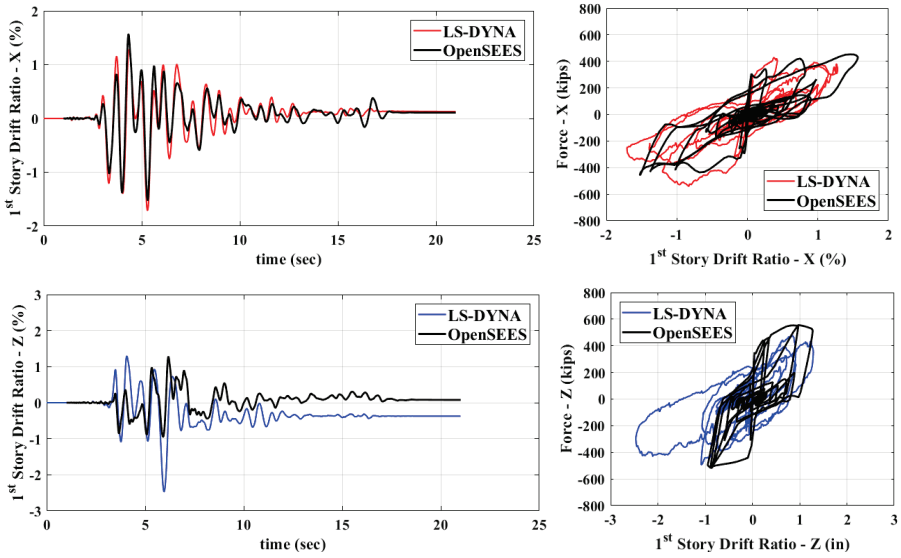

Figure B-15 Comparison of response histories for the first story: COM2 – Motion 2 (MCE_R).

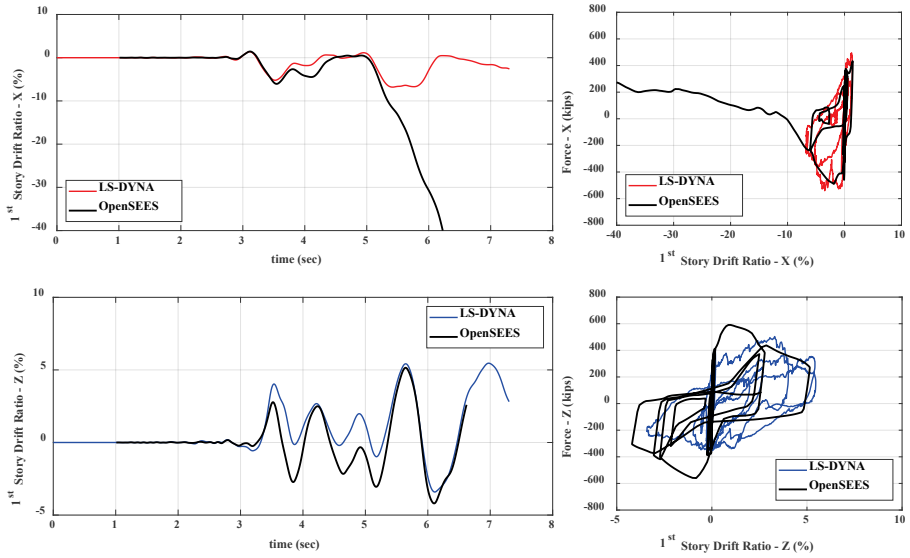

Figure B-16 Comparison of response histories for the first story: COM2 – Motion 2 ($2\times MCE_R$).

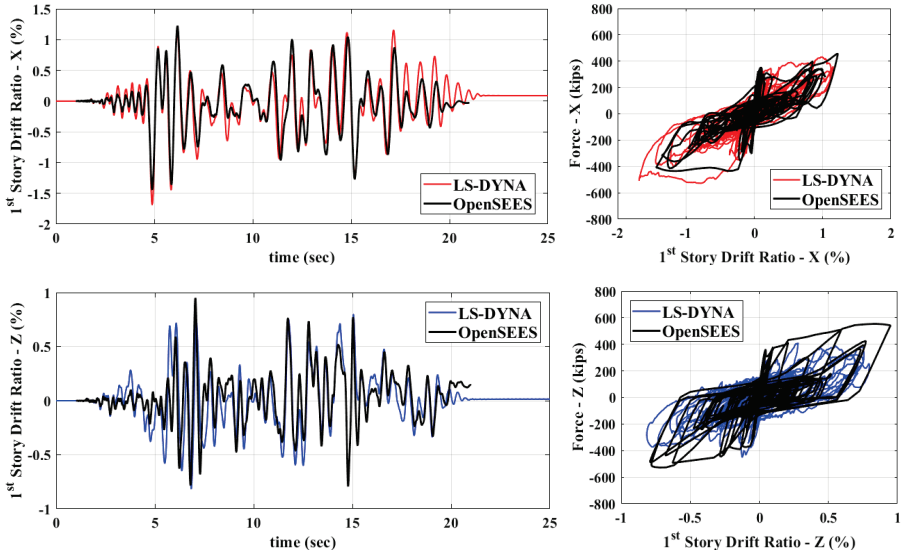

Figure B-17 Comparison of response histories for the first story: COM2 – Motion 17 (MCE_R).

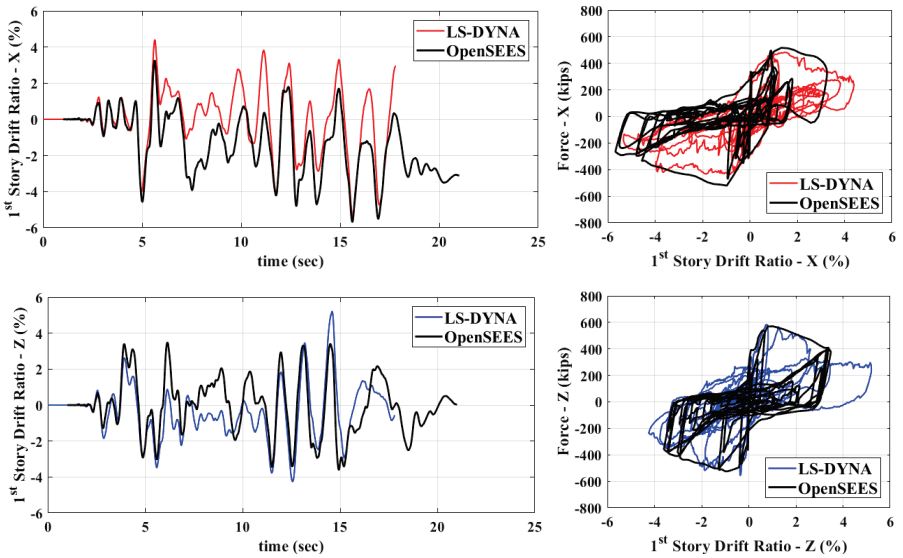

Figure B-18 Comparison of response histories for the first story: COM2 – Motion 17 ($2\times MCE_R$).

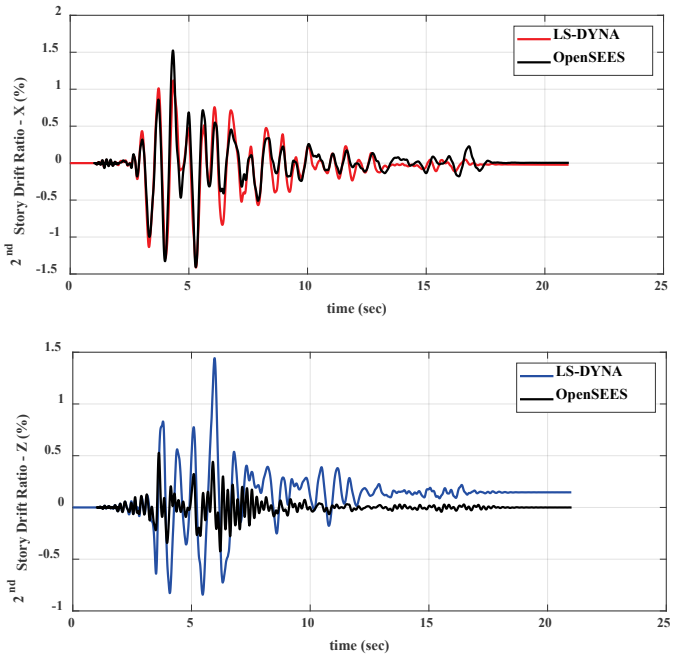

Figure B-19 Comparison of story-drift histories for the second story: COM2 – Motion 2 (MCE_R).

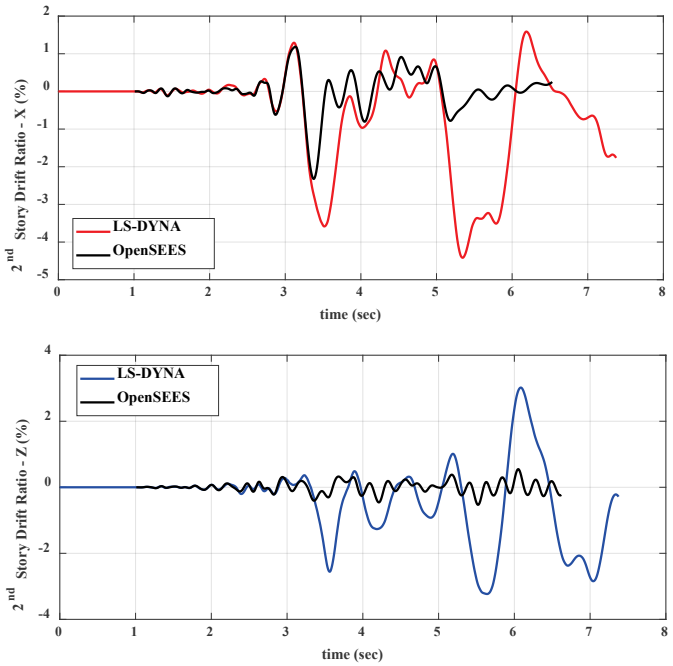

Figure B-20 Comparison of story-drift histories for the second story: COM2 – Motion 2 ($2\times MCE_R$).

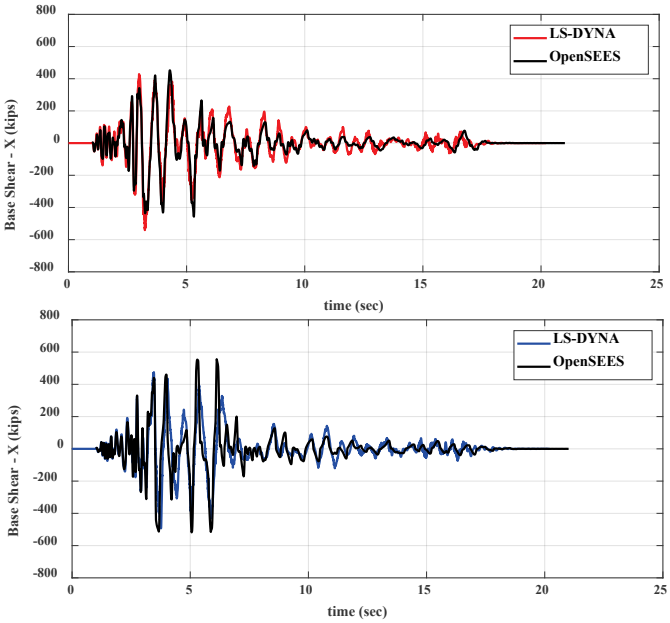

Figure B-21 Comparison of base-shear histories: COM2 – Motion 2 (MCE_R).

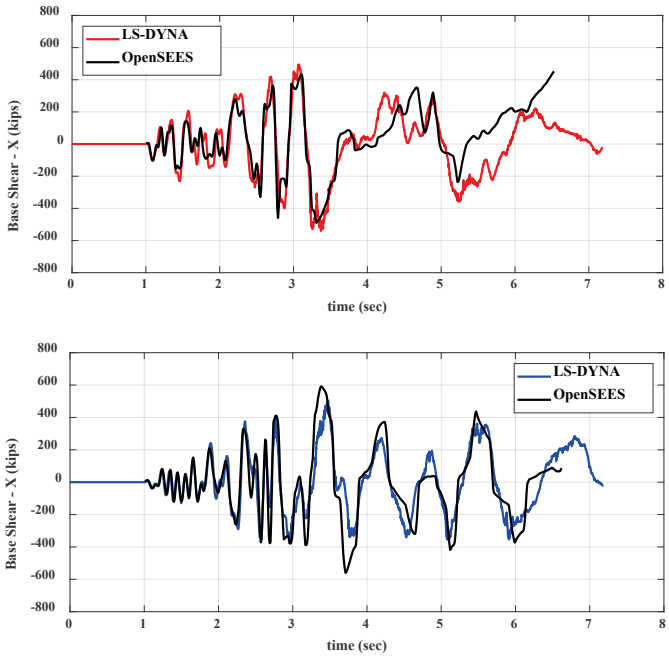

Figure B-22 Comparison of base-shear histories: COM2 – Motion 2 ($2\times MCE_R$).

B.3 Archetype COM3

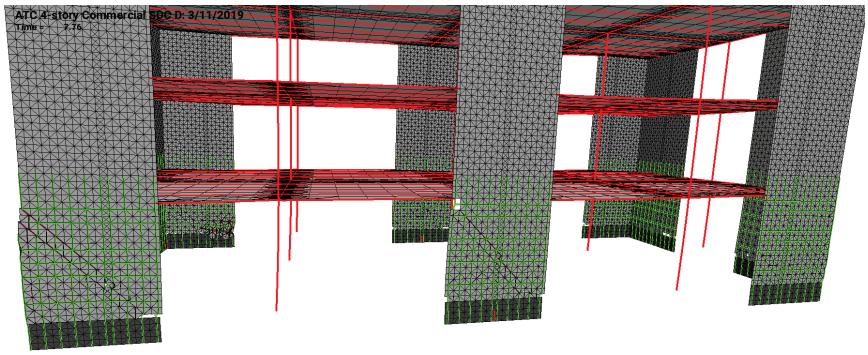

Figure B-23 Deformed meshes from refined model: COM3 (LS-DYNA) – Motion 1 ($2\times MCE_R$).

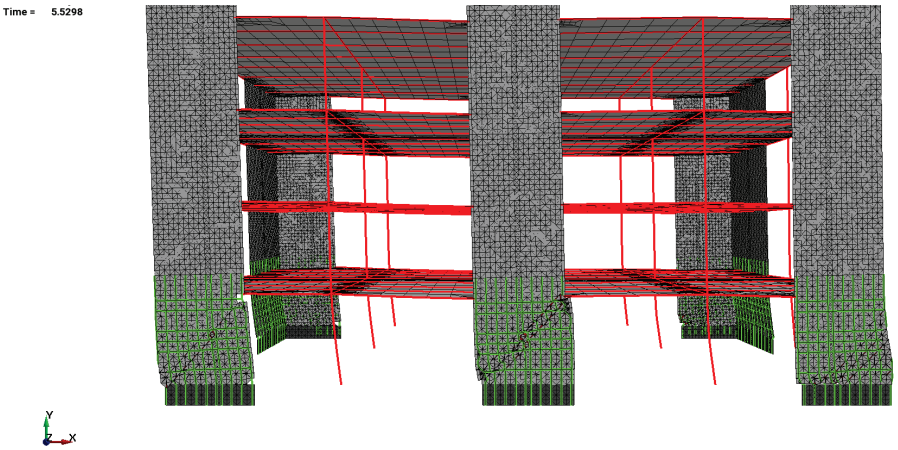

Figure B-24 Deformed meshes from refined model: COM3 (LS-DYNA) – Motion 2 ($1.8\times MCE_R$).

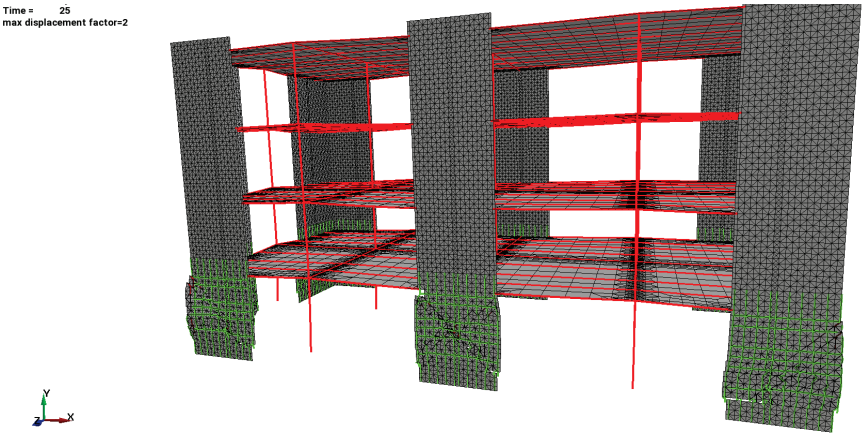

Figure B-25 Deformed meshes from refined model: COM3 (LS-DYNA) – Motion 17 ($2\times MCE_R$).

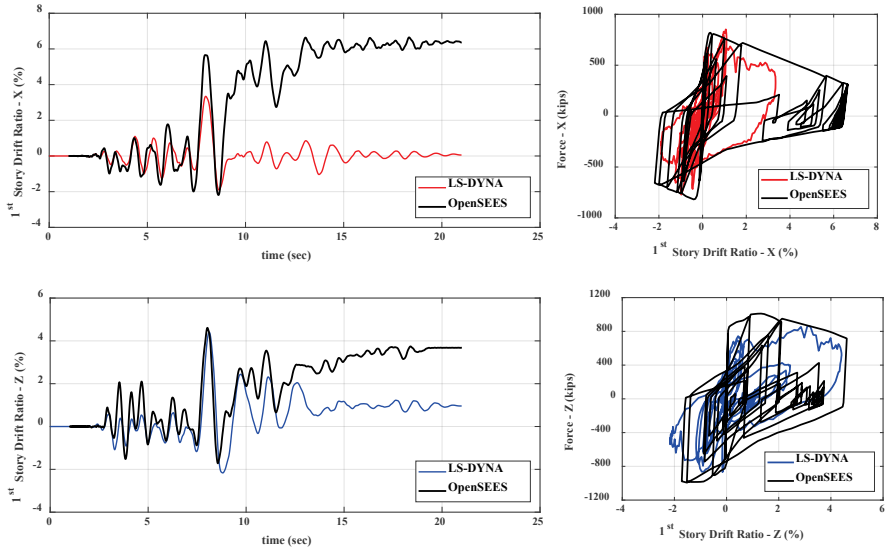

Figure B-26 Comparison of response histories for the first story: COM3 – Motion 1 (MCE_R).

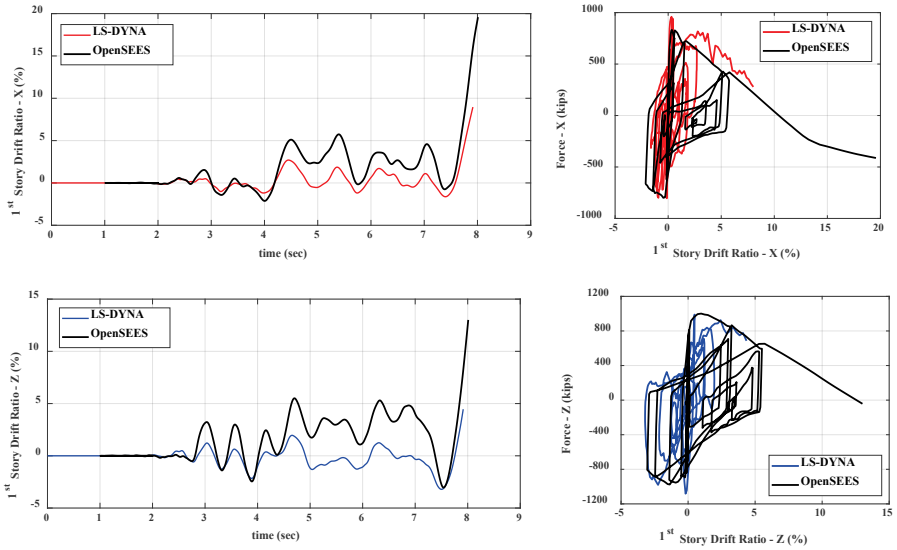

Figure B-27 Comparison of response histories for the first story: COM3 – Motion 1 ($2 \times MCE_R$).

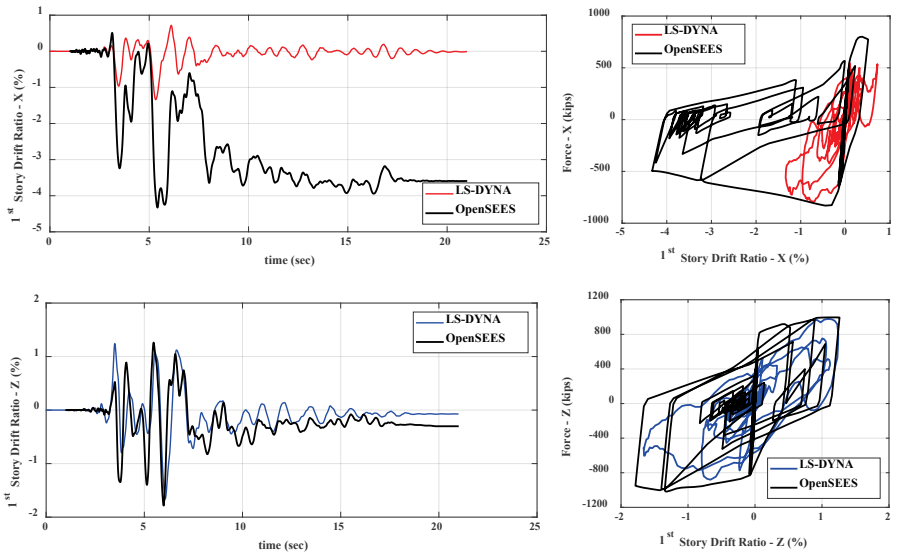

Figure B-28 Comparison of response histories for the first story: COM3 – Motion 2 (MCE_R).

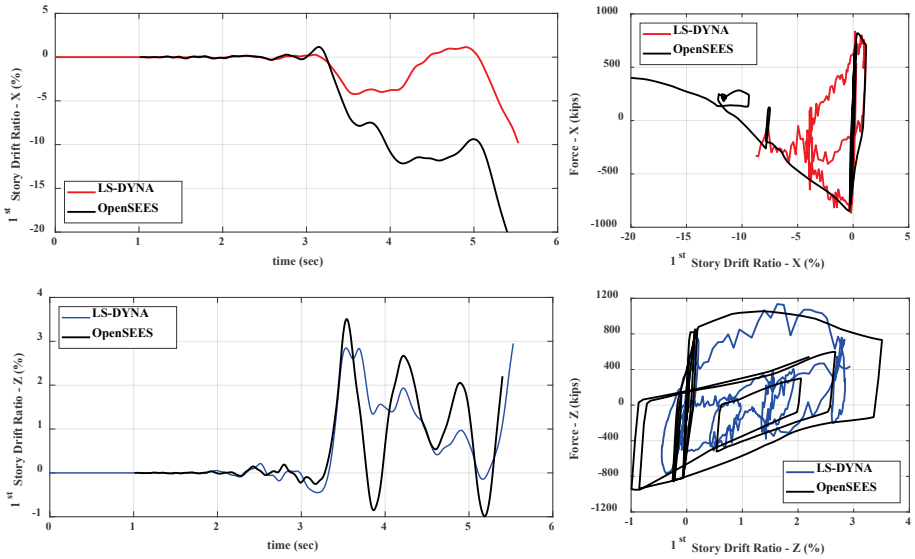

Figure B-29 Comparison of response histories for the first story: COM3 – Motion 2 ($1.8 \times MCE_R$).

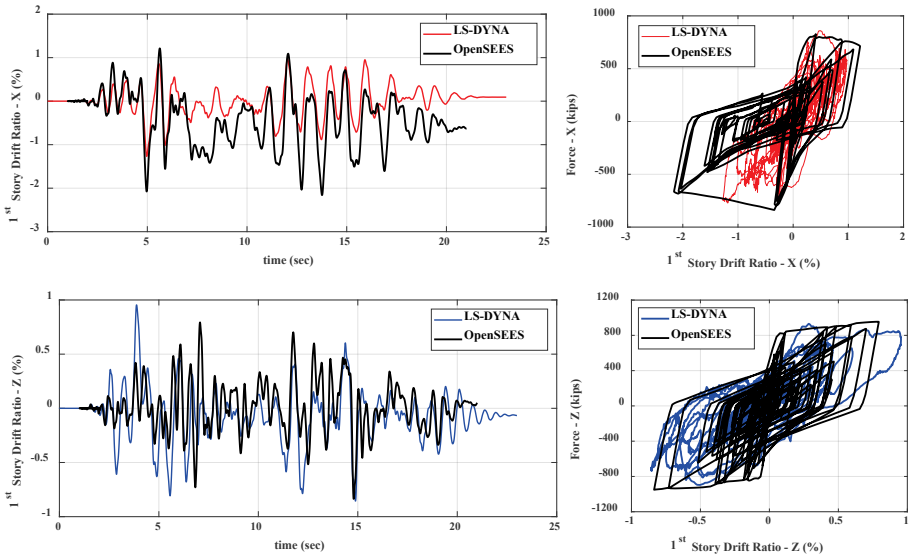

Figure B-30 Comparison of response histories for the first story: COM3 – Motion 17 (MCE_R).

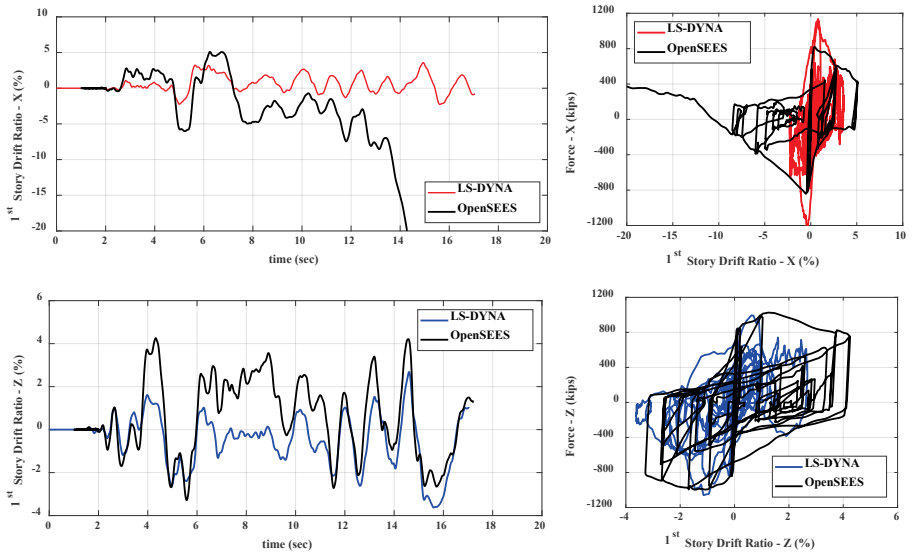

Figure B-31 Comparison of response histories for the first story: COM3 – Motion 17 ($2\times MCE_R$).

The nearly identical drift ratios for the second, third, and fourth stories of the LS-DYNA model shown in Figure B-32 and Figure B-33 are due to the rigid-body rotations of the walls above the first story. This was not captured by the OpenSees model, as previously discussed.

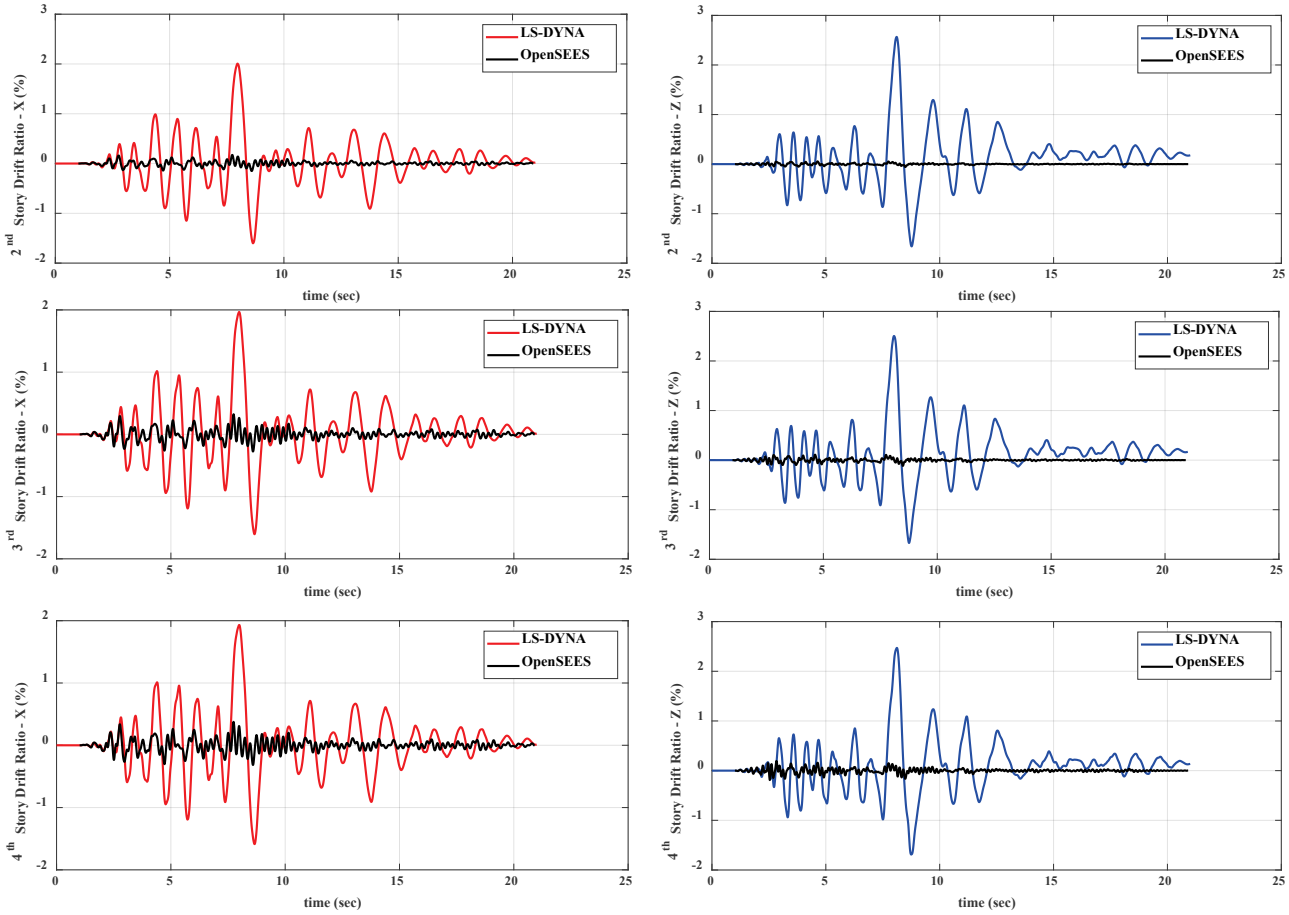

Figure B-32 Comparison of story-drift histories for the upper stories: COM3 – Motion 1 (MCE_R).

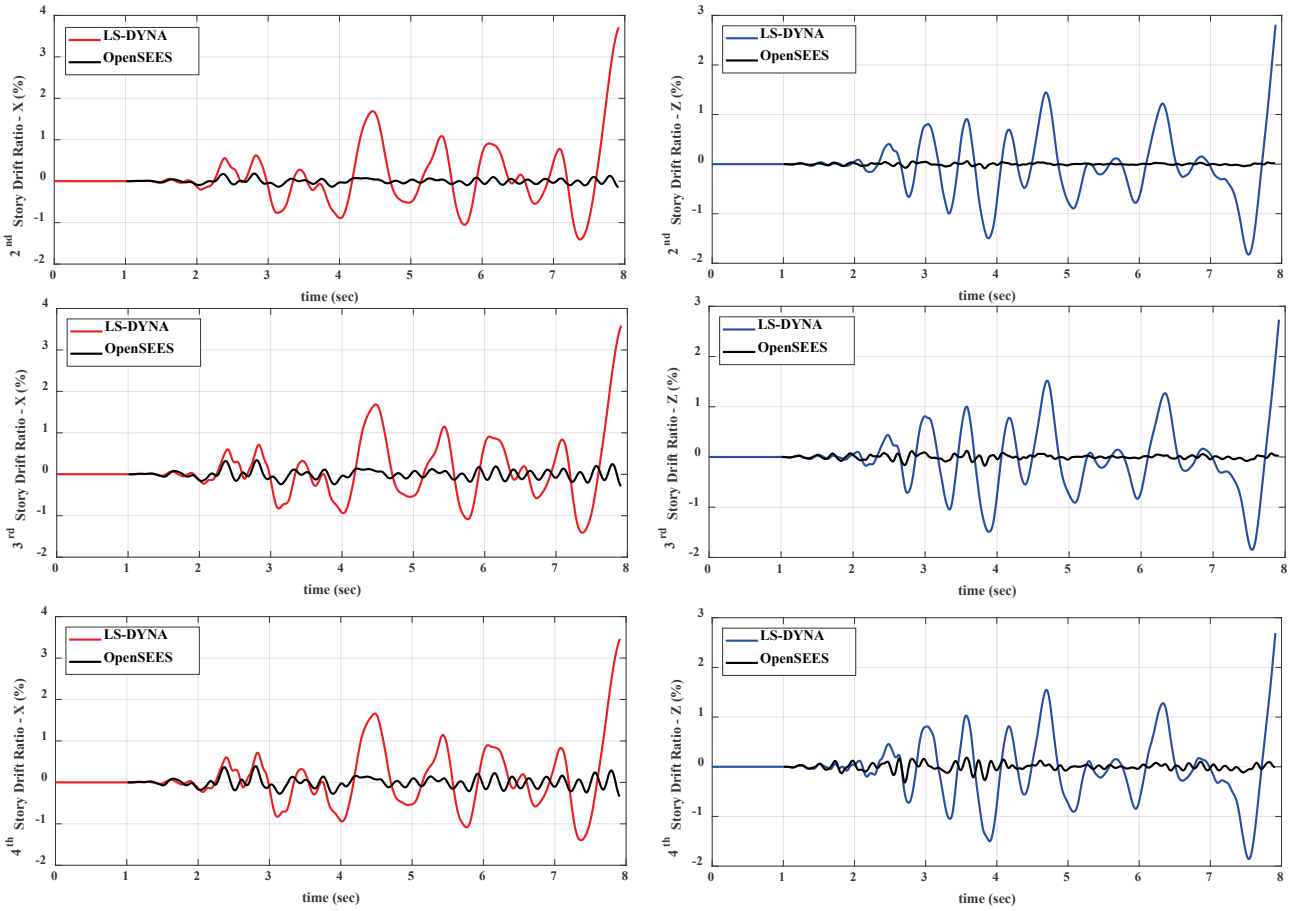

Figure B-33 Comparison of story-drift histories for the upper stories: COM3 – Motion 1 ($2\times MCE_R$).

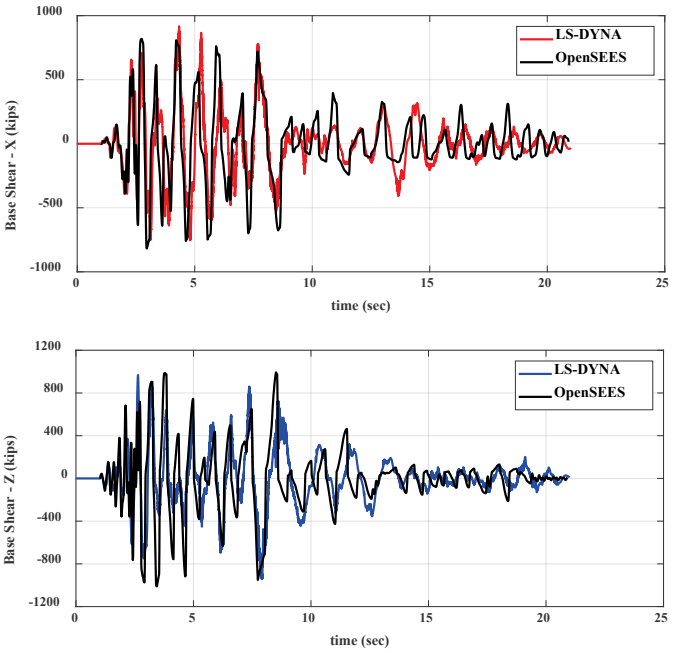

Figure B-34 Comparison of base-shear histories: COM3 – Motion 1 (MCE_R).

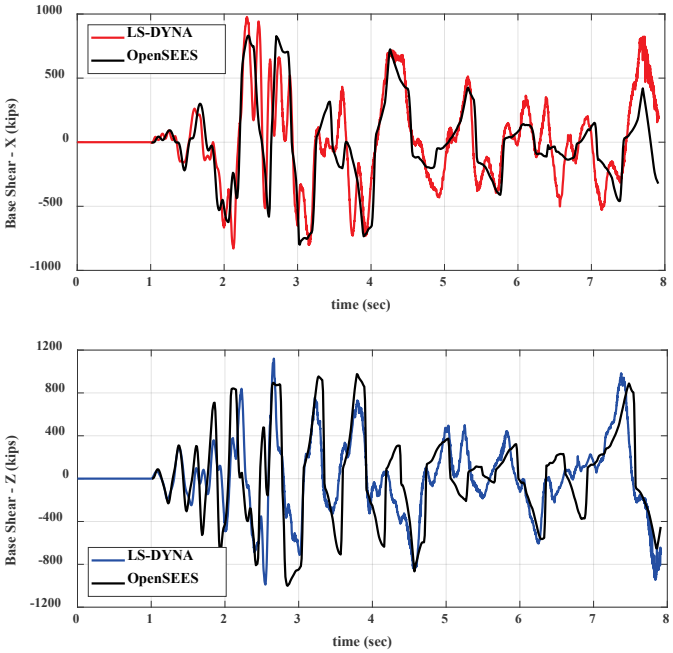

Figure B-35 Comparison of base-shear histories: COM3B – Motion 1 ($2\times MCE_R$).

B.4 Archetype COM4

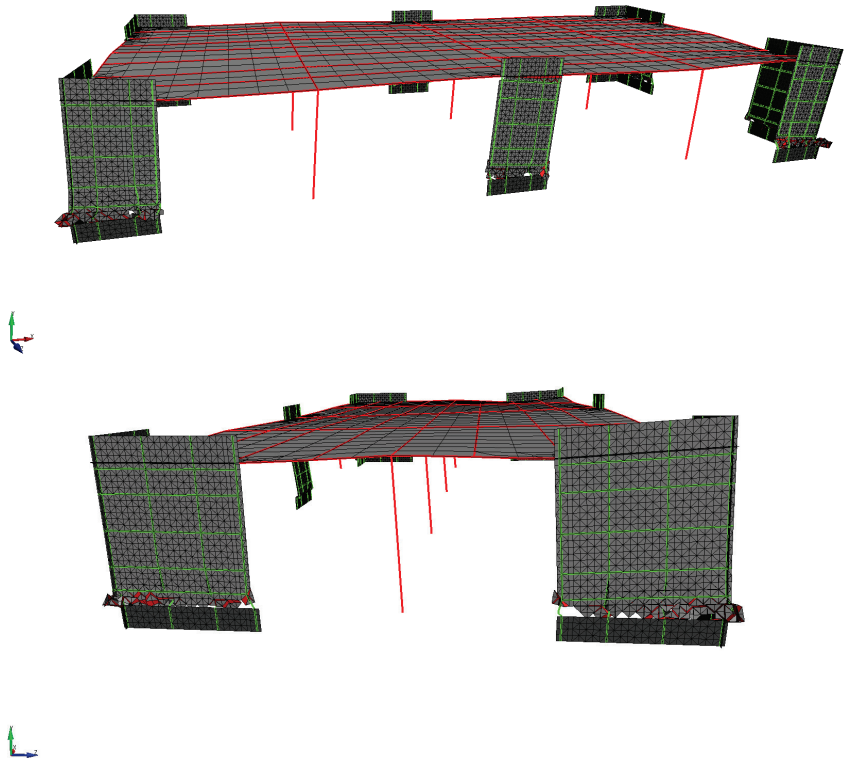

Figure B-36 Deformed meshes from refined model: COM4 (LS-DYNA) – Motion 1 ($2\times MCE_R$).

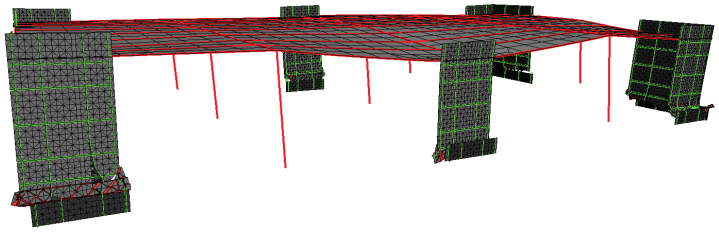

Figure B-37 Deformed meshes from refined model: COM4 (LS-DYNA) – Motion 2 ($1.8\times MCE_R$).

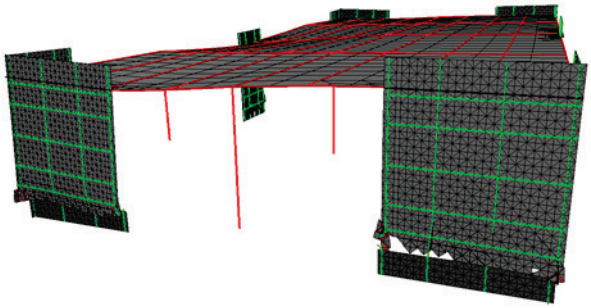

Figure B-38 Deformed meshes from refined model: COM4 (LS-DYNA) – Motion 17 ($2\times MCE_R$).

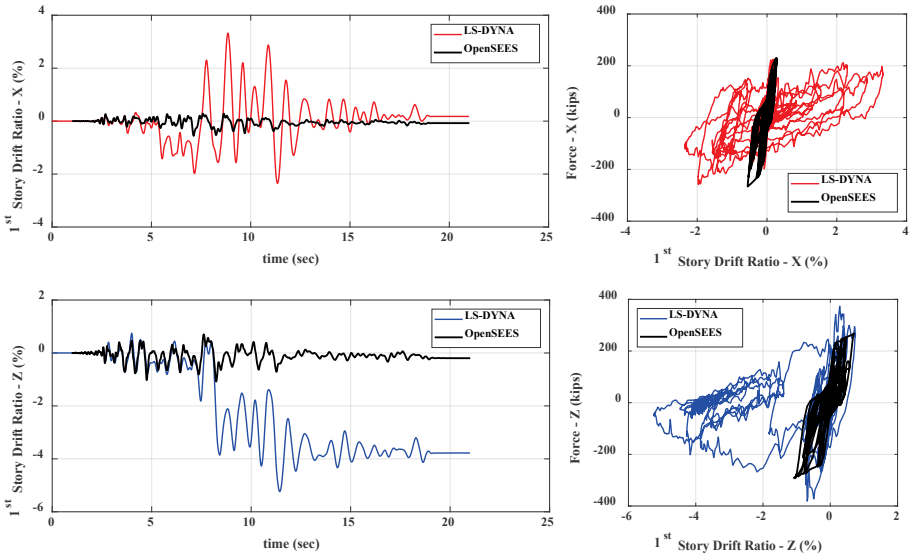

Figure B-39 Comparison of response histories for the first story: COM4 – Motion 1 (MCE_R).

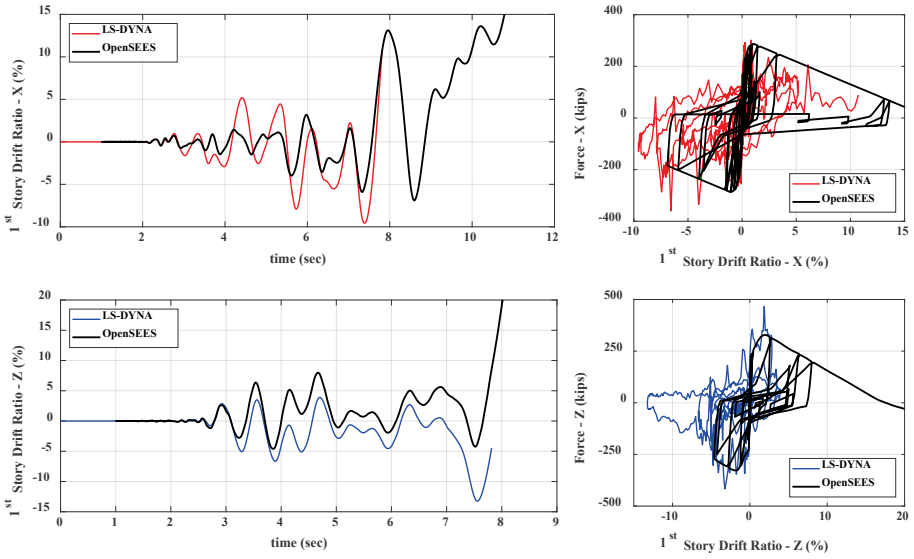

Figure B-40 Comparison of response histories for the first story: COM4 – Motion 1 ($2\times MCE_R$).

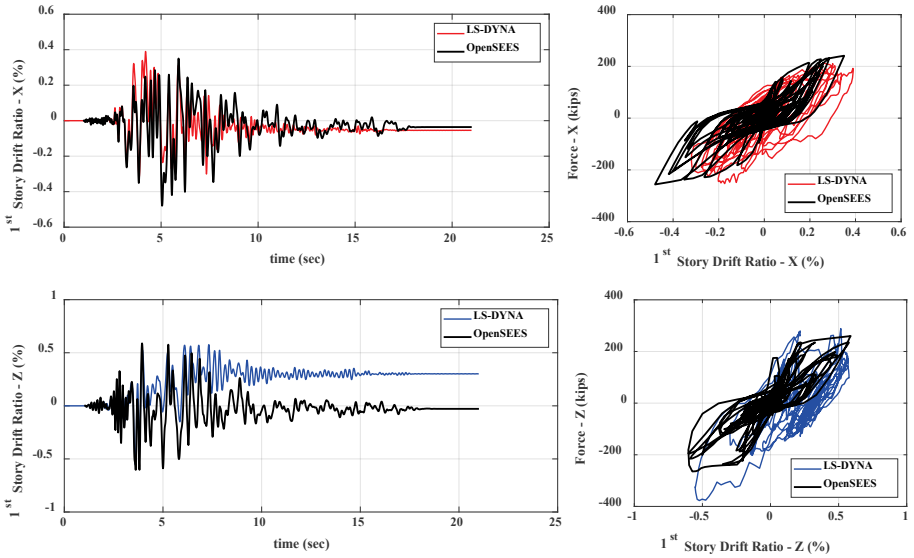

Figure B-41 Comparison of response histories for the first story: COM4 – Motion 2 (MCE_R).

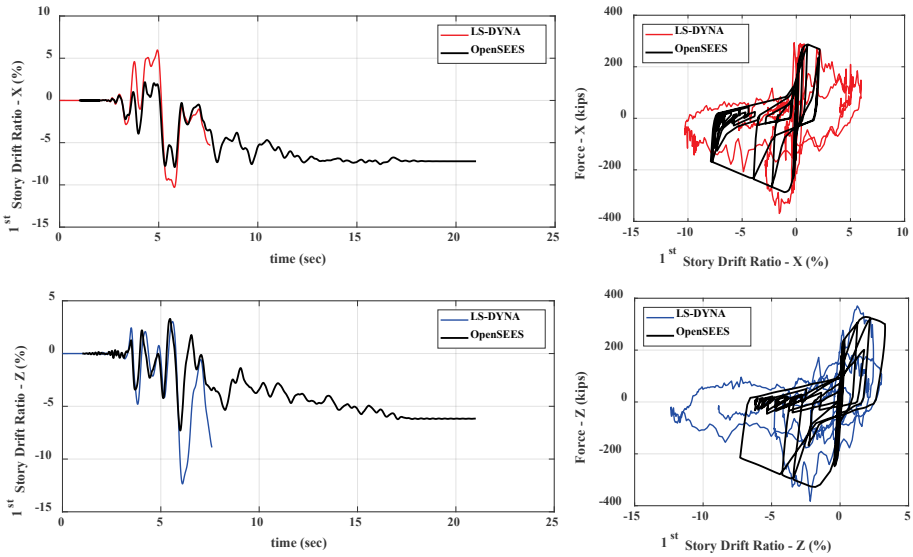

Figure B-42 Comparison of response histories for the first story: COM4 – Motion 2 ($1.8\times MCE_R$).

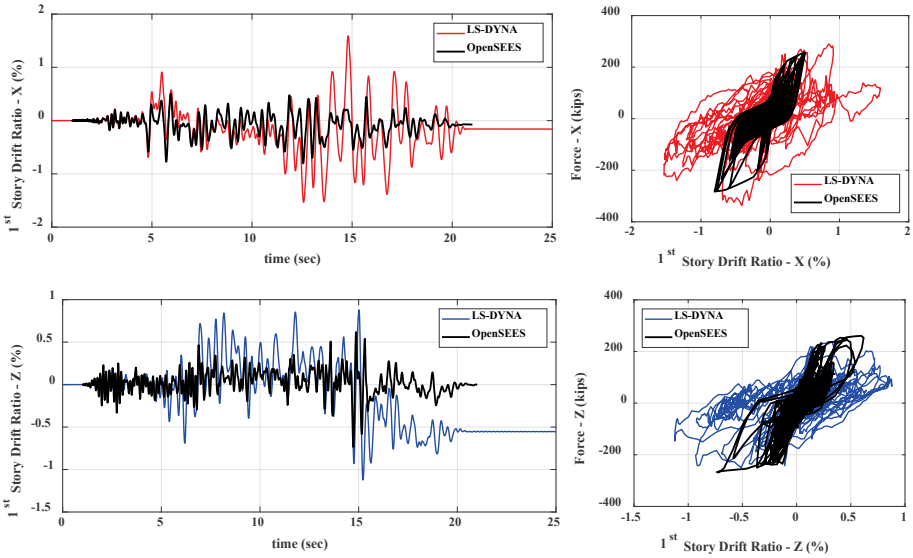

Figure B-43 Comparison of response histories for the first story: COM4 – Motion 17 (MCE_R).

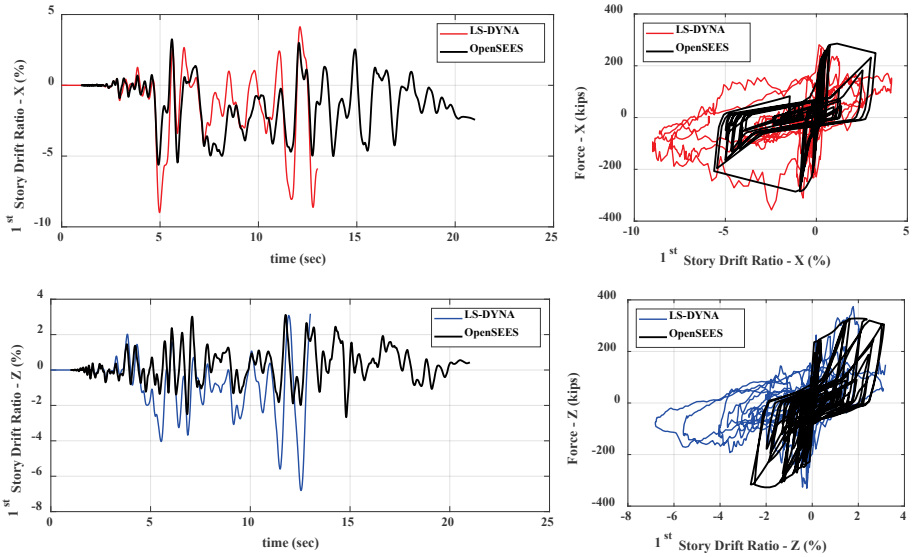

Figure B-44 Comparison of response histories for the first story: COM4 – Motion 17 ($2\times MCE_R$).

B.5 Archetype COM5

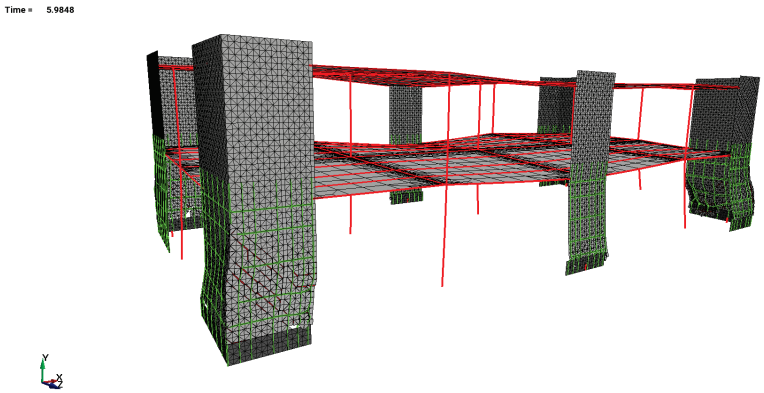

Figure B-45 Deformed meshes from refined model: COM5 (LS-DYNA) – Motion 1 (MCE_R).

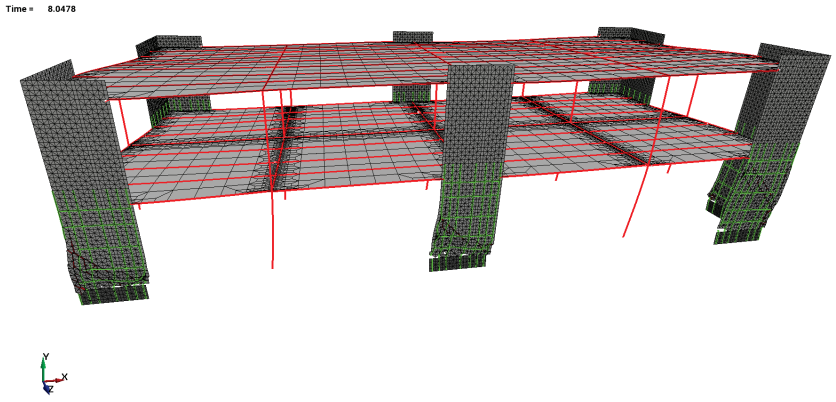

Figure B-46 Deformed meshes from refined model: COM5 (LS-DYNA) – Motion 2 ($1.9\times MCE_R$).

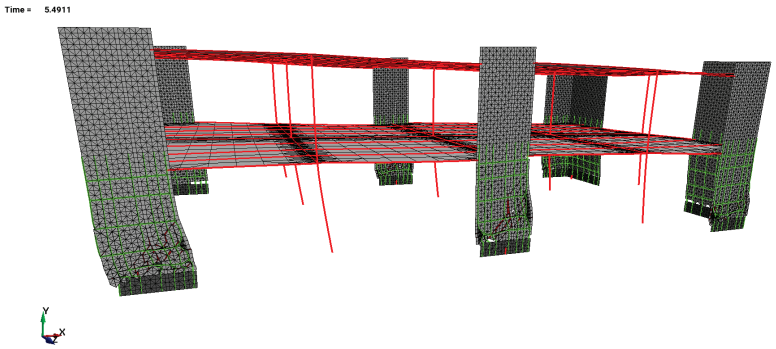

Figure B-47 Deformed meshes from refined model: COM5 (LS-DYNA) – Motion 17 ($2\times MCE_R$).

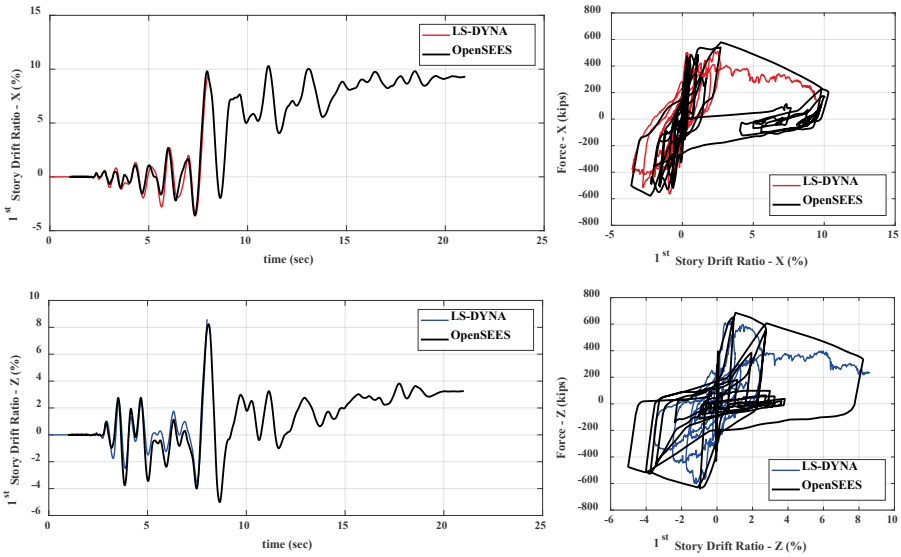

Figure B-48 Comparison of response histories for the first story: COM5 – Motion 1 (MCE_R).

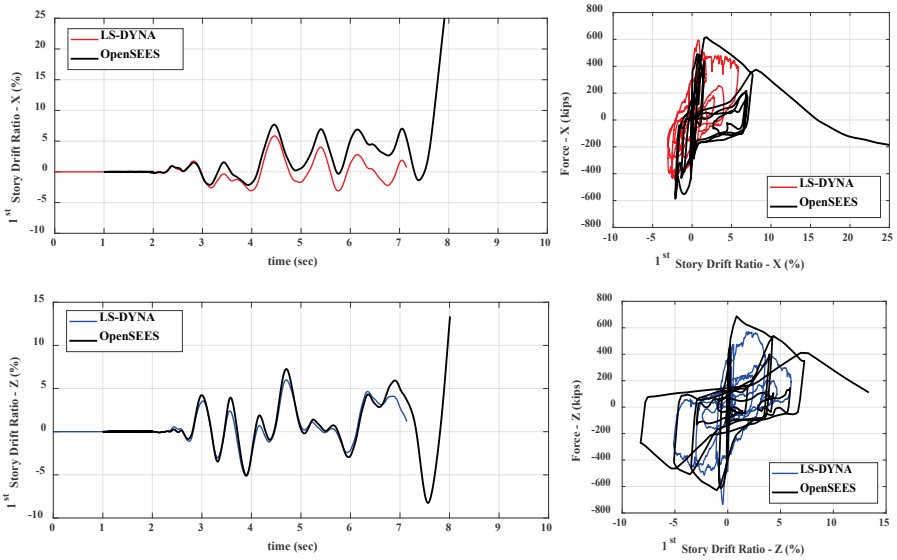

Figure B-49 Comparison of response histories for the first story: COM5 – Motion 1 ($2\times MCE_R$).

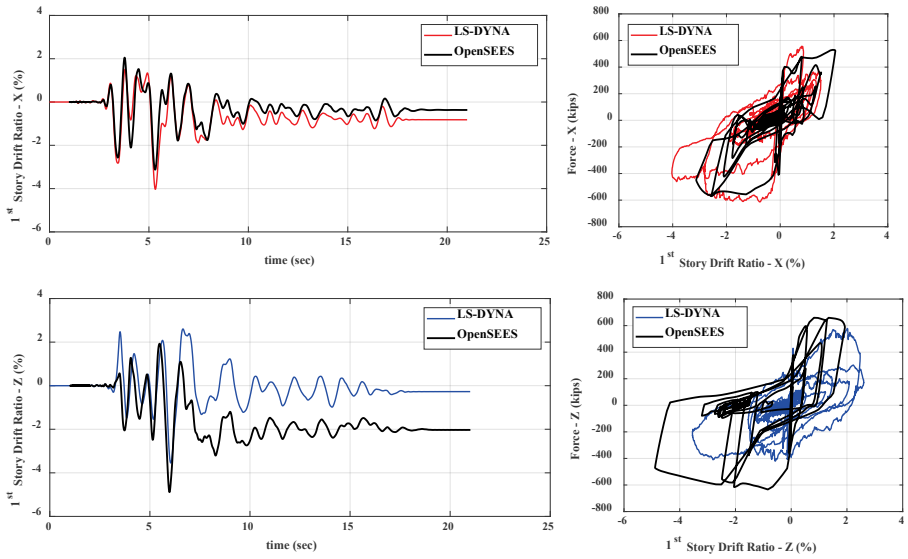

Figure B-50 Comparison of response histories for the first story: COM5 – Motion 2 (MCE_R).

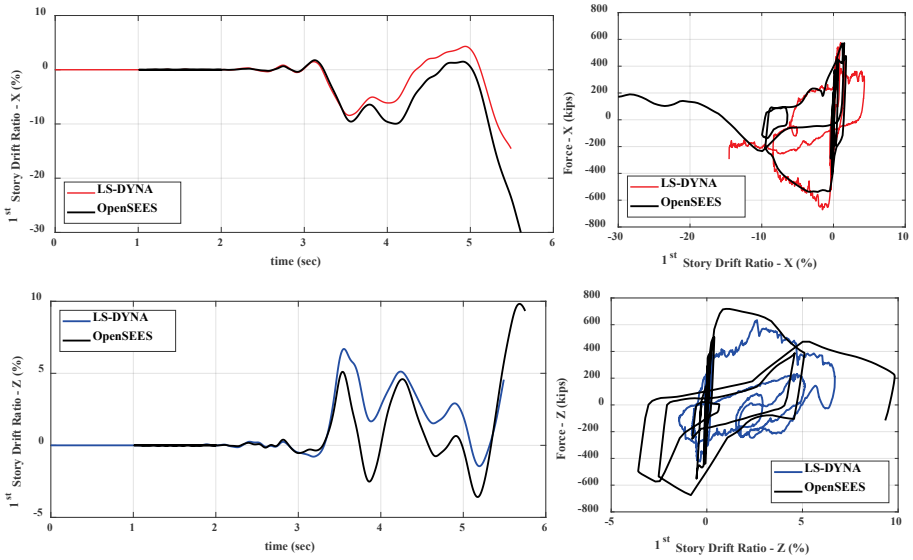

Figure B-51 Comparison of response histories for the first story: COM5 – Motion 2 ($1.9 \times MCE_R$).

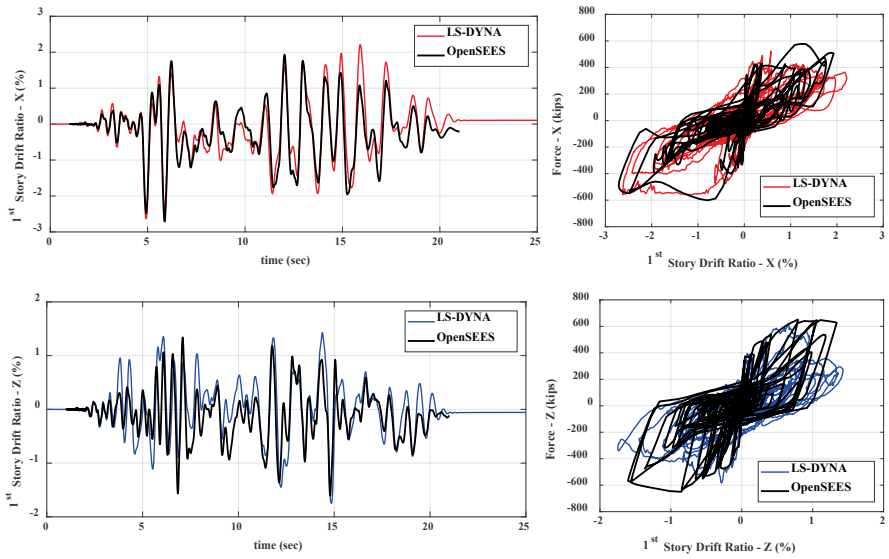

Figure B-52 Comparison of response histories for the first story: COM5 – Motion 17 (MCE_R).

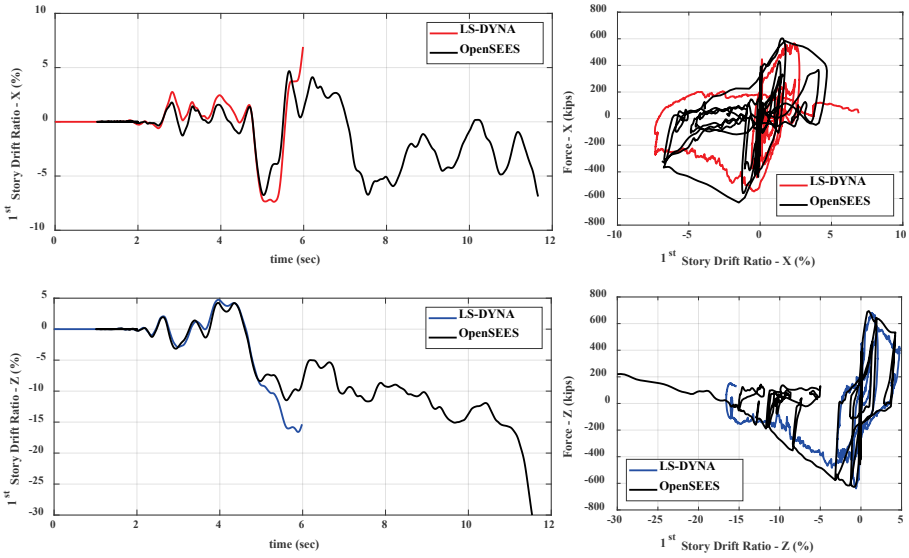

Figure B-53 Comparison of response histories for the first story: COM5 – Motion 17 ($2\times MCE_R$).

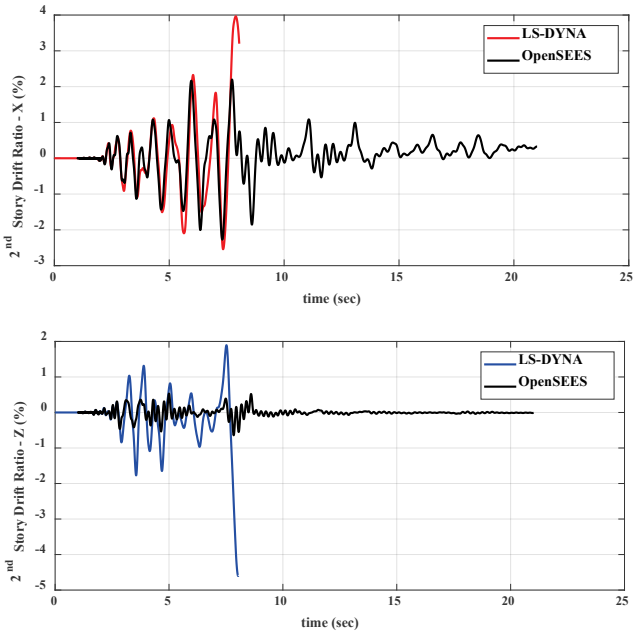

Figure B-54 Comparison of story-drift histories for the second story: COM5 – Motion 1 (MCE_R).

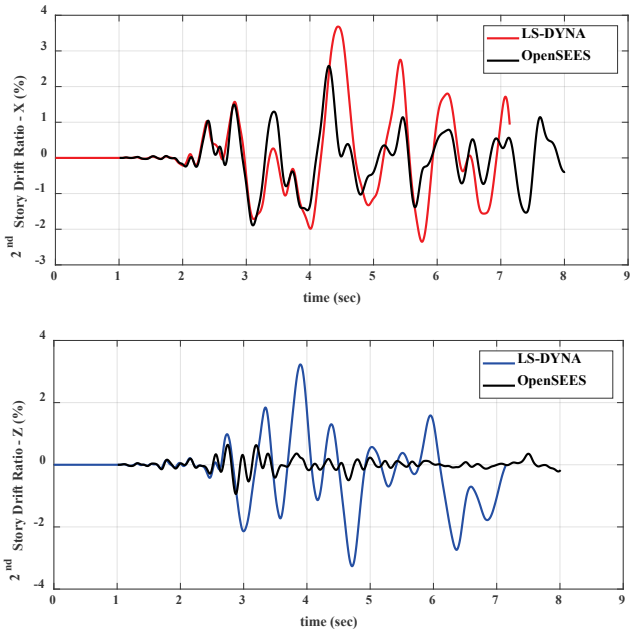

Figure B-55 Comparison of story-drift histories for the second story: COM5 – Motion 1 ($2\times MCE_R$).

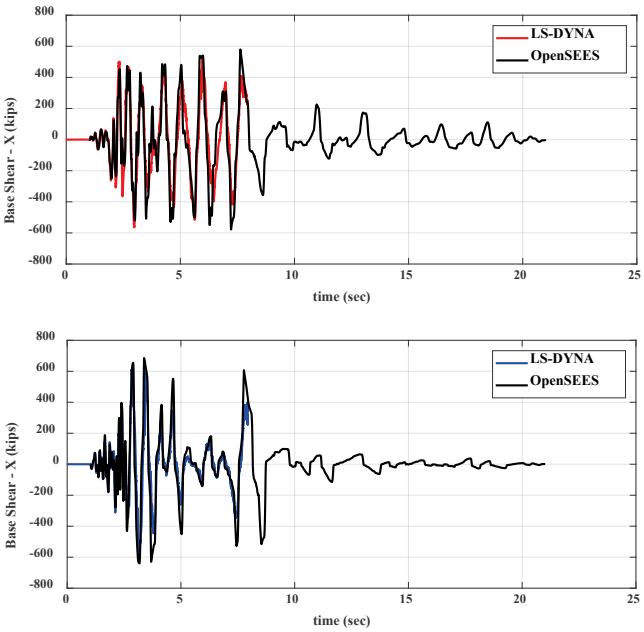

Figure B-56 Comparison of base-shear histories: COM5 – Motion 1 (MCE_R).

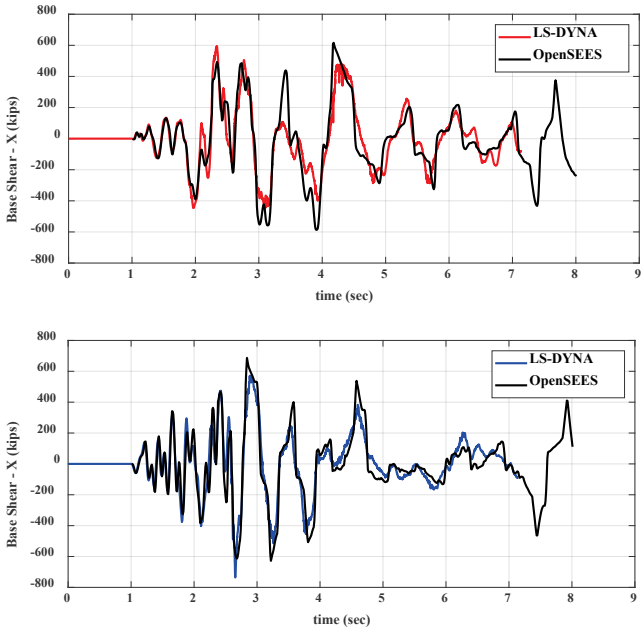

Figure B-57 Comparison of base-shear histories: COM5 – Motion 1 ($2\times MCE_R$).

B.6 Archetype COM6

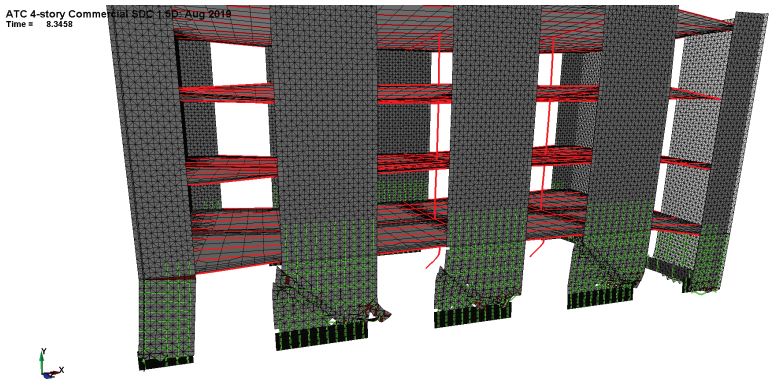

Figure B-58 Deformed meshes from refined model: COM6 (LS-DYNA) – Motion 1 ($2\times MCE_R$).

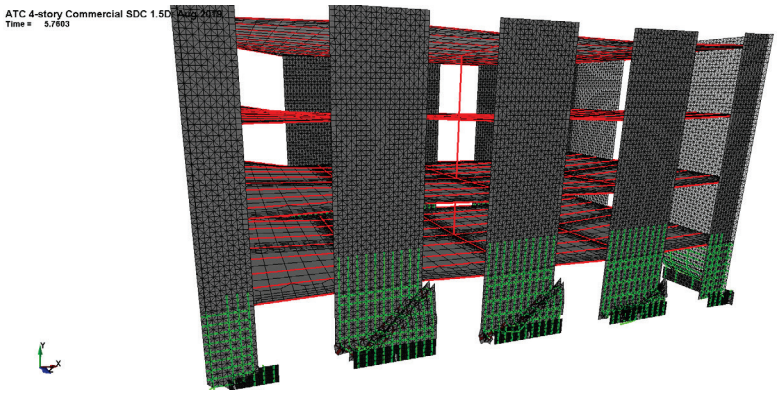

Figure B-59 Deformed meshes from refined model: COM6 (LS-DYNA) – Motion 2 ($2\times MCE_R$).

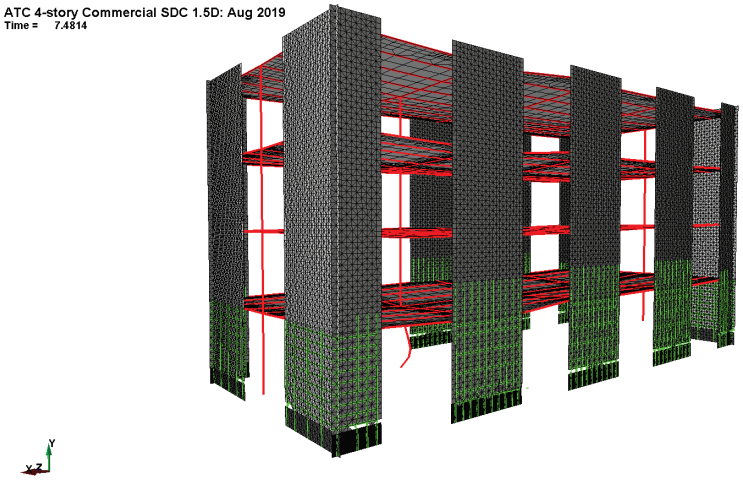

Figure B-60 Deformed meshes from refined model: COM6 (LS-DYNA) – Motion 17 ($2\times MCE_R$).

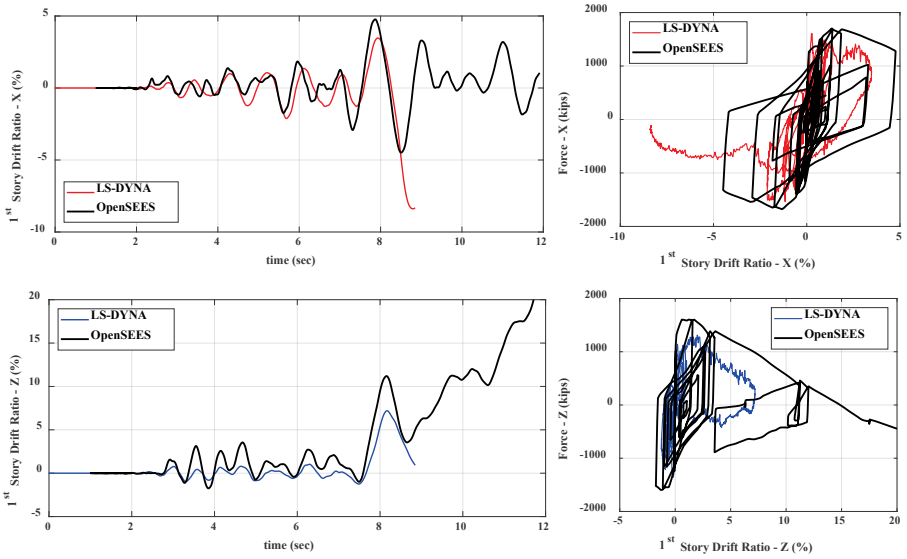

Figure B-61 Comparison of response histories for the first story: COM6 – Motion 1 (MCE_R).

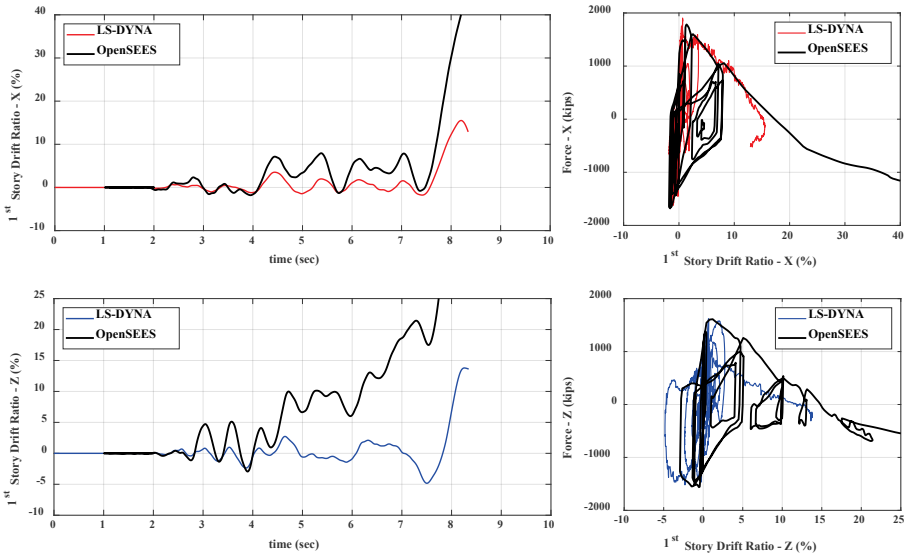

Figure B-62 Comparison of response histories for the first story: COM6 – Motion 1 ($2\times MCE_R$).

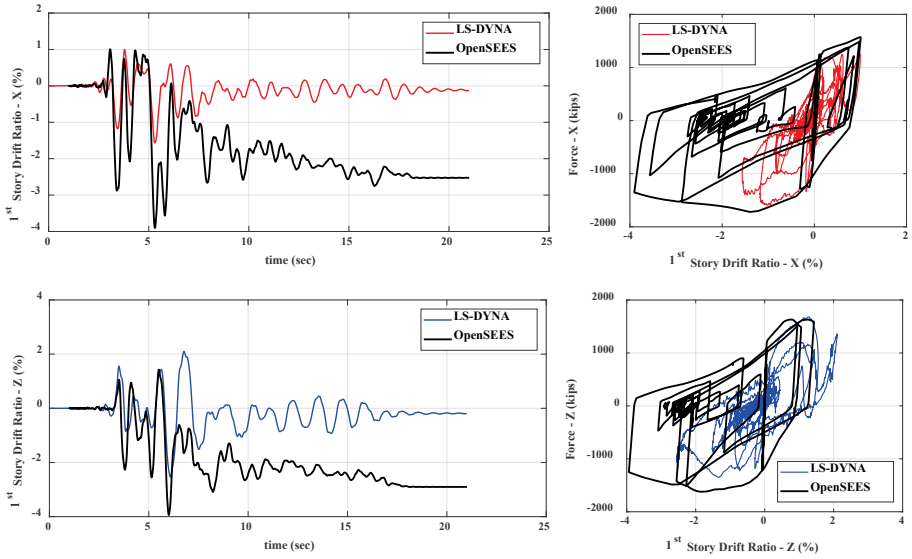

Figure B-63 Comparison of response histories for the first story: COM6 – Motion 2 (MCE_R).

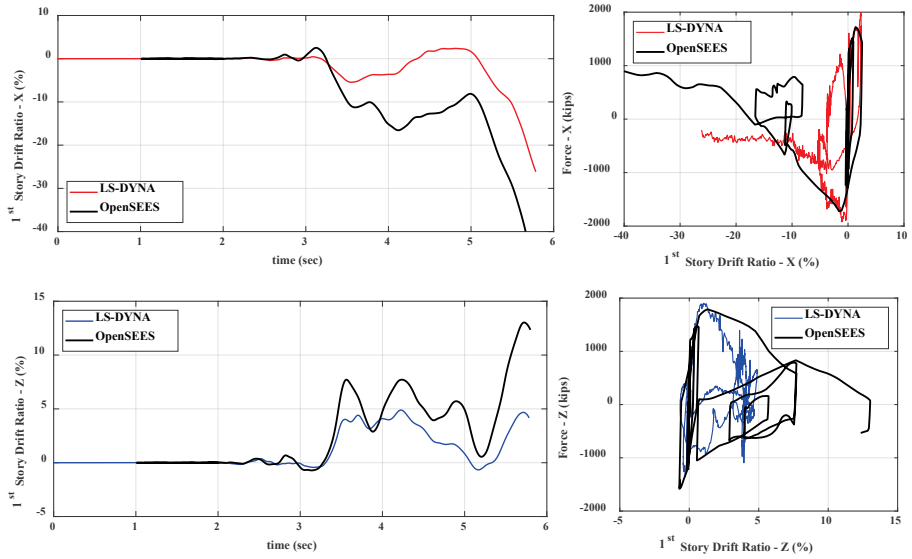

Figure B-64 Comparison of response histories for the first story: COM6 – Motion 2 ($2\times MCE_R$).

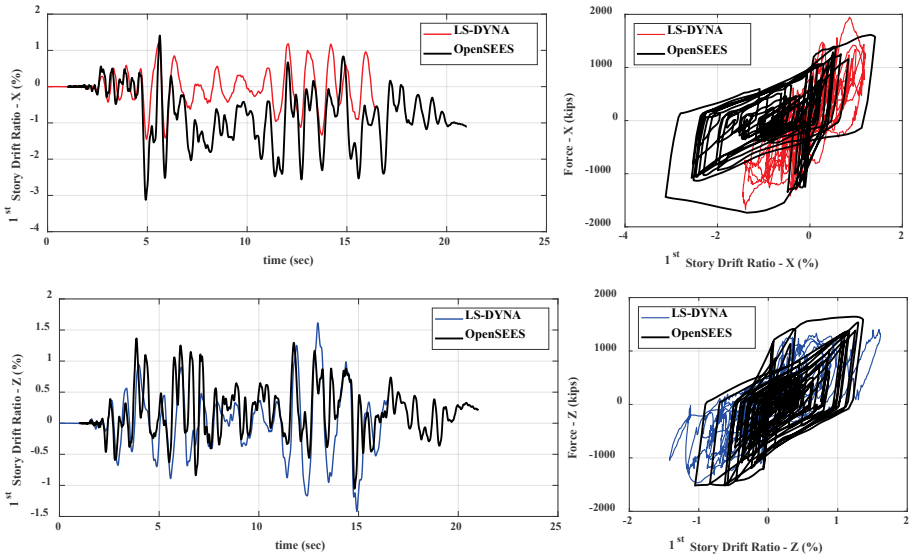

Figure B-65 Comparison of response histories for the first story: COM6 – Motion 17 (MCE_R).

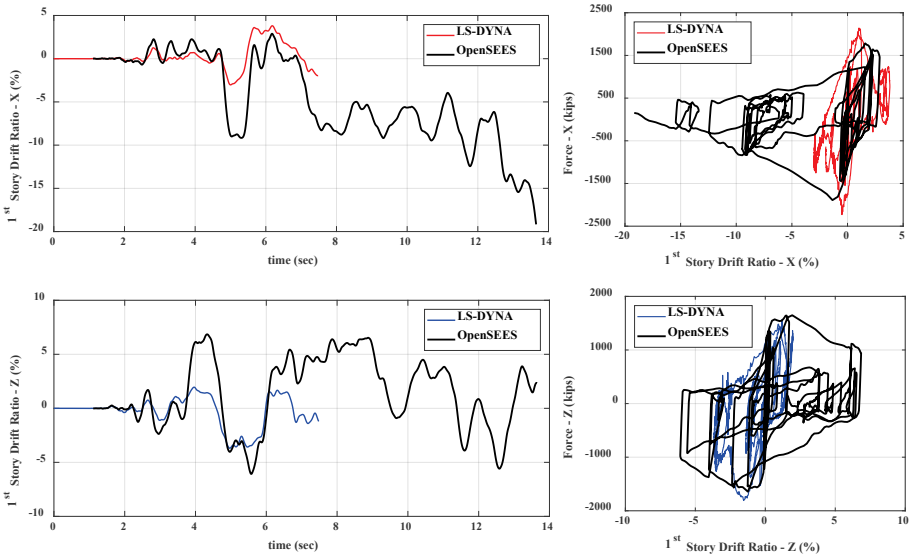

Figure B-66 Comparison of response histories for the first story: COM6 – Motion 17 ($2\times MCE_R$).

The nearly identical drift ratios for the second, third, and fourth stories of the LS-DYNA model shown in Figure B-67 and Figure B-68 are due to the rigid-body rotations of the walls above the first story. This was not captured by the OpenSees model, as previously discussed.

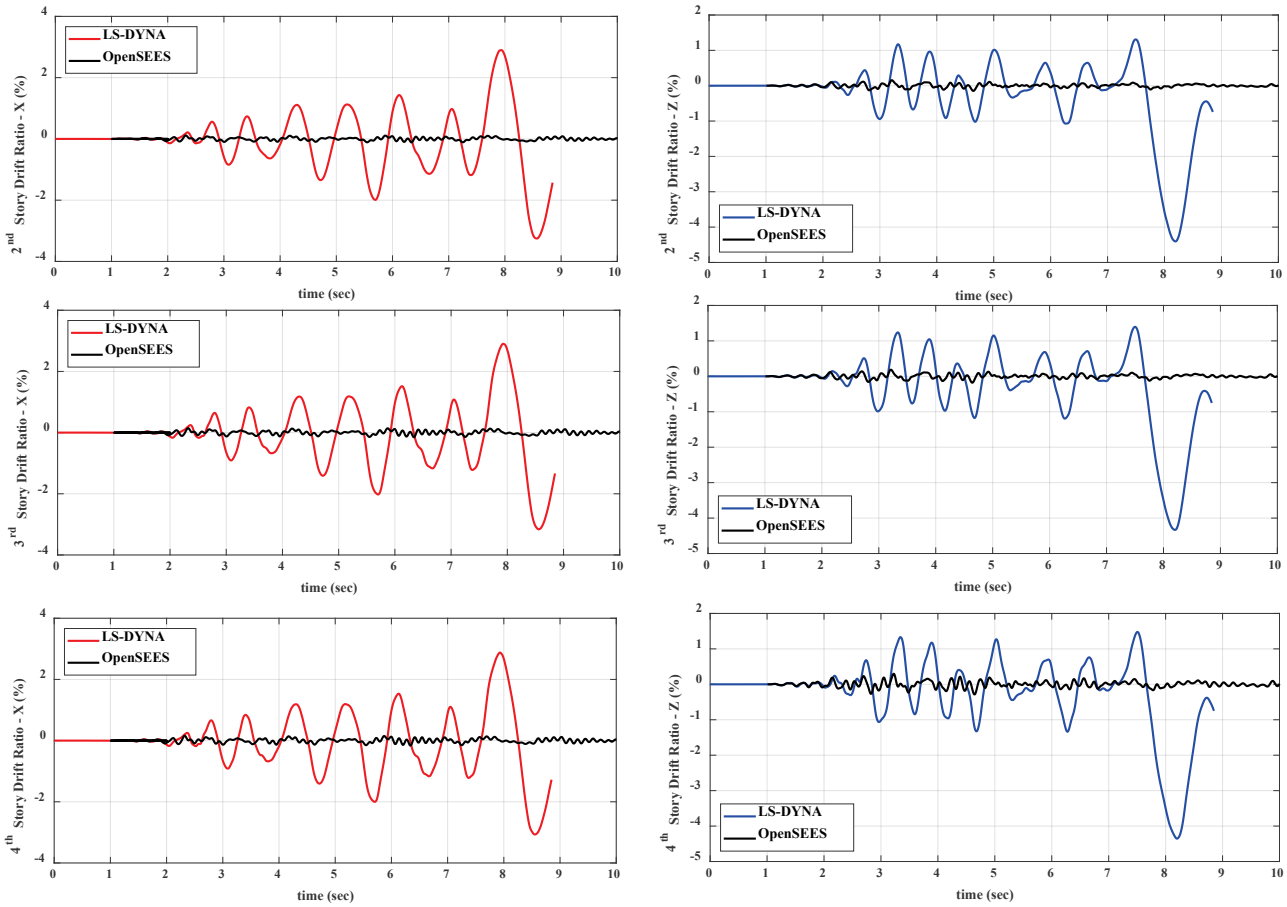

Figure B-67 Comparison of story-drift histories for the upper stories: COM6 – Motion 1 (MCE_R).

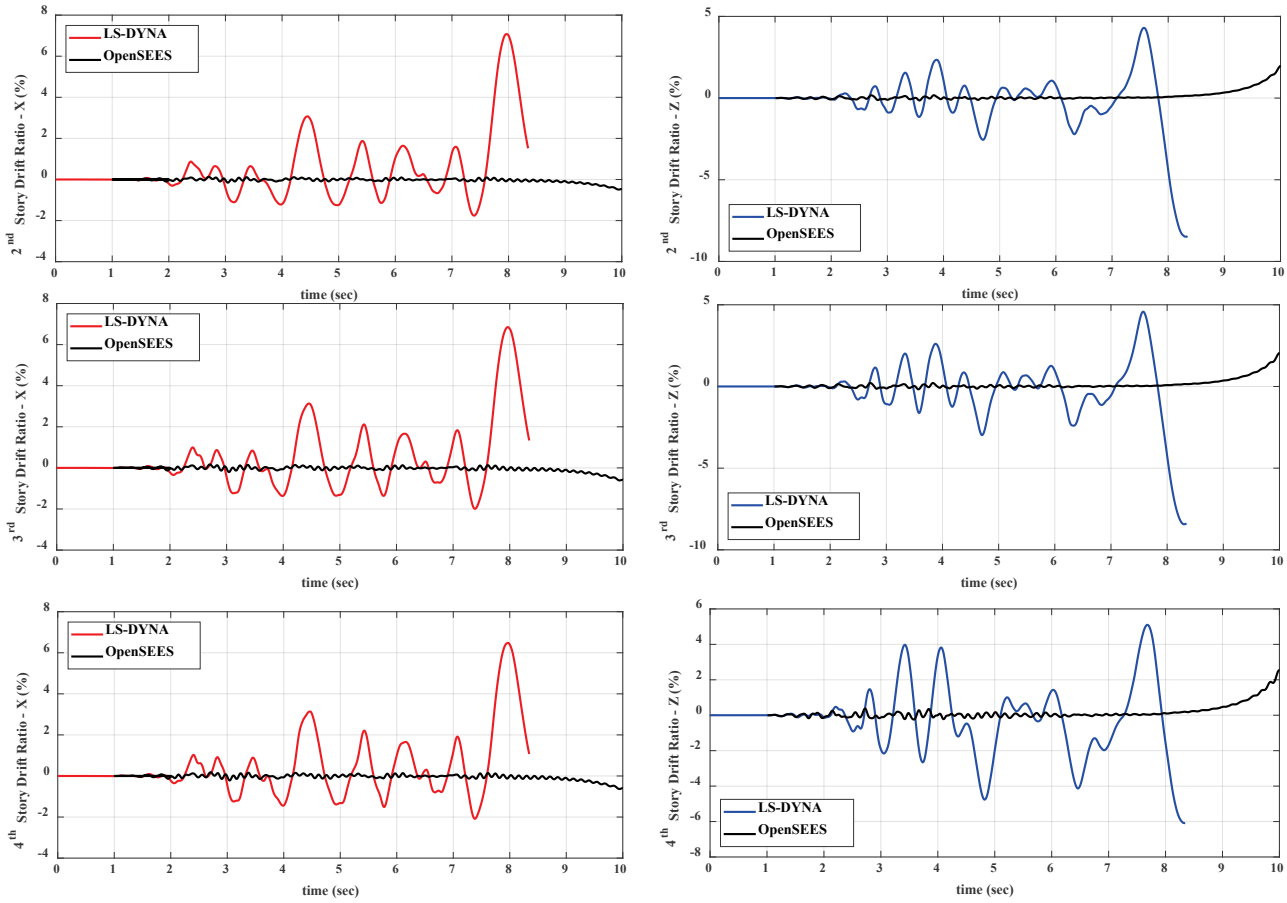

Figure B-68 Comparison of story-drift histories for the upper stories: COM6 – Motion 1 ($2\times MCE_R$).

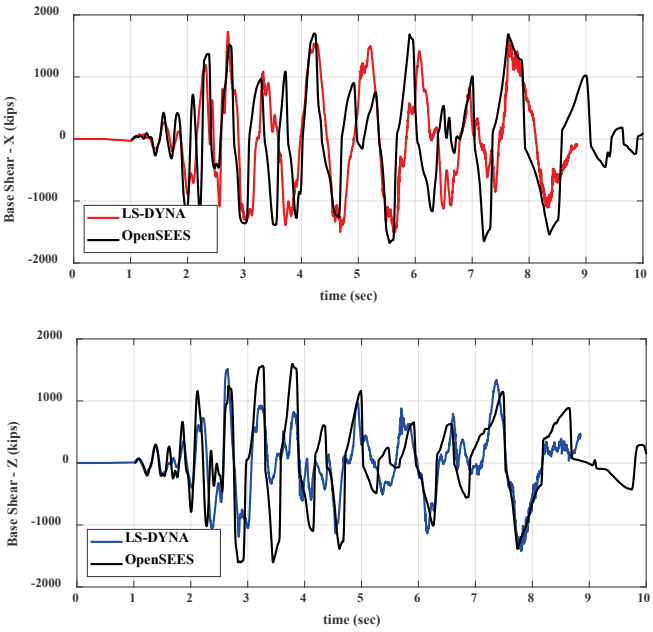

Figure B-69 Comparison of base-shear histories: COM6 – Motion 1 (MCE_R).

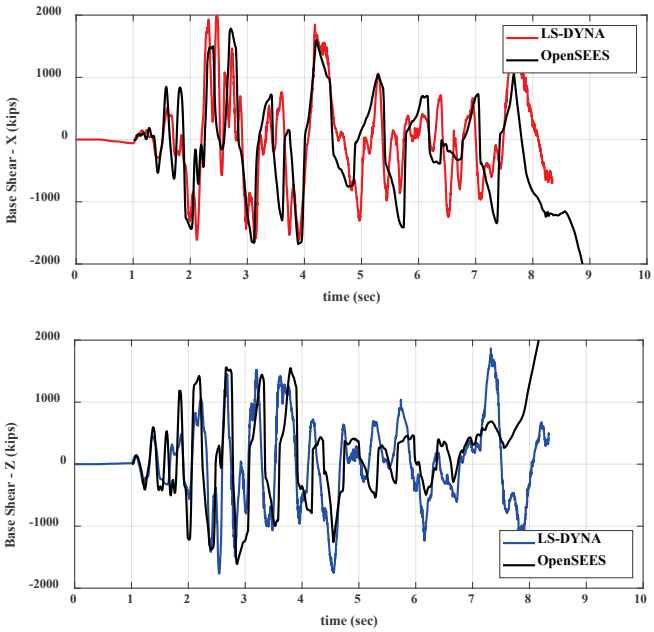

Figure B-70 Comparison of base-shear histories: COM6 – Motion 1 ($2\times MCE_R$).

Appendix C

Development of Soil Springs, Soil Dampers, and Frequency-Modified Ground Motion Records for the SSI Parametric Study

C.1 Introduction

This appendix introduces soil-structure interaction (SSI) theory and documents the means and methods used to develop soil springs, soil dampers, and frequency-modified ground motion records that are used in the SSI and foundation flexibility parametric study. More information about the implementation of the parameters and the results of the parametric study can be found in Chapter 4 and Chapter 5, respectively.

C.2 Background and Theory

The coupled response to ground movement of a structure and its foundation soil is identified here as soil-structure interaction. SSI is a complex phenomenon with a large body of literature. NIST GCR 12-917-21 (NIST, 2012b) synthesized the current state-of-the-art understanding of SSI effects and guidance on modeling techniques based on that knowledge. FEMA P-1050*, NEHRP Recommended Seismic Provisions for New Buildings and Other Structures* (FEMA, 2015b), includes guidance on seismic-design procedures including the effects of SSI. This appendix briefly introduces the physical effects of seismic SSI on a building system and summarizes some of the principal analysis methods as they relate to this study.

C.2.1 Inertial-Interaction Effects

Inertial interaction is caused by the inertia of the structure mass, which, during dynamic loading, imposes shear and moment loads on the foundation. These loads must then be supported by the surrounding soil and, due to soil flexibility, cause foundation translation and rotation.

The default case for the analysis of structural response is the *fixed-base* condition, where the foundation and supporting soil are assumed to be perfectly rigid. The *flexible-base* condition includes the deformation of the

soil and foundation. The soil flexibility increases the overall flexibility of the building, resulting in a lengthening of the fundamental period. As is well known from spectral acceleration diagrams, the energy content of an earthquake varies with frequency. Significant period lengthening will impact the seismic demand on the structure, as spectral acceleration is often used to estimate base shear for an elastic response of a structure. In general, for structures with short fundamental periods, period lengthening will cause an increase in spectral acceleration, whereas for structures with long periods, spectral acceleration decreases with period lengthening. The change in the flexibility of the system can also change the load and deformation distribution within the structure and foundation, the effects of which are often complicated.

In addition to changing flexibility, inertial interaction also provides two mechanisms for energy dissipation: (1) radiation damping; and (2) hysteretic or material damping. Radiation damping is caused by energy being radiated geometrically away from the foundation, out into the surrounding soil during vibration cycles. Hysteretic damping is caused by internal energy dissipation within the soil material. The increase in damping due to inertial-interaction effects will tend to decrease the response of a flexible-base structure.

Soil stiffness and damping are parameterized as impedance functions, which are theoretically known to be frequency dependent. Stiffness can be described as a spring coefficient, k, and damping can be given as a damping ratio, β. Translational stiffness is relatively constant with frequency, whereas rotational stiffness decreases and damping increases with increasing frequency.

C.2.2 Kinematic-Interaction Effects

In addition to inertial-interaction effects, SSI also changes the ground motions in the vicinity of the soil-structure system. The ground motions that would occur without the existence of the structure are known as free-field ground motions. The presence of the relatively stiff foundation, which imposes loads on the soil, changes the ground motions near the structure. Ground motions that include the altering effects of SSI are known as Foundation Input Motions.

Kinematic-interaction includes the phenomenon known as base-slab averaging, where the natural spatial variation in the free-field ground motions throughout the area occupied by the structure must be averaged due to the stiffness of the foundation. The spatial variation in ground motions includes both a deterministic component due to wave-passage effects and a stochastic

component due to natural seismic wave-path complexities. Kinematic interaction also includes effects due to foundation embedment, which are not discussed here in detail due to the shallow foundation depths of the building archetypes selected for this study.

Kinematic-interaction effects are estimated using transfer functions between the free-field ground motion and the foundation input motion. Semi-empirical models for the transfer function indicate that the foundation input motion will be smaller than the free-field motion at high frequencies, and they are predicted to be the same at low frequencies.

C.3 Representative Field Sites

Two soil sites with differing soil conditions were selected for the SSI study. The sites vary in terms of site class, which was classified based on the shear-wave velocity in the upper 30 meters (V_{s30}), per FEMA P-1050. The soft site was selected to be near the site class D/E boundary, with a target V_{s30} = 180 m/s (591 ft/s). The stiff site was selected to be near the site class C/D boundary, with a target V_{s30} = 360 m/s (1181 ft/s). More information about the conditions at the selected sites is given below.

C.3.1 Soft Site

The soft site was selected to be near the site class D/E boundary, with a target V_{s30} = 180 m/s (591 ft/s). The Imperial Valley Wildlife Liquefaction (WLA) site was selected as a representative site. The site consists of unsaturated soft clay near the soil surface. The shear-wave-velocity profile is documented in Star et al. (2015). The estimated V_{s30} at WLA is 183 m/s (600 ft/s). A simplified assumed shear-wave profile of the site is taken to be V_s = 100 m/s (328 ft/s) from surface to 3 m (10 ft) below the surface, V_s = 140 m/s (459 ft/s) from 3 m to 5 m (10 ft to 16 ft) below the surface, V_s = 170 m/s (558 ft/s) from 5 m to 12 m (16 ft to 39 ft) below the surface, and V_s = 230 m/s (755 ft/s) more than 12 m (39 ft) below the surface. Undrained shear strength of the soil was estimated as 32 kPa (668 lbs/ft^2). Poisson's ratio for the soil was estimated to be 0.45, and the unit weight was estimated to be 16 kN/m^3 (103 lbs/ft^3). At large strains, the shear modulus of the soil reduces from the maximum elastic value. The effective reduction factor for shear modulus was estimated to be 0.6.

C.3.2 Stiff Site

The stiff soil site was selected to be near the site class C/D boundary, with a target V_{s30} = 360 m/s (1181 ft/s). The Cholame Parkfield 12W site was selected as a representative site. The site consists of dense sands near the soil surface. The shear-wave-velocity profile is documented in Thompson et al.

(2010). Based on shear-wave velocity data, V_{s30} is estimated to be 354 m/s (1161 ft/s). A simplified, assumed shear-wave profile of the site is taken to be V_s = 295 m/s (968 ft/s) from surface to 1 m (3.3 ft) below the surface, V_s = 310 m/s (1017 ft/s) from 1 m to 2 m (3.3 ft to 6.6 ft) below the surface, V_s = 315 m/s (1033 ft/s) from 2 m to 10 m (6.6 ft to 33 ft) below the surface, V_s = 335 m/s (1099 ft/s) from 10 m to 15 m (33 ft to 49 ft) below the surface, V_s = 370 m/s (1214 ft/s) from 15 m to 20 m (49 ft to 66 ft) below the surface, and V_s = 415 m/s (1362 ft/s) more than 20 m (66 ft) below the surface. The friction angle of the soil was estimated to be 40 degrees, Poisson's ratio was estimated to be 0.35, and the unit weight of the soil was estimated to be 19 kN/m^3 (122 lbs/ft^3). At large strains, the shear modulus of the soil reduces from the maximum elastic value. The effective reduction factor for shear modulus was estimated to be 0.8.

C.4 Foundation Springs and Dampers

C.4.1 Development of the Foundation Impedances

This section summarizes the development of the foundation impedance functions (springs and dampers) for the COM2B design for the soft and stiff sites.

As described in Section 3.2.4, the foundation system consists of shallow, spread footings with a slab-on-grade. Figure C-1(a) shows the layout of the footing structures in the COM2B design for soft soil. For the soft site configuration, springs and dampers were developed for three different foundation types: under the long exterior strip foundations, under the shorter exterior strip foundations, and under the interior isolated footings. The soil-foundation springs and dampers were not included for the slab-on-grade.

Figure C-1(b) shows the layout of the footing structures in the COM2B design for stiff soil. For the stiff site configuration, springs and dampers were developed for five different foundation types: under the L-shaped corner foundations, under the rectangular wall foundations, under the external-wall isolated footings, under the interior isolated footings, and under the grade beams connecting the external perimeter foundations. The soil-foundation springs and dampers were not included for the slab-on-grade.

For all foundations located along the exterior of the structure (i.e., the long and short exterior strip foundations for the soft site, and the L-shaped corner foundations, rectangular wall foundations, external isolated footings, and the grade beams for the stiff site), springs and dampers were developed at nodes located at a 1-foot spacing along the center line of each foundation. Three springs and parallel dampers control translation in the two horizontal

(subscripts x, z) direction and one vertical (subscript y) direction. Rotation of the foundation in the in-plane direction is controlled by the vertical springs. Rotational springs (notated with the subscripts xx and zz) control the out-of-plane rotation. Figure C-2 shows a cross section through a single node of a foundation, with the vertical and horizontal translations and out-of-plane rotational springs and dampers shown. The spring controlling translation along the length of the foundation is not shown.

For each interior footing, the foundation spring stiffness and damping values were developed as lumped impedance values, located at a single node under the center of the square foundations. Five springs and parallel dampers control translation in two horizontal (subscripts x, z) directions and one vertical (subscript y) direction and rotations about the x and z axes (notated with the subscripts xx and zz).

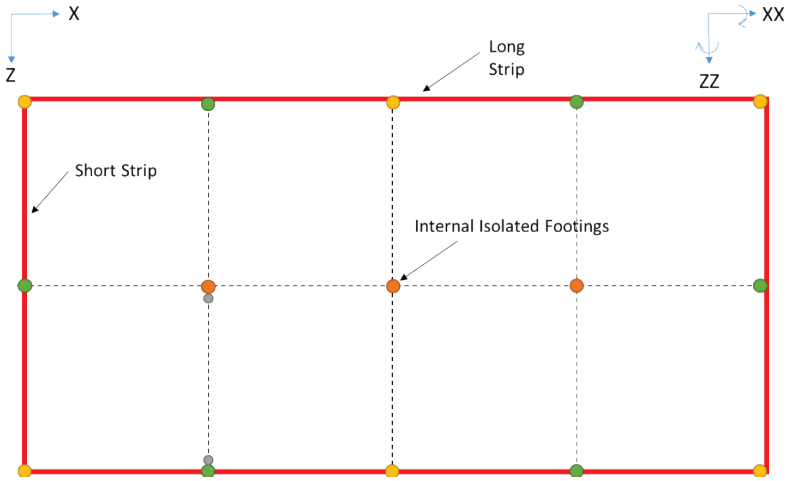

(a)

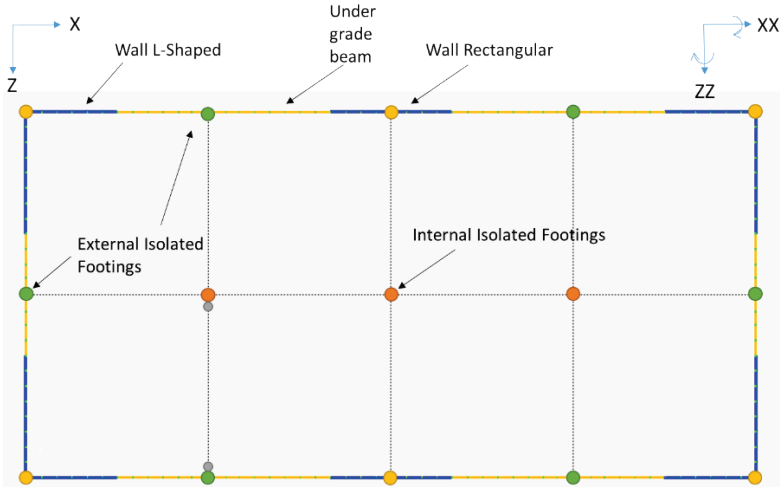

(b)

Figure C-1 Layout of COM2B modeled footings for SSI study: (a) soft site and (b) stiff site.

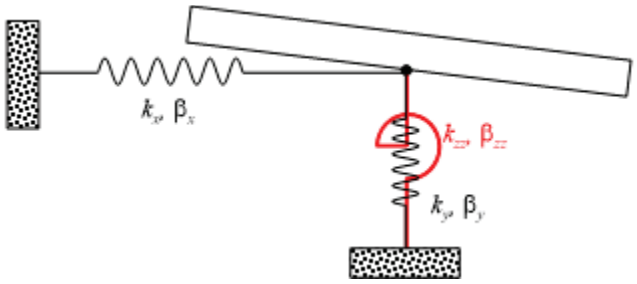

Figure C-2 Translational and rotational springs and dampers.

Foundation impedance functions are dependent on the foundation dimensions. Detailed foundation plans for COM2B are provided in Section A.3.1. The foundation dimensions in the X- and Z-directions used for the calculation of foundation impedances for each footing type are given in Table C-1 for the soft site and Table C-2 for the stiff site. These dimensions are equivalent to 2*L* and 2*B* used in NIST (2012b) and FEMA-P-1050. Determining the foundation dimensions for the square and rectangular foundations was straightforward. The foundation dimensions for the L-shaped wall was estimated based on an equivalent foundation with a moment of inertia matching that of the actual foundation.

Table C-1 X and Z Dimensions for Calculation of Foundation Springs and Dampers for COM2B Soft Site

Footing Type	Soft Site
Long Strip	96′ x 4′
Short Strip	4′ x 48′
Interior Isolated	9′ x 9′

Table C-2 X and Z Dimensions for Calculation of Foundation Springs and Dampers for COM2B Stiff Site

Footing Type	Stiff Site
Wall L-Shaped	12′ x 9′
Wall Rectangular	12′ x 3′
Exterior Isolated	4.5′ x 4.5′
Interior Isolated	6′ x 6′
Under Grade Beam	1.5′ x 14′

The average effective shear-wave velocity of the soil under each foundation is used, along with the density of the soil, to estimate the small strain shear modulus, G_0. As described in NIST (2012b), the effective depth interval for calculating the shear-wave velocity depends on the size of the foundation and the spring orientation. For the translations and vertical springs, the effective

depth is equal to the half-dimension of an equivalent square foundation with an area matching the actual foundation. For the rotational springs, it is equal to the half-dimension of an equivalent square foundation matching the moment of inertia of the actual foundation. The small-strain shear modulus is reduced by the strain reduction factors described in appendix Section C.3 to get a modulus appropriate for estimating springs and dampers for each footing type.

Foundation impedance values in the vertical, translational, and rotational directions were calculated using equations by Pais and Kausel (1988) for a rigid surface foundation, as given in Table 2-2a of NIST (2012b) for surface foundations. The foundation impedance values are divided by the area of the foundation and multiplied by the tributary area of each node in order to determine the final spring stiffness values. This approach, when applied to the vertical stiffness values, tends to underestimate the in-plane rotational stiffness of the foundation system compared to that predicted using the lumped impedance value. Using a similar process would tend to overestimate radiation damping from rocking. As rocking is considered more important to the behavior of the system compared to vertical translation, equations by Hardin and Hutchinson (2009) are used to increase the stiffness of the vertical springs and decrease the damping across the extent of the foundation, to better match the rotational behavior.

The impedance springs and dampers calculated using Pais and Kausel (1988) equations, as given in Table 2-2a of NIST (2012b), are frequency dependent. However due to the limitations of the modeling software, implementing frequency-dependent springs and dampers was not possible. Following NIST (2012b), a single frequency value was selected corresponding to the first-mode, flexible-base period of the system of approximately 0.3 seconds.

The ultimate capacity of the translational stiffness springs, $K_{x,capacity}$ and $K_{z,capacity}$, are controlled by the strength of the soil. The clay at the soft site was estimated to have an undrained soil-foundation interface strength of 32 kPa. The sand at the surface of the stiff site generates a friction angle between the soil and foundation of 40 degrees (friction ratio of 0.83). For all sites, strain hardening of 15 percent was included to account for additional sliding resistance due to passive pressure on foundation elements.

The capacity of the vertical springs, $K_{y,capacity}$, are controlled by the unfactored bearing capacity of the foundation. The vertical springs have no tension capacity and thus zero resistance to foundation uplift. Strain hardening of 15 percent was included.

As shown in Figure C-3, the capacity of the foundation in rotation is controlled primarily by the uplift of the foundation. The out-of-plane rotational springs capacity, $K_{oop,capacity}$, can be estimated using static equilibrium to estimate the maximum moment that the foundation could support knowing the average static vertical load on each foundation and the bearing capacity. In order to account for the reduction in vertical loads due to general rocking of the structure, the rotational capacities were reduced by 50 percent. No strain hardening was included.

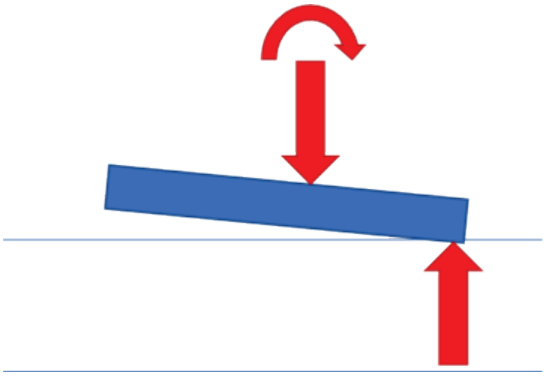

Figure C-3 Equilibrium estimation of rotational capacity of foundation.

Radiation damping is presented in terms of damping ratio percentages, β. Calculated spring and damper values for the soft and stiff sites are reported in Table C-3 to Table C-4, respectively.

Table C-3 Spring and Damper Properties Per Node for COM2B Soft Site

Footing Type	Translation-X	Translation-Z	Vertical-Y	Rotation-ZZ	Rotation-XX
Long Strip	$K_x = 1.5\text{x}10^2$ kips/ft $K_{x,capacity} = 2.7$ kips $\beta_x = 17.0\%$	$K_z = 2.0\text{x}10^2$ kips/ft $K_{z,capacity} = 2.7$ kips $\beta_z = 12.8\%$	$K_y = 3.0\text{x}10^2$ kips/ft $K_{y,capacity} = 16.3$ kips $\beta_y = 7.9\%$	-	$K_{xx} = 3.3\ \text{x}10^3$ kip-ft/rad $K_{xx,capacity} = 2.6$ kip-ft $\beta_{xx} = 0.03\%$
Short Strip	$K_x = 2.5\text{x}10^2$ kips/ft $K_{x,capacity} = 2.7$ kips $\beta_x = 10.5\%$	$K_z = 2.0\text{x}10^2$ kips/ft $K_{z,capacity} = 2.7$ kips $\beta_z = 13.0\%$	$K_y = 4.6\text{x}10^2$ kips/ft $K_{y,capacity} = 16.3$ kips $\beta_y = 2.6\%$	$K_{zz} = 2.8\text{x}10^3$ kip-ft/rad $K_{zz,capacity} = 2.6$ kip-ft $\beta_{zz} = 0.03\%$	-
Interior Isolated	$K_x = 5.5\text{x}10^3$ kips/ft $K_{x,capacity} = 54$ kips $\beta_x = 9.7\%$	$K_z = 5.5\text{x}10^3$ kips/ft $K_{z,capacity} = 54$ kips $\beta_z = 9.7\%$	$K_y = 7.7\text{x}10^3$ kips/ft $K_{y,capacity} = 354$ kips $\beta_y = 17.2\%$	$K_{zz} = 1.3\text{x}10^5$ kip-ft/rad $\beta_{zz} = 0.3\%$	$K_{xx} = 1.3\text{x}10^5$ kip-ft/rad $\beta_{xx} = 0.3\%$

Table C-4 Spring and Damper Properties Per Node for COM2B Stiff Site

Footing Type	Translation-X	Translation-Z	Vertical-Y	Rotation-ZZ	Rotation-XX
Wall L-Shaped	$K_x = 4.3x10^3$ kips/ft $\beta_x = 4.0\%$	$K_z = 4.2x10^3$ kips/ft $\beta_z = 4.1\%$	$K_y = 8.2x10^3$ kips/ft $K_{y,capacity} = 210$ kips $\beta_y = 0.03\%$	-	-
Wall Rectangular	$K_x = 4.1x10^3$ kips/ft $\beta_x = 2.2\%$	$K_z = 4.6x10^3$ kips/ft $\beta_z = 2.0\%$	$K_y = 1.1x10^4$ kips/ft $K_{y,capacity} = 118$ kips $\beta_y = 0.01\%$	-	$K_{xx} = 1.7x10^4$ kips-ft/rad $K_{xx,capacity} = 3.7$ kip-ft $\beta_{xx} = 0.00\%$
Exterior Isolated *(x and z given for footings on long wall. Reverse for short wall)*	$K_x = 8.8x10^3$ kips/ft $\beta_x = 1.8\%$	$K_z = 8.8x10^3$ kips/ft $\beta_z = 1.8\%$	$K_y = 2.9x10^4$ kips/ft $K_{y,capacity} = 249$ kips $\beta_y = 0.00\%$	-	$K_{xx} = 4.9x10^4$ kips-ft/rad $K_{xx,capacity} = 8.8$ kip-ft $\beta_{xx} = 0.00\%$
Interior Isolated	$K_x = 4.7x10^4$ kips/ft $\beta_x = 2.3\%$	$K_z = 4.7x10^4$ kips/ft $\beta_z = 2.3\%$	$K_y = 6.1x10^4$ kips/ft $K_{y,capacity} = 1960$ kips $\beta_y = 3.7\%$	$K_{zz} = 4.7x10^5$ kips-ft/rad $\beta_{zz} = 0.00\%$	$K_{xx} = 4.7x10^5$ kips-ft/rad $\beta_{xx} = 0.00\%$
Under Grade Beam *(x and z given for footings on long wall. Reverse for short wall)*	$K_x = 2.9x10^3$ kips/ft $\beta_x = 1.6\%$	$K_z = 3.5x10^3$ kips/ft $\beta_z = 1.3\%$	$K_y = 4.2x10^3$ kips/ft $K_{y,capacity} = 47$ kips $\beta_y = 2.3\%$	-	$K_{xx} = 4.7x10^5$ kips-ft/rad $K_{xx,capacity} = 0.9$ kip-ft $\beta_{xx} = 0.0\%$

C.4.2 Spring and Damper Example Calculations

The soil-foundation spring and damper values are calculated individually for each foundation configuration at each soil site. In the following calculations, the COM2B stiff site rectangular wall foundation was selected as an example case, with calculations necessary to compute the stiffness and damping parameters presented.

1. Determine the Effective Shear Modulus

Where soil profiles are non-uniform, it is necessary to determine an effective shear modulus to use for impedance calculations. As described in NIST (2012b), the first step is to calculate the effective depth intervals, z_p, based on the foundation plan area, A, for translations, and based on foundation moments of inertia, I_x and I_z, for rotation of the foundation following NIST (2012b) Equation 2-18 (b-c):

$$\textit{Horizontal}\ (x,z)\text{: } z_p^{\,A} = \sqrt{A/4} = 2.98 \text{ ft}$$

$$\textit{Rotation}\ (zz)\text{: } z_{p,zz}^{\,I} = \sqrt[4]{I_z} = 4.23 \text{ ft}$$

$$\textit{Rotation}\ (xx)\text{: } z_{p,xx}^{\,I} = \sqrt[4]{I_x} = 2.13 \text{ ft}$$

The average shear-wave velocity over the effective depths is calculated, as in NIST (2012b) Equation 2-18 (a):

$$V_{s,avg} = \frac{z_p}{\sum_{i=1}^{n}\left(\Delta z_i \Big/ \left(V_s(z)\right)_i\right)}$$

$$V_{s,\,avg,\,horiz} = 968 \text{ ft/s}$$

$$V_{s,\,avg,\,zz} = 968 \text{ ft/s}$$

$$V_{s,\,avg,\,xx} = 968 \text{ ft/s}$$

where Δz_p and $(V_s(z))_i$ are the thickness and the velocity of discretized layers of the soil profile.

The product of the density, ρ, and the square of the shear-wave velocity gives the small strain shear modulus. At large strains, the effective shear modulus, G_{eff}, of the soil reduces from the small strain value. The effective reduction factor for shear modulus was estimated to be 0.8.

$$G_{eff,\,horiz} = 0.8 \times \rho \times V_{s,avg,horiz}^2 = 2.82 \times 10^6 \text{ lb/ft}^2$$

$$G_{eff,\,zz} = 0.8 \times \rho \times V_{s,avg,zz}^2 = 2.82 \times 10^6 \text{ lb/ft}^2$$

$$G_{eff,\,xx} = 0.8 \times \rho \times V_{s,avg,xx}^2 = 2.82 \times 10^6 \text{ lb/ft}^2$$

2. Calculate the static spring stiffness

Pais and Kausel (1988) equations for a rigid surface foundation, as given in Table 2-2a of NIST (2012b), were used to estimate the static spring stiffnesses for the five degrees of freedom described in Section B.4.1. The inputs to these equations are the foundation length ($2L$ = 12 feet) and width ($2B$ = 3 feet), Poisson's ratio of the soil (ν = 0.35), and the shear moduli determined in Step 1 of these example calculations. The full equations are not reproduced here for brevity. Calculated static spring stiffnesses are:

$$K_{x,static} = 4.9 \times 10^4 \text{ kips/ft}$$

$$K_{z,static} = 5.5 \times 10^4 \text{ kips/ft}$$

$$K_{zz,static} = 1.5 \times 10^6 \text{ kip-ft/rad}$$

$$K_{xx,static} = 2.1 \times 10^6 \text{ kip-ft/rad}$$

$$K_{y,static} = 6.7\times10^4 \text{ kips/ft}$$

3. Determine the dynamic modifiers and damper values

Dynamic spring modifiers (α) and damper values (β) are frequency dependent. First, the dimensionless frequency is calculated following NIST (2012b) Equation 2-15:

$$a_o = \omega B / V_s = 0.03$$

where ω is angular frequency. In order to be compatible with the time-domain analysis used by the modeling software, a single value of angular frequency corresponding to the first-mode period of the undamaged COM2B soil-structure system (approximately 0.3 seconds) is selected.

A single value of α and β is then calculated for each of the five degrees of freedom using Pais and Kausel (1988) equations, as given in Table 2-3a of NIST (2012b). The input parameters for these calculations are the dimensionless frequency, the foundation dimensions L and B, the static spring stiffnesses determined in Step 2 of these example calculation, the shear moduli determined in Step 1 of these example calculations, and Poisson's ratio of the soil. The calculated dynamic spring modifiers and damper values are:

$\alpha_x = 1.00$	$\beta_x = 2.24\%$
$\alpha_z = 1.00$	$\beta_z = 1.99\%$
$\alpha_{zz} = 1.00$	$\beta_{zz} = 0.007\%$
$\alpha_{xx} = 1.00$	$\beta_{xx} = 0\%$
$\alpha_y = 1.00$	$\beta_y = 3.39\%$

The modifiers are multiplied by the static stiffnesses to get the final stiffness values:

$$K_x = \alpha_x \times K_{x,static} = 4.9\times10^4 \text{ kips/ft}$$

$$K_z = \alpha_z \times K_{z,static} = 5.5\times10^4 \text{ kips/ft}$$

$$K_{zz} = \alpha_{zz} \times K_{zz,static} = 1.5\times10^6 \text{ kip-ft/rad}$$

$$K_{xx} = \alpha_{xx} \times K_{xx,static} = 2.1\times10^5 \text{ kip-ft/rad}$$

$$K_y = \alpha_y \times K_{y,static} = 6.7\times10^4 \text{ kips/ft}$$

4. Determine the spring capacities

The capacity of the horizontal translation springs is dependent on the friction angle of the soil ($\phi' = 40$ degrees) and varies depending on the vertical foundation load (V) according to the equation:

$$K_{z,capacity} = V \times \tan\phi'$$

The vertical spring capacity is calculated using Meyerhoff's bearing capacity equation. Vesic's bearing capacity factors (N_q, N_γ) were used with Hansen's shape (F_{qs}, $F_{\gamma s}$) and depth (F_{qd}, $F_{\gamma d}$) factors. See, for example, Coduto et al. (2015) for bearing capacity equations. The input parameters for these calculations are the unit weight of the soil (γ), the dimensions of the foundation, and the friction angle of the soil. In the bearing capacity equation below, the width of the foundation is parameterized as $2B$ as in the NIST (2012b) report and the steps above, although it is more commonly reported in the literature as B. A factor of safety (FS) of 1 was applied to the bearing capacity.

$$K_{y,capacity} = \frac{Q_{ult}}{FS} = \left(D\gamma N_q F_{qs} F_{qd} + \frac{(2B)}{2} \gamma N_\gamma F_{\gamma s} F_{\gamma d} \right) \times L \times B / FS = 1.4 \times 10^3 \text{ kips}$$

where the depth (D) of the foundation is 2 feet.

The rotational spring capacity was estimated using static equilibrium. The vertical force on the foundation is assumed to be 61 kips. With the foundation rotated so that the majority of the footing experiencing uplift and a sliver at the edge of the footing at the bearing capacity, the moment at static equilibrium can be calculated as the vertical force, V, times the moment arm, a, between the vertical force assumed to be at the center of the foundation and the point of rotation at the edge of the foundation. The value is reduced by 50 percent to account for redistribution of the vertical load.

$$K_{xx,capacity} = V \times a \times 50\% = 44.0 \text{ kip-ft}$$

5. Determine the distributed spring properties

The nodes are located every 1 foot along the centerline of the foundation. That means that there are 12 nodes along the 12-foot-long foundation. The calculated foundation stiffnesses and capacities are divided by the number of nodes to get the nodal spring value. The damping ratios do not need to be reduced based on the number of nodes. The rotational stiffness, K_{zz}, is taken as null because the distributed vertical spring stiffness, K_y, will provide the stiffness against rotation. The vertical nodal spring stiffness and damping are modified by a stiffness factor, $R_{k,zz}$, and a damping factor, $R_{c,zz}$, to produce

values equivalent to the rotational impedances. Equation 2-20 and Equation 2-21 from NIST (2012b) are combined to obtain:

$$R_{k,zz} = \frac{3K_{zz}}{K_y L^2} = 1.88$$

$$R_{c,zz} = \frac{3c_{zz}}{c_y L^2 R_{k,zz}} = 0.0019$$

where c is the dashpot coefficient that is related to damping ratio by the equation:

$$c = \frac{2\beta k}{\omega} = 0.0019$$

Per node, the updated spring stiffness and damping properties are:

$$K_x = K_x/N = 4.1\times10^3 \text{ kip/ft}$$

$$K_z = K_z/N = 4.6\times10^3 \text{ kip/ft}$$

$$K_{zz} = —$$

$$K_{xx} = K_{xx}/N = 1.74\times10^4 \text{ kip-ft/rad}$$

$$K_y = K_y \times R_{k,zz}/N = 1.1\times10^4 \text{ kip/ft}$$

$$K_{xx,capacity} = K_{xx,capacity}/N = 3.7 \text{ kip-ft}$$

$$K_{y,capacity} = K_{y,capacity}/N = 118 \text{ kips}$$

$$\beta_x = 2.24\%$$

$$\beta_z = 1.99\%$$

$$\beta_{zz} = —$$

$$\beta_{xx} = 0\%$$

$$\beta_y = \beta_y \times R_{c,zz} = 0.01\%$$

C.5 Frequency-Modified Ground Motion Records

Kinematic-interaction effects are modeled using modified ground motions, known as the foundation input motions (FIM). This section discusses the modification of the suite of ground motions to account for kinematic-interaction effects.

The ratio of FIM and free-field ground motion in the frequency domain is presented as a transfer function, H_u. The period-dependent transfer function, H_u, is calculated using semi-empirical equations, as in NIST (2012b) Equation 3-3 and Equation 3-4. It is dependent on a parameter κ_a, the dimensions of the foundation, and the shear-wave velocity of the soil. The overall dimensions of

the structure in plan view (96 feet × 48 feet) were selected for calculating H_u, and the embedment was assumed to be negligible. The foundation parameter κ_a is calculated using the semi-empirical model by Kim and Stewart (2003), as given in NIST (2012b) Equation 3-5, based on the shear-wave velocity of the soil at the surface of the site, reduced by the effective reduction factor for shear modulus, which is estimated to be 0.8 for the stiff site and 0.6 for the soft site. Figure C-4 shows the calculated transfer functions for the soft and stiff sites.

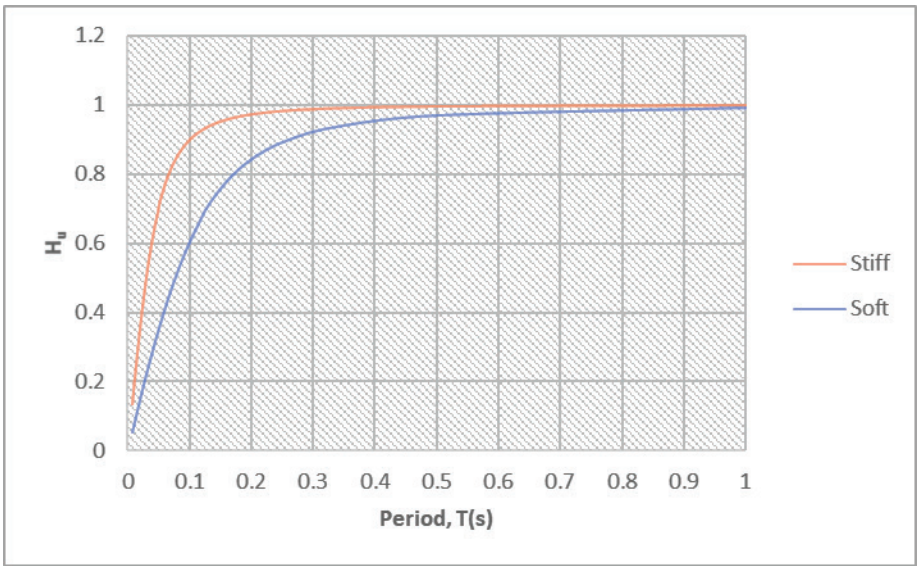

Figure C-4 Transfer function for soft and stiff sites.

The calculation of the FIM is achieved by converting the free-field ground motion to the Fourier domain. The frequency-dependent transfer function is then applied, and the ground motions are converted back to the time domain for use in the SSI modeling. The Matlab Fast Fourier Transform (FFT) function was used for the calculations. Figure C-5 shows a sample ground motion before and after the application of the transfer function. This process was applied to all motions in both horizontal directions for the suite of ground motions used in the SSI modeling.

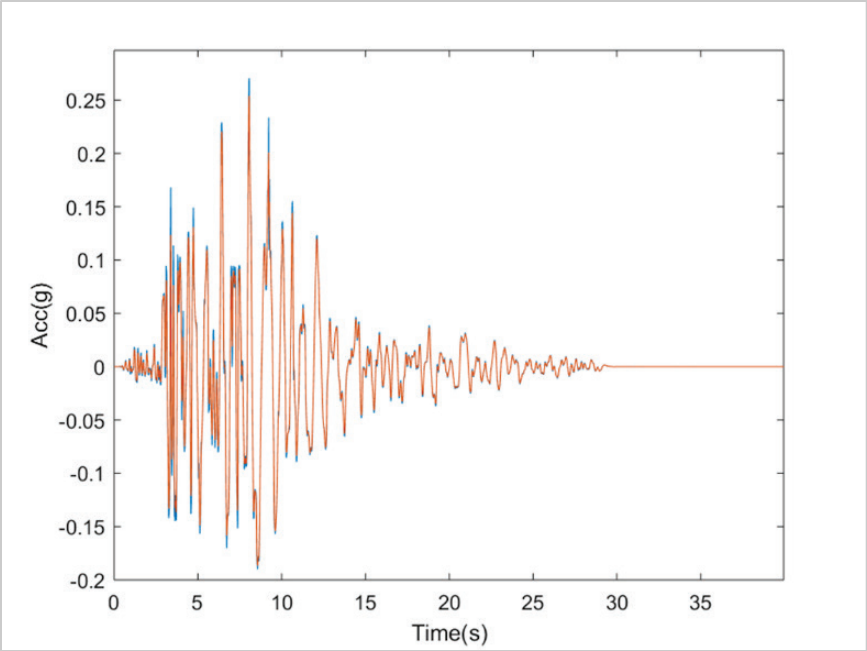

Figure C-5 Sample ground motion before (blue) and after (orange) application of frequency-dependent transfer function.

Appendix D

Archive of Peak Response Calculations

D.1 Peak Response Parameters Archived for Each Model

Response parameters of interest (stripe statistics) were post-processed and archived at each intensity stripe to determine the peak response for each archetype. For each archetype, an Excel spreadsheet containing these response parameters for each IDA and all intensity stripes was generated and archived. The names of the archive files for each archetype are listed in Table D-1. See Chapter 4, Table 4-5 for a list of the specific response parameters that were archived. The archives for all stripe statistics are available at https://femap2139.atcouncil.org.

Table D-1 Peak Response Archive Files for Short-Period Reinforced Masonry Commercial Building Archetypes

Archetype ID	No. of Stories	Seismic Region	Parametric Study	Peak Response Archiving Files
COM1B	1	High	Baseline	Stripe_Statistics_ATC116_COM1B
COM1B-DC	1	High	Displacement Capacity	Stripe_Statistics_ATC116_COM1B-DC1 Stripe_Statistics_ATC116_COM1B-DC2
COM2B	2	High	Baseline	Stripe_Statistics_ATC116_COM2B
COM2B-DC	2	High	Displacement Capacity(1)	Stripe_Statistics_ATC116_COM2B-DC1 Stripe_Statistics_ATC116_COM2B-DC2
COM2B-SS	2	High	SSI/Foundation Flexibility(2)	Stripe_Statistics_ATC116_COM2B-SS2-Unfiltered Stripe_Statistics_ATC116_COM2B-SS2-Filtered
COM3B	4	High	Baseline	Stripe_Statistics_ATC116_COM3B
COM3B-DC	4	High	Displacement Capacity(1)	Stripe_Statistics_ATC116_COM3B-DC1 Stripe_Statistics_ATC116_COM3B-DC2
COM4B	1	Very High	Baseline	Stripe_Statistics_ATC116_COM4B
COM4B-DC	1	Very High	Displacement Capacity(1)	Stripe_Statistics_ATC116_COM4B-DC1 Stripe_Statistics_ATC116_COM4B-DC2
COM5B	2	Very High	Baseline	Stripe_Statistics_ATC116_COM5B
COM5B-DC	2	Very High	Displacement Capacity(1)	Stripe_Statistics_ATC116_COM5B-DC1 Stripe_Statistics_ATC116_COM5B-DC2

Table D-1 Peak Response Archive Files for Short-Period Reinforced Masonry Commercial Building Archetypes (continued)

Archetype ID	No. of Stories	Seismic Region	Parametric Study	Peak Response Archiving Files
COM6B	4	Very High	Baseline	Stripe_Statistics_ATC116_COM6B
COM6B-DC	4	Very High	Displacement Capacity[1]	Stripe_Statistics_ATC116_COM6B-DC1 Stripe_Statistics_ATC116_COM6B-DC2

[1] Two drift capacity levels: 70% and 130% of the drift capacity of the baseline model.

[2] Soft site with unfiltered and filtered ground motions.

References

Ahmadi, F., 2012, *Displacement-based Seismic Design and Tools for Reinforced Masonry*, Ph.D. Dissertation, the University of Texas, Austin, Austin, Texas.

Ahmadi, F., Mavros, M., Klingner, R.E., Shing, P.B., and McLean, D., 2015, "Displacement-based seismic design for reinforced masonry shear-wall structures, part 2: Validation with shake-table tests," *Earthquake Spectra*, Earthquake Engineering Research Institute, Vol. 31, No. 2, pp. 999-1019.

ASCE, 2005, *Minimum Design Loads for Buildings and Other Structures*, ASCE/SEI 7-05, American Society of Civil Engineers, Reston, Virginia.

ASCE, 2010, *Minimum Design Loads for Buildings and Other Structures*, ASCE/SEI 7-10, American Society of Civil Engineers, Reston, Virginia.

ASCE, 2014, *Seismic Evaluation and Retrofit of Existing Buildings*, ASCE/SEI 41-13, American Society of Civil Engineers, Reston, Virginia.

ASCE, 2016, *Minimum Design Loads and Associated Criteria for Buildings and Other Structures*, ASCE/SEI 7-16, American Society of Civil Engineers, Reston, Virginia.

ASCE, 2017, *Seismic Evaluation and Retrofit of Existing Buildings*, ASCE/SEI 41-17, American Society of Civil Engineers, Reston, Virginia.

ATC, 1989, *Procedures for Postearthquake Safety Evaluation of Buildings*, ATC-20, Applied Technology Council, Redwood City, California.

ATC, 2005, *Field Manual: Postearthquake Safety Evaluation of Buildings Second Edition*, ATC-20-1, Applied Technology Council, Redwood City, California.

ATC, 2015, *Roadmap for Solutions to the Issue of Short Period Building Performance*, ATC-116 Report, Applied Technology Council, Redwood City, California.

Atkinson, R.H., and Kingsley, G.R., 1985, *A Comparison of the Behavior of Clay and Concrete Masonry in Compression*, Report No. 1.1-1, U.S.-Japan Coordinated Program for Masonry Building Research, Atkinson-Noland & Associates, Boulder, Colorado.

Bažant, Z.P., and Oh, B.H., 1983, "Crack band theory for fracture of concrete," *Matériaux et Construction*, Vol. 16, No. 3, pp. 155-177.

Brady, A.G., Etheredge, E.C., and Porcella, R.L., 1988, "The Whittier Narrows, California earthquake of October 1, 1987 – preliminary assessment of strong ground motion records," *Earthquake Spectra*, Earthquake Engineering Research Institute, Vol. 4, No. 1, pp. 55-74.

CEN, 2004, *Eurocode 8: Design of Structures for Earthquake Resistance - Part 1: General Rules, Seismic Actions and Rules for Buildings*, European Committee for Standardization, Brussels, Belgium.

Cheng, J., Koutras, A.A., and Shing, P.B., 2020, "Evaluation of collapse resistance of reinforced masonry wall systems by shake-table tests," *Earthquake Engineering and Structural Dynamics* (published online).

Coduto, D.P., Kitch, W.A., and Yeung, M-C.R., 2015, *Foundation Design: Principles and Practices*, 3rd Edition, Pearson, New York, New York.

Crisfield, M.A., 1990, "A consistent co-rotational formulation for non-linear, three-dimensional, beam-elements," *Computer Methods in Applied Mechanics and Engineering*, Vol. 81, No. 2, pp. 131-150.

Dizhur, D., Ingham, J., Moon, L., Griffith, M., Schultz, A., Senaldi, I., Magenes, G., Dickie, J., Lissel, S., Centeno, J., Ventura, C., Leite, J., and Lourenco, P., 2011, "Performance of masonry buildings and churches in the 22 February 2011 Christchurch earthquake," *Bulletin of the New Zealand Society for Earthquake Engineering*, Vol. 44, No. 4, pp. 279-296.

Dulacska, H., 1972, "Dowel action of reinforcement crossing cracks in concrete," *ACI Journal Proceedings*, Vol. 69, No. 12, pp. 754-757.

Essa, H.S., Tremblay, R., and Rogers, C.A., 2003, "Behavior of roof deck diaphragms under quasi-static cyclic loading," *Journal of Structural Engineering*, Vol. 129, No. 12, pp. 1658-1666.

FEMA, 2006, *Techniques for the Seismic Rehabilitation of Existing Buildings*, FEMA 547, prepared by Rutherford & Chekene Consulting Engineering for the National Institute of Standards and Technology and the Federal Emergency Management Agency, Washington, D.C.

FEMA, 2009a, *NEHRP Recommended Seismic Provisions for New Buildings and Other Structures*, FEMA P-750, prepared by the Building Seismic Safety Council of the National Institute of Building Sciences for the Federal Emergency Management Agency, Washington, D.C.

FEMA, 2009b, *Quantification of Building Seismic Performance Factors*, FEMA P-695, prepared by the Applied Technology Council for the Federal Emergency Management Agency, Washington, D.C.

FEMA, 2015a, *Rapid Visual Screening of Buildings for Potential Seismic Hazards: A Handbook*, Third Edition, FEMA P-154, prepared by the Applied Technology Council for the Federal Emergency Management Agency, Washington, D.C.

FEMA, 2015b, *NEHRP Recommended Seismic Provisions for New Buildings and Other Structures*, FEMA P-1050, prepared by the Building Seismic Safety Council of the National Institute of Building Sciences for the Federal Emergency Management Agency, Washington, D.C.

FEMA, 2018, *Seismic Performance Assessment of Buildings, Volume 1 – Methodology*, Second Edition, FEMA P-58-1, prepared by the Applied Technology Council for the Federal Emergency Management Agency, Washington, D.C.

FEMA, 2020a, *Short-Period Building Collapse Performance and Recommendations for Improving Seismic Design, Volume 1 – Overarching Findings, Conclusions, and Recommendations*, FEMA P-2139-1, prepared by the Applied Technology Council for the Federal Emergency Management Agency, Washington, D.C.

FEMA, 2020b, *Short-Period Building Collapse Performance and Recommendations for Improving Seismic Design, Volume 2 – Study of One-to-Four Wood Light-Frame Buildings*, FEMA P-2139-2, prepared by the Applied Technology Council for the Federal Emergency Management Agency, Washington, D.C.

FEMA, 2020c, *Short-Period Building Collapse Performance and Recommendations for Improving Seismic Design, Volume 4 – Study of One-to-Four Story Steel Special Concentrically Braced Frame Buildings*, FEMA P-2139-4, prepared by the Applied Technology Council for the Federal Emergency Management Agency, Washington, D.C.

Harden, C.W., and Hutchinson, T.C., 2009, "Beam-on-nonlinear-Winkler-foundation modeling of shallow, rocking-dominated footings," *Earthquake Spectra*, Vol. 25, No. 2, pp. 277-300.

Hart, G.C., Kariotis, J., and Noland, J.L., 1988, "The Whittier Narrows, California earthquake of October 1, 1987 – masonry building performance survey," *Earthquake Spectra*, Earthquake Engineering Research Institute, Vol. 4, No. 1, pp. 181-196.

ICBO, 1994, *Uniform Building Code*, 1994 Edition, International Conference of Building Officials, Whittier, California.

ICC, 2015, *International Building Code*, International Code Council, Washington, D.C.

Jiang, H., and Kurama, Y.C., 2010, "Analytical modeling of medium-rise reinforced concrete shear walls," *ACI Structural Journal*, Vol. 107, No. 4, pp. 400-410.

Kapoi, C.M., 2012, *Experimental Performance of Concrete Masonry Shear Walls under In-plane Loading*, M.S. Thesis, Washington State University, Pullman, Pullman, Washington.

Kim, S.H., and Koutromanos, I., 2016, "Constitutive model for reinforcing steel under cyclic loading," *Journal of Structural Engineering*, Vol. 142, No. 12.

Kim, S., and Stewart, J.P., 2003, "Kinematic soil-structure interaction from strong motion recordings," *Journal of Geotechnical and Geoenvironmental Engineering*, Vol. 129, No. 4, pp. 323-335.

Kircher, C.A., Whitman, R.V., and Holmes, W.T., 2006, "HAZUS earthquake loss estimation methods," *Natural Hazards Review*, American Society of Civil Engineers, Vol. 7, No. 2, pp. 45-59.

Kolozvari, K., Orakcal, K., and Wallace, J.W., 2014, "Modeling of cyclic shear-flexure interaction in reinforced concrete structural walls. I: Theory," *Journal of Structural Engineering*, Vol. 141, No. 5.

Kottari, A., 2016, *Horizontal Load Resisting Mechanisms of External Shear Keys in Bridge Abutments*, Ph.D. Dissertation, University of California, San Diego, La Jolla, California.

Kottari, A., Mavros, M., Murcia-Delso, J., and Shing, P.B., 2017, "Interface model for bond-slip and dowel-action behavior," *ACI Structural Journal*, Vol. 114, No. 4, pp. 1043-1053.

Koutras, A., 2019, *Assessment of the Seismic Behavior of Fully and Partially Grouted Reinforced Masonry Structural Systems Through Finite Element analysis and Shake-table Testing*, Ph.D. Dissertation, University of California, San Diego, La Jolla, California.

Koutromanos, I., and Shing, P.B., 2012, "Cohesive crack model to simulate cyclic response of concrete and masonry structures," *ACI Structural Journal*, Vol. 109, No. 3, pp. 349-358.

Lawson, J.W., 2013, *Seismic Design of Timber Panelized Roof Structures*, 2012 International Building Code (IBC) Edition, WoodWorks, Washington, D.C.

Liu, J., and Astaneh-Asl, A., 2000, "Cyclic testing of simple connections including effects of slab," *Journal of Structural Engineering*, Vol. 126, No. 1, pp. 32-39.

Liu, J., and Astaneh-Asl, A., 2004, "Moment-rotation parameters for composite shear tab connections," *Journal of Structural Engineering*, Vol. 130, No. 9, pp. 1371-1380.

Lotfi, H.R., and Shing, P.B., 1991, "An appraisal of smeared crack models for masonry shear wall analysis," *Computers and Structures*, Vol. 41, No. 3, pp. 413-425.

LSTC, 2018, *LS-DYNA Theory Manual*, *Release 11*, Livermore Software and Technology Corporation, Livermore, California.

Lu, Y., and Panagiotou, M., 2013, "Three-dimensional cyclic beam-truss model for nonplanar reinforced concrete walls," *Journal of Structural Engineering*, Vol. 140, No. 3.

Lu, Y., and Panagiotou, M., 2016, "Three-dimensional beam–truss model for reinforced concrete walls and slabs–part 2: Modeling approach and validation for slabs and coupled walls," *Earthquake Engineering & Structural Dynamics*, Vol. 45, No. 9.

Lu, Y., Panagiotou, M., and Koutromanos, I., 2016, "Three-dimensional beam-truss model for reinforced concrete walls and slabs–part 1: Modeling approach, validation, and parametric study for individual reinforced concrete walls," *Earthquake Engineering & Structural Dynamics*, Vol. 45, No. 9.

Luttrell, L.D., 1995, *Steel Deck Institute Diaphragm Design Manual*, Second Edition, Steel Deck Institute, Glenshaw, Pennsylvania.

Marini, A., and Spacone, E., 2006, "Analysis of reinforced concrete elements including shear effects," *ACI Structural Journal*, Vol. 103, No. 5, pp. 645-655.

Massone, L.M., Orakcal, K., and Wallace, J.W., 2009, "Modeling of squat structural walls controlled by shear," *ACI Structural Journal*, Vol. 106, No. 5, pp. 645-655.

Mavros, M., 2015, *Experimental and Numerical Investigation of the Seismic Performance of Reinforced Masonry Structures*, Ph.D. Dissertation, University of California, San Diego, La Jolla, California.

Mavros, M., Ahmadi, F., Shing, P.B., Klingner, R.E., McLean, D., and Stavridis, A., 2016, "Shake-table tests of a full-scale two-story shear-dominated reinforced masonry wall structure," *Journal of Structural Engineering*, Vol. 142, No.10.

Mazzoni, S., McKenna, F., Scott, M.H., and Fenves, G.L., 2006, *OpenSees Command Language Manual*, University of California, Berkeley, Berkeley, California.

Moharrami, M., and Koutromanos, I., 2017, "Finite element analysis of damage and failure of reinforced concrete members under earthquake loading," *Earthquake Engineering & Structural Dynamics*, Vol. 46, No. 15, pp. 2811-2829.

Moharrami, M., Koutromanos, I., and Panagiotou, M., 2015, "Nonlinear truss modeling method for the analysis of shear failures in reinforced concrete and masonry structures," *Proceedings of 2nd ATC & SEI Conference on Improving the Seismic Performance of Existing Buildings and Other Structures*, San Francisco, California.

Murcia-Delso, J., and Shing, P. B., 2014, "Bond-slip model for detailed finite-element analysis of reinforced concrete structures," *Journal of Structural Engineering*, Vol. 141, No. 4.

NIST, 2010, *Evaluation of the FEMA P-695 Methodology for Quantification of Building Seismic Performance Factors*, NIST GCR 10-917-8, prepared by the NEHRP Consultants Joint Venture, a partnership of the Applied Technology Council and the Consortium for Universities for Research in Earthquake Engineering, for the National Institute of Standards and Technology, Gaithersburg, Maryland.

NIST, 2012a, *Tentative Framework for Development of Advanced Seismic Design Criteria for New Buildings*, NIST GCR 12-917-20, prepared by the NEHRP Consultants Joint Venture, a partnership of the Applied Technology Council and the Consortium for Universities for Research in Earthquake Engineering, for the National Institute of Standards and Technology, Gaithersburg, Maryland.

NIST, 2012b, *Soil-Structure Interaction for Building Structures*, NIST GCR 12-917-21, prepared by NEHRP Consultants Joint Venture, a partnership of the Applied Technology Council and the Consortium of Universities for Research in Earthquake Engineering, for the

National Institute of Standards and Technology, Gaithersburg, Maryland.

NIST, 2014, *Seismic Design of Special Reinforced Masonry Shear Walls: A Guide for Practicing Engineers*, NIST GCR 14-917-31, prepared by the NEHRP Consultants Joint Venture, a partnership of the Applied Technology Council and the Consortium for Universities for Research in Earthquake Engineering, for the National Institute of Standards and Technology, Gaithersburg, Maryland.

NIST, 2017, *Recommended Modeling Parameters and Acceptance Criteria for Nonlinear Analysis in Support of Seismic Evaluation, Retrofit, and Design*, NIST GCR 17-917-45, prepared by the Applied Technology Council for the National Institute of Standards and Technology, Gaithersburg, Maryland.

Nowak, A.S., Szerszen, M.M., Szeliga, E.K., Szwed, A., and Podhorecki, P.J., 2008, *Reliability-Based Calibration for Structural Concrete, Phase 3*, Serial No. 2849, Portland Cement Association, Skokie, Illinois.

OES, 1995, *The Northridge Earthquake of January 17, 1994: Report of Data Collection and Analysis, Part A: Damage and Inventory Data*, Governor's Office of Emergency Services of the State of California, Sacramento, California.

Pais, A., and Kausel, K., 1988, "Approximate formulas for dynamic stiffnesses of rigid foundations," *Soil Dynamics and Earthquake Engineering*, Vol. 7, No.4, pp. 213-227.

Peruch, M., Spacone, E., and Shing, P.B., 2019, "Cyclic analyses of reinforced concrete masonry panels using a force-based frame element," *Journal of Structural Engineering*, Vol. 145, No. 7.

Petrangeli, M., Pinto, P.E., and Ciampi, V.,1999, "Fiber element for cyclic bending and shear of RC structures. I: Theory," *Journal of Engineering Mechanics*, Vol. 125, No. 9, pp. 994-1001.

Porter, M.L., 1987, "Sequential Phased Displacement (SPD) procedure for TCCMAR testing," *Proceedings of the Third Meeting of the Joint Technical Coordinating Committee on Masonry Research*, U.S.-Japan Coordinated Earthquake Research Program, Tomamu, Japan.

Rose, B.D., 2001, *A Constitutive Model for the Analysis of Reinforced Concrete Beam-Columns Subjected to Lateral Loads*, Ph.D. Dissertation, University of Colorado, Boulder, Boulder, Colorado.

Rots, J.G., 1988, *Computational Modeling of Concrete Fracture*, Ph.D. Dissertation, TU Delft, Netherlands.

Seible, F., Priestley, M.J.N., Kingsley, G.R., and Kürkchübasche, A.G., 1991, *Flexural Coupling of Topped Hollow Core Plank Floor Systems in Shear Wall Structures*, Structural Systems Research Project, Report No. SSRP-91/10, University of California, San Diego, La Jolla, California.

Sherman, J.D., 2011, *Effects of Key Parameters on the Performance of Concrete Masonry Shear Walls under In-plane Loading*, M.S. Thesis, Washington State University, Pullman, Pullman, Washington.

Star, L.M., Givens, M.J., Nigbor, R.L., and Stewart, J.P., 2015, "Field-testing of structure on shallow foundation to evaluate soil-structure interaction effects," *Earthquake Spectra*, Vol. 31, No. 4, pp. 2511-2534.

Stavridis, A., Ahmadi, F., Mavros, M., Shing, P.B., Klingner, R.E., and McLean, D., 2016, "Shake-table tests of a full-scale three-story reinforced masonry shear wall structure," *Journal of Structural Engineering*, Vol. 142, No. 10.

Thompson, E.M., Kayen, R.E., Carkin, B., and Tanaka, H., 2010, *Surface-wave Site Characterization at 52 Strong-motion Recording Stations Affected by the Parkfield, California, M6.0 Earthquake of 28 September 2004*, Open-File Report 2010-1168, U.S. Geological Survey, Reston, Virginia.

TMS, 1994, *Performance of Masonry Structures in the Northridge California Earthquake of January 17, 1994*, a report by the Investigating Disasters Reconnaissance Team, The Masonry Society, Longmont, Colorado.

TMS, 2013, *Building Code Requirements and Specifications for Masonry Structures*, TMS 402/602, The Masonry Society, Longmont, Colorado.

Tremblay, R., Martin, E., Yang, W., and Rogers, C.A., 2004, "Analysis, testing and design of steel roof deck diaphragms for ductile earthquake resistance," *Journal of Earthquake Engineering*, Vol. 8, No. 5, pp. 775-816.

Veletsos, A.S., and Newmark, N.M., 1960, "Effect of inelastic behavior on the response of simple systems to earthquake motion," *Proceedings of the 2nd World Conference of Earthquake Engineering*, Japan, Vol. 2, pp. 895-912.

Voon, K.C., and Ingham, J.M., 2006, "Experimental in-plane shear strength investigation of reinforced concrete masonry walls," *Journal of Structural Engineering*, Vol. 132, No. 3, pp. 400-408.

Wald, D., Somerville, P.G., and Burdick, L.J., 1988, "The Whittier Narrows, California earthquake of October 1, 1987 – simulation of recorded accelerations," *Earthquake Spectra*, Earthquake Engineering Research Institute, Vol. 4, No. 1, pp. 139-156.

Project Participants

Federal Emergency Management Agency

Mai (Mike) Tong (Project Officer)
Federal Emergency Management Agency
500 C Street, SW, Room 416
Washington, DC 20472

Robert D. Hanson (Technical Advisor)
Federal Emergency Management Agency
5885 Dunabbey Loop
Dublin, Ohio 43017

Applied Technology Council

Jon A. Heintz (Project Executive)
Applied Technology Council
201 Redwood Shores Parkway, Suite 240
Redwood City, California 94065

Scott D. Schiff (Associate Project Manager)
Applied Technology Council
201 Redwood Shores Parkway, Suite 240
Redwood City, California 94065

Justin Moresco (Project Manager)
Applied Technology Council
201 Redwood Shores Parkway, Suite 240
Redwood City, California 94065

Project Technical Committee

Charles A. Kircher (Project Technical Director)
Kircher & Associates
1121 San Antonio Road, Suite D-202
Palo Alto, California 94303

Jeffrey W. Berman
University of Washington
Dept. of Civil & Environmental Engineering
201 More Hall, Box 352700
Seattle, Washington 98195

Kelly Cobeen
Wiss, Janney, Elstner Associates, Inc.
2000 Powell Street, Suite 1650
Emeryville, California 94608

J. Daniel Dolan
Washington State University
Department of Civil and Environmental Engineering
P.O. Box 642910
Pullman, Washington 99164

Andre Filiatrault
University at Buffalo
Department of Civil, Structural and Environmental Engineering
134 Ketter Hall
Buffalo, New York 14260

James R. Harris
J. R. Harris & Company
1175 Sherman Street, Suite 2000
Denver, Colorado 80203

Gregory Kingsley
KL&A, Inc.
1717 Washington Avenue, Suite 100
Golden, Colorado 80401

Dawn Lehman
University of Washington
Dept. of Civil & Environmental Engineering
201 More Hall, Box 352700
Seattle, Washington 98195

Weichiang Pang
Clemson University
Glenn Department of Civil Engineering
312 Lowry Hall
Clemson, South Carolina 29634

P. Benson Shing
University of California, San Diego
Department of Structural Engineering
9500 Gilman Drive
La Jolla, California 92093

Project Review Panel

Anthony Court (ATC Board Contact)
A.B. Court & Associates
4340 Hawk Street
San Diego, California 92103

James O. Malley
Degenkolb Engineers
375 Beale Street, Suite 500
San Francisco, California 94105

William T. Holmes
Structural Engineer
2600 La Cuesta Avenue
Oakland, California 94611

Steve Pryor
Simpson Strong-Tie
5956 W. Las Positas Boulevard
Pleasanton, California 94588

Onder Kustu
OAK Structural (retired)
P.O. Box 2074
Danville, California 94526

Jason Thompson
National Concrete Masonry Association
13750 Sunrise Valley Drive
Herndon, Virginia 20171

Masonry Working Group

Jianyu Cheng
University of California, San Diego
Department of Structural Engineering
9500 Gilman Drive
La Jolla, California 92093

Andreas A. Koutras
University of California, San Diego
Department of Structural Engineering
9500 Gilman Drive
La Jolla, California 92093

Jeff Corson
KL&A, Inc.
1717 Washington Avenue, Suite 100
Golden, Colorado 80401

Linda Peters
KL&A, Inc.
1717 Washington Avenue, Suite 100
Golden, Colorado 80401

Soil-Structure Interaction Working Group

Lisa Star
California State University, Long Beach
Department of Civil Engineering and Construction Engineering Management
1250 Bellflower Boulevard
Long Beach, California 90840

Jonathan P. Stewart
University of California, Los Angeles
Department of Civil and Environmental Engineering
5731 Boelter Hall
Los Angeles, California 90095

Reinforced Masonry Workshop Participants

David Bonneville
Degenkolb Engineers
1300 Clay Street, 9th Floor
Oakland, California 94612

C.B. Crouse
AECOM
1111 3rd Avenue, Suite 1600
Seattle, Washington 98101

Chukwuma Ekwueme
Thornton Tomasetti
707 Wilshire Blvd, Suite 4450
Los Angeles, California 90017

Sonny Fite
Target Corporation
50 South 10th Street, Suite 400
TP3-1110
Minneapolis, Minnesota 55403

Tom Gangel
Wallace Engineering Structural Consultants, Inc
200 East Mathew Brady Street
Tulsa, Oklahoma 74103

Steve Harris
Simpson Gumpertz & Heger
100 Pine Street, Suite 1600
San Francisco, California 94111

John Hochwalt
KPFF
1601 Fifth Avenue, Suite 1600
Seattle, Washington 98101

John Hooper
Magnusson Klemencic Associates
1301 Fifth Avenue, Suite 3200
Seattle, Washington 98101

Ed Huston
Huston Structural Engineering
8618 Roosevelt Way NE
Seattle, Washington 98115

Andres Lepage
University of Kansas
Dept. of Civil, Environmental & Architectural Engineering
2150 Learned Hall
1530 West 15th Street
Lawrence, Kansas 66045

Juan Murcia-Delso
University of Texas at Austin
Dept. of Civil, Architectural, and Environmental Engineering
301 East Dean Keeton Street, Stop C1700
Austin, Texas 78712

Arturo Schultz
University of Minnesota
Dept. of Civil, Environmental & Geo-Engineering
500 Pillsbury Drive SE
Minneapolis, Minnesota 55455

Paul Scott
Caruso Turley Scott, Inc.
1215 West Rio Salado Pkwy, Suite 200
Tempe, Arizona 85281

Kurt Siggard
Concrete Masonry Association of California and Nevada
6060 Sunrise Vista Drive, Suite 1990
Citrus Heights, California 95610

Andreas Stavridis
University at Buffalo
Dept. of Civil, Structural and Environmental Engineering
224 Ketter Hall
Buffalo, New York 14260

Jennifer Tanner Eisenhauer
University of Wyoming
Department of Civil & Architectural Engineering
2161 North 16th Street
Laramie, Wyoming 82072

FEMA

FEMA P-2139-3